Lehrstuhl für
Werkzeugmaschinen und Fertigungstechnik
der Technischen Universität München

Bifocal Hybrid Laser Welding: A Technology for Welding of Aluminium and Zinc-Coated Steels

Andreas Trautmann

Vollständiger Abdruck der von der Fakultät für Maschinenwesen der Technischen Universität München zur Erlangung des akademischen Grades eines

Doktor-Ingenieurs (Dr.-Ing.)

genehmigten Dissertation.

Vorsitzender: Univ.-Prof. Dr.-Ing. Horst Baier

Prüfer der Dissertation:

1. Univ.-Prof. Dr.-Ing. Michael Zäh
2. Univ.-Prof. Dr.-Ing. habil. Helmut Hügel,
   Universität Stuttgart

Die Dissertation wurde am 09.09.2008 bei der Technischen Universität München eingereicht und durch die Fakultät für Maschinenwesen am 17.12.2008 angenommen.

Andreas Trautmann

Bifocal Hybrid Laser Welding

A Technology for Welding of Aluminium and Zinc-Coated Steels

Herbert Utz Verlag · München

Forschungsberichte IWB

Band 230

Zugl.: Diss., München, Techn. Univ., 2008

Bibliografische Information der Deutschen Nationalbibliothek: Die Deutsche Nationalbibliothek verzeichnet diese Publikation in der Deutschen Nationalbibliografie; detaillierte bibliografische Daten sind im Internet über http://dnb.d-nb.de abrufbar.

ISBN 978-3-8316-0876-8

Printed in Germany
Herbert Utz Verlag GmbH, München
089-277791-00 · www.utzverlag.de

pro domo meo

et patria benedicta Bavaria mea

Geleitwort der Herausgeber

Die Produktionstechnik ist für die Weiterentwicklung unserer Industriegesellschaft von zentraler Bedeutung, denn die Leistungsfähigkeit eines Industriebetriebes hängt entscheidend von den eingesetzten Produktionsmitteln, den angewandten Produktionsverfahren und der eingeführten Produktionsorganisation ab. Erst das optimale Zusammenspiel von Mensch, Organisation und Technik erlaubt es, alle Potentiale für den Unternehmenserfolg auszuschöpfen.

Um in dem Spannungsfeld Komplexität, Kosten, Zeit und Qualität bestehen zu können, müssen Produktionsstrukturen ständig neu überdacht und weiterentwickelt werden. Dabei ist es notwendig, die Komplexität von Produkten, Produktionsabläufen und -systemen einerseits zu verringern und andererseits besser zu beherrschen.

Ziel der Forschungsarbeiten des *iwb* ist die ständige Verbesserung von Produktentwicklungs- und Planungssystemen, von Herstellverfahren sowie von Produktionsanlagen. Betriebsorganisation, Produktions- und Arbeitsstrukturen sowie Systeme zur Auftragsabwicklung werden unter besonderer Berücksichtigung mitarbeiterorientierter Anforderungen entwickelt. Die dabei notwendige Steigerung des Automatisierungsgrades darf jedoch nicht zu einer Verfestigung arbeitsteiliger Strukturen führen. Fragen der optimalen Einbindung des Menschen in den Produktentstehungsprozess spielen deshalb eine sehr wichtige Rolle.

Die im Rahmen dieser Buchreihe erscheinenden Bände stammen thematisch aus den Forschungsbereichen des *iwb*. Diese reichen von der Entwicklung von Produktionssystemen über deren Planung bis hin zu den eingesetzten Technologien in den Bereichen Fertigung und Montage. Steuerung und Betrieb von Produktionssystemen, Qualitätssicherung, Verfügbarkeit und Autonomie sind Querschnittsthemen hierfür. In den *iwb* Forschungsberichten werden neue Ergebnisse und Erkenntnisse aus der praxisnahen Forschung des *iwb* veröffentlicht. Diese Buchreihe soll dazu beitragen, den Wissenstransfer zwischen dem Hochschulbereich und dem Anwender in der Praxis zu verbessern.

Gunther Reinhart *Michael Zäh*

Vorwort

Die vorliegende Dissertation entstand während meiner Tätigkeit als wissenschaftlicher Mitarbeiter am Institut für Werkzeugmaschinen und Betriebswissenschaften (*iwb*) der Technischen Universität München.

Herrn Prof. Dr.-Ing. Michael Zäh und Herrn Prof. Dr.-Ing. Gunther Reinhart, den Leitern dieses Instituts, gilt mein besonderer Dank für die wohlwollende Förderung und großzügige Unterstützung meiner Arbeit.

Bei Herrn Prof. Dr.-Ing. habil. Helmut Hügel (i.R.), dem ehemaligen Leiter des Instituts für Strahlwerkzeuge der Universität Stuttgart, möchte ich mich für die Übernahme des Korreferates und die aufmerksame Durchsicht der Arbeit sehr herzlich bedanken.

Herrn Prof. Dr. Seiji Katayama, dem Leiter des Katayama Laboratoriums am Joining und Welding Institute der Universität von Osaka, gilt mein besonderer Dank für Gastfreundschaft und die wohlwollende Begleitung meiner Arbeit im Rahmen meines Predoc-Fellowships der Japanese Society for the Promotion of Science an der Universität von Osaka.

Darüber hinaus bedanke ich mich bei allen Mitarbeiterinnen und Mitarbeitern des Instituts sowie meinen Semestranden Florian Oefele, Stefan Hatzl, Michael Gruber, Julia Roelofsen, Florian Winkle, Martin Haberzettl, Benjamin Simstich, Wolfram Murr und Recep Burma sowie bei meinen Praktikanten Thomas Brandl, Guillaume Jolly, Stefan Kopicok und Felicitas Kopp, die mich unterstützt haben, recht herzlich.

München, im Dezember 2008 *Andreas Trautmann*

Contents

List of Symbols

$\overline{P}$	mean power
$\bar{v}$	average velocity of gas molecules
A	coefficient of optical absorption
A	cross-sectional area of the fusion zone/seam
a	amplitude of oscillation in LSW
a	variable of length defined in the pertinent chapter
a	half major axis of an ellipse
A_f	cross-sectional area of the filler wire
A_{gap}	cross-sectional area of a gap
A_{hole}	cross-sectional area of a circular hole
A_p	cross-sectional area of pores
A_{slot}	cross-sectional area of a slotted hole
$A_{1,2}$	cross-sectional areas of a nozzle
b	half minor axis of an ellipse
B	factor depending on beam profile
c	speed of light
c	length of a line in a conic section
c_b	silicon content in the base material
c_f	silicon content in the filler wire
c_{fz}	silicon content in the fusion zone
c_p	specific heat capacity at constant pressure
C_{sca}	scattering cross-section

d	diameter of a gas hose
d	depth of the keyhole
d	length of a line in a conic section
d	diameter of a particle
D	diffusion coefficient
d_0	diameter of the beam at the beam waist
d_f	diameter of the focal spot on the workpiece
D_o	diameter of nozzle at the orifice
d_w	diameter of the wire
e	length of line in a conic section
E_a	energy absorbed by the workpiece
E_m	energy to melt the base metal
f	focal length
f	designates a function
F	standard free energy (Helmholtz)
F	upthrust force
g	gravitational acceleration
H	enthalpy
h	relative height
I	laser intensity
I_{abs}	true current
I_s	reference current
K	beam propagation factor
L	mean free path

L	characteristic length
m’	mass of a vaporizing atom
M	factor depending on material
M^2	beam quality factor
n_g	density at surface of Knudsen layer
$Ø_f$	diameter of filler wire
p_{abl}	ablation pressure
Pe	Peclet number
p_g	hydrostatic pressure
p_{gas}	dynamic pressure of the process gas
p_{hd}	hydrodynamic pressure
p_i	partial pressure in a component of a mixture
p_l	radiation pressure
p_{total}	total pressure in a mixture of gases or vapours
p_v	vaporization pressure
$p_{\sigma\ tip}$	surface tension at keyhole tip
P_{HPDL}	power emitted by an HPDL
P_{BHLW}	total power emitted by BHLW
P_L	irradiated laser power
$P_{Nd:YAG}$	power emitted by an Nd:YAG laser
p_σ	surface tension per unit area
q	beam parameter product
r	radius
R	coefficient of reflection

Re	Reynolds number
Ry	Rykalin number
r(z)	radius of nozzle at height z
r(z)	radius of keyhole at depth z
r_b	radius of a gas bubble
r_1	radius at aperture
$r_1(z)$	principal radius of curvature or keyhole radius
$r_2(z)$	principal radius of curvature or keyhole radius
r_C	radius of a circle in a conic section
R_m	tensile strength
r_o	initial radius
$R_{p0.2}$	yield point
R_t	surface roughness
S_I	area of interface surface
S	entropy
t	angle for curve parameterization
T	thermodynamic temperature
T_n	nucleation temperature
T_m	melting temperature
T_v	vaporization temperature
u_g	velocity at surface of Knudsen layer
v	velocity of gas
v	velocity of a medium
v_{max}	maximum liquid flow velocity around keyhole

v_{min}	minimum liquid flow velocity around keyhole
$v_{1,2}$	velocity of a fluid
V	characteristic volume
V	factor depending on velocity
V	volume of the fusion zone
V_b	volume of the base metal
v_f	feed velocity of filler wire
V_f	volume of the filler wire
v_{gas}	velocity of gas particles
v_w	velocity of welding
V_w	wire deposition
w	width of weld seam
x_p	magnitude of porosity
z	depth of a cavity, i.e. of the keyhole
z	variable of length between 0 and length of a nozzle
α	thermal diffusivity of a workpiece
α	torch tilting angle
α	tangent angle
α	half the apex angle of a rotation cone
β	ratio of cross-sectional areas
ΔH_m	enthalpy of melting
Δp	pressure loss
Δp_i	individual pressure loss

Δp_{total}	total pressure loss
Δr	change of radius
ζ	loss or resistance number
η	viscosity
η_{EI}	efficiency of energy input
η_M	melting efficiency
η_p	process efficiency
θ	angle of divergence
κ	curvature
λ	wavelength of the laser
λ_{th}	thermal conductivity
μ	friction number
ν	kinematic viscosity
π	Archimedes' or Ludolph's constant
ρ	density
ρ_{air}	density of air
ρ_{gas}	density of gas
ρ_l	liquid density
σ	surface tension coefficient
σ	power fluctuation
τ	shear stress
τ_i	transmission coefficient
φ	tilting angle of optic or nozzle to surface normal of workpiece

List of Abbreviations

AC	alternating current
BHLW	Bifocal Hybrid Laser Welding
BPP	beam parameter product
BTR	brittle temperature range
c.f.	comparationem facere
CMW	conduction mode welding
cw	continuous wave
DFG	Deutsche Forschungsgemeinschaft; German Research Foundation
DIN	Deutsches Institut für Normung; German Institute for Standardization
DPW	deep penetration welding
ed.	designates the editor of a reference
e.g.	exempla gratia
EBW	electron beam welding
FDF	filler dilution formula
fps	frames per second
FWHM	full width half maximum
GMAW	gas metal arc welding
GTAW	gas tungsten arc welding
HAZ	heat affected zone
HPDL	high power diode laser

i.e.	id est
ISO	International Organization for Standardization
ITER	International Thermonuclear Experimental Reactor
LSF	line spread function
LSW	laser stir welding
LBW	laser beam welding
max.	maximum
MIG	metal inert gas
min.	minimum
mod. acc.	modified in accordance to a reference
Nd:YAG	neodymium doped ytterbium aluminium garnet laser
NIF	National Ignition Facility
RIM	Rimray aberration plot
RSP	resistance spot welding
rpm	rotations per minute
RT	room temperature
RZ	noise number, from German ‚Rauschzahl'
SCI	solidification crack index
SFB/TR10	Sonderforschungsbereich Transregio 10, collaborative research centre
SMB	small and medium sized business
tr.	designates the translator of a reference
USA	United States of America

Abstract

This doctoral dissertation presents the process innovation of Bifocal Hybrid Laser Welding (BHLW) and its application for highest quality seams in welding of aluminium, zinc-coated steels, and its potential for the welding of other materials. Over the last decade a plethora of process models has been conceived for fusion welding of aluminium. The respective empirical process models claim one of the following mechanisms as the cause for instabilities: intensity distribution fluctuations, deformation of the geometry of the keyhole, resonant vibrations within the melt pool, or detrimental physical properties of the melt. Although these empirical models are hardly senseless, this dissertation shows that none fully accounts for the formation of instabilities. State-of-the-art process technology for laser welding of aluminium and zinc-coated steels are detailed: gas metal arc welding, laser augmented arc welding, and multiple or specifically Twin Spot welding. For the last two technologies the results of individual benchmark studies are presented to allow for a fair comparison with BHLW for the reference alloy used in this dissertation.

A novel empirical process model for coated materials is developed herein. This model is predicated on a new categorisation of welding materials; the traditional one – according to their metallurgy – is replaced by one based on laser weldability. This new empirical process model rests on two propositions. The strata proposition accounts for surface coatings such as zinc and aluminium oxide. This proposition is based on an empirical observation previously unreported to account for instabilities: obstruction of the keyhole orifice by surface oxide of aluminium. The influence of vapour explosions inducing instabilities is expressed in the phase transition proposition. The explanatory amendments accompanying each individual proposition supply rules for the laser welder to design the process to counteract instabilities. The influence of invasive process gas shielding causing process pores in laser welding by a straw effect within the keyhole leads to a caveat concerning process gas; this caveat is based on empirical observations derived from in-situ high-speed x-ray photography. Based on these observations, a new empirical process model for laser beam welding of aluminium is developed accounting for all hitherto inexplicable phenomena for welding in vacuum and with nitrogen as shielding gas. Consistent with the empirical data a novel analytical mathematical-physical process model for the formation of gas porosity in aluminium is presented to amend the mathematical process model developed over the last few decades.

In a digression, ancillary technology for BHLW is presented that puts the new empirical and mathematical model to the test. To counteract the cause of porosity, as described by the gas entrainment caveat, a novel coaxial nozzle system for perfect shielding – as to which, if inert gases are used, gas is saved – during laser welding is introduced. By virtue of this nozzle system pores in aluminium can be eliminated, a fact that distinguishes this innovative coaxial nozzle system from state-of-the-art nozzles. This experimental result both verifies the empirical process model and validates the analytical mathematical-physical process model. All that is to the good, but note that the nozzle system is an innovation in itself as it allows for a minimum reduction of inert gas consumption of 60% and carcinogenic NO_x-emissions are simultaneously extinguished, again, in contrast to state-of-the-art nozzles. This is most welcome in light of increasingly stringent European regulation as to occupational exposure limits.

Proven process synergies warrant terming BHLW a ‘hybrid’. The doubling of process efficiency of BHLW as compared to its constituting laser welding processes – namely, HPDL and Nd:YAG laser welding – comes to explain the synergies observed in BHLW: increase of welding speed and penetration depth, reduction of porosity, and superior surface quality. Advantages of BHLW, not to be confused with synergies, and later treated separately, follow: robustness, segmentation of seams by avoidance of stop crater cracks, and defect-free seams in zinc-coated steels. Flawless welding of zinc-coated steels is a singular contribution to production engineering. Later the system technology of BHLW is presented. A sustainable prototype optic head was constructed for BHLW to be applied in industrial circumstances. The innovations in system technology of the optic head are these: easy adjustment of dichroic mirror mount by novel frame-in-frame gimbal construction and a beam trap utilizing a novel absorptive coating.

Filler material is necessary for some alloys of aluminium to avoid hot cracking. A novel filler dilution formula is deduced to adjust the process variables and filler feed rate to prevent cracks. The application of this filler dilution formula establishes that the process technology of BHLW generally reduces the absolute crack susceptibility of alloys, which, being sensitive, are otherwise very likely to crack due to the heat of laser beam welding. Further, BHLW is the first technology truly to ensure a continuous transfer of filler wire without droplet formation. In sum, an inexpensive and safe quality control of filler fire supply by an indicator current enables the foregoing complex optical signal processing.

Finally, the ramifications of the innovative BHLW for production and laser industry in Germany are discussed.

How to read this dissertation

This dissertation presents the state-of-the-art of research and technology in such a way as to advance modestly the subject by prolegomena on terminology and experimental method in welding technology in chapter 2 and by reiterated remarks on methodology whenever this is warranted by what is derived from the received literature. This knowledge establishes a framework to categorize, distinguish, and subsume the plethora of empirical and mathematical process *models* of instabilities found in the literature as described in section 3.1. Each empirical model is treated in isolation, and each is shown to be defective. However, an empirical process model has to be kept apart from the empirical results of its associated process technologies. The model may indeed have been misconceived, yet the welding results of a designed process based on its technology could surprisingly have their merits. Therefore, the results of process *technologies* are presented separately. In order to compare objectively the welding results of these competing technologies to BHLW, individual benchmark studies were conducted. In these studies, welding results for arc welding, laser augmented gas metal arc welding, and Twin Spot laser welding of aluminium were generated for the *reference* alloy used within this dissertation employing the same monitoring and preparation methods and devices as for BHLW. Since the reference alloy is an extrusion alloy, hardly any data for the reference alloy could be found in the literature. Extrusion alloys are notoriously difficult to fusion weld as detailed in paragraph 8.2 due to their susceptibility to cracking. EN AW-6060 is a challenging alloy in fusion welding and was *not* selected to be the reference alloy to put state-of-the-art process technologies and BHLW to a discriminating test but rather to satisfy the requirements of the collaborative research centre SFB/TR10. The objective of this SFB, which is kindly supported by the German Research Foundation (DFG), was the "integration of forming, cutting, and joining for the flexible production of lightweight space structures".

The production of aluminium profiles is an economical and well-established industrial process. The creation of value by assembling such profiles to lightweight space-frame structures hinges on a flexible joining technology. Laser welding can eliminate flanges and satisfies the demand of lightweight construction. LBW is evidentially advantageous as a technology for the challenge of *fusion* welding of aluminium. However, the intrinsic problems encountered in fusion welding of *aluminium* must be solved. Although the process technologies

of arc welding, laser augmented gas metal arc welding, and Twin Spot laser welding *are* state-of-the-art technologies, the welding results for the *reference* alloy and for zinc-coated steels of these technologies are scantly represented in the literature. Thus, the results of the benchmark studies of those technologies presented in paragraph 3.2 represent an *original* contribution to the state of research of laser beam welding, which is dealt with throughout chapter 3. For the remaining process technologies of multiple spot laser welding, oscillation and laser stir welding, and beam amplitude modulation welding, which are also featured in paragraph 3.2, benchmark studies could not be conducted as these technologies were unavailable commercially, the author not excepted. The results for other aluminium alloys and zinc-coated steels, other than the reference materials considered in this dissertation, are gathered from the literature and presented in such a way as to substantiate well-informed speculation regarding how the reference materials might behave for these process technologies as compared to BHLW. The reader must concur or not with these arguments after deliberation. The results of BHLW are briefly stated there and are detailed later, in chapters 6 and 7.

In order to understand the process of BHLW, the constituting processes are briefly described. New experimental results are presented to the reader in paragraph 4.1, though conduction mode welding (CMW) by high power diode lasers (HPDL), keyhole welding by the Nd:YAG laser, and influence of process gases have been well researched over the last few decades. Thus, a *phenomenological* account to understand deep penetration welding by BHLW is given. The interpretation of this phenomenological evidence represents *fundamental* knowledge for the reader to appreciate the development of a novel empirical process for laser beam welding of aluminium and other coated materials. This model is encoded in *abstract* propositions. The experimental evidence very briefly rears its head but is later described in detail in chapters 6 and 7. It is left to the reader to judge whether the new process model ought to be accepted. However, as the experimental evidence of the *effects* of BHLW is presented without reference to the model, the merits of BHLW should not called into question if the *causes* thought to arise from the model are overhauled or rejected in the future.

Before the results of BHLW are presented a *digression* on ancillary technology is inserted. The reader only interested in the technology of BHLW might skip chapter 5, a self-contained discussion of shielding gas nozzle, though the chapter does advance welding technology; it is given in the interest of thoroughness. Its

results are later quoted in chapters 6 and 7 on the synergies and advantages of BHLW. The digression will surely be of interest to the scientific reader.

In chapter 8 the system technology of BHLW is detailed. The continuity of filler wire supply is an easy means of quality control of filler transfer, suggesting an economic case, which is briefly outlined for the reader's own appraisal. As most chapters on BHLW are interconnected, *forward* references are in some cases unfortunately unavoidable. Results denoted by these references are generally the final upshot of a topic; whether or not the reader checks the later pertinent chapter immediately, the reader can *trust* that they will be satisfactorily established.

1 Introduction

1.1 Lasers are a key technology in the present

LASER is an acronym for light amplification by stimulated emission of radiation. But what *is* light? Light is *the* fundamental entity. In one notion, light was the first entity to be called into existence: "Let there be light" [GOD, p. 1]. In another notion the beginning of the universe was dominated by light or photons according to current theories in cosmology [LONGAIR 2003, p. 535].

More down to earth, lasers constitute a commonplace technology. Whether we are conscious or not of their being mundane depends on our understanding of the word *light* in what constitutes a laser. Light designates the visible range of the electromagnetic spectrum. Although the first laser ever built by Maiman [MAIMAN 1961] emitted in the visible range, Albert Einstein's theory, which describes its physical principle, is by no means limited to *light* but applies to *radiation* in general. In fact, most modern lasers do *not* emit in the visible part of the electromagnetic spectrum. The term 'laser' is misleading - it encourages misconceptions. Putting aside superficial aspects of the laser's history militates in favour of calling it today what it actually is:

electromagnetic radiation amplification by stimulated emission of radiation,

namely: ERASER.

The acronym '*eraser*' is a pun and does not allude to the *power* of the radiation those systems generate, but 'eraser' is very descriptive. However, the author will regrettably use the nowadays more conventionally acceptable acronym 'laser' instead of the precise 'eraser'. The properties of the radiation are characteristic of lasers. Their radiation is monochromatic, exhibits little divergence, and is temporally and spatially coherent. There are laser systems, which are subsumed in this category, whose radiation is neither stimulated nor amplified. Emitting semiconductors assembled in high power diode laser are exemplary. LEDs should therefore be treated as sources of laser radiation since their radiation is monochromatic and shows, within certain limits, reduced divergence.

Keeping this in mind one should reconsider and, it is hoped, broaden one's views of lasers. Lasers are an integral part of everyday life. Most little flashing lights

are actually sources of radiation that have the properties characteristic of lasers. They are built into CD players, handyman tools to regulate water levels, and even cutting-edge kitchens in London where they are used by prominent gourmet chefs [KALWA 2005].

This is contrary to the use of lasers in films other than documentaries. In science fiction and other imaginative works, lasers serve as a symbol of inexplicable powers. In Star Wars villains cut other beings heads off with a 'laser sword', and James Bond was almost cleaved in half by Goldfinger's laser. Never mind that in reality the Star Wars swords are pyrotechnic effects and that the laser that seared through the gilded plate to which 007 was chained was actually an acetylene flame. However, though these pictures were fictional at the time they were being shot, what they envisaged is reality *now*. Laser beams have been developed to serve as defensive weaponry. Ballistic missiles are to be destroyed in the stratosphere by stupendous laser beams. Needless to say, lasers were capable of cutting and welding metal just a few years after Goldfinger's premiere. Seeming fantasy can indeed pave the way to the breakthroughs now shaping our reality. Such fantasy serendipitously points the way to the innovations shaping our reality.

1.2 The future is 'Laser Age'

The history of civilization can be divided by the technology extant in each epoch: The Stone Age was followed by the Bronze Age and then the Iron Age. And knowledge and technology appear to accelerate as age follows age. The industrial revolution was followed comparatively not long thereafter by the Nuclear Age. Where are we now going?

The ages are normally named retrospectively - later generations appraise their ancestors' times based on the decisive advance the impact of which can be said to have brought about a revolution. Indeed, such an advance is necessary for us to note with clarity the demise or subordination of the old and the dawning of a new age.

Let us consider the current situation and peer into the future in order to guess what age our descendants may judge us to have inaugurated. Within a mere six years of the new millennium, in 2006, the Nobel Prize for physics honoured contributions to the development of laser-based precision spectroscopy including

the optical frequency comb technique, the details of which will not herein be given [HÄNSCH 2006]. Suffice it to say that the ramifications of Hänsch’s findings are obvious to the scientifically informed public. The laser frequency comb allows an improvement of at least one order of magnitude in the accuracy of time measurements. This will in due course lead to a greatly enhanced insight into the physics of our world, as did all previous improvements of accuracy. Concurrent with the turn of the century, laser systems capable of output powers of several hundred kilowatts were designed. Their funding may have been due chiefly to their potential use in preemptive missile defence, but they are put to other uses as well.

At the National Ignition Facility (NIF) of the Lawrence Livermore Laboratory, in the American state of California, 192 ultraviolet lasers eventually came to form the world’s largest laser [BIBEAU 2006]. This laser has an output power of 1.8 MJ which will be deposited into a hohlraum target. By 2010 this deuterium-tritium target will be so compressed that it will ignite and burn, which in turn will liberate more energy than is required for the laser to ignite the fusion reaction. The International Thermonuclear Experimental Reactor (ITER) championed by the European Union serves the same objective. Early in the Nuclear Age *fission* provided energy to power our civilization. However, fission creates radioactive waste and the proliferation of this waste engenders the enormous hazard of the potential construction of illicit nuclear weapons. Therefore the nuclear age cast a pall from its inception, and, in the current geo-political climate, fraught as it is with the possibility of additional crises, one cannot be sure how the Nuclear *Fission* Age will terminate, a fact that confounds an assessment now of retrospective judgment decades or centuries in the future. Although nuclear fission does allow for the triggering of a fusion reaction in the form of a hydrogen bomb, it is clear that this energy can be put to entirely peaceful ends. *If* nuclear fusion can be tamed by a controlled reaction in the National Ignition Facility, this would be a scientific achievement unparalleled in world history, one comparable only to stupendous leaps in evolution such as the development of language. It would potentially transform our world for the better.

The Club of Rome predicted in 1972 ‘The Limits to Growth' [MEADOWS 1972, MEADOWS 1974]. And indeed we are now experiencing scarcity of basic commodities with the constant rise in the cost of energy and other resources. An inconsumable, virtually infinite, and emission-free source of energy, which is precisely what fusion would put at our disposal, would enable humanity to commence a new kind of *civilization*. Energy in the coming Nuclear *Fusion* Age

will not stem from consumption of *resources*, which are by definition only accessible *locally* or *nationally,* but will be *derived* from *science*, which by definition is shared *globally*. Nuclear fusion will guarantee the welfare of humanity for centuries or millennia. This breathtaking accomplishment, being potentially enabled by laser technology, would earn our transitory age the epithet: Laser Age.

Savour this outcome, because it will solve an immense problem already bedevilling the planet: the shortage of energy.

1.3 Lasers are the key to welding novel materials

Notwithstanding the decisive contribution lasers can make to civilization's advancement, less ethereally, one has to notice the immediate importance of lasers to Germany's economy. Germany lost out in many areas of technology in the past decade or could not capitalize fully on inventions and innovations it generated. Laser technology is an exception. Globally Germany is a leader both in markets and in technology. Its share of the world's laser system market is about 40%. This is a tremendously enviable situation, which can be retained and even expanded. The market research of the Spectaris/VDMA report 2006, however, shows that production is outsourced to countries with lower labour costs. Innovations are crucial if Germany wants to secure and expand its position.

However, innovating is in many cases difficult. Take welding, which is an ancient technology. In antiquity some regarded Glaukos of Chios to be the inventor of welding. He produced a vessel by *solid phase joining*, that is, by a blacksmith hammering two iron pieces together. After that seminal event, innovations were extremely slow-paced [AICHELE 2005].

Today welding can be described as the joining of two components by coalescence of the surfaces in contact with each other. This coalescence can be achieved by melting the two parts together, termed *fusion welding*, or by bringing the two parts together under pressure, perhaps with the application of heat, to form a metallic bond across the interface.

This glacial progress is true even in our day. Classical arc welding has experienced only small steps forward in the past decade. Electron beam welding allowed welding of joints of high aspect ratio (c.f. equation 3.3) in vacuum. The advent of high-power laser systems manifested additional progress. In laser

welding technology each new laser system available facilitated novel processes. For industrial laser welding the following systems were chronologically employed: CO_2 lasers, Nd:YAG lasers, high power diode lasers (HPDL), and - at this writing - disc or fibre laser technology is being considered.

However, for welding, the weld*ability* of the materials to be joined is a prerequisite; where it is lacking, even elaborate welding technology seemingly cannot compensate. Very much the same holds for any other joining technology; indeed, the pivotal point for introduction of new materials into a production chain is the joining technology. Unfortunately, this is not always borne in mind when novel materials are designed. Semi-finished products, such as sheets or profiles, which cannot be joined, can never become products. Adequate joining technologies are absent for many materials. Hence, they have been developed in vain because they cannot be used.

This is notable for the application of aluminium in car body manufacturing. Forecasts suggest that Europe and North America will retain the biggest shares of the global automotive market until 2011 or later. Thus, most car manufacturers try to satisfy the demands of both markets to maximize the number of potential customers. And most European car producers are as much dependent on their North American as on their home markets.

In late 2004 the U.S. Secretary of Transportation proposed a major regulatory upgrade in side-impact crash protection for all passenger vehicles [INTERNET 1]. Accordingly, Federal Motor Vehicle Safety Standard 214 is about to be strengthened with consequent requirements for crashworthiness. Passive security systems alone will not meet the demands of this new dispensation. Indisputably the space frame and body shell will have to be toughened to absorb the additional distortional energies. It seems inevitable that the car chassis will weigh more.

Europe has bound itself to reduce overall CO_2-emissions to fight climate change. The 2007 Bali agreement, which followed up on Kyoto, may or may not be implemented worldwide: On the one hand, pressure from environmentalist groups is formidable; on the other hand, costumers are seeking more economical vehicles since fuel prices are high owing both to the high price of oil, now at a decade-high, and to petroleum taxes.

To meet these demands the automotive industry has to pursue two diametrically opposed aims. In the USA vehicles need to be much tougher, meaning heavier, but, in Europe, lighter, in order to consume less fuel [ZÄH & TRAUTMANN 2005].

Light-weight design and further application of light-weight alloys can deal with this predicament by reducing weight as well as increasing strength. Light-weight material and design construction can cut the Gordian knot of these seemingly contradictory demands. Hence, joining techniques are needed that satisfy the requirements of modern vehicle manufacturing [ZÄH & TRAUTMANN 2004].

These techniques need to be reliable and robust. They need to yield structures that can be mass-produced in such a fashion as to ensure quality control that can be monitored by sensor systems [ZHAO 1990]. They need to meet the disparate expectations of both corporations – which seek profits – and consumers – who aspire to thrift. Thus, the new technologies will be scrutinized by manufacturing, economics, and sales.

The objective of this dissertation is to present an innovative process in laser technology for **robust** and **stable** welding of *all* alloys of aluminium *and* of zinc-coated steels. The process is termed Bifocal Hybrid Laser Welding (BHLW), as it utilizes two separate laser sources, namely an Nd:YAG laser and an HPDL. These laser sources can be independently focused on different focal planes: the system is thus termed *bifocal*. The lasers interact in the same process zone; hence, they constitute a *hybrid.* Proven synergies are presented to justify indisputably the designation of the process as ‘hybrid’, a designation that seems, in other contexts, to have been misplaced or which has been used hyperbolically. Additionally, advantages of BHLW for process robustness are detailed to convince the reader of its unparalleled successes in contrast to other laser welding techniques.

1.4 Current laser sources and their system properties

In figure 1.1 the commonly available laser sources for welding are shown. They are characterized by their wavelength, which is typical of their laser active medium.

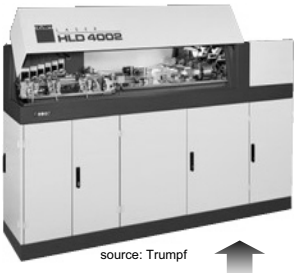

source: Trumpf

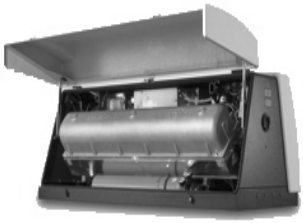

source: Rofin

laser system	fibre	Nd:YAG	HPDL	CO_2	GMAW
wavelength	1070 nm	1064 nm	808 - 940 nm	10640 nm	---
power	20000 W	100 - 4000 W	100 - 6000 W	100 - 20000 W	~ 3000 W
BPP	8 mm*mrad	12 - 25 mm*mrad	40 - 400 mm*mrad	4 - 10 mm*mrad	---
relative focal spot size	●	●	▬	●	---
intensity	10^6 - 10^8 W cm^{-2}	10^5 - 10^7 W cm^{-2}	10^4 - 10^5 W cm^{-2}	10^6 - 10^8 W cm^{-2}	10^3 - 10^4 W cm^{-2}
efficiency	approx. 25%	3 ÷ 5%	approx. 35%	approx. 10%	approx. 90%
beam guide	fibreoptic cable	fibreoptic cable	fibreoptic/ direct emission	mirror systems	---

source: ipg

source: Laserline

source: Lorch

Figure 1.1: Technical digest of laser systems and comparison to a gas metal arc welding system

For scientific investigations the quality of the beam is of primary interest. It is described by the M^2 factor:

$$M^2 = \frac{1}{K} = \frac{\pi}{\lambda} \cdot \frac{d_0 \cdot \theta}{4} = \frac{\pi}{\lambda} \cdot q \qquad \text{(Equation 1.1)}$$

where M^2 is the beam quality factor, K is the beam propagation factor , λ is the wavelength of the laser (m), d_0 is the diameter of the beam at the beam waist (m), θ is the angle of divergence (mrad), π is Archimedes' or Ludolph's constant, q is the beam parameter product (mm * mrad). The M^2 factor is defined for a diffraction-limited Gaussian beam [DIN ISO 11146-1].

With regards to manufacturing, secondary virtues of individual laser systems play a key role. For brevity's sake only continuous wave (cw-lasers) are considered. The CO_2 laser can provide multi-kilowatt output powers at excellent beam quality. Its wavelength does not permit efficient fibre transmission; mirror guiding systems are needed which infringe on flexibility during production when flanged to a robot arm. Yet the CO_2 laser is the most common laser in manufacturing. High power diode lasers are assembled from semiconductor LED's; their wall-plug efficiency is superior as they lack a resonator medium which degrades electro-optic efficiency. However, their beam quality is poor. The stack by which the LED's are interconnected can be mounted to a robot arm. Such a directly emitting laser permits beam formation - rectangular intensity distributions as well as rotationally symmetric intensity distributions in diode ring laser setups - according to need. Its radiation can be delivered via a fibreoptic cable but only at the cost of a power loss of approximately 25%. The Nd:YAG laser is a classical slab laser, which provides superior beam quality at a very low wall-plug efficiency and can be easily guided by fibres. Disc and fibre laser system were just recently cleared for application in manufacturing. Both systems are distinguished by their excellent beam quality and can be delivered by fibreoptic cable. A disc laser is scaled in power intervals based on how many active discs are combined within the system. A fibre laser is made up of individual single or multimode fibre laser modules, whose feeding fibres are spliced together to achieve the output power desired. The maximum attainable output power and beam parameter product appear to be inversely proportional and can be varied within certain limits according to the manufacturing objective. The fibre laser is more flexible with regards to selection of beam parameters and output powers than the disc laser. The system technology of fibre lasers facilitates later up-scaling if necessary.

2 Prolegomena on Terminology and Experimental Methods

It has been shown above that the acronym ‘laser’ does not fully convey the properties that are actually characteristic and typical of itself – eraser is more apt. The term, ‘laser’ potentially misleading for many, is especially so for persons unfamiliar with the subject, a group constituted in no small part by students. Like confusion prevails regarding the word “hybrid”. Indeed, it seems to have transmogrified into a fancy label for almost anything to which attention is sought to be drawn.

‘hybrid’ is used in science to designate the crossbreed of two distinct entities, such as the hybridization of genes of different origin in microbiology, to create a new united entity by advantageous *interaction*. The mere combination of two processes does not make up a ‘hybrid’ but only represents augmentation without interaction. Hence, whether a combination of two processes constitutes a hybrid depends in turn on whether the combination *transgresses* the sum of the constituting processes. In a word: The whole must be more than the sum of its parts.

Hence, the epithet ‘hybrid’ inherently demands a synergy. In laser welding, ‘hybrid’ habitually refers to the combination of gas metal arc welding (GMAW) with laser deep penetration welding. However, as will be argued in paragraph 3.2, this is not a true hybrid because claimed synergies do not seem to materialize. The laser beam does nothing more than support the arc process by advantageous redistribution of melt. Again, this terminology is misleading since the ‘hybrid’ evidentially is not a true one but merely an arc welding process supported by laser. It is therefore called laser augmented GMAW welding herein.

This dissonance is implicated in the experimental methods used by numerous experimenters. In this context the notion of *ceteris paribus* conditions - all other things being equal - should be noted. Varying one parameter while keeping the others fixed does not in all cases allow comparison of results as normalization might be necessary for this objective. For example, when measuring the heat released on variations of the speed of LBW in a given workpiece one must be cognisant of the *relative* flow of process gas. Helium is a better cooling agent than argon due to its high volatility. When the speed of welding is increased, the flow of process gas must be increased also in order to *normalize* its cooling effect

with regards to the heat released per unit length if the heat input is to be accurately measured. It is obvious too that the absolute flow and the flux of process gas needs to be recorded and stated in publications; the full set of parameters must be quoted to make comparison of results feasible.

Authors must indicate whether graphs are *charts* or *diagrams*. The *calculus of errors* needs to be adhered to. Disappointingly, these things are more often honoured in the breach in welding research. By obeying this code of good practice in experimental technique, the author hopes that this dissertation offers substantial advances. In the pertinent chapter these caveats on experimental methodology are outlined in more detail.

The reference sample within this paper is, unless explicitly stated otherwise, a 100 x 100 x 2 mm^3 extruded flat profile of EN AW-6060, temper T66, abutted perpendicular to the direction of extrusion in a butt-joint setup. Temper T66 means that the alloy was solution heat-treated and artificially aged. The chemical composition of EN AW-6060 is given in table 8.2.

No root protection process gas was used. The samples were parallel clamped at a distance of about 3 cm from the seam. The setup can be seen in figure 3.6. The same material was used for the benchmark studies of laser augmented MIG (also known as Laser-MIG-Hybrid) and Twin Spot welding. The process gas was supplied by a coaxial nozzle shown in figure 5.15. The experimental optical systems were moved by a KUKA 150 robot. The setup is described in chapter 8 and can be seen in figure 8.1.

The high-speed camera system permitted the adjustment of the rate of frames per second (fps). To judge the time scale of phenomena as depicted by the associated snapshots the exposure time would best be quoted. However, the camera system adjusted the exposure time for fluctuating brightness to prevent damage to the recording unit by excess luminosity. Hence, for technical restrictions only the frame rate could be recorded; note that the recorded *maximum* exposure time, that is the reciprocal value of the frame rate, might be lower in reality.

Further remarks on terminology and experimental methodology follow as a preliminary section to each respective chapter. Examples include the distinction between empirical and mathematical process models in paragraph 3.1 and demands and rules for empirical process model building in paragraph 4.2.

3 State of Research and Technology of Laser Beam Welding of Aluminium

3.1 Process models of instabilities

In this chapter the state-of-the-art of process models of instabilities is dealt with. The major propositions of these models are enumerated and discussed with regards to the references. Some of these models sparked the development of novel process technologies to counteract instabilities. The results of these welding technologies might be significant even if the process technology was based on a defective process model. Their experimental results are treated separately since these technologies might have their practical merits.

3.1.1 Introduction to process modelling

The modelling of laser beam welding (LBW) can be subdivided into two major classes: empirical and mathematical process models.

Empirical process models are based on *intuitive* concepts that stem from empirical process monitoring, *in-situ* by high-speed photography, or x-ray imaging. Empirical observations also originate from *a posteriori* interpretation of cross-section macrographs, x-ray photography, ultrasonic testing, and EDX-analysis of element content distribution or from other sources.

This is to name but a few hitherto employed techniques in the empirical analysis of laser beam welding. The accuracy and quality of pictured data is strongly dependent on the technical capabilities of the technology with which it was visualized. The in*sight*, which this data provides, can be altered or even changed when the technology of its visualization is refined. The interpretation of these snapshots of welding processes leads to the formulation of an abstract empirical process model.

Such a model is represented by a *common set of rules of behaviour*. This set of rules represent the propositions of the model. The notion of rules suggest that *equivalent* species behave according to the same common set of rules under *comparable* (or *ceteris paribus*) conditions. These conditions are set by the intensity distribution created by the specific laser, the shielding gas, and the

welding speed. Hence, these models tacitly imply *categories* in which the species involved and the conditions imposed can be subsumed.

Positively, the utility of such empirical process models rests upon their ability to predict the behaviour of cases, which were hitherto not assayed. These models enable an *extrapolation* of behaviour within the limits of their applicability set by their categories and rules. *Negatively*, if the processes suffer from problems rife in LBW such as formation of humps, pores, and spatter, empirical process models suggest how to design a counteracting technology. The process technologies of laser augmented GMAW, laser stir, and oscillation laser welding (c.f. paragraph 3.2) were developed with explicit reference to a specific empirical process model of *instabilities*, i.e. as formation of humps, pores, and spatter.

This chapter attempts to state the descriptive rules of behaviour of the empirical process model for LBW of aluminium to explicate the categorization of the species employed. This chapter tries to clarify which conditions can be assumed to be *ceteris paribus*. The empirical models will be validated by their *success* in extrapolation, i.e. achieving desired results, or by their *ability* to lead to the development of technologies counteracting undesired behaviour.

Mathematical process models are based on the laws of physics. They *vary* according to the laws of thermodynamics governing LBW and can be assumed to be *a priori*, because these laws have never been falsified. If the theoretical reasoning is stringent and complete in the sense that all simplifying assumptions are stated, the equations expressing the associated dependencies should not be readily cast with doubt. Whenever they are made quantitative, they rest upon the accuracy of those natural and material *constants* entering the calculation. The values of those constants are determined by experiments. Hence, they represent a possible source of error. One has to bear in mind that the *concept* of constants in the realms of physics eventually means that within the theory sustained they are regarded as *unchangeable*. They are only measured to a certain degree of accuracy. The experiments suffer from certain shortcomings (c.f. paragraph 5.2) imparting errors on the magnitudes measured. Or as far as material constants are concerned, their values vary from one alloy of aluminium to another or even more malignantly from batch to batch for a given alloy. Although a very accurate measurement is necessary to quantify the mathematical model, these measurements are often too time and money consuming to be carried out for each individual case.

The *success* of such a mathematical process model is determined by the degree of congruence with the experimental measurements, i.e. how good it ‘fits’ and therefore *explains* the data. It is sometimes not easy to test the equations of a mathematical process model against experimental data in cases where these formulas are not *analytical*. The method of finite elements (FEM), which requires a *numerical* solution at discrete points being meshed according to interest, reaches a compromise between a desired accuracy, which is scaling with the interstitial distance within the mesh, and the processing resources of the computers deployed. But even by *simulating* the continuity of solutions of functions by fitting up the FEM discretization, the results could not always be matched with experimental data [DAVÉ 2003].

At this point a caveat should be stated: the above is not intended to cast doubt on the fact that mathematical process models *do* actually fit experimental data and that they explain this data by *deduction* from the underlying laws of physics; this is most positively stated. It is merely pointed out that it may be difficult to establish the *success* of a mathematical model owing to the complexity of calculus and inaccuracy of constants measured. If the mathematical process model can easily be quantified and does nonetheless not fit the experimental data, the experiment needs to be critically questioned and not the mathematical process model, which is deduced from the laws of physics.

In this chapter some mathematical process models for LBW are presented and the assumptions on which they are based. It is shown that the problems of these mathematical models, when applied to LBW of aluminium, root in a misconceived design of experiment. Such models can be mathematically correct but whether they mirror empiric reality is difficult to comprehend. In paragraph 4.3 the author will present his mathematical process model for process gas porosity formation in LBW of aluminium.

3.1.2 Empirical process modelling of instabilities

In this dissertation *any* seam imperfection introduced by the welding process adding to blow holes, pores, and spatter is subsumed in the general *category* of 'instability'. Rapp *claimed* that all these instabilities are just different manifestations which originate from the *same* physical cause [RAPP 1996, p. 115].

Over the years a plethora of empirical models explaining the instabilities in LBW have been discussed. Seam imperfections in LBW were rife in industry and sparked a lot of research. The approach of this research was *negative*, because the objective was to improve on the empirical process models of *instabilities*. This was seen to be the key to eventually obviate these instabilities by design of an apt process technology, which stabilizes the welding process.

A recent review paper on empirical process models of instabilities is not available since it seems almost impossible to describe all the models in detail. In particular, some authors support opposing views with regard to one aspect of some model but the same idea when it comes to other aspects.

To summarize the state of research the major *conceptual hypotheses* are presented by stating the corresponding **proposition**. The proposition states the *mechanism of instability* which *causes* a seam imperfection in LBW. The authors championing those propositions can be found in the references given.

Instabilities are due to:

Proposition 1: Fluctuations of the intensity distribution on the workpiece

Proposition 2: Deformation of the geometry of the keyhole

Proposition 3: Resonant vibrations of the melt being part of a self-exciting system

Proposition 4: Physical properties of the melt of a specific material

3.1.2.1 Intensity distribution fluctuations

Let us follow the laser beam's path of propagation to consider sources of intensity fluctuations in turn.

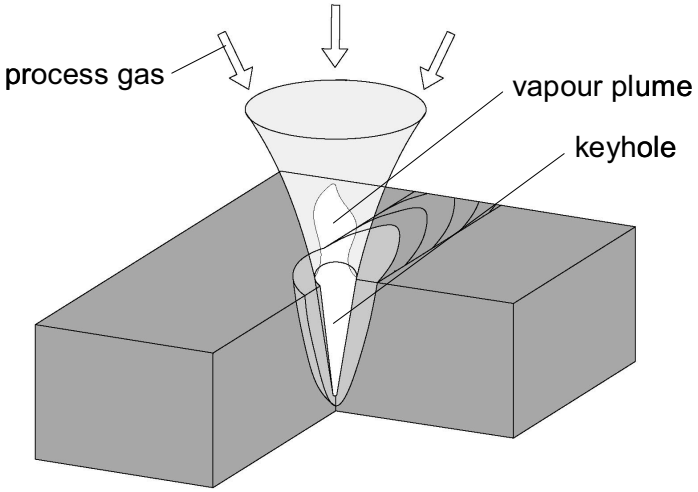

Figure 3.1: Laser keyhole welding: beam caustic is indicated by a cone, welding direction out of page alongside elevation

The first source of such fluctuations can be variations of *power emitted* by the laser system:

$$RZ = \frac{\sigma}{\overline{P}} \qquad \text{(Equation 3.1)}$$

In this equation σ is a measure for the power fluctuation represented by the root mean square deviation scaled to the mean power $\overline{P}$ of a given laser system.

Nowadays, variations in output power of cw-laser systems are negligible with regards to the welding result, because modern laser systems exhibit noise numbers *RZ* as low as 0.1.[1]

Subsequently to the resonant chamber the beam passes through some optical systems focusing, collimating, or guiding the beam. The lenses' shapes and their coatings are not perfect enough to prevent heating-up, which is leading to a degradation of beam quality. This is overcome by proper cooling of the optical systems, which keeps the temperature constant during laser emission preventing any corresponding fluctuations. The excellent M^2 values recently attainable by disc or fibre lasers allow small aperture lenses to be used, which are much more demanding to be cooled uniformly.

Beyond the focusing lens the laser beam propagates through space possibly encountering a vapour plume with which it could interact. This vapour plume forms above the melt pool if the intensity of the laser irradiated on the workpiece is beyond threshold to initiate vaporization. For steels this threshold is in the order of magnitude of 10^6 W m^{-2}, whereas for aluminium it is $2 \div 4 \cdot 10^6$ W m^{-2}.

The mechanism of inverse bremsstrahlung was believed to cause a power *absorption* by the metal vapour plume [KATAYAMA 2007b]. If a free electron is in the vicinity of an ion they form a dipole, which can absorb a photon and thereby increase its energy. The prerequisite for inverse bremsstrahlung are free charges. The interaction between vapour plume and laser radiation is strongly dependent on the laser's wavelength, because the absorption coefficient of the vapour scales according to $\sim \lambda^2$. Plasma absorption mechanisms can be theoretically neglected for HPDLs, whose wavelength is 808 and 940 ± 10 nm (FWHM), for Nd:YAG lasers, whose wavelength is 1064 ± 1 nm, and for fibre and thin disc lasers, whose wavelength is 1070 ± 1 nm. Though possible according to theory, plasma absorption could not be experimentally sustained for CO_2 lasers, whose wavelength is 10640 nm.

[1] The noise number is defined for laser systems without *load*, i.e. no radiation is re-entering the resonant chamber via back reflection into the optical system from the workpiece. Such back reflections lead to a reduction of emitted power in some dated CO_2 lasers and cause a corresponding reduction in penetration depth in LBW of highly reflective materials. In current CO_2 laser systems such artefacts are prevented by a shutter.

The experimental evidence against plasma absorption for *Nd:YAG lasers* when welding *aluminium* will be briefly outlined in the following. Plasma absorption would lead to a very hot vapour plume and an associated ionic spectrum, which could not be proven by spectroscopic measurements of the aluminium vapour plume's temperatures [FRANZ 1998, p. 28].

In fact, the aluminium plume turned out to reach a maximal temperature of only 7000 K [FUNK 1994, p. 76]. Thus, fluctuations by plasma absorption had to be rejected even under the most favourable circumstances for them to arise.

The vapour plume seemed to glow when viewed by a camera system. In section 4.1.3 high-speed photography of keyhole dynamics in aluminium welding is discussed. Aluminium is covered by a sturdy oxide layer, which occasionally covers the keyhole. The glow does not instantaneously stop upon coverage of the keyhole. This shows that the glow of the vapour plume is not caused by an emitting plasma. The emissions from plasma should not *instantaneously* cease when the keyhole is closed, because the exciting laser beam is still propagating through the plasma plume above the keyhole. It was accidentally proven that the glow seen in high-speed photography stems from secondary radiation, which emerged from the keyhole and was subsequently scattered towards the camera by particles within the vapour plume.

Whether this vapour plume is actually ionized to form plasma depends on the wavelength, the metal vaporized, and its alloying elements as well as on the ionization potentials of the gases in the surrounding atmosphere. The formation of plasma is suppressed in LBW if *inert* gases are used, since inert gases show characteristically low first ionization energies.

Diametrically opposed views can be found in the extensive literature on this topic: Quite a number of authors discuss plasma shielding effects, which reduce intensities [BECK 1996, p. 79 f.; BEYER 1995, p. 75 f.]. Some authors even postulated a 'lensing' effect, which increases the intensity.

A *direct* measurement can be performed utilizing a second metrology laser beam, which emits at the same wavelength as the laser used for welding. This metrology laser beam was passed through the vapour plume at right angle to the beam for welding. The power of this metrological beam is incident on a measuring detector [SEPOLD 1976; BESKE 1991 & 1992; KLASSEN 2000, p. 17; FABBRO 1990; MAZUMDER 1987]. Franz refined this experiment by designing a setup in which the metrology laser propagates coaxially to the laser beam

employed for welding [FRANZ 1998, p. 51 f.]. All these experiments showed that no significant absorption of power took place regardless whether the aluminium plume was vapour *or* plasma. In fact, the power density distribution spreads out upon passing through the vapour plume, whereas the total power irradiated stays constant. The absence of a power loss implies *elastic* that is *Rayleigh scattering*.

For welding with Nd:YAG lasers the clusters of vapour particles fulfil the conditions for the Rayleigh approximation of scattering that is for small clustered particles. In this case the scattering cross section C_{sca} is proportional to the diameter d of the clustered particles [LANDOLT BÖRNSTEIN 2004, p. 21]:

$$C_{sca} \sim d^6 \qquad \text{(Equation 3.2)}$$

The vapour plume can be regarded as nearly *transmitting* but gives rise to a significant spread of the beam by scattering. Scattering decreases the intensity on the workpiece and reduces the *causal* vapour plume. The intensity and the vapour plume constitute a *system*. For the scope of this dissertation the author holds the experimental result of a divergence of the laser beam and that the scattering mechanisms are complicated. Diffraction is not considered herein.

Hence, the temporal degree of *vaporization* above threshold intensity and the local fluctuation of intensity dependent on the temporal degree of *scattering* by this vapour constitute a *chaotic system* responsible for instabilities of welding due to fluctuations of the intensity distribution on the workpiece (Proposition 1, c.f. p. 14).

Process gas is the remedy of these causes of instabilities as it affects the size of the vapour plume and supports its spatiotemporal stability. The physical properties of the most common process gases are given in table 3.1:

process gas	symbol	density at 15°C (kg m^{-3})	1st ionization energy (eV)	heat coefficient at 20°C (W m^{-1} °C^{-1})
argon	Ar_2	1.67	15.76	0.016
helium	He_2	0.17	24.58	0.143
carbon dioxide	CO_2	1.85	13.70	0.014
oxygen	O_2	1.34	12.50	0.024
nitrogen	N_2	1.17	15.80	0.024

Table 3.1: Physical properties of selected process gases

These gases can be used as *process* gases in laser welding. In fact, the absence of a voluntarily introduced gas normally means that one is merely unaware that ambient air acts as process gas.

The major constituents of air are nitrogen, oxygen, and carbon dioxide. These *active* process gases lead to exothermic chemical reactions in the keyhole in deep penetration laser welding of aluminium thereby enlarging the vapour plume. Argon and helium are *inert* process gases with respect to such chemical reactions. It is a well accepted observation that the use of helium is to be favoured to argon, because helium is better than argon to reduce the vapour plume [FABBRO 2007]. Most authors gave as explanation that helium requires about 10 eV more to be ionized as compared to argon (c.f. 1st ionization energies in table 3.1). The formation of a plasma plume is claimed to be *suppressed*, if helium is used. However, the difference in ionization energy is within the *same* order of magnitude. As far as the literature is concerned, the formation of plasma itself has not yet been convincingly demonstrated by experimental evidence for aluminium. From high-speed photography carried out for the standard shielding gas nozzle presented in this dissertation in paragraph 5.1 another explanation seems compelling: The volatility of helium is much higher than the volatility of the constituent gases of ambient air, as the density of helium is *one* order of magnitude lower. The vapour forms an aerosol or smoke within the helium, i.e. the vapour is being *removed* from above the keyhole *together* with the helium, which is escaping due to its volatility. This mechanism adds to the 'cooling effect' of helium due to its high thermal conductivity as compared to air. The aerosol formed by the vapour with argon does not escape from above the keyhole, because the density of argon is close to the density of air. This explains why helium was observed to be *generally* advantageous in laser welding as compared to argon.

Even if helium is used as a process gas, instabilities were reduced but not avoided. Thus, proposition 1 (c.f. p. 14) does not solely describe the cause for instabilities.

3.1.2.2 Deformation of keyhole geometry

The source of instabilities according to this process model's proposition is seen in the highly dynamical behaviour of the melt covering the keyhole's walls during LBW.

The phenomenon which degrades the seam by *humps*, i.e. the formation of droplets in the seam, arises in the train of melt behind the keyhole and does therefore not fall into the *category* of instability as defined above. Humps do not introduce instabilities to the keyhole itself, but they are a *defect* of the seam initiated by keyhole dynamics. This defect is *spatiotemporally* separated from the keyhole. Hump formation exhibits a periodicity and is commonly observed in steels. It is caused by an abrupt cooling of a previously runny melt. This phenomenon could be overcome by proper post-heating reducing the cooling rate of the melt. Thus, humps do not cause instabilities of the *keyhole* as they do not affect keyhole geometry.

The keyhole itself is surrounded by melt. However, the thickness of the melt film depends on position. The film is quite thin at the melting front of the keyhole and increases in thickness on the sides and behind the keyhole, as shown schematically in figure 3.1. The temperature gradients decrease accordingly by typically more than five orders of magnitude. The melt is in rapid motion around the keyhole exhibiting measured velocities higher than 100 m s^{-1} on the orifice of the keyhole. This was determined in an experiment by monitoring solid tungsten carbide particles following the flow lines of the melt. X-ray transmission high-speed photography is needed to measure average velocities inside the keyhole. Although no measurement of velocities of the melt on the keyhole's walls has been published to the knowledge of the author, it may well be the case that velocities are higher on the keyhole walls.

In the literature two mechanisms are expounded that alter the geometry of the keyhole and cause instabilities. In one proposed model the keyhole experiences a *random closure* entrapping the vapour filled capillary as waves of melt strike the orifice. A line of elongated pores along the direction of motion of the keyhole remains in the seam [RAPP 1996, p. 96]. In this concept spatter is caused by rapid

evaporation from the upper part of the melt that closes the orifice or by bursts of entrapped bubbles. In direct observation of the orifice by high-speed photography of the keyhole (described in detail in section 4.1.3) *no* closure of the keyhole orifice could be seen in steels. Also note, no closure could be observed in aluminium *without* an oxide layer. Hence, this explanation is cast with doubt.

Another empirically based model describes the collapse of the keyhole around the middle of the capillary's tube by necking. According to this model the keyhole is instable if the aspect ratio satisfies:

$$\text{aspect ratio} \equiv \frac{d}{w} >> 1 \qquad \text{(Equation 3.3)}$$

where d is the depth of the keyhole and w the width of the overbead. Katayama observed this deformation of the keyhole geometry by x-ray transmission imaging. A bulging projection of melt closes up the tube of the keyhole around its middle part. The high intensity of the laser impinges on this bulge from above and reopens the keyhole by high recoil pressure leading to an oscillation of the keyhole geometry. By x-ray transmission high-speed photography Katayama proved experimentally that the keyhole showed fluctuations in depth and radial direction and that *all* the bubbles emerged from the *bottom* tip of the keyhole. The bubbles then moved along the solidifying wall and mostly remained in the weld seam after solidification. This is the *best* empirically established account of porosity formation. It could be shown that these bubbles were filled with the process gas used [KATAYAMA 1999, 2000a, 2000b, 2006]. Katayama's findings are phenomenologically undisputable and are very important empirical observations. They are revisited in section 4.2.5 in greater detail.

According to his reasoning the bubbles are formed by intense evaporation from the keyhole front wall. It was noted before that this cannot explain why the bubbles form solely at the keyhole bottom tip and not alongside the whole length of the front wall [TSUKAMOTO 2004]. The laser's intensity, i.e. energy per unit area, is lowest on the walls as compared to the orifice and the bottom of the keyhole. Although the *actual* intensity distribution acting on the keyhole's wall could differ from the delivered intensity distribution, the *delivered* intensity distribution is mirror symmetric for front and rear wall during welding. How can such a distribution support excess evaporation from the *front* wall? Hence, proposition 2 (c.f. p. 14) cannot be sustained to be the only source of instabilities.

3.1.2.3 Resonant vibrations

Klassen used a different method to prove that keyhole oscillations lead to instabilities [KLASSEN 2000, p. 71-88]. He took a *negative* approach by intentionally introducing instabilities, because he had no x-ray transmission visualization at his disposal. According to his reasoning a mechanism which effectively causes these instabilities should provide a clue to a remedy against them. The laser power was pulsed over large frequency band widths leading to catastrophic spatter. Klassen induced instabilities by using short pulses, i.e. deliberately creating pores typical of aluminium laser welds. This implies a resonance phenomenon excited by short pulses and eventually reaching catastrophic resonance. The system consisting of vapour capillary, melt pool, and vapour plume is self-exciting. In the ersatz system the components, i.e. spring, damping, and mass, are associated as follows: the cavity and vapour represent the spring, the viscous deformation of the melt pool provides damping, and the mass is associated with the amount of melt. The laser is the source term for capillary and vapour. According to this model the system can explicitly *not* exhibit an eigenfrequency. In this model it is necessary to extract energy from the system to prevent it from catastrophic resonance. This is only possible by an external sinusoidal excitation of ever increasing frequency. In experiments the number of instabilities could be reduced by excitation frequencies from 10 ÷ 300 Hz. This pore suppression mechanism is disadvantageous, because the laser's mean power had to be considerably reduced. This lowers the welding speed. The efficiency of the laser process is reduced and expensive output laser power wasted. No easy method is presented by Klassen to determine the specific frequencies. Numerous trial and error experiments were necessary instead. In spite of all these elaborate efforts, instabilities were reduced but not eliminated by Klassen. Hence, there is a remaining source of instabilities still unknown.

Tsukamoto found frequencies of 10 ÷ 16 Hz by measuring the oscillations of the vapour plume [TSUKAMOTO 2004]. He could achieve a reduction of porous instabilities of the same order of magnitude as Klassen by modulation of the laser power. Tsukamoto builds upon the empirical findings of Katayama. However, Tsukamoto supposes a constant eigenfrequency, as he regards the bulge to be the cause for a later oscillation of the plasma. Nonetheless, pores could not be extinguished completely by his method.

This leads to diametrically opposed views of Klassen and Tsukamoto: Eigenfrequencies are the core of Tsukamoto's model but would contradict

Klassen's model. Both empirical models have in common that an accordingly designed process technology failed in eliminating instabilities. Berkmanns found that pulsing can reduce instabilities but leads to a smaller process window, i.e. reduction of accessible parameters of speed and penetration depth. His method increased the temperature gradients and would therefore lead to a higher susceptibility to hot cracks [BERKMANNS 1998, p. 60]. In sum, pulsing does not give the full picture, as it cannot completely eliminate instabilities. There is still room for another unknown source of instabilities not expressed by proposition 3 (c.f. p. 14).

3.1.2.4 Physical properties of the melt

If the physical properties of the melt are the cause of instabilities, this means that some alloys cannot be welded by a laser, as these properties are not at the welder's disposal. A higher susceptibility to instabilities of aluminium alloys as compared to steels is argued for by consideration of the physical properties of the elementary composition of the pertinent material. The reflectivity of aluminium is up to 87% and much higher as compared to the reflectivity of iron of 58% [RYKALIN 1988]. This necessitates lasers of higher intensities or shorter wavelengths to initiate keyhole welding in aluminium as compared to steel.

In aluminium a laser heats a larger volume in a shorter time in the vicinity of the keyhole as compared to steel, since the conductivity of heat and temperature is much higher in aluminium (c.f. table 3.2). This is even more obvious by taking into account the temperature interval between melting and vaporization. For aluminium this interval is 1858 K compared to 1323 K for iron and thus by 535 K larger (c.f. table 3.2).

The volume of melt surrounding the keyhole is higher in aluminium than in steel welding. Although higher laser intensity is necessary to initiate keyhole welding in aluminium, the penetration depths in aluminium are typically lower. This is owed to onset of 3D-heat conduction, because the heat conductivity for aluminium is seven times higher than for iron. In iron 2D-heat conduction would still be sustained under ceteris paribus conditions. Whether a higher volume of melt and vapour induces instabilities has not been fully experimentally established. The mathematical model by Berkmanns given in the following chapter seems to prove the opposite.

physical property	**unit**	**Al**	**Fe**
specific heat capacity at RT	$J\ K^{-1}\ cm^{-3}$	2.47	3.6
specific enthalpy of melting	$kJ\ cm^{-3}$	1.1	2.2
specific enthalpy of vaporization	$kJ\ cm^{-3}$	20.1	41.8
temperature of melting	°C	660	1536
temperature of vaporization	°C	2518	2859
conductivity of heat at RT	$W\ K^{-1}\ cm^{-1}$	2.7	0.4
conductivity of temperature at RT	$cm^2\ s^{-1}$	1.1	0.1

Table 3.2: Physical properties of aluminium and iron [LANDOLT BÖRNSTEIN 2004, p. 27]

For aluminium the rate of vaporization depends on the composition and physical properties of the alloying elements. A higher rate of vaporization leads to instabilities, as small droplets are ejected by the stream of vapour. Rapp presents a model based on Newton's law of friction [RAPP 1996, p. 151]. The frictional force of the vapour exerts a tension on the walls of the capillary. The shape of the cavity is approximated to be cylindrical in this model. Alloying elements such as Cu and Si do not have an influence, whereas Mg and Zn increase the rate of vaporization. To prove this empirical model Rapp displays good welds in alloys that are depleted in these elements in comparison to welds in alloys that are abundant in these elements and are therefore degraded by instabilities. Rapp recommends defocusing the laser by a *positive* z-axis offset above the materials' surface to overcome these instabilities [RAPP 1996, p. 151]. The novel empirical model developed in this dissertation will explain these results by a different reasoning.

3.1.3 Mathematical process modelling of instabilities

From the experimental data presented above it has to be concluded that instabilities are caused by keyhole fluctuations. In the following, only mathematical models dealing with the formation and geometry of the keyhole in laser welding are considered.

If the power density on the workpiece surface is below threshold, the absorbed power released as heat in the workpiece is not high enough to initiate vaporization. In this case, the beam irradiates an even melt pool surface, and the radiation power absorbed is conducted into a hemispherical volume below. This type of welding is called *conduction mode welding* (CMW). If the power density is above threshold, the laser irradiates a cavity, termed *keyhole*, wherein by multiple reflections the radiation power is absorbed and the energy released in the workpiece is increased. This type of welding is called *deep penetration welding* (DPW).

The threshold power density for transition of CMW to DPW can be approximated [BECK 1967, p. 129; KLEMENS 1967; ARATA 1987]:

$$\frac{P_L}{d_f} = \underbrace{\sqrt{\pi}}_{\mathrm{B}} \cdot \underbrace{\frac{T_v \cdot \lambda_{th}}{A}}_{\mathrm{M}} \cdot \underbrace{\sqrt{\frac{Pe}{2} + 1.1}}_{\mathrm{V}} = B \cdot M \cdot V \qquad \text{(Equation 3.4)}$$

The terms are grouped according to source: B (beam), M (material), and V (velocity) [LONDOLT BÖRNSTEIN 2004].

P_L is the irradiated laser power, d_f is the diameter of the focal spot on the workpiece, T_v is the vaporization temperature, λ_{th} the thermal conductivity, A the coefficient of optical absorption, and Pe the Peclet number. Pe is defined as follows:

$$Pe = \frac{v_w \cdot \rho \cdot c_p \cdot L}{\lambda_{th}} \qquad \text{(Equation 3.5)}$$

where v_w is the transverse velocity, ρ is the density, c_p the specific heat at constant pressure, L a characteristic length, i.e. in this case d_f , and λ_{th} is the thermal conductivity. If $Pe << 1$, accurate calculations of heat transfer can be done by considering heat conduction alone. Whereas if $Pe >> 1$, heat transport occurs primarily by convection. In this case, the heat conduction in the melt pool

is not important. The factor B depends on the beam profile. For a Gaussian beam, e.g. an Nd:YAG-laser used in BHLW:

$$B = \sqrt{\pi}$$

For a top hat beam profile, e.g. an HPDL used in BHLW:

$$B = 1.25\sqrt{\pi}$$

These empirical facts and formulas determine whether for a given power density CMW or DPW is initiated.

The geometry of the vapour cavity is *stable* if the vapour pressure within it balances all forces which would lead to a collapse of the cavity. For equilibrium at the surface of the vapour cavity the surface tension per unit area p_σ, the hydrostatic pressure p_g, and the hydrodynamic pressure p_{hd} are balanced by the ablation pressure p_{abl}:

$$p_{abl} = p_\sigma + p_g + p_{hd} \qquad \text{(Equation 3.6)}$$

The surface tension on the surface of the cavity p_σ is given by:

$$p_\sigma = \frac{\sigma}{r} \qquad \text{(Equation 3.7)}$$

where r is the principal radius of curvature and σ is the surface tension coefficient of the melt. The hydrostatic pressure depends on the density of the melt ρ (which in turn depends on its temperature, c.f. table 3.2), the acceleration due to gravity g, and the depth of the cavity z:

$$p_g = \rho \cdot g \cdot z \qquad \text{(Equation 3.8)}$$

However, the contribution of p_g is about 10^3 Pa and therefore one order of magnitude below the mean pressure due to surface tension. Hence, it is regarded negligible.

The hydrodynamic pressure can be estimated [BECK 1996, p. 87; GREF 2005, p. 82]:

$$p_{hd} \sim v_w^{3.5} \qquad \text{(Equation 3.9)}$$

which can be neglected for small welding speeds v_w.

A *stability factor* can be defined for a cylindrical keyhole cavity, i.e. a *Rayleigh-instability* arises if the depth of the cavity z exceeds its perimeter [KLEIN 1993; RAYLEIGH 1892; CHANDRASEKHAR 1961]:

$$z > 2\pi \cdot r \text{ or } \frac{z}{d_f} = \pi \qquad \text{(Equation 3.10)}$$

Thereupon Beck builds a mathematical model, which describes the frictional flow in a tube with variable diameter allowing exchange of mass via the tube's wall. To calculate the vapour flow by conservation of mass and momentum the flow is simplified to be laminar, incompressible, and isothermal. As the cavity is assumed to be cylindrical symmetric, the radial component of the pressure gradients vanishes. According to this model two stable types of cavity geometry are calculated. They are displayed in figure 3.2.

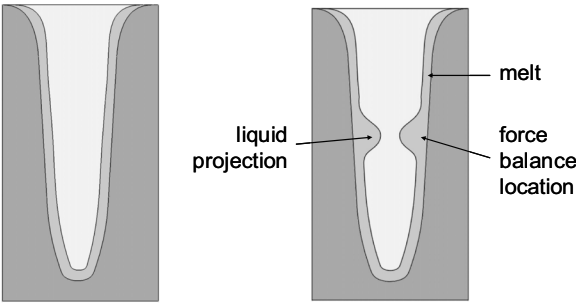

Figure 3.2: Keyhole geometries according to Beck's model; left: type A; right: type B [ZHAO 1999]

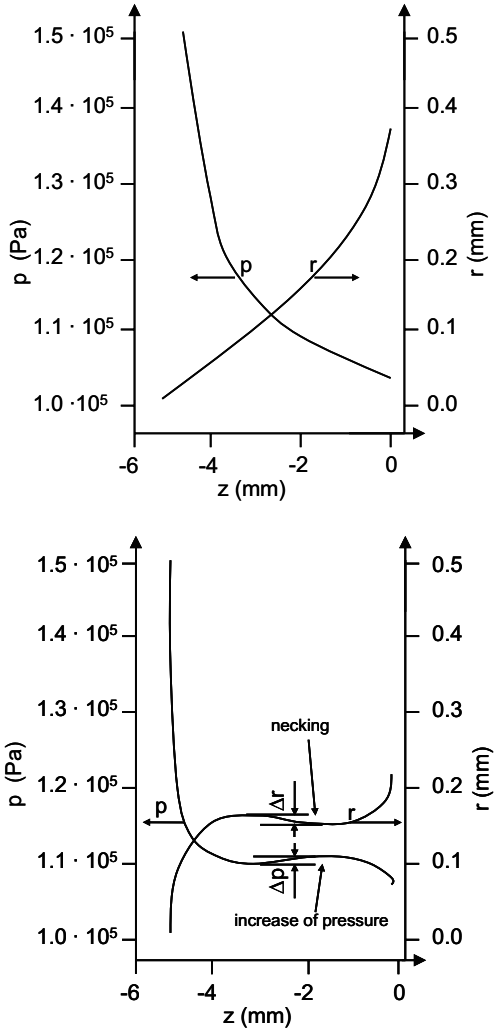

Figure 3.3: Calculation of pressure within the keyhole versus depth z and radius r; top: type A; bottom: type B [BECK 1996, p. 93]

For type A cavities in figure 3.3: if the vapour temperature is sufficiently high, the drop in pressure for a simultaneously increasing cavity diameter results in an acceleration of the vapour gas particles towards the orifice of the cavity. Type B cavities show a contraction towards the orifice, as can be seen in figure 3.3. The

vapour flow is not only decelerated by friction but also by the increase in pressure at the projection. If the kinetic energy of the vapour leaving the contracted orifice is not sufficient to overcome the pressure increase, the flow is obstructed or even reversed in direction. This blockade of vapour flow affects - according to this model - keyhole stability leading to entrapments of vapour as bubbles. This mathematical model delivers an explanation for bubble formation **towards** the *tip* of the cavity and was invoked by Tsukamoto.

This mathematical model **necessitates** the following two conditions to be true:

a. The keyhole is sustained by the vapour-jet originating from surface evaporation.

b. The contraction is cylindrically symmetric and caused by a depression in local pressure.

Katayama intensively researched keyhole dynamics, as stated above. His empirical findings are phenomenologically undisputable as far as experimental evidence is concerned. Katayama *proved* that process gas was contained within the pores.

In this dissertation an *absolutely pivotal* conclusion is drawn from these observations for the first time: The keyhole is *not* completely filled with metallic vapour, since the pores are filled with process gas. This process gas *must* have reached the region towards the tip of the cavity overcoming the vapour-jet streaming in the opposite direction: This rejects condition a. In this dissertation a *new* empirical process model will be developed in paragraph 4.2, which is fundamental to the formulation of a *new* mathematical process model for pore formation in paragraph 4.3.

Katayama [KATAYAMA 1999, 2000a, 2000b] observed a large wave of melt propagating in the rear part of the melt pool when the cavity was open. For this observation he traced out the flow lines of the melt by tungsten particles. The reflection of the wave from the rear melt pool boundary obstructed the cavity. This rejects condition b. The necking is not radial symmetric, since it is caused by a wave of melt. *This* mechanism of pore formation will be explained by a *new* empirical phenomenon described in paragraph 4.2.

Beck's [BECK 1996] model was very influential, as it supported the view that by increasing the rate of vaporization and widening the contraction of the keyhole the formation of porosity could be prevented. The objective of pore prevention

sparked the development of multiple or Twin Spot laser welding technologies. These technologies are evaluated in the next paragraph.

3.2 Process technologies

In this paragraph the state of research and development of technologies designed to prevent the problems encountered in welding of aluminium is presented and discussed. These technologies were conceived and appraised to solve the problems notorious in classical arc welding of aluminium: porosity, blow holes, and spatter. The process technologies of beam oscillation and laser stir welding (LSW) deflect the beam during welding. Other procedures modulate the power of the beam to fight instabilities. These technologies seem not to have reached the production lines. On the contrary, Laser-MIG-Hybrid welding technology is used in automotive manufacturing of car doors and various other industrial applications. Multiple spot laser welding appears to be researched only. But the specific variety of Twin Spot laser welding has a few applications in aeronautic welding, for which highest demands on quality are enacted. For reasons of comparability of results of these technologies within this dissertation, individual benchmark studies of Laser-MIG-Hybrid and Twin Spot laser welding were conducted with the same aluminium alloy, process gas, and setup. *Ceteris paribus* conditions are ensured to allow evaluating the results. In addition, the ease and robustness of filler material supply is considered to enable a full comparison to BHLW.

3.2.1 Arc welding of aluminium

Classical gas metal arc welding (GMAW) and fusion welding techniques, such as MIG, or GTAW, or other arc and plasma utilizing processes, can achieve satisfactory welds. However, cracks, pores, inclusions, and other defects in the fusion zone are to be heeded when aluminium is to be welded [MATHERS 2002, p. 18-27]. Conventional GMAW enables to bridge gaps in the joint geometry by introducing filler material to the fusion zone. The chemical composition of the filler can be customized to improve on material properties.

Porosity, the oxide layer, and hot cracking are well known problems in classical arc welding of aluminium. In gas shielded arc welding there is a phenomenon known as *cathodic cleaning,* which can be employed to avoid oxide entrapment

in the fusion zone. The surface oxide layer of the abutted edges is stamped into the root of the weld. Porosity is hard to prevent even in bead on plate welds, as can be seen in figure 3.4, where small hydrogen pores are visible.

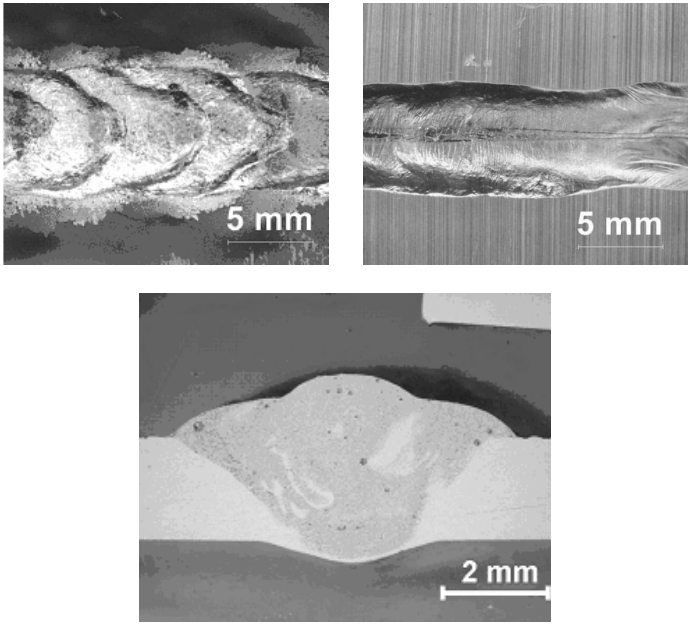

Figure 3.4: GMAW top and bottom photograph of seam surface and cross-section macrograph; small hydrogen pores visible in the cross-section, bead on plate; EN AW-6060 (AlMgSi0.5) T66; filler Al4047 A (SG-AlSi12); $Ø_f$ = 1 mm; torch distance s = 22 mm; torch inclination angle α = 20°; argon flow 8 L min^{-1}; v_w = 0.5 m min^{-1}; v_f = 4.7 m min^{-1}; I_s = 80 A; I_{abs} = 95%

Figure 3.5 is a high-speed snapshot of a MIG welding process. The distance between the workpiece and the filler wire tip is about three times larger than in Laser-GMAW-Hybrid welding, as shown in figure 3.7. The filler dilution is not homogeneous, as can be seen in the bottom picture of figure 3.4. This is due to the *discontinuous* transfer of filler material. In this dissertation any transfer of filler by ever so small droplets is termed discontinuous. A droplet of filler material just about to be detached from the tip of the filler wire is shown in figure 3.5. The periodic transfer of filler material droplets leads to the prominent chevron pattern, c.f. top left picture in figure 3.5. The surface and the bottom of

the MIG weld is stained with carbon black and soot indicating that the flow of shielding gas is not sufficient. However, even on increasing the argon flow to 30 L min^{-1} the soot cannot be completely suppressed. MIG welds in EN AW-6060 release a lot of heat to the surroundings and show a high energy is input per unit length, because MIG welding is restricted to moderate speeds. The additional heat per unit length leads to reduced cooling rates. This may result in improved ductility of MIG welds as compared to laser welds. However, the penetration depths of MIG welds are rather low as compared to Nd:YAG laser welds. Porosity and stop crater hot cracks of such welds are discussed in paragraph 7.2.

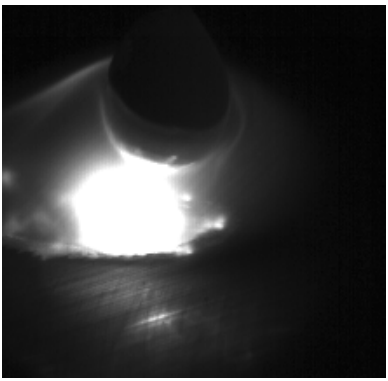

Figure 3.5: High-speed photograph snapshot of MIG welding; 1000 fps; bead on plate; EN AW-6060 (AlMgSi0.5) T66; filler Al4047 A (SG-AlSi12); $\varnothing_f$ = 1 mm; torch distance s = 22 mm; torch tilting angle α = 20°; argon flow 15 L min^{-1}; v_w = 0.75 m min^{-1}; v_f = 5.5 m min^{-1}; I_{abs} = 95%; I_s = 80 A

Generally, if aluminium is to be joined cohesively, i.e. by fusion welding, thermal welding technologies that gave good result for welding of steels cannot be transferred to aluminium. This is mainly due to the physical properties of aluminium melts, e.g. higher affinity to hydrogen, lower viscosity, and higher thermal conductivity as compared to steels. The major influence of the oxide layer is considered in detail in paragraph 4.1.

The welding process itself induces a heat affected zone (HAZ) in the material. In classical arc welding this zone is considerably enlarged as compared to laser welding leading to an undesired distortion and buckling of the structure [ROEREN & TRAUTMANN 2005]. The strength losses in 6xxx alloys are less in the naturally aged metals than in an artificially aged alloys. EN AW-6060 was welded as

received in temper T6, i.e. solution heat treated and artificially aged. Those advantageous effects are lost in the HAZ for heat tempered material. The strength of the weld and the HAZ in the artificially aged condition generally drop to match that of the naturally aged alloy with a narrow solution-treated zone on either side of the weld and an overaged zone beyond this that is weaker than the T6 condition. By a controlled low-heat input welding procedure the strength of the weld will not drop to that of an annealed structure but will be close to that of the T4 condition, i.e. solution heat treated and naturally aged [MATHERS 2000, p. 45]. However, welding by laser reduces the size of the HAZ as well as the overall heat input into the structure. Several techniques have been developed to utilize this advantage and simultaneously reduce the formation of cracks, pores, and other defects problematic in MIG and other arc welding techniques.

3.2.2 Laser augmented gas metal arc welding

The combination of a laser beam and an electrical arc in a hybrid welding process was first investigated in the late 1970s at Liverpool University [STEEN 1979 & 1980]. Since then a plethora of combinations of almost any GMAW process with high power laser sources such as CO_2, Nd:YAG, and recently fibre and disc lasers were researched. It was found that the thermally affected zone produced by the focused laser beam roots the arc.

Figure 3.6: Experimental head for laser augmented MIG welding; MIG torch arranged in pushing backward position with regards to laser spot

This stabilization of the process results in a better transfer of filler material in GMAW welding by an increase of droplet detachment rate. The focused energy of the laser beam results in a narrow HAZ that can lead to steep spatial and temporal heat gradients able to embrittle microstructures. The combination with a MIG arc process mitigates these gradients. Laser-MIG-Hybrid welding is meanwhile utilized in industrial applications of automobile car door [GRAF 2002, STAUFER 2003], oil tank, circumferential pipe [REUTZEL 2005], and thick sheet welding for shipbuilding.

For this dissertation a benchmark study was conducted for EN AW-6060 to investigate whether the commonly claimed synergistic effects materialize for Laser-MIG-Hybrid welding: increase of feed speed, penetration depth, and weld pool stability. The experimental setup is shown in figure 3.6. The quality of the Laser-MIG-Hybrid overbead is superior to MIG welding alone, c.f. figure 3.7.

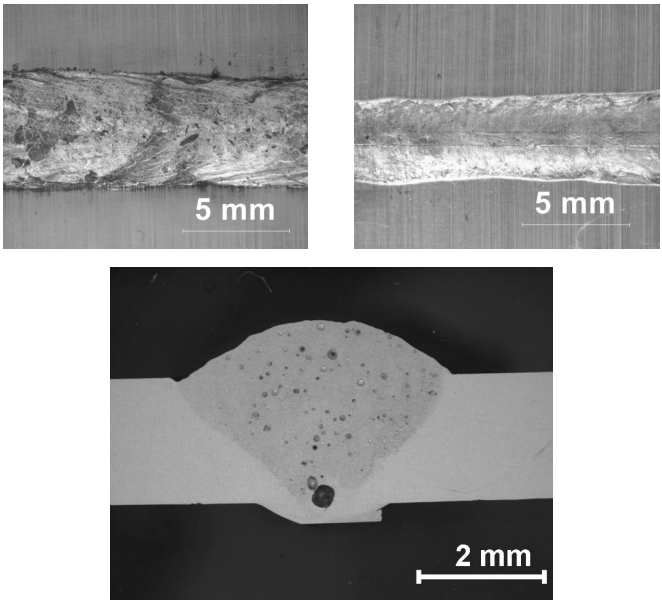

Figure 3.7: *Nd:YAG laser augmented MIG weld: top and root surface photograph and cross-section macrograph; increased hydrogen porosity throughout the weld and a prominent process pore at the root (c.f. p. 164); bead on plate; EN AW-6060 (AlMgSi0.5) T66; filler Al4047 A (SG-AlSi12); $Ø_f$ = 1 mm; $P_{Nd:YAG}$ = 3 kW; torch distance s = 22 mm; optic tilting angle φ = 30°; torch angle α = 4°; argon flow 15 L min^{-1}; v_w = 2.5 m min^{-1}; v_f = 8.0 m min^{-1}; I_s = 100 A; I_{abs} = 95%*

This hints at a stabilization of the welding process. However, there is still substantial spatter present in Laser-MIG-Hybrid welding. The spatter droplets are flung far away. This is the reason why those droplets do not contaminate the vicinity of the weld seams shown. The root of the weld is much more even than in MIG welding. Constant welding parameters do not necessarily reproduce the same weld quality, which seems to be very sensitive to transient phenomena. The welds lack reproducibility.

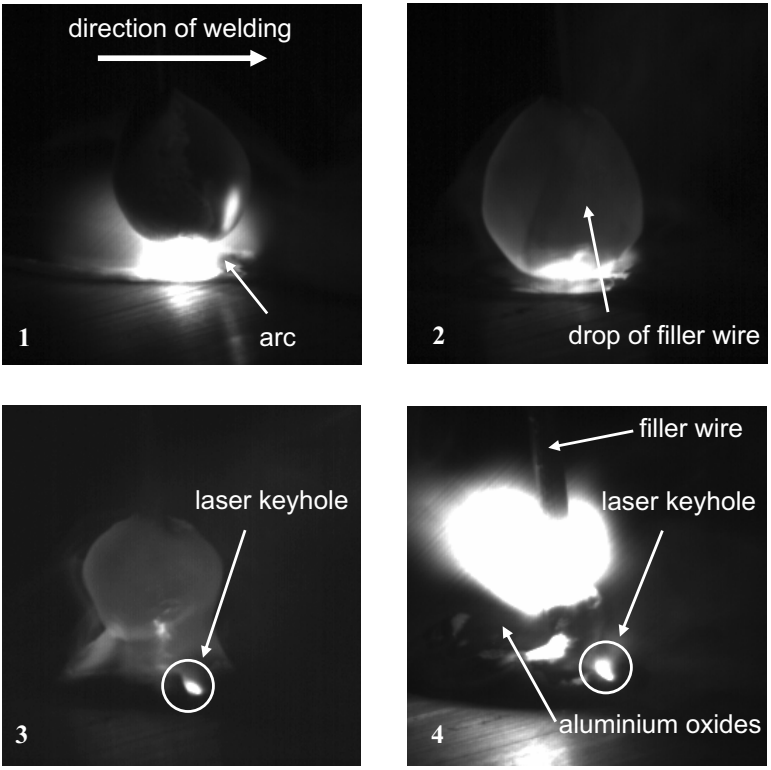

Figure 3.8: Nd:YAG laser augmented MIG welding, high-speed photograph snapshots; 1000 fps; bead on plate; EN AW-6060 (AlMgSi0.5) T66; filler Al4047 A (SG-AlSi12); $Ø_f$ = 1 mm; $P_{Nd:YAG}$ = 3 kW; torch distance s = 22 mm; inclination angle of optic φ =30°; torch angle α = 4°; argon flow 15 L min^{-1}; v_w = 3.0 m min^{-1}; v_f = 8.0 m min^{-1}; I_{abs} = 90%; I_s = 60 A

Some remarks on terminology are in place: Steen termed the process 'arc augmented laser welding' [STEEN 1980]. For the increasing number of combinations the GMAW process was named in the first place followed by the laser employed, e.g. 'MIG-Laser-Hybrid' or 'MIG-Nd:YAG-Laser-Hybrid' welding. Some distinguish the process according to whether the GMWA torch is forehand to the laser, which is termed 'MIG-YAG-hybrid', or backhand, i.e. 'YAG-MIG-hybrid' [KATAYAMA 2006]. Meanwhile the process is simply referred to as 'hybrid laser welding' omitting the associated GMAW process

[ION 2005, p. 413]. Some just use ‘hybrid welding’ without mentioning the specific laser employed.

However, the benchmark study conducted for this dissertation showed that the laser merely *supports* the GMAW process by desirable redistribution of melt and arc root stabilization. This allows for automation of an otherwise hand manipulated GMAW process, as hinted at by Hügel [HÜGEL 2002].

Although the performance of a hybrid system is invariably better as compared to each individual process alone, it does not *transgress* their sum. The velocity of Laser-MIG-Hybrid welding is increased from 0.5 to 2.5 m min^{-1} as compared to MIG welding alone (c.f. figure 3.4 and 3.6). However, this is equal to the velocity at which the Nd:YAG laser would weld the same specimen of EN AW-6060. Thus, the utilization of the laser beam merely represents an *auxiliary* process with regards to GMAW technology. Correct *terminology* commendably mirrors this finding by naming horse and horsemen: i.e. *laser augmented MIG welding* to express the hierarchical interdependencies. The epithet ‘hybrid’ seems unjustified, as major advantages of laser beam welding are lost in laser augmented GMAW. For example, the heat input into the structure is considerably increased. This causes distortions.

The fundamentals of the physics of the process are not well understood. It should be noted that two fundamentally different thermal fusion welding processes are combined. The physics of the interactions of electric arc and laser beam are not known. Reutzel reports that a closer spacing between the torch and the laser focus in Nd:YAG augmented MIG welding increased the "complex interactions between the laser beam and the GMA, which made it difficult to identify parameters" [REUTZEL 2006; ZÄH & TRAUTMANN 2004]. As the parameters of the two welding techniques seem not to be linearly independent, a statistical planning and analysis to determine empirical dependencies according to methods of design of experiments is not possible [DREYER 1993]. As a result, it is difficult to establish a practical operating window of processing parameters from the number of variables, thereby necessitating cost and time intensive trial-and-error testing. This may explain the seemingly irreconcilable results that a number of researchers produced over the years. Take for example the different views on whether it is advantageous to use backhand or forehand orientation of the arc welding torch with respect to the laser [KATAYAMA 2006; FELLMAN 2006].

3.2.3 Multiple and Twin Spot laser welding

In the following multiple spot laser welding procedures are evaluated. Multiple spots are employed to design an intensity distribution on the workpiece to induce favourable melt pool geometry and melt pool dynamics. Unfortunately, the terminology of multiple spot laser welding is confusing. Henceforth, in this dissertation, if the spots on the workpiece are generated by *distinct* optical guiding systems, it is spoken of dual, triple, or quadruple spot welding. In this case the spots can be independently adjusted. If, however, the beams *share* optical components, such as a common focusing lens or are partitioned by prism optics, they should be termed: *Twin* Spot welding for two spots or triplet for three spots and so on. Those beams are *siblings* because they passed through the same optical components. This is shown in figure 3.9.

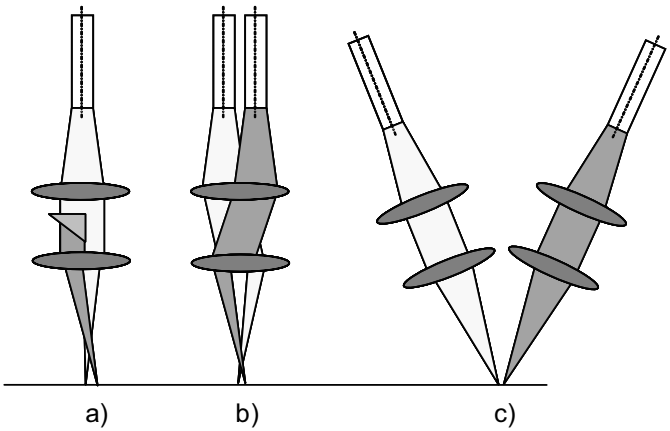

Figure 3.9: Multiple spot optic setups: a) prism twin spot; b) optical twin spot; c) dual spot

In 3.1.2.2 the empirical process model was detailed that explains instabilities by deformation of the geometry of the keyhole. Multiple and Twin Spot laser welding technology were specifically conceived to eliminate these instabilities by stabilization of the keyhole by several spots. It was hoped that by widening of the keyhole its closure could be avoided. This is shown schematically in figure 3.10.

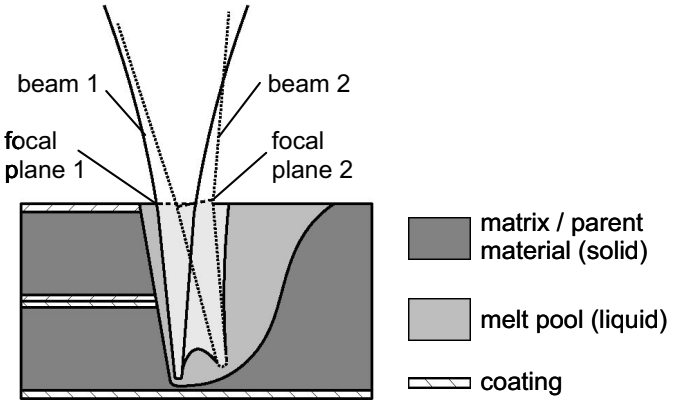

Figure 3.10: Keyhole stabilization by keyhole widening for Twin Spot or dual spot laser welding

Multiple spots were evaluated in their potential to increase process robustness and weld quality by Glumann, who employed a CO_2 laser [GLUMANN 2003]. Hohenberger held that the uninhibited venting of the metal vapour from the vapour cavity is fundamental for a robust and stable welding process [HOHENBERGER 2003, p. 43]. Hohenberger tried to achieve this by using a dual spot optic system. The final study in this succession was conducted by Gref in 2005 [GREF 2005]. He used dual, triple, and quadruple spot setups to weld aluminium and zinc-coated steels with Nd:YAG and disc lasers. In some specific alloys and joint geometries pores could be eliminated and generally be reduced as compared to single spot laser welding. The determination of the parameters to adjust the intensity distribution and the relative focal spot positions was complex. The integration of filler wire constrained the accessible range of parameters and thereby limited penetration depth and porosity suppression. Eventually, Gref admits that dual spot disc laser welding of zinc-coated steels "could not create welds free of pores and expulsions by widening of the vapour cavity" [GREF 2005, p. 114]. The empirical process model according to which multiple spot laser welding was designed did not guide it to success. It was obviously expected from the beam's diffraction angle that a widening of the cavity is achieved. Whereas it seems more likely that beam *channelling* took place [ALLMEN 1995, p. 38].

In order to assess the potential merits of Twin Spot welding a benchmark study had to be conducted for the following two reasons: First, there were no results

available for the reference alloy EN AW-6060 in the literature. Second, *ceteris paribus* conditions had to be guaranteed to demonstrate that the results of BHLW are not due to the mere fact that the reference alloy is incidentally well behaved.

On the contrary, the hot cracking susceptibility of the reference alloy EN AW-6060 represents a major challenge to fusion welding, c.f. section 8.2.1. The Twin Spot optic head is shown in figure 3.11 [DE 196 19 339 A1]. This head was available commercially and was equipped with a filler wire batch. For all following experiments in this section the Nd:YAG laser was set to its maximum nominal output power of 3 kW. Other twin and dual spot optical setups were designed and are meanwhile patented [DE: 40 24 299 A1; DE 197 51 195 C1; DE 196 19 339 B4].

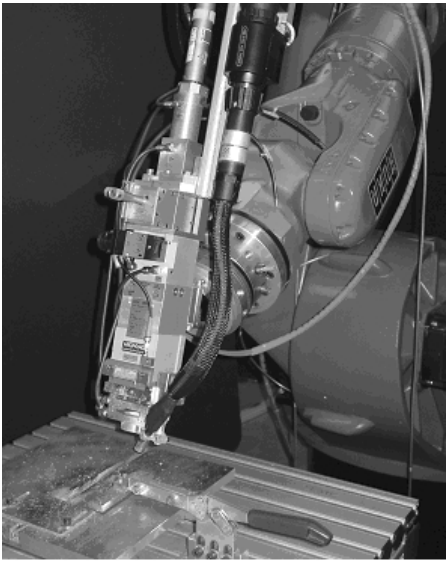

Figure 3.11: Commercial Twin Spot optic head with filler wire batch attached to a robot

The relative geometrical positions of the two foci in Twin Spot welding are shown in figure 3.12.

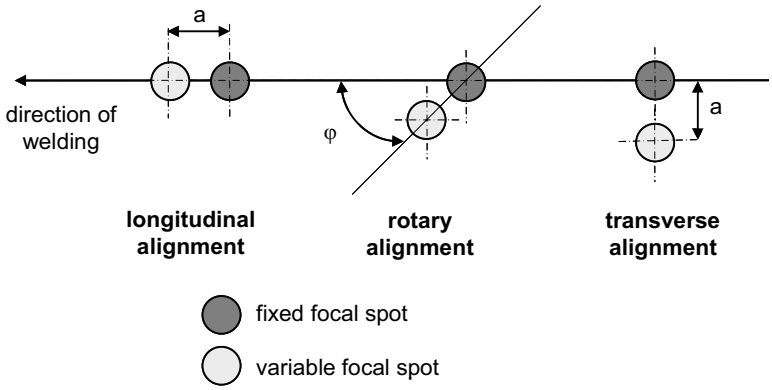

Figure 3.12: Relative focal position in Twin Spot welding with regards to the direction of welding, φ is the inclination angle and a *is the relative distance of the two foci*

A partial overlap of the focal spots results in an increased intensity in the overlap region. Additionally, the Twin Spot head allows to unequally partition the power between the two spots by a prism optic. The contours of the resulting intensity distributions and the influence of a longitudinal focus distance variation can schematically be seen in figure 3.13.

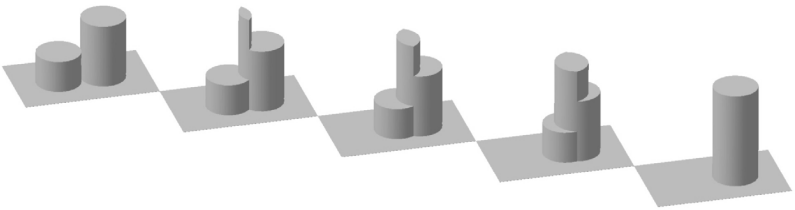

Figure 3.13: Contours of intensity distribution for a gradual overlap of two focal spots in Twin Spot welding with a power distribution partition in percent 33/66 between the two spots

A 5xxx alloy was used for fundamental experiments to shirk the need for filler material. The welds displayed in figure 3.15 show that the surface quality is improved the farther the spots are distanced.

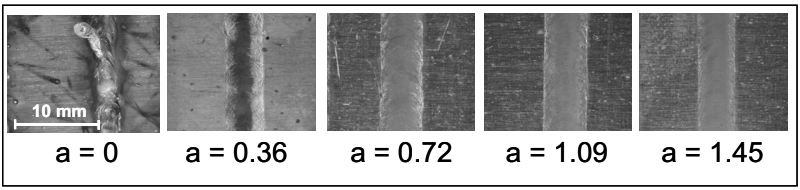

Figure 3.14: Surface photographs of Twin Spot overbead for $P_{Nd:YAG}$ = 3 kW; power distribution between the two spots in percent 50/50; a *is the relative distance of the two foci; longitudinal alignment of* a*; v_w = 3 m min^{-1}; EN AW-5082; argon flow 20 L min^{-1}*

If the cross-section macrographs are considered, keyhole formation is no longer ensured for longitudinal focus separation distances above 1.09 mm, c.f. figure 3.15. The penetration depth decreases linearly with focus separation. The maximum penetration is expectedly achieved for a complete overlap of the two spots.

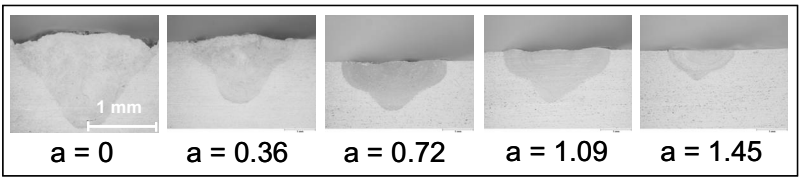

Figure 3.15: Cross-section macrographs of Twin Spot seams for $P_{Nd:YAG}$ = 3 kW; power distribution between the two spots in percent 50/50; a *is the relative distance of the two foci; longitudinal alignment of* a*; v_w = 1 m min^{-1}; EN AW-5082; argon flow 20 L min^{-1}*

The penetration depth is linearly decreasing for the farther the two spots are separated. It could not be established that a combined keyhole did actually form as otherwise the surface quality should not improve and the penetration depth should reach a saddle point. For the longitudinal alignment no increase of melting efficiency could be demonstrated by widening of the keyhole orifice and thereby promoting multiple reflections within the keyhole. The formation of a combined keyhole was, however, claimed by many researchers. The results can also be explained by proposition II of the new empirical process model described in section 4.2.4. For a single beam a three-phase transition occurs, which leads to spatter by evaporative expulsions. Longitudinal Twin Spot welding melts the

workpiece and decreases the heat gradients such that immediate sublimation does not occur. Hence, spatter is suppressed.

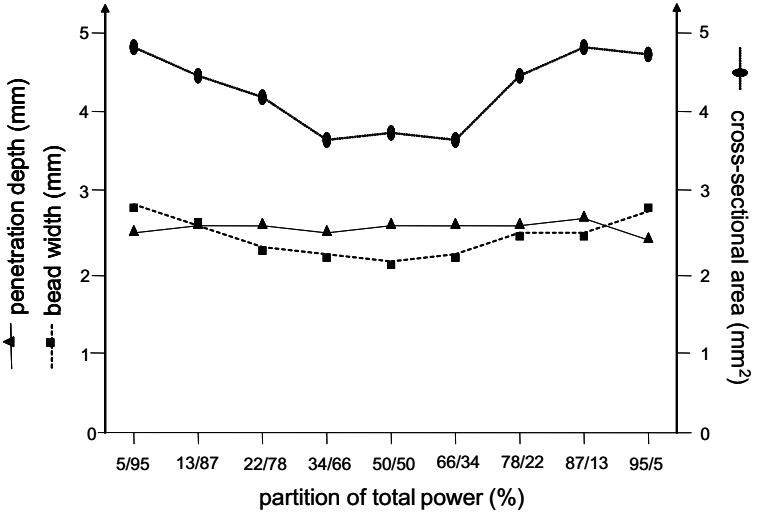

Figure 3.16: Variation of penetration depth, width of weld seam, and cross-sectional area for Twin Spot welding versus power partition among the two spots; $P_{Nd:YAG}$ = 3 kW; a= *0.36 mm longitudinal alignment; v_w = 3 m min^{-1}; EN AW-5082; argon flow 20 L min^{-1}*

To further challenge the received process model for Twin Spot welding the longitudinal alignment was evaluated for various partitions of power among the two spots. Figure 3.16 shows that the cross-sectional area of the weld seam and the penetration depth exhibits a minimum for an even partition of the available 3 kW-Nd:YAG laser power. This could be expected. However, figure 3.16 additionally shows that these parameters are otherwise fairly mirror symmetric with regards to variations of power partition.

This proves that stabilization of the keyhole by the Twin spot welding did not take place, at least not the way it was anticipated for the following reasons: Japanese researches established by real time x-ray transmission observation of keyhole deformation that the formation of porosity sets in from the rear of the keyhole. Matsunawa underpinned this notion by theory. As the welding velocity increases, the energy intensity at the rear wall decreases, which leads to a reduction in the recoil force acting to maintain the rear wall [MATSUNAWA 1997]. Stabilizing the rear part of the keyhole by increasing the power by a

second spot, as in Twin Spot welding, should give improved results as compared to single spot welding, as the obviation of instabilities should reduce ‘spiking’ of the root and increase the overall melting efficiency. Figure 3.16 indicates that no difference could be observed for whether or not the rear wall was stabilized by a higher share of power than the front wall. X-rays showed that the porosity was always in the order of two pores per centimetre and cross-section macrographs looked identical. This process model seems not to be sustained by experimental results.

Twin Spot laser welding was assayed in a joint study by Matsunawa and the group of the IFSW. The results were not conclusive. The parameters for spatter free welds were identical to those found to be best in this benchmark study, i.e. $a \geq 0.36$ mm. The study concludes, “the large keyhole opening, which was observed at a large beam distance, is *thought* to result in a stable welding process” [DAUSINGER & MATSUNAWA 2000]. The authors of the study were obviously a bit wary whether their findings can be explained by their own process model.

These results can be perfectly reconciled with the new empirical process model developed in paragraph 4.2: the first spot removes the oxide layer and the second spot is not obstructed by oxides. Thus, spatter is suppressed. This scenario coincides with the strata proposition I of the empirical process model in section 4.2.3. For this proposition to be true, it is not important whether the preceding spot has more power than the subsequent spot, but only whether it effectively melts away the surface oxide layer. Thus, instabilities such as pores were generally reduced to less than 2 pores per centimetre. If the parameters are set such that the subsequent spot has substantially more power than the first spot, the seam did not exhibit the same number of pores per centimetre. However, it should have been less according to the process model. As can be seen in figure 3.14, the melting efficiency is substantially reduced by Twin Spot welding as compared to Nd:YAG laser single spot welding. Since the same energy per unit length was transferred in either setting to the workpiece, this means that the melt solidified later in Twin Spot than in single spot welding. This enabled bubbles to rise to the surface and release their enclosed content thereby reducing porosity. This has to be compensated for by a decreased melting efficiency, i.e. reduction of penetration depth and speed of welding.

There are further drawbacks of Twin Spot welding: filler wire cannot be easily and robustly supplied to the fusion zone, as can be seen in figure 3.17.

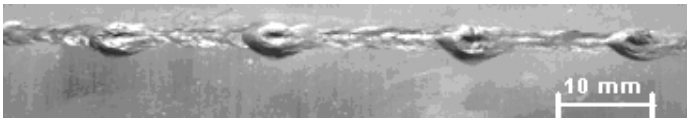

Figure 3.17: Inhomogeneous filler wire transfer in Twin Spot welding, overbead exhibits drop formation; $P_{Nd:YAG}$ = 3 kW; partition of power between the two spots in percent 34/66; v_w = 3 m min^{-1}; v_f = 3 m min^{-1}; a= *0.54 longitudinal alignment; EN AW-6060 T66; filler Al4047 A (SG-AlSi12); $Ø_f$ = 1 mm; argon flow 20 L min^{-1}*

Gref found that filler wire could not robustly be integrated in a four spot arrangement as to create quattro spot welding [GREF 2005, p. 105]. Multiple spots are detrimental to filler wire supply. An individual spot of a multiple spot arrangement may accidentally be obstructed by the wire swaying into a solid angle that is increasing the farther the wire supply tip is positioned away from the specimen's surface. Once one of the beams it obstructed by the wire, the wire is softened and the sway angle is increased. This leads in most cases to the obstruction of another beam. Drops of filler wire get discontinuously detached, as can be seen in figure 3.17. If the filler wire is transferred to the melt pool, its homogeneous dilution is not secure. Gref admits, "for a focal distance of 0.4 mm where the process is *still relatively* efficient and the penetration depths for *possible* application are still sufficient […], the necessary filler supply rate was very high and no dilution of the filler material with the base metal was achieved. Due to the high velocity at which the filler material is supplied, the filler material is only deposited on top of the seam, as the laser melts the base metal in advance of the filler's deposition" [GREF 2005, p. 108]. Gref shows cross-section macrographs. These macrographs are spoiled by a substantial process pore at the root. The velocity was in the range of 3 ÷ 6 m min^{-1}. It should be noted that Gref considered such velocities to be 'very high'. In BHLW perfect results and homogeneous dilution are achieved for $v_w = v_f$ = 5.5 m min^{-1}.

In Twin Spot welding filler wire supply proves difficult but it is possible for restricted cases. Thereby, the gap bridging ability of Twin Spot welding could be evaluated. The largest gap which could be robustly bridged had a gap width of w = 0.5 mm. The results for increasing gap widths are shown in figure 3.18. For comparison, BHLW can robustly bridge widths of up to 1 mm as detailed in paragraph 8.2.

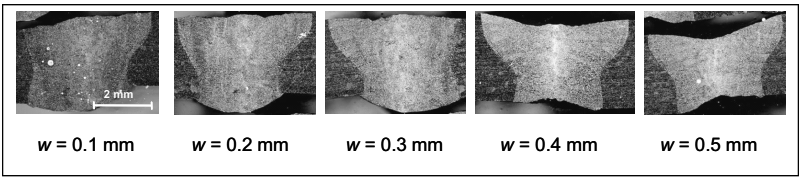

Figure 3.18: Cross-section macrographs of Twin Spot welds with intentionally introduced gaps of width w*; $P_{Nd:YAG}$ = 3 kW; power partition among the two spots in percent 66/34; transverse direction of* a*; v_w = 3 m min^{-1}; v_f = 3 m min^{-1}; a= 0.36 mm; tilted alignment, α = 30°; EN AW-6060 T66; filler Al4047 A (SG-AlSi12); $Ø_f$ = 1 mm; argon flow 20 L min^{-1}; butt weld*

The results of Twin Spot laser welding for zinc-coated steels are briefly summarized following [GREF 2005, p. 111-117]. They are rendered here for comparison with BHLW. By defocusing the first spot no improvement could be achieved, as the zinc layer in the overlap could not be removed. The best results are obtained if the second beam is defocused. The longitudinal distance was selected such that the second beam did not interact with the leading spot. Then the surface is smoothed by subsequent remelting. This is assumed to be just an optical improvement of the overbead, because without smoothing the weld seam exhibits instabilities, which originated from the zinc layer in the overlap. These defects are not eliminated by remelting of the surface and will surely degrade the properties of the welded piece in mechanical loading: Thus, Twin Spot welding merely achieved ‘laser dressing’ of the overbead.

3.2.4 Oscillation and laser stir welding

The concept of stabilization and influence of the keyhole geometry by oscillation and laser stir welding is based on the same process model as multiple or Twin Spot laser welding. The instabilities are to be prevented by widening of the keyhole. The process was originally invented and patented for gap bridging and

for tailored welded blanks. Tailored blanks differ in thickness [COSTE 1997, RUBBEN 1997, STOL & MARTUKANITZ 2004]. Oscillation welding has recently been researched for aluminium and zinc-coated steels. Gref conducted experiments up to 200 Hz in EN AW-6082 with an amplitude of a = 0.24 mm. He achieved the best results for 150 Hz. Porosity was not eliminated [GREF 2005, p. 72]. Meier and collaborators built an advanced optical setup, which by virtue of a scanner mirror generated oscillations up to 1500 Hz [MEIER 2005]. Although oscillating at 1500 Hz decreased porosity, elimination of porosity was not achieved in aluminium welds. The surface roughness was decreased. The influence of oscillation on zinc-coated steels was evaluated as well. The results are shown in figure 3.19:

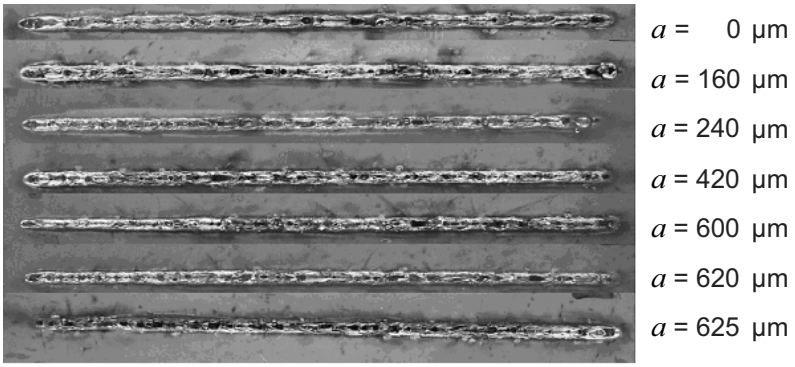

*Figure 3.19: Oscillation Nd:YAG laser welding, surface photograph of zinc-coated steel seam; $P_{Nd:YAG}$ = 3 kW; v_w =2 m min^{-1}; frequency of oscillation 1500 Hz; a is the amplitude of oscillation; zinc coating not given in reference [*MEIER *2005]*

As can be clearly seen, there is no positive effect of oscillation laser welding on weld quality. Gap bridging is achieved without filler wire but limited to about 0.4 mm for an oscillation frequency of 1500 Hz, as can be seen in figure 3.20. For comparison, without oscillation gaps of 0.1 mm could be bridged by the laser alone.

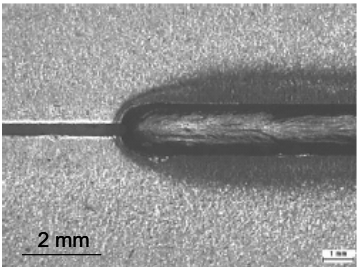

*Figure 3.20: Gap bridging ability of oscillation Nd:YAG laser welding: surface photograph of steel; $P_{Nd:YAG}$ = 3 kW; v_w =3 m min^{-1}; gap width: 0.4 mm; frequency of oscillation 1500 Hz; amplitude of oscillation a= 600 µm; S235 JR [*MEIER *2005]*

The range of future applications of this technology is limited, since the oscillation of the beam prevents filler wire to be integrated into the welding procedure, and an elaborate and expensive optic system is required.

The process of laser stir welding (LSW) was presented to the public by [MARTUKANITZ 2005]. The optic to enable LSW is simpler than for oscillation welding and rotates the laser for hydrodynamic stirring of the weld pool. The principle of the welding process is shown in figure 3.21.

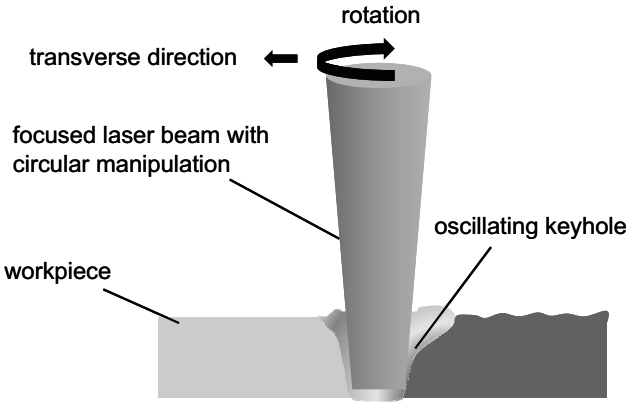

Figure 3.21: Schematic diagram of the laser stir welding (LSW) using circular beam manipulation [mod. acc. MARTUKANITZ *2005, p. 713]*

The results for EN AW-5083 with LSW are shown in figure 3.22.

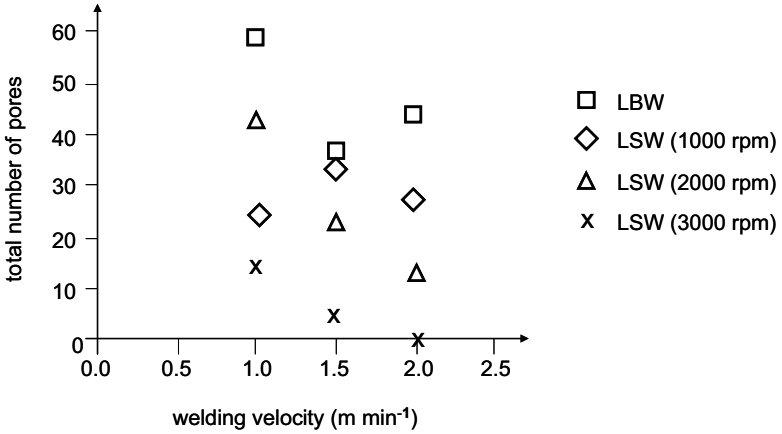

Figure 3.22: Porosity as a function of welding velocity for Nd:YAG laser stir welds; rotation circle diameter = 3.0 mm; $P_{Nd:YAG}$ = 3 kW; EN AW-5083 [mod. acc. MARTUKANIZ *2005, p. 717]*

Porosity is greatly reduced by LSW as compared to laser beam welding (LBW). It should be noted that porosity is decreased for increased velocities of welding. This is in accordance with Rykalin's number (c.f. equation 7.1) and can be taken as a general rule. LSW also decreases the sensitivity to wire misalignment when adding filler material. No results for zinc-coated steels with LSW were published in the literature at writing.

Oscillation beam welding and LSW are similar as far as the effect on the workpiece is concerned. The motion of the beams as viewed from the inertial frame of the workpiece results in a sinusoidal and spiral-like pattern. There is a crossover of subsequent turns in LSW for the parameters employed by Martukanitz, as shown in figure 3.23. The respective patterns are getting ever more congruent for either technique for high enough rpm and transverse speeds. This suggests that oscillation beam welding and LSW can eventually be reduced to the same mechanism with regards to the workpiece. The laser beam crosses over again for the parameters given in figure 3.22. Hence, the results of LSW as far as porosity is concerned can be explained by remelting. Remelting reduced the heat gradients in the workpiece and prolongs cooling, which in turn allows for degassing of the melt pool. Porosity is greatly reduced in oscillation beam welding [MEIER 2005].

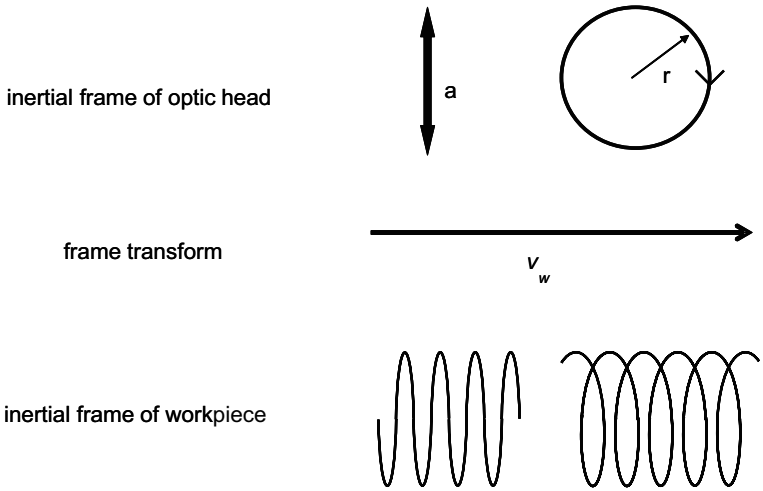

Figure 3.23: Path of the modulated beam as viewed from the inertial frame of the optic head and from the inertial frame on the workpiece; left: oscillation laser welding; right: LSW

Expulsions of steel melt caused by vaporization of zinc from the overlap joint are responsible for the defective results of oscillation laser welding in zinc-coated steels. The material properties of zinc as compared to iron are responsible: the boiling temperature of zinc is even below the melting temperature of iron. Iron is the major constituent of steel, the effect of which is detailed in paragraph 4.2. Oscillation beam welding could not produce defect-free welds even with the highest frequency of 1500 Hz . LSW achieves merely 50 Hz on the workpiece by 3000 rpm. Thus, it can be extrapolated that LSW is not able to generate better results, as the frequency of motion in the inertial frame of the workpiece is by two orders of magnitudes lower than the frequencies of oscillation beam welding.

3.2.5 Beam amplitude modulation welding

According to another process model defects and instabilities are caused by intensity fluctuations on the workpiece and within the cavity. The keyhole was modelled to oscillate with an eigenfrequency [TSUKAMOTO 2004]. Tsukamoto tried to compensate for these periodic power fluctuations by square wave pulses. He accordingly modulated the laser at the eigenfrequency, which he determined from experiment for each welding task. He found frequencies around 16 Hz.

Despite his efforts, porosity was not completely eliminated and only decreased substantially in specific cases. Klassen pulsed a laser at around 100 ÷ 200 Hz and did arrive at a comparable result with regards to porosity [KLASSEN 2000]. However, Klassen explicitly negated eigenfrequencies (c.f. section 3.1.2.3).

Hence, amplitude modulation does not generate perfect welds and is difficult to adjust to new welding tasks in industrial production, as the eigenfrequency can only be determined in a laboratory. A specific laser system needs to provide power amplitude modulation at the eigenfrequency. The laser has to weld at a reduced power, because the average output power has to enable these overshoots. The maximum power utilized for welding is sometimes half the nominal output power, and the penetration depths and velocities of welding are simultaneously decreased. Expensive nominal output laser power is wasted.

4 Bifocal Hybrid Laser Welding (BHLW) of Aluminium

4.1 BHLW process technology for stability in aluminium welding

In this chapter the process technology of BHLW for aluminium is detailed. The stability and robustness of the constituting processes of conduction mode welding by an HPDL and keyhole welding by an Nd:YAG laser are described and analyzed. Two pivotal findings of this dissertation are presented in this chapter: First, the aperiodical closure of the keyhole orifice by the sturdy aluminium oxide layer. Second, the causal effect of the process gas on pore formation is proved. These two findings are especially important for aluminium welding in industrial circumstances where instabilities are rife. The attention is concentrated on aluminium. Steels are considered briefly whenever this is elucidating. The results, synergetic effects, and the system technology of BHLW for aluminium and for other materials are described in chapter 8. At the end of this chapter a novel mathematical process model of the formation of process porosity is attempted.

4.1.1 Conduction mode welding

For conduction mode welding (CMW) the laser beam is focused to a power density of the order of magnitude of 10^3 W mm^{-2}. A power density of this order of magnitude is used to fuse materials to create a joint *without* significant vaporization. The wavelets collapse upon being intersected by the material according to Bohr's principle of complementarity in the Copenhagen interpretation of Quantum Mechanics. The energy of the wavelets is input by direct heating into the workpiece. The heat flow is governed by thermal conduction from a surface heat source, and the weld is made by melting portions of the base material. These principles are relatively well understood enabling analytical modelling to be applied to joining of metals and alloys.

A hemispherical weld bead and heat affected zone (HAZ) is formed, as can be seen in figure 4.1. Conduction-limited welds exhibit a low aspect ratio according to equation 3.3. Such welds show a broad bead, which is desirable when gaps are

to be bridged, but a low depth, which is in some cases deliberately aimed at, e.g. if materials of different thickness are to be welded to highest quality. HPDL systems recommend themselves for CMW as they readily deliver moderate beam quality which is still good enough to melt the material. HPDLs exhibit a very high wall-plug efficiency compared to solid state lasers and are comparably cheap, c.f. table 1.1.

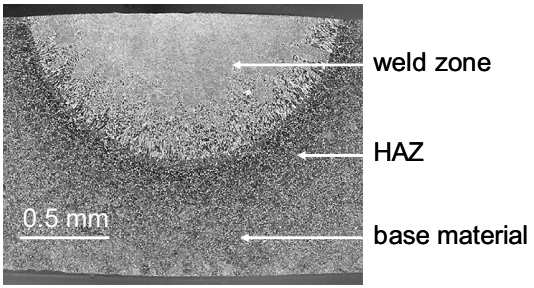

Figure 4.1: HPDL cross-section macrograph of hemispherical weld pool and heat affected zone (HAZ); P_{HPDL}= 3kW; argon flow 20L min^{-1}; EN AW-6060 T66; v_w = 0.5 m min^{-1}

In equation 3.5 the *Peclet number* was introduced as a measure for the importance of convectional flow and heat conduction in the distribution of the radiation power absorbed throughout the melt pool. For a typical case of aluminium welding *Pe* scales with $54.8 \cdot v_w$. In the melt pool induced by an HPDL the velocity of the fluid is considerably higher than the velocity of welding. The velocity of the fluid can be estimated by monitoring oxide particles staying afloat on the melt pool as tracer particles. Hence, the *Pe* is estimated to be about 5 for aluminium indicating that heat is transported by conduction as well as convection. For steels *Pe* scales with $294 \cdot v_w$. Invoking the average velocity in melts, *Pe* is of the order of magnitude of 15. Thus, indicating that in steels convection is dominant. Secondly, the Peclet number provides a measure of the relative effectiveness of heat transport by convection and conduction. Near the fusion boundary of the melt pool the flow of melt is stagnant. Since the Peclet number is one order of magnitude lower for liquid aluminium than iron, heat transfer by conduction is more efficient in aluminium than in steel melts.

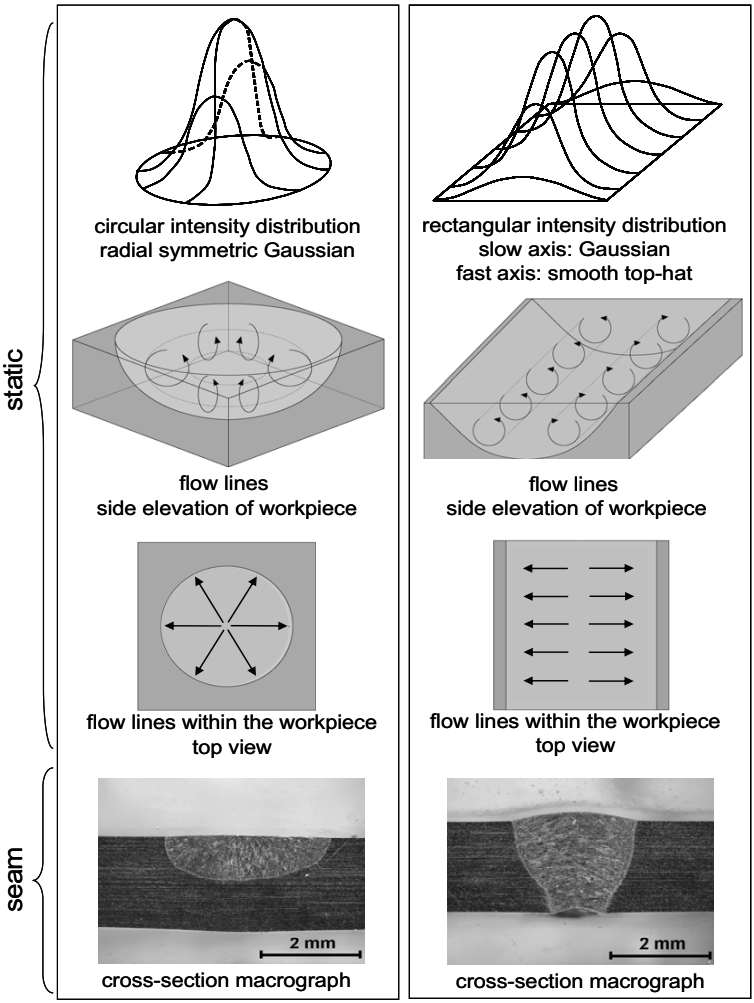

Figure 4.2: Effect of welding with a circular (right) or a rectangular (left) HPDL focal spot: relative intensity distribution not to scale; steel was used to make the dependence of penetration depth on associated melt motion more obvious; parameters of cross-section macrographs (bottom row): P_{HPDL}= 3 kW; argon flow 20 L min^{-1}; v_w = 0.5 m min^{-1}; stainless steel 1.4301(X5 CrNi18 10); right: rectangular spot 1.7 mm x 3.8 mm; left: circular spot diameter 2 mm

Thirdly, the *Marangoni effect*, i.e. the spatial temperature gradient of the surface tension, creates a driving force by which the melt tends typically to be pulled away from hotter towards cooler regions. During laser welding this surface tension force dominates the flow of the melt.

For a *radial symmetric* Gaussian intensity distribution, shown on the left in figure 4.2, the flow lines describe circles moving up in the middle and being deflected towards the perimeter of the melt pool. The melt is rising up towards the peak of the distribution, since the laser acting as a surface heat source creates the hottest spot there. This leads to an efficient mass transport by convection transferring enough heat into the fusion zone for further melting. The laser needs to be moved along the joint line to weld *linear* seams. The laser constantly alters its position while *transgressing* the workpiece. This effects the flow lines along *this* line of motion. The melt elements at the melting front rise towards the centre peak of the distribution, i.e. *opposite* with regards to the direction of motion of the laser beam, since the peak of the distribution is approaching these melt elements and the heat gradient points away from the peak: In the rest frame of the workpiece the melt elements are *reversed* in direction once the peak of the distribution has transgressed them. This is because once the peak has transgressed these melt the heat gradient still points away from the peak, but the melt element and the peak have exchanged their relative position. Then, for the very same melt element the flow line points *along* the direction of motion. This gives a *net* **stagnant** motion.

In other parts of the melt, i.e. off-axis with regards to the line of linear motion, the melt elements experience radial deflections while in motion. This leads to an overall reduced amount of melt being transported to the boundaries of the melt pool by convectional flow: the melting efficiency is decreased. The weld pools become shallower and broader. This results in a decrease of penetration depth as compared to the rectangular intensity distribution, c.f. macrographs at the bottom of figure 4.2.

A *rectangular* intensity distribution is shown on the right hand side of figure 4.2. In the intensity distribution the slow axis still represents a Gaussian profile, but the fast axis exhibits a smooth top-hat profile. The latter distribution is more efficient for melting. The following account of flow lines and behaviour of melt element motion is based *only* on heat gradient considerations. Again, the flow lines describe circles rising up towards the plane where the peak of the Gaussian lies. It should be noted that there is no significant temperature gradient along the fast axis, because the top-hat axis has a plateau of intensity. The direction of

welding is parallel to the fast axis. Hence, when such a heat source is moved along the fast axis the flow lines do not get deflected. The melt elements' motion is mainly restricted to a plane. This plane is parallel to the slow axis and perpendicular to the direction of welding. Such a square or rectangular spot provides conditions for 2D-convectional flow as compared to the 3D-flow pattern for the spherical spot of a radial symmetric Gauss profile. In figure 4.2 the intensity distribution, the flow lines, and the associated cross-section macrographs are displayed. Apart for the intensity distribution the other parameters of welding are equal, i.e. ceteris paribus. The increase in cross-sectional area demonstrates an increase in melting efficiency. The increase in penetration depth should be noted.

For the following results a 3 kW-Laserline HPDL-system with a beam parameter product (BPP) of 85 x 200 mm*mrad was employed. This translates with a spherical lens of f = 150 mm into a *rectangular* focal spot of 1.658 x 3.820 mm^2 where the fast axis is aligned with the transverse direction of welding. The wavelengths of the HPDL are centred on 808 & 940 ± 10 nm (FWHM). The compact multi-kilowatt diode laser head can be mounted on an appropriate robot to create a flexible welding tool. When the radiation of an HPDL is coupled to a fibreoptic cable a power loss of approximately 25% is incurred. The caustic and intensity distribution of the head are displayed in figures 4.3 and 4.4.

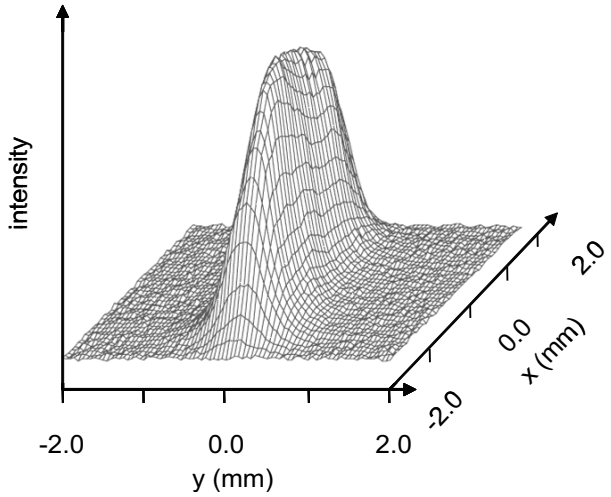

Figure 4.3: 3D-intensity distribution of HPDL, intensity qualitatively in arbitrary units

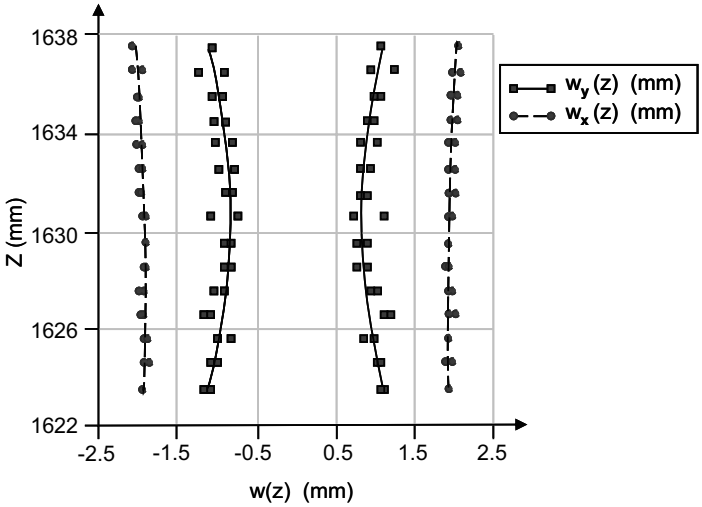

Figure 4.4: 3D-beam caustic of HPDL; z-axis in arbitrary units

For reasons of intensity, an HPDL can merely initiate heat conduction mode welding in aluminium alloys such as EN AW-6060. In steels the transition from heat conduction mode welding to deep penetration welding can be observed. Since the reflectivity of aluminium is up to 87% (c.f. steel: 58%) and its thermal conductivity is considerably higher than that of iron, the threshold for keyhole welding cannot be reached [RYKALIN 1988, p. 358-418].

Keyhole welding is a critical deciding factor to avoid the 'kissing bond' phenomenon in aluminium welds, as shown in figure 4.4.

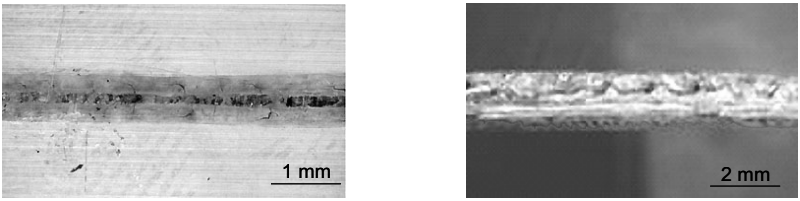

Figure 4.5: HPDL surface (right) and broken seam photograph (left) of a 'kissing bond'; butt joint EN AW-6060; P_{HPDL}= 3 kW; argon flow 20 L min^{-1}; v_f = 0.5 m min^{-1}

Heat conduction mode welds lack coalescing fusion of the alloy's matrix without special pre-process treatment, such as pickling or in-process removal of the surface oxide layer. Butt joints show the former divide. The surface oxide layer on the edges cannot be dispersed by convectional fluid flow throughout the melt pool. The vaporization temperature of aluminium T_v = 2060°C is practically coinciding with the melting point of aluminium oxide T_m = 2054°C. The thermal conductivity of Al_2O_3 is an order of magnitude below that of pure aluminium. Excess heat energy can accumulate in the aluminium oxide layer before it undergoes its phase transition from solid to melt. Concomitantly, the evaporating base aluminium causes characteristic voids. The evaporating aluminium can be seen to bubble through the Al_2O_3 on the perimeter of the weld pool in figure 4.6. The HPDL cannot satisfactorily join aluminium alloys. The penetration depth is often limited to about 1 mm, and root fusion cannot be achieved.

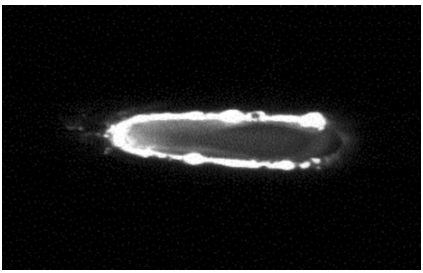

Figure 4.6: High-speed snapshot of HPDL melt pool surface; bead on plate; EN AW-6082; P_{HPDL}= 3 kW; 10000 fps; f = 150 mm; φ = 20°; Lasgon™ flow 25 L min^{-1}; v_w= 2 m min^{-1}

Besides all these drawbacks, the HPDL induces several advantageous effects in aluminium alloys. Heat conduction welding causes a characteristic sedation of the melt pool dynamics by convectional fluid flow. The oxide layer breaks up upon melting on the top surface of the workpiece. Pure aluminium melts at T_m = 660°C, whereas the melting point of Al_2O_3 is T_m = 2054°C. The heat gradient induced in the workpiece by a discrete heat source explains why solid aluminium oxide initially floats on the molten base metal until it melts away. Even more likely the oxide submerges as its density of $\rho(Al_2O_3)$= 3.9 g cm^{-3} is higher than that of aluminium of ρ(Al)= 2.7 g cm^{-3}. The dissolving oxide film appears bright on the melt pool's surface, as can be seen in figure 4.7.

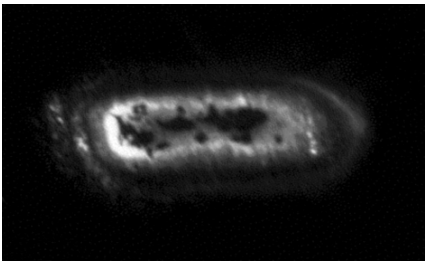

Figure 4.7: High-speed snapshot of HPDL melt pool surface; bead on plate; EN AW-5754; P_{HPDL}= 3 kW; 10000 fps; f = 150 mm; φ = 20°; Lasgon™ flow 25 L min^{-1}; v_w= 1 m min^{-1}

In sum, an HPDL with a square or rectangular focal spot induces calm melt pool dynamics by CMW. The melt pool is governed by 2D-flow lines resulting in an increased amount of melt, which is transported to a greater depth. Additionally, the surface oxide layer is removed from the surface of the molten parent material. Heat conduction and melt convection are equally important in aluminium welding and the Marangoni stress is the dominant force in determining melt pool dynamics in HPDL welding. The flow lines behave according to the intensity distribution.

4.1.2 Keyhole welding

If the beam's power density incident on the workpiece is high enough to initiate vaporization, keyhole mode laser welding is occurring. An estimate of the power density necessary for keyhole welding is given in equation 3.4. Since the reflectivity of aluminium is above the reflectivity of iron and steel, the power density produced by the laser system needs to be higher to induce keyhole welding in aluminium. Such high power densities are only attainable by multi-kilowatt lasers with a good BPP. A narrow, deeply penetrating vapour cavity - referred to as 'keyhole' - is formed and sustained by multiple internal reflections of the beam. The keyhole is surrounded by molten material. When moving the beam relative to the workpiece, a narrow weld bead is formed with a high aspect ratio, as can be seen qualitatively in figure 4.9.

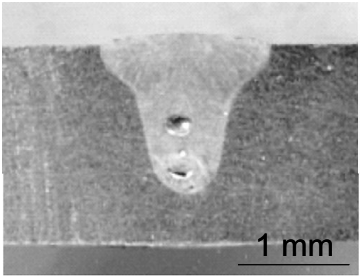

Figure 4.9: Cross-section macrograph of Nd:YAG laser weld; bead on plate; EN AW-5082; $P_{Nd:YAG}$= 3 kW; argon flow 25 L min^{-1}; v_w = 1.5 m min^{-1}

A multi-kilowatt CO_2 laser is the most economical source for welding linear and rotationally symmetric joints, since the beam can be manipulated using mirrors. Complex three-dimensional parts are more easily welded using Nd:YAG laser radiation, which can be coupled to a fibreoptic cable due to its shorter wavelength of 1064 ± 1 nm. Such a cable can be fixed to a robot and is more flexible than a mirror system. The mirror system is necessary to guide a CO_2 laser, which has a wavelength of 10640 nm. A 3 kW-Nd:YAG laser with a nominal BPP of 25 mm*mrad was deployed for the following experiments. An optical system of focal length (f = 150 mm) focuses the laser's radiation to a circular spot of 0.45 mm diameter. The intensity distribution and the caustic of the Nd:YAG laser are displayed in figures 4.10 and 4.11.

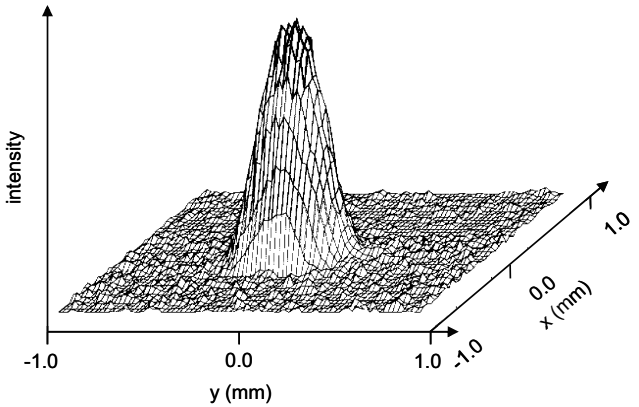

Figure 4.10: 2D-beam intensity distribution of an Nd:YAG laser; intensity qualitatively in arbitrary units

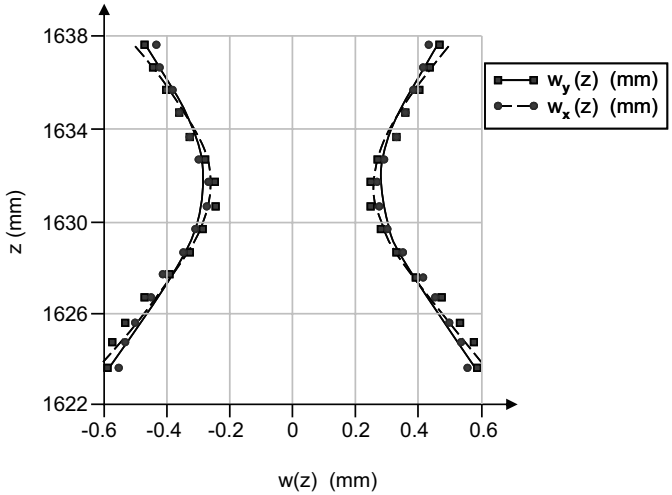

Figure 4.11: 2D-beam caustic of an Nd:YAG laser; z-axis in arbitrary units

The size of the Nd:YAG laser's focal spot necessitates precise positioning of the workpieces. The laser beam is not obstructed by the workpiece if the gaps are in the order of magnitude of the beam waist in the focal plane. In this case, the beam is not absorbed and the workpieces do not melt. The energy density within the focal spot of this Nd:YAG laser is well above the threshold to vaporize aluminium. Hence, keyhole welding is achieved in aluminium alloys. The characteristic fluid dynamics show vigorous fluid flow within the vapour cavity. Welding by avail of a keyhole accomplishes the dispersion of the oxide layer on the surface and more importantly on the edges of workpieces throughout the fusion zone. Hence, the Nd:YAG laser prevents a 'kissing bond' typical for HPDL weld beads.

As beam and material move relative to one another, material is progressively melted at the front edge of the melt pool and flows around the deep penetration cavity to the rear of the pool where it solidifies in a characteristic chevron pattern. The shape and the size of the keyhole fluctuate during welding, which results in instabilities. The diameter of the keyhole is generally approximately the size of the beam diameter. Although the thickness of this film at the melting front is only as few tenths of a millimetre, the beam does considerably irradiate the melt film. In high-speed imaging the surface aluminium oxide layer can be seen to stay intact and is kept aloft by the underneath evaporating base material, since the temperature of vaporization of the aluminium matrix and the temperature of

melting of aluminium oxide are very close to each other. Because the melt film is very thin and the melt pool surface preceding the orifice is very short, the aluminium oxide layer does not break up and not enough time is allowed as in HPDL welding for the aluminium oxide layer to submerge. The orifice of the cavity and the surrounding melt pool fluctuate vertically. The melt pool train shows ripples. Those ripples solidify to a form a rough overbead. The molten surface oxide layer gets pushed away by the vapour-jet from the front edge of the keyhole sometimes obstructing the keyhole's orifice. This happens to a lesser degree at the side edges, as can be seen in figure 4.12.

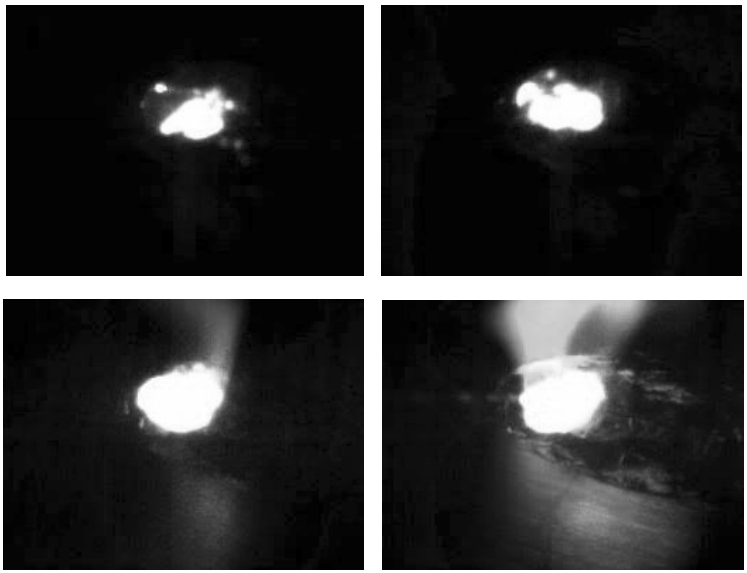

Figure 4.12: Oxide layer obstruction in Nd:YAG laser welding: series of subsequent high-speed photography snapshots; bead on plate; EN AW-6060; 10000 fps; $P_{Nd:YAG}$ = 3 kW; f = 200 mm; φ = 15°; argon flow 25L min^{-1}; v_w = 2 m min^{-1}

As a consequence, the surface oxide layer acts as source of intensity variations within the keyhole. This phenomenon seems not to have been reported anywhere in the literature. Aluminium was thought of as a homogeneous material like steel. The intensity variations induced by a non-periodic obstruction of the keyhole by the oxide layer give rise to instabilities. It has been experimentally demonstrated that the removal of the oxide layer by brushing of the plates' surfaces previous to

welding greatly reduced porosity formation [SATOH 1997]. Brushing, however, does only decrease the thickness of the oxide layer formed by the autopassivation mechanism of aluminium. Thus, this experimental observation of obstruction of the keyhole orifice by the surface oxide layer is a *completely new* insight.

The corollaries of this experimental observation are: the melt film is comparably thin on the vaporizing edge and perturbed by the vapour-jet. The coating of the parent material by a surface layer of aluminium oxide, which gives rise to instabilities, plays a *pivotal* role in the development of a new *empirical* process model of aluminium welding in the next paragraph.

4.1.3 Process gas induced porosity

Chapter 3 dealt in detail with the state of research on the formation of instabilities in laser beam welding. In section 3.1.2 all seam imperfections such as blow holes, pores, and spatter were subsumed in the category of '*instability'*. Although the empirical or mathematical process models in chapter 3 each claimed a *different* physical mechanism for the formation of instabilities, they were all based on a *monocausal* physical mechanism: i.e. intensity distribution fluctuations, *or* deformation of keyhole geometry, *or* resonant vibrations, *or* physical properties of the melt. A more *integrative* approach was rarely adopted. Even if a wider approach was taken, the considerations were limited to the *system* consisting of keyhole *and* laser radiation. A cause *external* to the keyhole-laser-radiation-system was not thought of, because the quest for a *third* unknown entity related to those two specific known things, i.e. keyhole and laser radiation, seemed to be spurious. Or classically expressed: tertium quid? tertium non datur.

In the previous section 4.1.2 the obstruction of the keyhole orifice by the oxide layer was shown to potentially be a *new* source for instabilities so far not reported in the literature. This cause of instabilities can be obviated in BHLW, as described in the section 4.2.3 outlining the strata proposition.

In this section a *third,* specific cause for process pores will be presented: process gas. On the one hand, perturbations induced by process gas were considered to lead to a reduced surface quality. The phenomenological influence of process gas on porosity formation had been noticed before [BEYER 1987]. On the other hand, process gas was never regarded as the *cause* for process pores. Experiments with the most advanced diagnostic technology were conducted in order to establish this *casualty*. At Katayama's laboratory at Osaka University in Japan an x-ray

high-speed camera system especially designed to monitor keyhole motion in laser welding was made available to the author. X-ray high-speed imaging enables *in-situ* observation of keyhole geometry variations *during* welding. Observations of the laser welding process with this experimental setup are immediate and therefore *most* reliant.

The significance and quality of these x-ray images differ *fundamentally* from the empirical observations that sparked the empirical process model outlined in section 3.1. These models were predominantly based on interpretation of cross-section micrographs, EDX-analysis of element content distribution, ultrasonic testing, and x-ray photography. The interpretation was done *subsequent* to welding.

A sample was prepared in which foils or pieces of wire in several layers at various depths were embedded to observe variations of the keyhole diameter [BEYER 1995, p. 87-93; BERKMANNS 1998, p. 43]. The material of those foils or wires was selected such that its melting point was very close to the temperature of vaporization of aluminium, i.e. 2500°C. Beyer used Tantalum (T_m = 2996°C) and Tungsten (T_m = 3410°C). Berkmanns used Neodymium (T_m = 2468°C). The traces of perforation of these foils or wires by the keyhole were analyzed *subsequently* to welding to *approximately* determine the keyhole geometry variation *during* welding, c.f. section 3.1.2.2. In order to explain resonant vibrations of the keyhole it was claimed in section 3.1.2.3 that such a keyhole will exhibit a range of characteristic mechanical vibrational modes (eigenmodes) that can support oscillation at certain frequencies (eigenfrequencies). Although the identification of those eigenmodes is a straightforward mathematical problem, the measurement of the associated eigenfrequencies is critical for aluminium. Most researches used variations of luminosity of the reemitted process radiation from the keyhole to determine those frequencies. Excited vibrational modes correlate directly to emissions from the vapour plume and result in a temporal variation of the diameter of the keyhole orifice [TSUKAMOTO 2004].

However, as was shown in section 4.1.2 for keyhole welding in figure 4.12, the orifice in aluminium laser welding is aperiodically covered by a sturdy aluminium oxide layer. This new empirical observation casts doubt on the validity of the measurement methods for the eigenfrequency in aluminium. The *aperiodical* coverage of the orifice would supersede and interfere with the eigenfrequency even if eigenmodes are actually excited. This might serve as an

explanation why Klassen, Tsukamoto, and others measured a range of frequencies differing up to a few orders of magnitude. Additionally, a finding from section 4.1.5 should be anticipated: By *virtue* of BHLW (i.e. removal of the oxide layer ahead of the Nd:YAG laser keyhole) oscillations of the keyhole's aperture *completely* ceased and no variation of luminosity of the vapour plume or keyhole could be detected for a time base of up to 2 kHz (i.e. 2000 fps). These findings call into question the *a priori* assumption that there is *any* correlation of eigenfrequencies and keyhole or vapour emissions in laser welding of aluminium.

All these methodical attempts to reconstruct a general or *normative* conclusion from particular cases represent a logical **induction**. In the following the approach towards an empirical process model is reversed: In this section experimental data by immediate x-ray observation of the keyhole geometry is *described* together with a full account of process gas shielding. No *interpretation* is attempted in this section. The interpretation of this experimental data within a new empirical and mathematical process model is left to section 4.2 and 4.3. In this section it is proceded by **deduction**.

Figure 4.13 shows the experimental setup at Katayama Laboratory at Osaka University in Japan. The apparatus consists of a micro-focused x-ray tube, which can be adjusted to focal lengths of 10 to 500 µm. The sample was fixed on a linear drive moving at right angle to the path of propagation of the x-ray beams. A fluorescing image intensifier makes the x-ray radiation visible and is recorded by a high-speed camera system at a maximum rate of 1000 fps. The gas nozzle was integrated into the optical system. The apparatus is lead shielded for x-ray protection.

The resolution of this x-ray system depends on the distance of the image intensifier to the sample, the sample thickness, and the measurements of the induced keyhole. The laser employed was an IPG fibre laser YLR 10000, i.e. with a maximum output power of 10 kW. The caustic and system parameters are given in figure 4.14.

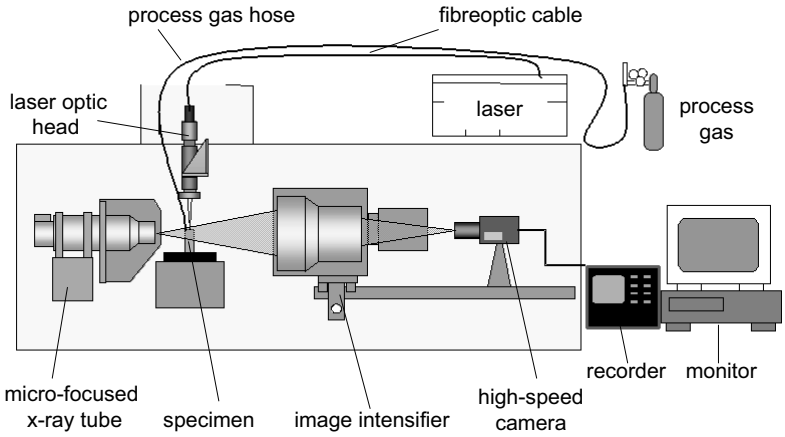

Figure 4.13: Schematic setup of high-speed x-ray imaging system at Katayama Laboratory at Osaka University in Japan

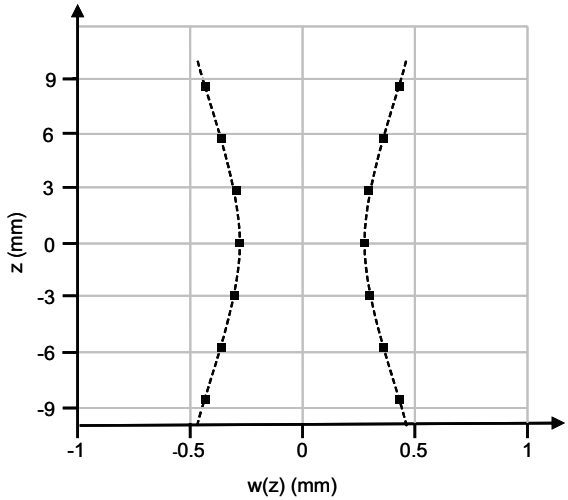

*Figure 4.14: 2D-caustic of fibre laser; P_{fibre} = 7 kW; BPP = 4.5 mm*mrad; f= 250 mm; feeding fibre Ø = 300 µm; spot diameter in focal plane is 560 µm*

Figure 4.15 shows a sequence of snapshots taken with this apparatus. The results are comparable as far as the lasers are concerned: In Japan the spot diameter in

the focal plane is 560 µm for the fibre laser (λ = 1070 ± 1nm FWHM); in Germany the spot diameter is 450 µm for the Nd:YAG laser (λ = 1064 ± 1nm FWHM), which was employed for BHLW. It should be noted that the gas supply nozzle was in this case a single lateral nozzle (c.f. figure 5.1) with a diameter of 8 mm.

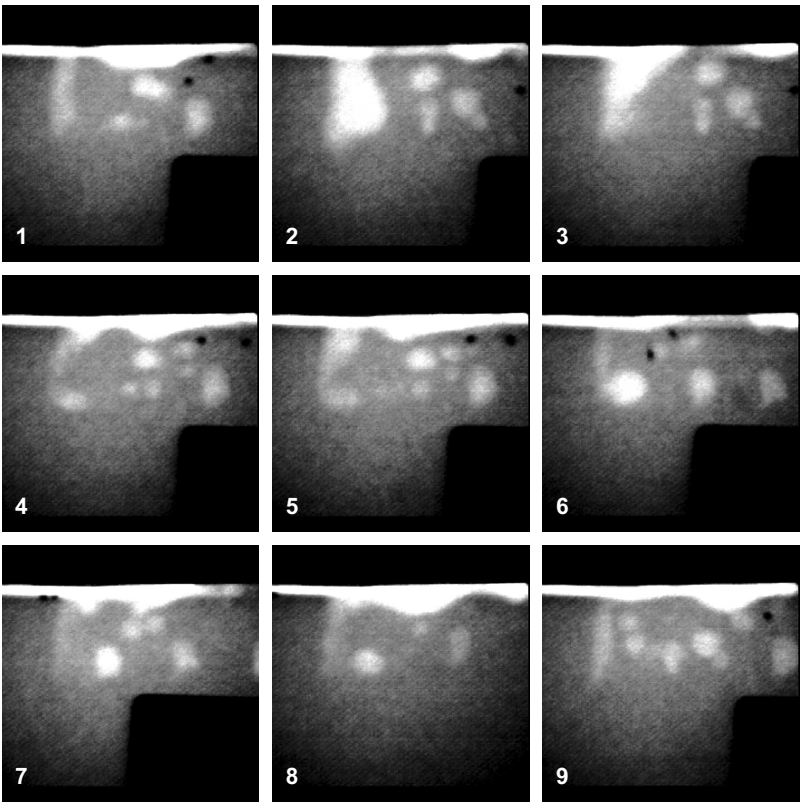

Figure 4.15: Sequence of high-speed x-ray transmission snapshots of fibre laser welding; 1000 fps; P_{fibre} = 6 kW; φ = 6°; laser specifications given in figure 4.14; v_w= 3 m min^{-1}; argon flow 25 L min^{-1}; argon flux 50 L min^{-1} cm^{-2}; nozzle inclination angle 45° leading the laser beam axis; EN AW-5083; bead on plate

In frame 1 of figure 4.15 a depression of the melt pool surface can be seen. In frame 2 a displacement of the weld pool along the keyhole rear wall takes place. The content of this displacement is released to the atmosphere in frame 3. A

travelling wave agitates the melt pool surface and a bubble forms at the keyhole tip in frame 4. The bubble detaches in frame 6 and rises upwards in the melt pool, and several bubbles form in a similar manner. Some of these bubbles are present simultaneously in frame 9. In addition to the sequence in figure 4.15 for EN AW-5083 a sequence of EN AW-6061 is shown in figure 4.16 taken under ceteris paribus conditions. EN AW-6061 is the wrought alloy of the extrusion alloy EN AW-6060, which is the reference alloy within this dissertation. EN AW-6060 could not be assayed in the x-ray apparatus, since a sample thickness of 6 mm for x-ray transmission was not available for the extrusion alloy. The reason is rather mundane: such thicknesses are not sensible for extrusion processes. In figure 4.17 the alloy EN AW-6061 is used and the focal spot diameter is decreased, because a feeding fibre of smaller diameter and an optical system with a shorter focal length is employed. The caustic is shown in figure 4.17. Figure 4.18 is displayed to account for the influence of a smaller keyhole diameter. The observations are otherwise equivalent to those described for figure 4.15.

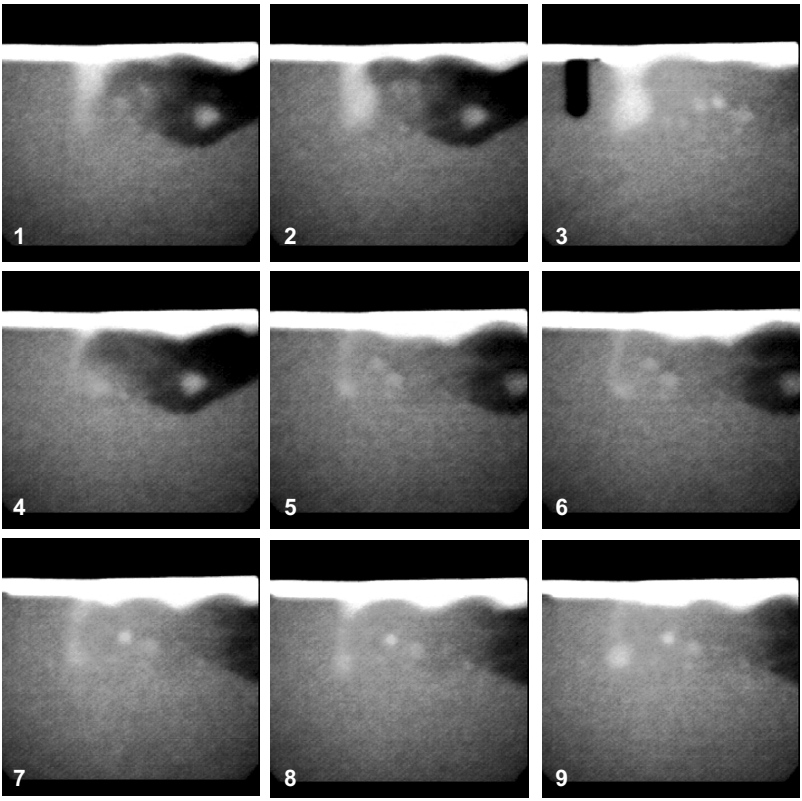

Figure 4.16: Sequence of high-speed x-ray transmission snapshots of fibre laser welding; 1000 fps; P_{fibre} = 6 kW; φ = 6°; laser specifications given in figure 4.14; v_w = 3 m min^{-1}; argon flow 25 L min^{-1}; argon flux 50 L min^{-1} cm^{-2}; nozzle inclination angle 45° leading the laser beam axis; EN AW-6061; bead on plate

For completeness the caustic of the optical system to achieve a focal spot diameter of 130 µm is given in figure 4.17.

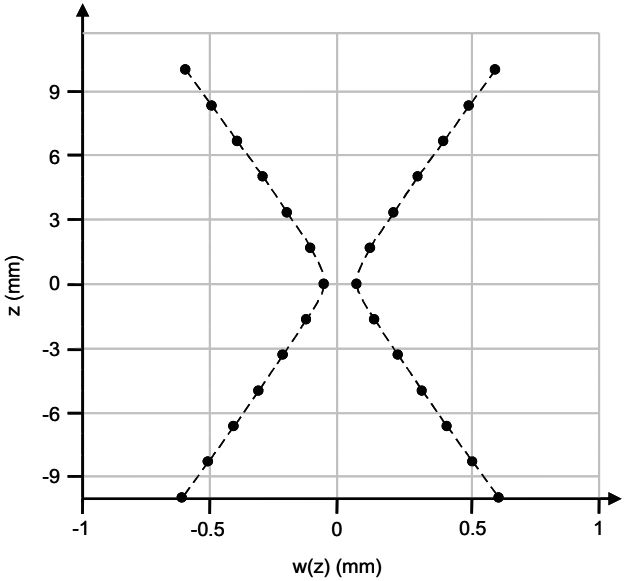

*Figure 4.17: 2D-caustic of fibre laser; P_{fibre} = 300 W; BPP = 4.5 mm*mrad; f = 150 mm; feeding fibre Ø = 100 µm; spot diameter in focal plane is 130 µm*

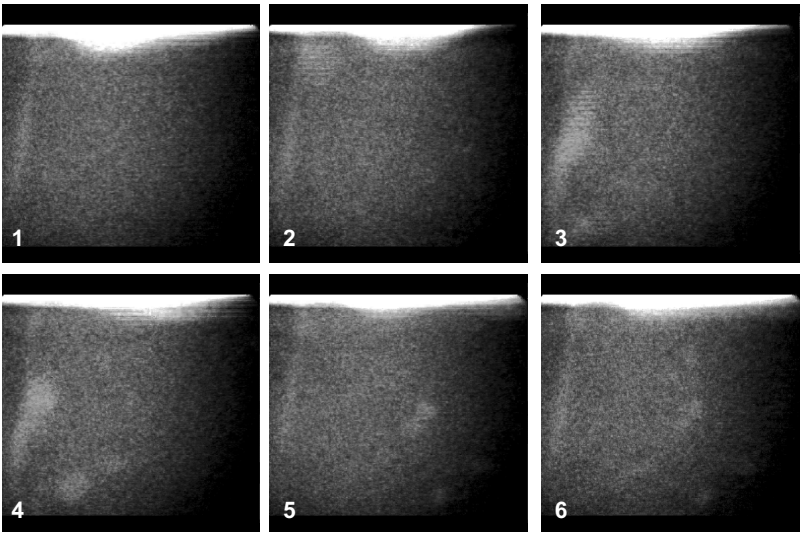

Figure 4.18: Sequence of high-speed x-ray snapshots of fibre laser welding; 1000 fps; P_{fibre} = 6 kW; φ = 6°; laser specifications as in figure 4.17; v_w= 3 m min^{-1}; argon flow 25 L min^{-1}; argon flux 50 L min^{-1} cm^{-2}; nozzle inclination angle 45° leading the laser beam axis; EN AW-6061; bead on plate

The high-speed sequences of x-ray images in figures 4.15, 4.16, and 4.18 are only snapshots of the films from which they were excerpted. The laser beam's axis tilted by 6° to prevent back reflection from the aluminium surface. Although single snapshots can show the origin of every bubble and of the necks of the melt pool, the slow motion picture sequence allows the concentrated viewer to clearly identify common features of the melt pool dynamics. For the reader merely the snapshots are accessible, as slow motion sequences cannot be reproduced in a printed dissertation. The reader is referred to the experimental observations published by Katayama himself, who gives an equivalent phenomenological *description,* to convince the reader that another researcher than the author arrives at analogue observations [KATAYAMA 2000a, 2000b, 1999].

The observations of Katayama and the author of this dissertation can be summarized as follows:

1. A depression of the melt pool surface forms behind the orifice of the keyhole

2. The cavity is obstructed by a neck of melt
3. A wave of melt travels from the rear of the melt pool towards the orifice of the keyhole
4. *All* bubbles form at the tip of the keyhole cavity
5. The cavity fluctuates in depth and radial direction
6. These bubbles move into the melt train and remain as a pore after solidification
7. The pores are filled with process gas

Figure 4.19 gives a qualitative account of the author's x-ray images:

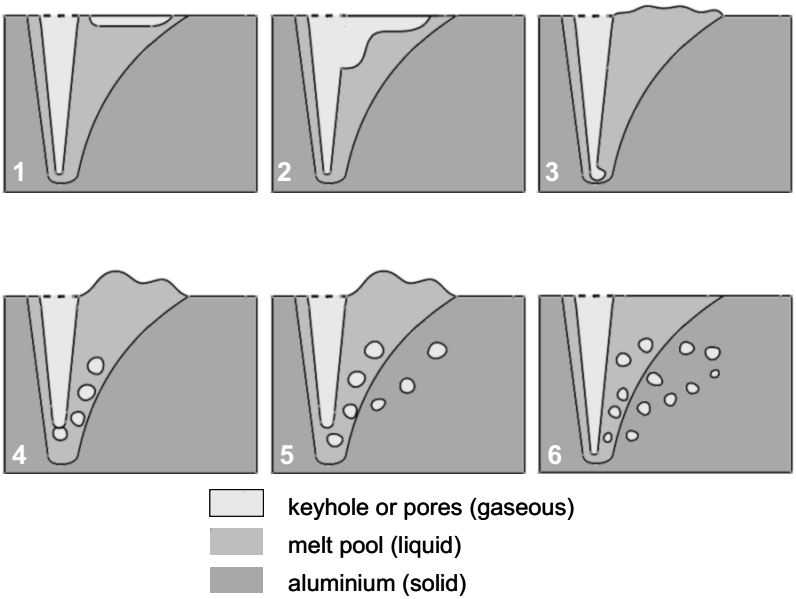

Figure 4.19: Schematic representation of x-ray imaging of process gas pore formation in single spot laser welding

This dissertation follows Katayama as far as the experimental *description* is concerned, because his empiric findings are undisputable. Admittedly, Katayama gives a different *interpretation* of these experimental observations. Section 3.1.3 cites a mathematical process model from literature, which gave an explanation

for bubble formation **towards** the tip of the cavity. Katayama interpreted his observations according to this mathematical model by suggesting that the bubble formed from intense evaporation from the keyhole front wall. Tsukamoto rejects Katayama's explanation, because it cannot explain why the bubbles form predominantly *at* the tip of the keyhole [TSUKAMOTO 2004]. He explains the neck formation otherwise: The tube of a cylindrical keyhole experiences necking close to the orifice. Such an explanation is supported by mathematical modelling; c.f. section 3.1.3 [RAPP 1996, p. 109]. In all these models the narrowing of the keyhole takes place along the perimeter, i.e. obeying *rotational symmetry*, because these models are based on a pressure balance and on the rate of flow of vapour (c.f. equation 3.7). All these mathematical models assume that the keyhole is made up and sustained by the vapour flow originating from its walls. This explanation is not exhaustive, since the bubbles that formed at the tip of the keyhole are filled with *process* gas. This was proven by Katayama who released the content of those pores by micro-drilling and determined their gas content by mass spectroscopy [KATAYAMA 2000a, 2000b, 1999]. Out of necessity, the process gas *must* have traveled through the keyhole capillary to actually reach the tip.

A further experimental finding should be quoted within the scope of this section. The number of pores per unit length of seam and the magnitude of porosity depend on the process gas mixture used. The number of pores is higher and those pores are bigger if pure argon is used as process gas instead of a gas mixture of argon with a high share of helium, as can be seen in figure 4.20. If nitrogen is used as process gas, no process pores could be observed, as can be seen in figure 4.20 and was reported in the literature [KATAYAMA 2007a, BACHHOFER 1997, ZÄH & TRAUTMANN 2004b]. The absence of pores in laser welding with nitrogen as process gas has so far not been consistently and conclusively explained.

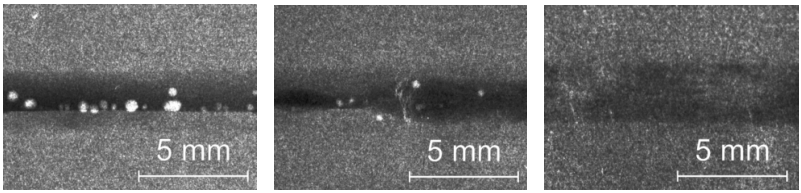

Figure 4.20: Dependence of porosity on process gas mixtures; x-ray transmission photographs; left: argon flow 30 L min^{-1}; argon flux 60 L min^{-1} cm^{-2}; middle: gas mixture flow 40 L min^{-1}; gas mixture flux 80 L min^{-1} cm^{-2}; right: nitrogen flow 12 L min^{-1}; nitrogen flux 24 L min^{-1} cm^{-2}; P_{BHLW} = 3 kW + 3 kW; f = 150 mm; φ = 20°; v_w= 3.0 m min^{-1}; v_f= 1.7 m min^{-1}, butt joint; EN AW-6060; filler Al4047 A

Katayama conducted experiments in an evacuated chamber. This is a very special condition, since literally no process gas and no ambient air affects the welding process. Katayama observed that in vacuum *no* bubbles formed in the melt pool originating from the keyhole although the middle parts of the keyhole swelled up in the molten pool. When welding in vacuum countercurrent liquid flows as well as different melt pool geometries were observed as compared to welding at normal atmospheric pressure with a coaxial process gas. Namely, during welding with a process gas the circulation of a vigorous downward flow of melt was observed along the keyhole. The flow streamed from the keyhole tip along the bottom of the melt pool to the upper rear and subsequently below the surface back to the keyhole. When welding in vacuum the liquid flowed upwards along the rear keyhole wall, but there was no such strong flow near the bottom and the rear parts of the molten pool. It should be carefully noted that **no** porosity could be found in the weld seam when welding in vacuum [KATAYAMA 2001].

All these observations and experimental findings will be accounted for by the new empirical and mathematical process model in sections 4.2 and 4.3.

4.1.4 Influence of process gases on seam quality

The temperature gradient of the surface tension can be influenced by surface active elements, i.e. sulphur or oxygen. The direction of the Marangoni stress can be inverted and the fluid flow reversed. Härtl shielded steel melt pools by CO_2 process gas thereby supplying radical oxygen from the dissociation reaction of CO_2 [HÄRTL 2006]. When welding steels with an HPDL the inversion of fluid flow resulted in an increase in penetration depth. CO_2 gas or any other source of radical oxygen leads to an unacceptable surface quality of aluminium seams as compared to inert gases, as can be seen in figure 4.21. Hence, for aluminium welding and for all following considerations active process gas is ruled out.

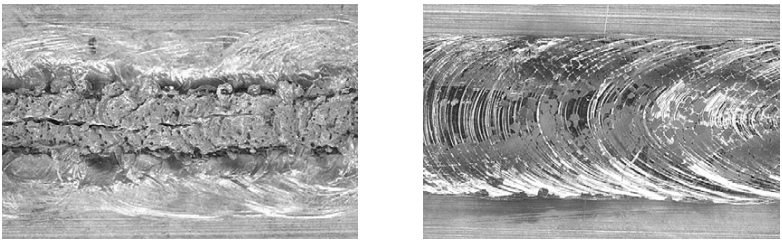

Figure 4.21: Nd:YAG laser welding; left: CO_2 shielded surface; bead on plate; EN AW-6060; $P_{Nd:YAG}$ = 3 kW; f = 150 mm; φ = 20°; CO_2 flow 25 L min^{-1}; v_w= 2 m min^{-1}; right: argon shielded surface; bead on plate; EN AW-6060; $P_{Nd:YAG}$ = 3 kW; f= 150 mm; φ = 20°; argon flow 25 L min^{-1}; v_w= 1.5 m min^{-1}

The energy input into aluminium is increased by CO_2 shielding, because an exothermal reaction takes place resulting in an increase in cross-sectional area or transverse velocity for a given penetration depth.

The best fit of the free-energy data to a linear equation by linear regression analysis is adequate for most thermodynamic calculations:

$$\Delta F = \Delta\widetilde{H} - T\Delta\widetilde{S},$$

where F is the standard free energy, H is the enthalpy, T the thermodynamic temperature and S the entropy. The tilde designates the average value for the stated range of temperatures: $\langle solid \rangle, \{liquid\}$, and (gas).

	$\Delta\widetilde{H}$ (kJ mol^{-1})	$\Delta\widetilde{S}$ (kJ K^{-1} mol^{-1})
$(CO_2)\rightarrow(CO)+\frac{1}{2}(O_2)$	283.0	0.0868
$2\{Al\}+\frac{3}{2}(O_2)\rightarrow\langle Al_2O_3\rangle$	-1688.4	-0.3270

Table 4.1 Enthalpy and entropy for Al_2O_3 formation

For an average temperature in the vapour plume of about 3000 K the dissociation of CO_2, and the oxidization reaction is taking place on the liquid surface of the vapour cavity at about 660 K, which corresponds to the melting point of aluminium. The total free energy per mole is -1400 kJ. This gives an overall exothermal reaction.

The energy balance for N_2 as process gas is:

	$\Delta\widetilde{H}$ (kJ mol^{-1})	$\Delta\widetilde{S}$ (kJ K^{-1} mol^{-1})
$\{Al\}+\frac{1}{2}(N_2)\rightarrow\langle AlN\rangle$	-327.3	-0.1156

Table 4.2 Enthalpy and entropy for AlN formation

The total free energy is -250 kJ for the same average temperature in the vapour, and the dissociation of N_2 and the oxidization reaction taking place on the liquid surface of the vapour cavity. This gives an exothermal reaction. This result is revisited in chapter 6.2. A caveat on usage of N_2 should be noted, because the formation of AlN results in a weakening of the dynamical properties [ZHAO 1999].

In sum, only inert gases should be used in aluminium laser welding. Reactive gases are not permissible, because of the elevated process temperatures as compared to classical arc welding techniques where no vaporization takes place. The increase of melting efficiency generated by diatomic shielding gases in aluminium welding has been known since the late 1950s. However, further machining of the overbeads was necessary for arc welded joints. This technique was employed in the former German Democratic Republic (Socialist Democratic Republic), because it was the only solution in those days, as there were supply shortages of inert gases, such as helium. During the 1980s and 1990s process

gases doped with N_2 or O_2 as little as 150 ppm were employed (in the West) to satisfy both objectives, i.e. increased penetration and no excess oxidation in aluminium arc welding. These elements embrittle aluminium welds and have henceforth not been used in laser beam welding of its alloys.

4.1.5 Deep penetration welding with BHLW

For bifocal *hybrid* laser welding the independent beams emerging form the two laser systems HPDL and Nd:YAG laser are superimposed by the optical system to act in the *same* process zone. As the two beams are delivered at different wavelengths, each beam maintains spatiotemporal coherence relationships among itself and not among the other beam. This welding technology is rightly termed a *hybrid*, because the beams' radiation, which eventually generates the two superimposed surface heat sources within the skin depth of the material, propagates independently through space prior to absorption. The beams do not interact as far and their respective parameters are concerned. For such linearly independent variables the methods for statistical design of experiments can be applied to establish empirical laws. For the objective of this section the focal planes of those two laser beams are focused as congruently as possible on the surface of the material to be welded.

However, the optical system allows for the two focal planes to be offset in the vertical direction. This offset is the seminal parameter for welding zinc-coated steels or other coated materials in an *overlap* joint setup. The beam material interactions are strongest in the focal plane. Hence, it is crucial that the system is *bifocal*.

The relative position in the x-y-plane of the two focal spots is schematically shown in figure 4.22. A few terms should be clearly defined for the following: If the fast axis of the rectangular spot of the HPDL is aligned with the traverse direction, this is termed *longitudinal* setup. And if at right angles, this is termed *transverse*. If the beam's direction of propagation makes an obtuse angle with the direction of welding, this is called drag welding. And if the angle is acute, it is called push welding. Further, the circular Nd:YAG laser spot can be positioned with respect to the direction of travel *ahead*, *middle,* i.e. centre of cross hairs, or *behind* the rectangular HPDL spot.

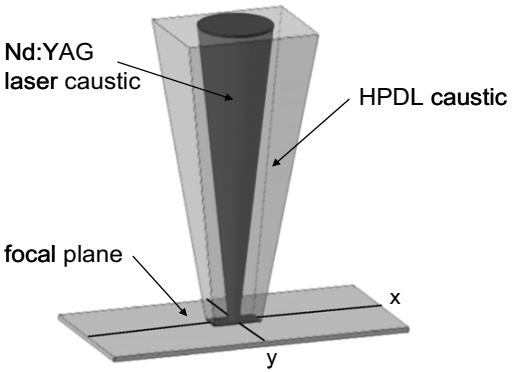

Figure 4.22: HPDL and Nd:YAG laser beam caustics and their relative position in BHLW: rectangular HPDL focal spot and circular Nd:YAG focal spot in a reticule position

In figure 4.23 the intensity distribution of BHLW is shown:

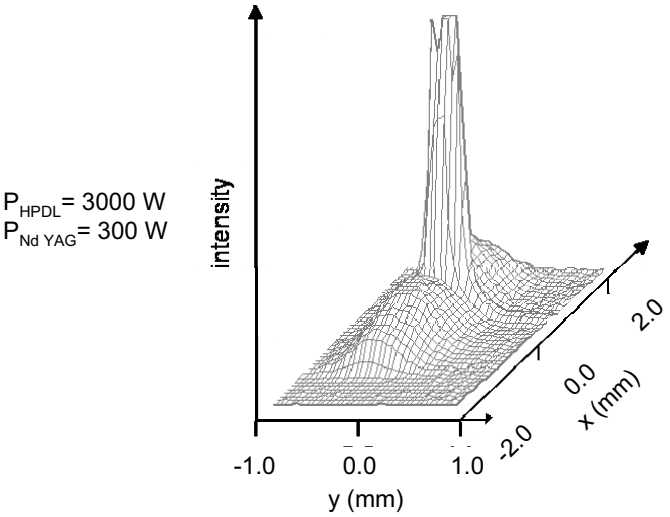

Figure 4.23: Intensity distribution of the optic system in BHLW; the power of the Nd:YAG laser was reduced by a factor of 10 in order to resolve the contribution of the HPDL within the scaled sensitivity range of the power density meter; intensity given qualitatively in arbitrary units

The transverse direction did not yield any improvements in preliminary experiments. Transverse orientation was therefore not adopted. The longitudinal position of the Nd:YAG laser was varied to be in the middle, ahead, and behind the HPDL. It was found that within the limits of experimental error those positions could not be distinguished as far as the cross-sectional area of the weld seam is concerned, as shown in figure 4.22. The reticule position was set as the standard position for the following experiments in bead on plate and butt joints, c.f. figure 4.24.

The focal plane of the Nd:YAG laser was congruent with the surface of the sample. The HPDL was 1 mm above the focal plane of the Nd:YAG laser due to constructional constraints of the optic system. This can be seen by comparing figure 4.3 and figure 4.9 for *z*-axis values. The difference in relative position of HPDL and Nd:YAG laser can be determined although absolute magnitudes of *z*-axis values are arbitrary. The constraint on the focal plane was judged to be a minor drawback, since the beam quality of the HPDL is inherently quite moderate as compared to the beam quality of the Nd:YAG laser. Deep penetration welding is very sensitive to defocusing of the Nd:YAG laser and can only be initiated for the focal plane of the Nd:YAG laser positioned congruently with the workpiece's surface. For CMW defocusing of the HPDL can be tolerated within certain limits. In the following experiments the beam material interactions are unfortunately not as strong as they could have been for perfect alignment. It should be noted, that all experimental results presented within this dissertation were achieved with this drawback of the experimental optic setup.

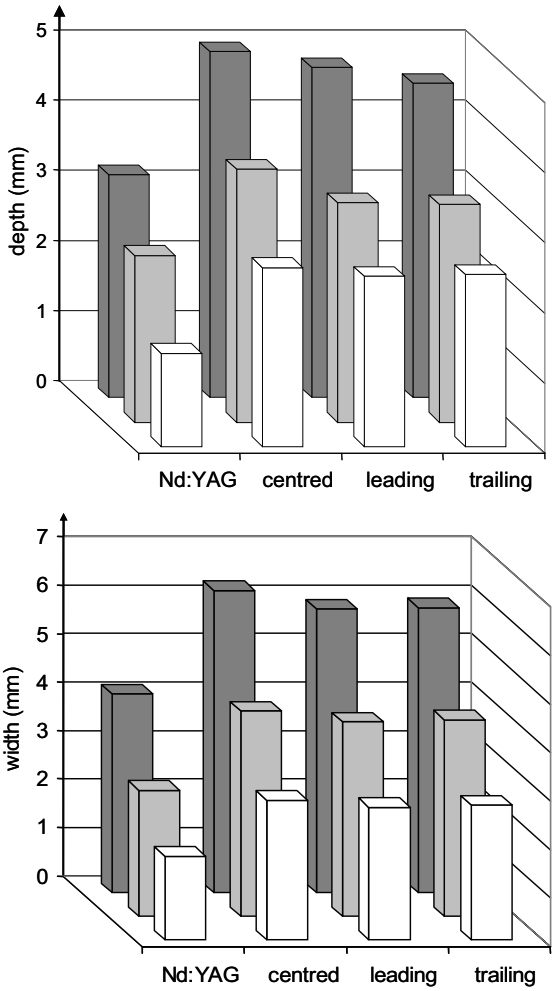

Figure 4.24: Variation of penetration depth (top) and width (bottom) versus relative focal positions of the Nd:YAG laser alone and as part of BHLW process with regards to the reticule of the HPDL for the three principal relative positions, different transverse speeds: ■ 1 m min^{-1}, ■ 2 m min^{-1}, □ 4 m min^{-1}; $P_{Nd:YAG}$ = 3 kW; P_{BHLW} = 3 kW + 3 kW; bead on plate; focal position: transverse; z axis offset = 1 mm; shielding gas: 50% He + 50% Ar; gas mixture flow 25 L min^{-1}; material thickness: 5 mm; AlMgSi1

The melt pool dynamics in BHLW were studied by high-speed imaging. A typical image is displayed in figure 4.25.

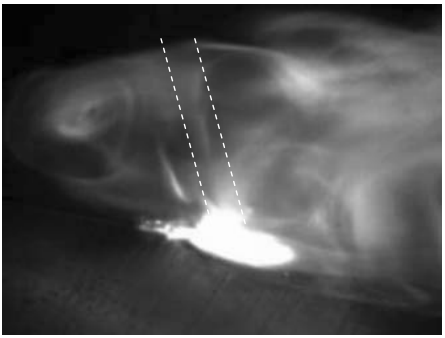

Figure 4.25: High-speed snapshots of BHLW with filler wire; P_{BHLW} = 3 kW + 3 kW; EN-AW 6060; butt weld; 2000 fps; f = 150; φ = 20°; filler wire Al4047 A (AlSi12) indicated by dashed lines; argon flow 25 L min^{-1}; v_w = 3.25 m min^{-1}; v_f = 1 m min^{-1}

High-speed photography revealed that oscillations of the keyhole's orifice *completely* ceased in BHLW. The surface aluminium oxide layer is removed ahead of the Nd:YAG laser by the HPDL. The melt pool is protected from reoxidisation by inert gas shielding. The perimeter of the keyhole is stable and unperturbed, as it cannot be obstructed by surface oxide. The Nd:YAG laser takes care of the surface oxide layers on the abutted edges of the plates by completely dispersing those layers. The train of the melt pool is completely calm resembling the sedated CMW melt pool of the HPDL.

In summary, the melt pool dynamics of BHLW appear more *stable* than for the Nd:YAG laser alone. This implies the *obviation of the causes* of instabilities. The cross-section macrographs of BHLW show excess filling due to the addition of filler wire (c.f. figure 4.26). The advantages of BHLW when welding aluminium with regard to filler wire supply are detailed in paragraph 8.2.

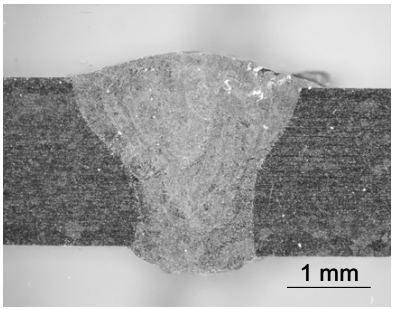

Figure 4.26: Cross-section macrograph of BHLW seam; P_{BHLW} = 3 kW + 3 kW; EN AW-6060; butt weld; f = 150; φ = 20°; filler wire Al4047 A (AlSi12); argon flow 25 L min^{-1}; v_w = 5.5 m min^{-1}; v_f = 5.5 m min^{-1}

4.2 Empirical process model for laser beam welding of aluminium

In this paragraph an abstract empirical model is developed. The propositions and assumptions are clearly stated. The empirical evidence on which the model is based was presented in the preceding paragraph 4.1. The empirical model recommends parameter settings for seams of high quality. The results are presented in chapter 6 and 7. These results can be taken as a proof of the empirical process model. They are convincing by themselves and are presented separately as not to be devalued if the process model is falsified.

4.2.1 Introductory remarks on empirical process modelling

In section 3.1.2 the major lines of thought on empirical process models were summarized. Experimental observation is the necessary input to all *empirical* model building, i.e. experimental data *precedes* the empirical model. When these models are written up to be presented to the scientific community it is common to proceed as follows: the full model is laid out at the *beginning,* and the experimental evidence from which the model was *deduced* is given *thereafter* as experimental proof.

This approach is good practice for *mathematical* process models that are based on the *laws of physics*. These laws are by definition *a priori*. If experimental data

fits *a posteriori* the predictions, such a model can claim to explain the findings. This expresses the conviction that the laws of physics are fundamental and describe the underlying *reality* to observations from experiments.

Several disadvantages are incurred when this approach is transferred to empirical process models. Although the empirical model was *deduced* form experimental data, the same data is presented in such a way as to *support* the model. The settings of parameters which are not considered in the model are not reported. Even if those parameters had been recorded when the observations were made, they would have been disregarded later anyway, as they would have been judged to be unimportant with regards to the model. The recipients in the scientific community are conditioned by the empirical model presented at the beginning of a paper and are even more patronized by the *eclectic rendition* of evidence, which is selected from the full record of the experimental data. If the empirical model is *later* rejected by contradicting observations, the experimental data will be devalued by its eclectic presentation and will not be able to be used to support or even validate another novel empirical model. This approach is ineffective as equivalent experiments have to be performed anew.

Hence, in this dissertation the following set of rules was chronologically satisfied. This represents a **code of conduct** of good practice for empirical models:

1. Present a full record of any experimental data and render all parameters and circumstantial information.
2. Develop the empirical model and express it in propositions.
3. State all the assumptions on which the model is based, i.e. simplifications or omissions of what had been considered to be negligible.
4. Support and underpin the propositions by revisiting the experimental data. (in this dissertation the data is presented in paragraph 4.1)

The forth and final step enables the recipients to concur or not. This step allows for the propositions to be verified or falsified by future experiments fulfilling Poppers demands of falsibility [POPPER 1989, p. 183].

This code of conduct rests on the conviction that all observations are *for themselves* of scientific value. If calculus of error is properly employed, one can discard those observations, which are mere *artefacts*. The purged remaining data are true *phenomena*. The term *phenomenon* means that they are *appearances*. All model building implies an underlying rule or even *law*. The models claim to represent *noumena*. The term *noumenon* incorporates the *abstract and general rules* of behaviour of which a single phenomenon is just a *specific* appearance [KANT 1787, B202-215].

In this chapter own seminal experimental data, data already published, and data quoted above are revisited if the parameters and circumstances given in their completeness allow this data to be used within the new model. The supply of process gas is particularly difficult in this respect. Some authors just name the gas used, others give its absolute flow. The *flux*, i.e. the flow through unit area per unit time, is quoted *rarely*. Additionally, the diameter of the nozzle tip, the distance of the nozzle tip to workpiece, and the type of nozzle used, should be specified, since these pieces of information are necessary for different gas nozzles to be compared. A direct comparison is not possible and estimates need to be made unless these figures are given.

A **new empirical process model for laser beam welding for specific metals** will be developed in this disseration. *Categorization* is the key to reach this objective. These categories subdivide the materials (genus) to be welded in distinct groups (species) being specific to the model.[2] The propositions encoding the new empirical model are specific to these groups of materials. The categories are quite general and therefore embody simplifications and assumptions, which are stated clearly in order to be refined as further investigations proceed.

Finally, the experimental data will be assessed according to the novel process model and shown to be *consistent*. This is aimed to convince the reader of the validity of the novel model. This new model rests solely on two propositions and nonetheless fully explains the data. The reader is reminded of *Occam's Razor,*[3]

---

[2] This way of classification by dichotomy is made *per genus et differentiam (by their kind and difference)* according to the *arbor porphyriana*. C.f. Porphyry, Isagoge, chapter 2.

[3] William of Occam (+1349), Doctor Singularis et Invincibilis: Entia non sunt multiplicanda praeter neccesitatem. (Entities ought not to be multiplied except for necessity).

that is the theory with fewer propositions explaining the data is to be accepted. Some readers might take the view of incommensurability, i.e. each model has a right in itself and must not be compared to others. It is hoped that the *success* of this novel empirical process model in predicting behaviour and improving on weld quality might also convince those sceptics.

4.2.2 Categorization

Customary classification is based on *chemical* compositions of metals. This novel categorization considers **exclusively** the material's *morphology* with regards to welding. Such categorization is helpful for the welder to design and adjust the welding procedure accordingly. Traditional categorisation is not infringed [ISO TR 20172]. The new empirical process model for laser beam welding of metals rests on this novel categorization of materials as *continuous* or *coated* materials. Continuous materials are conceived of in this dissertation to be all pure and homogeneous metals *and* their alloys, e.g. iron and steels. However, metals such as aluminium or magnesium show a strong affinity to oxygen forming a ceramic oxide surface layer by diffusion. Surface layers of Al_2O_3 and MgO form naturally if air is the ambient atmosphere. This process is called auto-passivation and advantageously prevents corrosion. For steels a similar effect is achieved by a zinc coating.

All *intentionally* coated materials or *naturally* coated materials, such as aluminium and magnesium, are subsumed under the category of coated or self-coating metals. This distinction and categorization seems to be completely new to laser welding; it seems that aluminium and its alloys were taken to be equal to steels as far as *welding* was concerned. They were hitherto only valued as being different in their *bulk* physical properties. In this novel categorization aluminium and zinc-coated steels deserve analogue treatment in welding, because they are coated materials. Aluminium and zinc-coated steel fall in *one* category. Steels are continuous materials and fall in *another* category, which requires a different treatment in welding.

4.2.3 Strata proposition

4.2.3.1 Zinc-coated steels

This part of the empirical model describes the rules of behaviour for *coated* materials. The material properties of zinc and iron are given in table 4.3. The vaporization temperature of zinc is even below the melting temperature of iron. If a *surface* covered with zinc is irradiated by a laser beam the zinc coating evaporates away easily before the material underneath even starts melting. The coupling rate of laser radiation depends on material and is much higher for iron than for zinc.

material property	**unit**	**Fe**	**Zn**
melting temperature T_m	K	1811	693
vaporization temperature	K	3134	1180
thermal conductivity λ_{th} at RT	W m^{-1} K^{-1}	80	120
density ρ at RT	kg m^{-3}	7874	7140

Table 4.3 Material properties of iron and zinc at room temperature (RT)

When welding zinc-coated thin steel sheets in an overlap joint there are two touching zinc layers to be accounted for in the overlap gap. Single spot laser welds are prone to instabilities. In the top of figure 4.27 a longitudinal elevation of the melt pool is shown for Nd:YAG laser welding of a zinc-coated steel in an overlap joint setup. If a single Nd:YAG beam transects the workpiece, the zinc coating on the top surface vaporizes *simultaneously* to the two layers of zinc coating in the overlap gap in a shared liquefying front. While the iron is melting through, the zinc on the touching surfaces in the overlap vaporizes. The rapid vapour expansion of the zinc blows away the covering iron melt leading to blow holes. The focal plane is congruent with the top surface zinc layer in single spot Nd:YAG laser welding, as shown in the top picture of figure 4.16. A gap has to be introduced within the overlap gap to allow for the vaporizing zinc to expand.

It was thought that enlarging the keyhole would help the zinc to exit the capillary without creating blow holes. But it was shown in paragraph 3.2 that neither Twin Spot nor oscillation welding have produced satisfactory results. In Twin Spot welding zinc layers on the surface *and* in the gap were *simultaneously* intersected by the same laser beam. Generally, the isotherms of melting and vaporization lie

very close to each other at the melting front in keyhole welding. In the case of an overlap joint, they also locally intersect. *At first* the beam is absorbed at its front by the top layer. This leads to immediate vaporization of this layer. *Shortly later*, the melt film of the vapour capillary touches the two zinc layers in the overlap. The zinc evaporates while being covered by a film of molten iron. This leads to expulsions by vapour expansions as described above. The zinc can dissolve within the steel melt. Note that aluminium oxide is not soluble within aluminium. BHLW can create perfect welds in zinc-coated steels, as described in paragraph 7.3.

The beam material interactions are strongest in the **focal** plane of the laser beam. For reasons of clarity of terminology, a beam is called 'focused' in this dissertation if its focal plane coincides with the plane it is *focused* on. All other conditions are regarded as defocusing of the laser beam, i.e. normally an offset in z-direction. In BHLW the focal plane of the HPDL is congruent with the surface zinc layer, i.e. is focused on this layer. The surface zinc layer is evaporated and the underlying steel sheet is melted. The melt pool in conduction mode welding created by the HPDL does not penetrate deep enough to touch the two zinc layers in the overlap joint if the parameters are adjusted appropriately. The removal of the top zinc layer is robust and stable, because the Nd:YAG laser beam is focused on the two zinc layers in the overlap. The strong interaction between the zinc layers and the focused Nd:YAG laser beam leads to immediate vaporization of these two layers. The vaporizing zinc induces the capillary and its vapour fills it to a great degree. Such a keyhole is particularly stable, as the zinc has a very high rate of vaporization due to its lower enthalpy of vaporization compared to the surrounding iron. The increased flow of vapour particles and the corresponding ablation pressure exerted by the zinc vapour balancing the surface tension forces of the iron melt stabilize the keyhole. This is schematically shown in the bottom picture of figure 4.27.

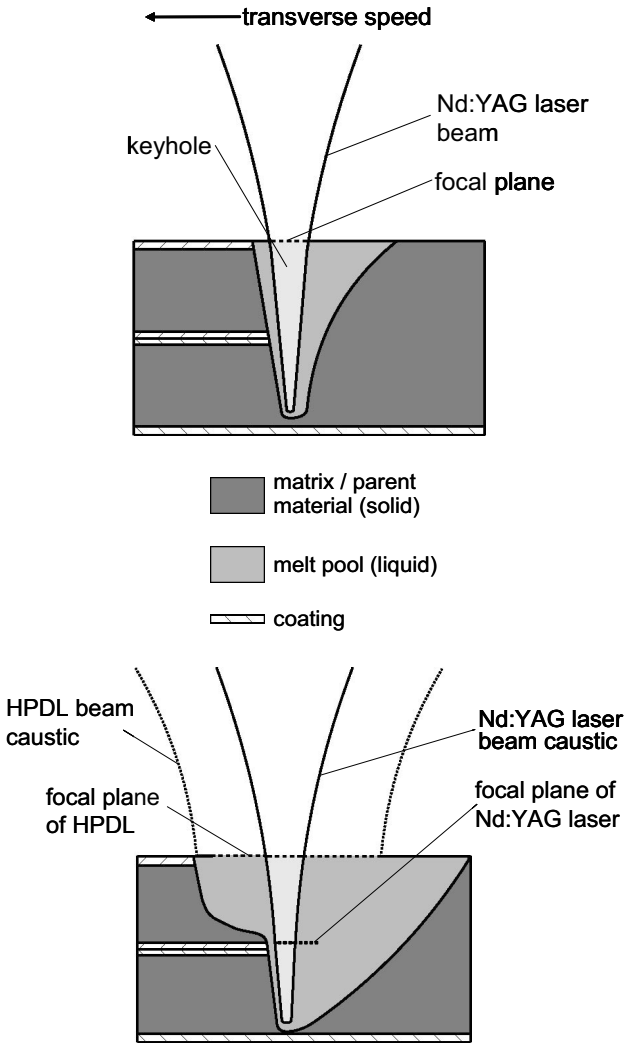

Figure 4.27: Longitudinal elevation of overlap joint for single spot Nd:YAG laser welding and BHLW to visualize the treatment of coatings and the geometry of the melt pool

This notion explains the stability of welding of zinc-coated steels by BHLW.

4.2.3.2 Aluminium

Aluminium sheets are naturally coated with Al_2O_3. Things behave differently in aluminium, since the material properties of the coating compared to the parent metal are dissimilar to the zinc-iron-system.

Table 4.4 gives the material properties of Al and Al_2O_3. The melting point of the surface oxide layer is very close to the temperature of vaporization of the aluminium matrix underneath this surface. In high-speed photographs of Nd:YAG laser welding it can be seen that this layer melts but stays intact, as described in section 4.1.3. It is lifted up and down by the expanding aluminium vapour layer forming underneath in the melt surrounding the vapour capillary, as shown in figure 4.12. This oscillation can be understood as follows: The pressure building up below this ductile melt equilibrates by release of vapour through the keyhole. The vapour vents through the keyhole orifice, as a consequence, the molten oxide layer moves down. This molten layer is almost transmissive for the Nd:YAG laser's wavelength [HÜGEL 2008]. The transmitted beam evaporates new matrix material and the pressure builds up again, and the loop starts anew. When the oxide melt film rises it moves over the orifice of the keyhole thus partly covering it. This introduces intensity variations within the keyhole resulting in instabilities.

material property	**unit**	**Al**	**Al_2O_3**
melting temperature T_m	K	933	2314
vaporization temperature	K	2320	·/·
thermal conductivity λ_{th} at RT	W m^{-1} K^{-1}	238	39
density ρ at RT	kg m^{-3}	2700	3970

Table 4.4 Material properties of aluminium as compared to aluminium oxide

In BHLW the surface oxide layer is removed by the HPDL ahead of the Nd:YAG laser, as described in section 4.1.1. Both lasers are focused on the surface of the aluminium sheet. Hence, in BHLW no oscillation can be observed and the beam cannot be obstructed above the keyhole. The keyhole does neither close up nor collapse. The train of melt and the melt pool dynamics are very calm and stable close to the solidifying front.

The welding of overlap joints of aluminium should not encounter problems according to this model, as the oxide layer in the overlap is liquefying when the parent material evaporates. No rapid vapour expansion creating blow holes of coating material is possible throughout the melt of the parent material.

These experimental observations are summarized in the following proposition:

> Proposition I: Strata Proposition
>
> For coated metals each stratum of coating must be removed by a separate laser beam that must not intersect other strata.
>
> Explanatory amendment:
>
> If the temperature of vaporization of the coating material is below that of the base material, the coating of each stratum needs to be *evaporated* separately by a beam focused on it for immediate sublimation. If, however, the temperature of vaporization of the base material is above the temperature of vaporization of the coating, each stratum of coating needs to be *melted* away separately by a laser beam, which therefore needs not necessarily be focused on it, provided the beam's intensity is otherwise high enough.

4.2.4 Phase transition proposition

This part of the empirical model describes the rules of behaviour for *continuous* metals and rests upon the *bulk* physical properties of their melt. The empirical models of instabilities, which attributed them to the physical properties of the melt according to proposition 4 (c.f. p. 14), are revisited and interpreted within the approach taken here:

In steels the isotherms of melting and vaporization lie spatially closer to each other as in comparison to aluminium, because the heat conductivity of iron is much lower and the temperature interval between melting and vaporization is smaller by 535 K as compared to aluminium. Superheating is more readily achieved for the same energy input per unit length. The heat gradients are steep and the melt film in steels on the vaporization front is much thinner than in aluminium. When the Nd:YAG laser keyhole is moved through the workpiece the laser partly irradiates *solid* material if the thin film of melt breaks down. The *sublimation* of this material constitutes a *phase transition*. The vaporization from

a liquid interface is a stable process; a two-phase transition is notorious for its unstable behaviour due to the rapid expansion of the vapour.

Taking into account the dependence of the rate of vaporization on alloying elements, such as Mg and Zn, this source of instabilities is cogent even without the assumption of melt film breakdown. In the keyhole the melt is *superheated* and such liquids tend to boil. *Boiling*, or volume evaporation, requires nucleation and growth of vapour bubbles and constitutes a *single first order phase transition*. The *homogeneous* nucleation rate increases sharply above a relatively well defined nucleation temperature T_N. Whether this temperature is attained, is difficult to judge. For very fast and high energy input a considerable superheating of the liquid is possible leading to homogeneous bubble nucleation: At temperatures of about 90% of the critical temperature instabilities within the liquid may quickly produce a significant number of vapour bubbles leading to what is called *phase explosion* or spinodal decomposition [LANDOLT BÖRNSTEIN 2004, p. 33]. Boiling may also develop at much lower temperatures as a result of *heterogeneous* nucleation in the presence of alloying elements. Since a large change in density is associated with vapour nucleation, the strong increase in the nucleation rate above T_N causes violent expansion of the superheated liquid, known as *vapour explosion* [TABOR 1991, p. 289; ALLMEN, p. 120].

Reducing the temperature gradients by increasing the thickness of the melt film around the keyhole cavity is the key to counteract instabilities by volume evaporation or vapour explosion. In BHLW the HPDL melts the metal ahead of the Nd:YAG laser, which evaporates it in the keyhole. A two-phase transition is thereby prevented in BHLW. Providing overall *more* melt decreases the temperature gradients and counteracts superheating of the melt by increased mixing, which in turn promotes surface vaporization.

Berkmanns postulates that the viscosity of the melt is a means of damping of instabilities by sheer stresses [BERKMANNS 1998, p. 36]. Whether the lower viscosity of a (pure) aluminium melt is actually responsible for instabilities by less damping than compared to steels, whose melts exhibit higher viscosities, cannot be decided here, as the oxide layer of aluminium is neglected by Berkmanns. In general, if there is more melt around the keyhole better damping can be provided, as a bigger melt pool can dissipate more energy and level off arising instabilities. Hence, the following proposition can be stated:

Proposition II: Phase Transition Proposition

For continuous metals and their alloys the phase transitions from solid to liquid and from liquid to vapour have to be locally separated and the temperature gradients to be sufficiently decreased.

Explanatory amendment:

This proposition can be satisfied by melting the material well ahead of the location where it is vaporized and by distancing out the isotherms of melting and vaporization by increased generation of melt.

For welding of aluminium *defocusing* is often recommended to reduce the formation of pores. One party recommends *positive* defocusing, i.e. the focal plane is located above the workpiece, in order to enlarge the keyhole preventing it from closing up at the orifice [RAPP, p. 149]. Another party advocates *negative* defocusing, i.e. the focal plane is located within the workpiece, in order to prevent the keyhole from necking within the capillary and therefore holds the view that porosity is more likely to occur for positive defocusing [TSUKAMOTO 2004, p. 123]. It is, however, observed that either defocusing, i.e. positive as well as negative, reduces porosity [ION 2005, p. 427]. These seemingly contradictory findings are consistent with the empirical model developed herein: positive or negative defocusing widens the beam. This condition fulfils proposition II, since beam-material surface interactions are strongest in the focal plane and can initiate a two-phase transition. However, bubbles do not form for a defocused beam.

It is an important observation that the melt pools of steels and the alloys of aluminium cannot be told apart in high-speed photography of BHLW. Since the aluminium oxide layer has been removed ahead of the Nd:YAG laser beam by the HPDL (c.f. paragraph 4.1), the keyhole in BHLW in a pure aluminium alloy looks *identical* to a keyhole in steels where the HPDL has in turn supplied more melt surrounding the vapour cavity.

4.2.5 Process gas entrainment caveat

So far a *positive* approach embodied in propositions I and II to the new empirical process model was taken. However, attention was devoted to present a subsistent and holistic empirical process model. Ion's remark should be heeded: "Because of the large number of variables in laser welding, it is unlikely that a complete process model could ever be developed. A small change in, for example, the shielding gas flow rate is sufficient to produce a dramatic effect on the geometry of the weld bead" [ION 2005, p. 435]. This seems to be truly the case for a *complete* mathematical process model. A *novel* mathematical process model for porosity formation by invasive process gas is presented in paragraph 4.3. Whether the new *empirical* process model presented in this paragraph 4.3 might in fact have considered the *principal* material or process variables is left to the reader for (empirical) judgement.

In the introduction the *rules for good practice* in welding experiments have been stated. Gas supply is a notorious topic in this respect. The record of experimental data is scant as far as process gas is concerned. In this dissertation a *complete* set of process parameters shall explicitly include the following parameters: the type process gas, its flux, its relative flow (for reasons of normalization explicated in more detail in chapter 5), the type of gas nozzle used, and the parameters of its positioning with respect to the melt pool and the laser beam. This enables further reference of experimental data within the scientific community, as otherwise experimental results cannot be reproduced or repeated by other researches as they cannot guarantee ceteris paribus conditions. For reasons of *scaling* and *normalization* the flow and flux values are necessary. What constitutes a *complete* set of parameters in laser welding is unfortunately not standardized. This might explain why experimental findings are sometimes diametrically opposed even if supposedly the same 'process parameters' are employed: The parameters of process gas supply were not ceteris paribus [HERMANN 2006].

In section 4.1.3 the experimental evidence for how process gas affects porosity formation was – hopefully impartially - presented. In this section this material will be *interpreted* within a new empirical process model. Figure 4.28 is partly identical to figure 4.19 above, which is a schematic representation of Katayama's and the author's observations [KATAYAMA 2000a, 2000b, 1999]. The difference being the gas nozzle, which is *explicitly* shown in figure 4.28 as compared to figure 4.19 and to Katayama's abstraction. A diagram showing the length scales of the keyhole, workpiece, and gas nozzle is given in the top of figure 4.28.

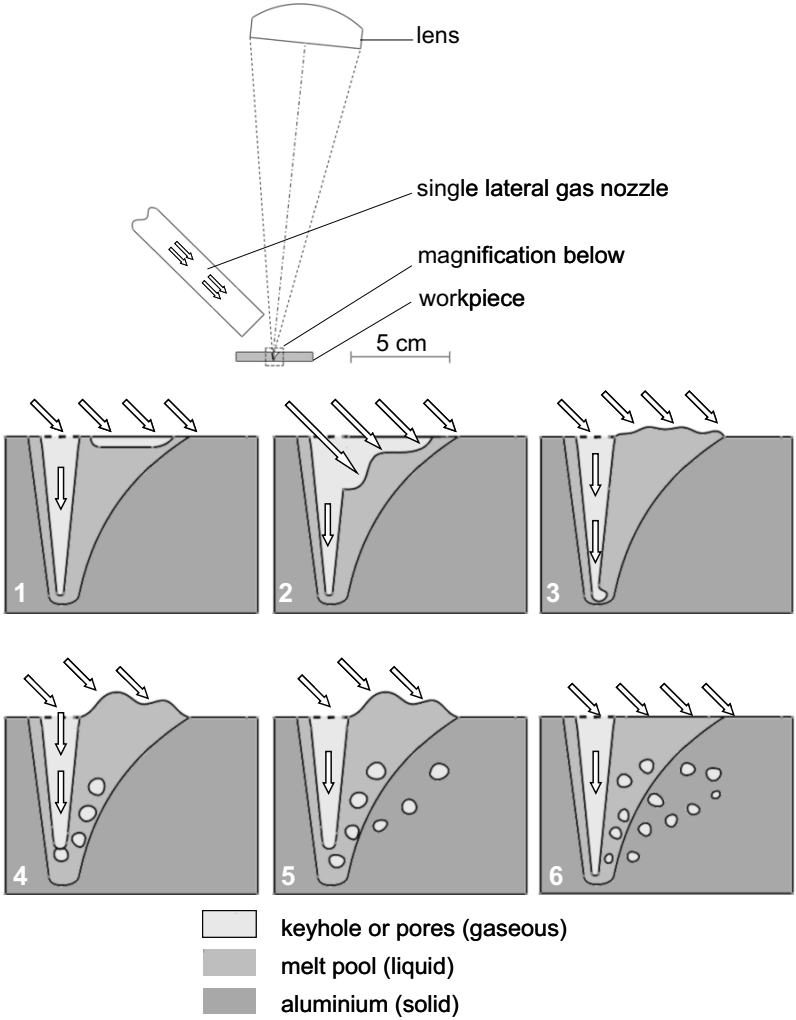

*Figure 4.28: Top: setup of workpiece for a single lateral nozzle, **all** dimensions to scale; explicit rendition of gas nozzle, gas flow indicated by white arrows; bottom: schematic representation of process gas pores formation in single spot Nd:YAG laser welding*

The summary of the empirical evidence given in section 4.1.3 (figures 4.15, 4.16, and 4.18) will be revisited one by one and interpreted within this new model:

1. A depression of the melt pool surface forms behind the orifice of the keyhole (c.f. frame 1 in figure 4.28)

This depression is due to the recoil force of the gas flow exerted on the melt pool surface. The gas particles impinge on the surface, and a force balance can only be established if there is a counteracting force. Only if the melt pool surface is concave, the surface tension can provide a restoring force, i.e. the action equals the reaction force as in Newton's third law.

2. The cavity is obstructed by a neck of melt (c.f. frame 2 in figure 4.28)

The process gas flow is invasive with regards to the keyhole. It can only affect the rear of the keyhole, which lies next to the train of the melt pool. Only the melt at the rear can easily be displaced by an invasive gas flow. The viscosity of aluminium at its melting point is nine times lower than the viscosity of steel at the melting point of iron. The viscosity of aluminium is still three times lower at its boiling point as compared to the viscosity of steel at the boiling point of iron. Hence, displacements can more easily be induced in a melt made up of aluminium [BERKMANNS 1998, p. 33]. The rear part of the keyhole orifice can therefore be deformed by the gas resulting in a necking phenomenon, which frequently results in a bulge of melt close to the keyhole.

3. A wave of melt travels from the rear of the melt pool towards the orifice of the keyhole (c.f. frame 3 and 4 in figure 4.28)

This displaced bulge of melt experiences a force by the surface tension as to restore it to form an even melt pool surface, which is in force equilibrium (neglecting the depression of the melt pool by the process gas). An oscillatory motion is induced leading to waves travelling backward on the melt pool surface. The reflection of this wave from solidified rear parts of the melt pool, i.e. the seam, leads to a travelling wave in the direction towards the keyhole at the front of the melt pool. This reflection is enabled, since the rear of the solidified melt pool acts as a node for the wave. Once the wave reaches the keyhole, its geometry is deformed close to the orifice. This geometry deformation mechanism is not radial symmetric but limited to the *rear* part of the keyhole wall. The melt film of the keyhole at the melting front is very *thin* when the keyhole moves

through the workpiece during welding. Hence, this part of the keyhole cannot be displaced substantially. Only the rear part can be displaced, as a reservoir of melt is provided by the melt pool in the train of the keyhole.

4. All bubbles form at the bottom of the keyhole cavity (c.f. frame 4 in figure 4.28)

This is the most decisive observation of the author, because the location of bubble formation **at** the bottom of the keyhole is fundamental to the mathematical process model developed in 4.3. As described in section 3.1.3, Beck developed a mathematical process model which accounts for the formation of pores by constriction of the keyhole **towards** the bottom of the keyhole [BECK 1996, p. 93]. In Beck's model the metal vapour-jet changes travel direction in the lower part of the keyhole. At this shed point the distribution of *relative* velocities of the gas particles travelling in *opposite* direction has a maximum; this results in a reduction of the associated pressure according to the V*enturi-effect*.[4]

In the higher part of the keyhole the vapour-jet moves towards the orifice where it exits the keyhole, whereas in the lower part of the keyhole the jet moves in the opposite direction towards the tip of the keyhole. At the shed point the pressure drops and results in a projection of melt into the keyhole. According to Beck a bubble filled with *vapour* is detached form the keyhole. This supposedly accounts for pore formation in the seam.

Hohenberger and Gref received experimental data from Katayama's apparatus. Both interpreted the x-ray images as to experimentally verify Beck's model. However, as shown at the end of section 3.1.3, Beck's model **necessitates** the pores to be filled with metal vapour. Therefore, both Hohenberger and Gref who follow Beck's model *claim* that the pores are *actually* filled with metal vapour, but they did not conduct any experiment to *prove* this assumption [HOHENBERGER 2003, p. 60; GREF 2005, p. 31].

Katayama released the content of those pores by micro-drilling and determined the gas by mass spectroscopy, as stated in section 4.1.3 [KATAYAMA 1999, 2000a, 2000b]. He established beyond any doubt that the pores are filled with process gas and *not* with metal vapour.

---

[4] Venturi-effect: The pressure in a fluid decreases when its velocity increases.

Hence, in this dissertation it is suggested by the author that the process gas is bubbled into the melt pool through the keyhole. The keyhole acts like a *straw*. Bubbles caused by virtue of this straw-mechanism form *only* **at** the keyhole tip, as will be shown in paragraph 4.3. This *novel* explanation constitutes a **shift of paradigm**: It explains all hitherto unexplainable observations: absence of pores when welding in vacuum, as detailed in section 4.1.3, e.g. absence of pores for nitrogen as process gas. To term this novel explanation a shift of *paradigm* according to [KUHN 1962, p. 121] seems justified if the ramifications of this finding are considered: According to Beck's model process technologies to stabilize and prevent closures of the keyhole's *orifice* were designed and researched by Hohenberger, i.e. Twin Spot laser welding, and by Gref, i.e. multiple spot laser welding. Neither Twin Spot nor multiple spot laser welding could produce porosity-free seams even if the parameters were optimized according to Beck's model.

In order to prevent pores according to this new paradigm a process gas supply must be designed such that the gas is non-invasive with regards to the keyhole's lower part. In chapter 5 a gas nozzle system providing such conditions is presented. The results show that pores are absent if BHLW, which is removing the sturdy oxide layer of aluminium, is used in combination with this novel double coaxial nozzle system. The absence of pores *validates* this new empirical process model by experimental evidence.

5. The cavity fluctuates in depth and radial direction (c.f. frame 2 in figure 4.28)

The flow of process gas causes substantial distortions of the keyhole close to the orifice. It looks as if the slim keyhole 'swallows and chokes' on process gas which got entrained. In the x-ray images the melt pool surface is displaced such as to induce a travelling wave. This deformation of the whole shape of the keyhole influences the position of the tip of the keyhole. Despite the fact that the position of the tip is displaced, it should be noted that the bubbles still detach *at* the bottom of the keyhole.

According to Pascal's principle[5] the melt experiences a pressure on the interface between the wall of the melt pool train and the keyhole. The incompressible melt in the vicinity of the bubble has to make room for the bubble by expanding into the cavity of the keyhole. The bubble displaces the vapour and process gas in the keyhole to satisfy the *continuity of mass*. The keyhole contracts right above the bubble. The bubble is detached and *simultaneously* the keyhole depth is reduced while the gas is moving through the keyhole, whose flow is affected by various deformations of the keyhole geometry. This induces reorientations of the process gas flow within the keyhole. In turn, the gas flow itself influences keyhole geometry. The keyhole is moving ahead at the transverse speed of the laser beam. The bubble is not located exactly in the axis of the laser beam but moves towards the solidifying melt pool. This results in a buckling of the keyhole shape. The melt pool is compressed, because the melt pool cannot easily expand towards its free surface behind the keyhole. This free surface is in this case represented by the interface to atmosphere. This surface is cooling rapidly. The system of laser beam, gas flow, and melt pool exhibits a chaotic, non-linear dynamic motion of the keyhole. A motion in depth and radial direction of the whole keyhole geometry is excited.

6. These bubbles move into the melt train and remain as a pore after solidification (c.f. frame 6 in figure 4.28)

Once the bubbles detached from the keyhole, they rise within the melt pool by buoyancy, as the amount of liquid displaced by the bubble is much heavier than the process gas contained within, c.f. Archimedes' principle. The rear of the melt pool constitutes the front of solidification. If the time until the melt pool solidifies is too short for the bubbles to rise to the surface, the bubbles get entrapped in the melt pool as a pore, if the melt pool solidified before the bubble reached the surface. All bubbles can only rise for finite time and are therefore very rarely found *at* the tip of the keyhole. They are located further up in a metallurgic cross-section macrograph of the seam, as can be seen in figure 4.8. The notion that the pores form *towards* the tip of the keyhole was *supposedly* underpinned by such *a posteriori* macrographs.

[5] Also called Pascal's Law: In fluid (gas or liquid) mechanics, statement that in a fluid at rest in a closed container a pressure change in one part is transmitted without loss to every portion of the fluid and to the walls of the container. The principle was first enunciated by the French scientist Blaise Pascal.

If the rise time was increased, more bubbles could reach the surface and release their process gas content to atmosphere. A reduction of porosity in the weld seam would be a consequence. This provides another novel explanation of the experimentally well established observation that porosity in laser seams of steels is much lower than in aluminium alloys welded under ceteris paribus conditions: the solidification time of a steel melt pool is longer, since the heat conductivity of iron of 80 $W\,m^{-1}\,K^{-1}$ (c.f. table 4.3) is three times smaller than the heat conductivity of pure aluminium of 238 $W\,m^{-1}\,K^{-1}$(c.f. table 4.4). Note, however, that heat conductivities of specific steels and aluminium alloys might differ by up to a factor of 10.

These considerations make the slight reduction of porosity in multiple and Twin Spot laser welding in section 3.2.3 as well as in oscillation and laser stir welding in section 3.2.4 plausible: the time for solidification was *simply* prolonged by these process technologies. Gref doubled the laser power available. For a constant penetration depth the velocity of welding had to be accordingly reduced leading to an increase of power per unit length. The same applied to Twin spot laser welding. The process technologies of oscillation and laser stir welding also prolonged the time for the melt pool to solidify by reheating the melt by a subsequent pass or rotation of the beam. Those technologies exhibited a *factual* double effect although they *intentionally* aimed to widen or stabilize the keyhole.

7. The pores are filled with process gas

Apart form the *direct* determination of the pore content by Katayama, which has been expounded on several occasions in this dissertation, an *indirect* argument supports this fact: the individual size of a particular bubble remains *constant* while rising in the melt pool. A bubble filled with metal vapour should decrease in volume, as a fraction of the vapour condenses on the inner surface of the bubble made up of melt of the *same* material. Once the bubble is detached from the keyhole, no laser radiation or other source of energy is heating up the metal vapour to compensate for the losses of internal energy of the vapour due to conduction of heat into surrounding melt. The temperature *interval* between melting temperature and vaporization temperature of pure aluminium and iron are almost equal, i.e. $\Delta T_{Fe} = 1323$ K, (c.f. table 4.3) and $\Delta T_{Al} = 1387$ K (c.f. table 4.4), but the conductivity of heat is, as stated previously, three times higher in pure aluminium than in iron. Bubbles made up of aluminium metal vapour should condensate more quickly than those made up of iron vapour. This is

clearly contradictory to acknowledged experimental evidence according to which porosity is much higher in aluminium.

It seems fairly unlikely that bubbles filled with metal vapour could in *any* circumstances be entrapped as pores. Katayama found that the seams were free of pores when welding in vacuum [KATAYAMA 2001]. In vacuum all bubbles have to be filled *exclusively* with metal vapour. Hence, no pores are present in seams welded in vacuum, because such pores collapse by instantaneous condensation.

Bubbles consisting of *inert* process gases, such as argon or helium or mixtures of those gases, *cannot* dissolve within liquid aluminium. Hence, if the rise time is not long enough for such a bubble to release its content to the atmosphere by reaching the surface of the melt pool, a pore is entrapped within the weld seam.

For other *reactive* gases, such as nitrogen, no pores were observed by the author as well as [BACHHOFER 1997, ZÄH & TRAUTMANN 2004b]. Nitrogen can form AlN with liquid aluminium and consequently no pores can be detected in the weld seam, as detailed in section 4.1.3 and proved by figure 4.19.

The formation of pores for *soluble* gases in liquid aluminium depends on the function of solubility depicted in the phase diagram of aluminium. Hydrogen can be considered as a general example: The solubility of hydrogen in aluminium melts of 6.5 10^{-3} ml g^{-1} drops to 0.34 10^{-3} ml g^{-1} upon solidification. Small sized hydrogen pores precipitate in the fusion zone close to free surfaces. Those hydrogen pores are dealt with in paragraph 6.2. The solubility of nitrogen in solid aluminium is negligible [WRIED 1986].

Therefore, the following hypothesis is *in agreement* with the seven observations and the experimental evidence stated above:

> Gas Entrainment Caveat:
>
> The process pores in keyhole laser welding are caused by a straw effect of a jet of invasive process gas generating bubbles at the keyhole tip. Process pore formation depends on the reactivity or sufficiently high solubility of the particular process gas (mixture) used with regards to the liquid metal surrounding the keyhole.

Although the use of nitrogen as process gas does not yield pores, AlN is critical for the properties of the welded structure in mechanical loading. This will be discussed in more detail in section 6.2.

Welding in vacuum is only interesting for scientific research. In industrial circumstances this would create further expenses. The costs for vacuum technology are already detrimental to electron beam welding, which requires a vacuum to prevent a dispersion of the electron beam. Exceptions might apply.

In most applications *inert* gases need to be deployed to guarantee the quality of the seam, because pure aluminium reacts with the ambient air to form its oxide Al_2O_3. A *non-invasive* inert gas supply with perfect coverage of the melt pool is needed to prevent process porosity. A nozzle which can provide such gas coverage and might serve as a standard gas nozzle for experiments that should satisfy ceteris paribus conditions is described in the next chapter 5.

4.3 Mathematical process model of process gas porosity formation

In section 3.1.3 the mathematical process models of instabilities were presented. Duley summarizes the authors who support the approach of a pressure balance [DULEY 1998, p. 83]: [ANDREWS & ATTHEY 1976, KLEMEANS 1976, DOWDEN et al. 1987, BECK & BERGER & HÜGEL 1992, MATSUHIRO & INABA & OHJI 1994, KROOS & GRATZKE & SIMON 1993a, KROOS et al. 1993b, MÜLLER 1994, KAPLAN 1994, SCHULZ et al. 1996]. Duley's list is by far not complete to name only Beyer, whom he did not mention [BEYER 1995, p. 78]. After the publication of Duley's book in 1998 Hohenberger and Gref supported the model and tried to reconcile it with experimental results [HOHENBERGER 2003, p. 60; GREF 2005, p. 31]. The mere number of publications proves how influential this approach was and how attractive and compelling it still is today [KÄGELER et al. 2007].

The state-of-the-art of mathematical process modelling of keyhole instabilities is represented by equation 3.6, as quoted and presented in section 3.1.3 [BECK 1995, p. 87]. These equations are revisited in the following and reformulated to *integrate* the new theory.

In an initial simplification the motion of the keyhole through the workpiece is neglected and the terms are evaluated that act on a stationary keyhole. The pressure balance is:

$$p_v + p_l = p_\sigma + p_g + p_{hd} \qquad \text{(Equation 4.1)}$$

where p_v is the vaporization pressure and p_l the radiation pressure from the keyhole wall. Those pressures are balanced by the surface tension per unit area p_σ, the hydrostatic pressure p_g, and the hydrodynamic pressure p_{hd}.

The pressure terms p_v, and p_l tend to keep the keyhole open, whereas p_{hd}, p_g and p_σ are restoring pressures. All terms depend on the depth of the keyhole z and the keyhole's radius $r(z)$. Table 4.5 gives the functional form of the pressure terms and a typical value for iron and aluminium.

		Fe	Al
pressure term	**functional form**	**typical value (N m^{-2})**	**typical value (N m^{-2})**
p_g	$\rho_l g z$ (eq. 4.2)	75	25
p_l	$\frac{I}{c}(A+2R)$ (eq. 4.3)	50	120
p_σ	$\sigma\left[\frac{1}{r_1(z)}+\frac{1}{r_2(z)}\right]$ (eq. 4.4)	10^4	10^4
p_{hd}	$\frac{\rho_l}{2}\left[v_{\min}^2(z)-v_{\max}^2(z)\right]$ (eq. 4.5)	0*	0*
p_v	$\sim m' n_g u_g^2$ (eq. 4.6)	10^4	10^4

*Table 4.5: Pressure terms to describe a laser keyhole: * for low welding speed; ρ_l = liquid density (kg m^{-3}); g = acceleration due to gravity (m s^{-2}); z = depth of the keyhole (mm);*
I = laser intensity (W m^{-2}); c *= speed of light (m s^{-1});*
A = absorptivity of material; R = reflectivity of material;
σ = surface tension (N mm^{-1}); r_1, r_2 = keyhole radii (m);
$v_{\min}$,$v_{\max}$ = liquid flow velocity around keyhole (m s^{-1});
m' *= mass of vaporizing atom (kg); n_g = density at surface of Knudsen layer (m^{-3}); u_g = gas velocity at Knudsen layer (m s^{-1}); [mod. acc.* DULEY *1998, p. 84]; values for Fe by the author*

The typical values in table 4.5 show that p_l and p_g are small compared to p_σ and p_v. The hydrodynamic pressure vanishes for low welding speeds. For elevated welding speeds v_w the hydrodynamic pressure can be estimated (c.f. equation 3.6) [BECK 1996, p. 87; GREF 2005, p. 82]:

$$p_{hd} \sim v_w^{3.5} \qquad \text{(Equation 4.7)}$$

This is considered negligible for the subsequent discussion.

Then,

$$p_v \approx p_\sigma \qquad \text{(Equation 4.8)}$$

The leading terms show that the pressure term for the surface tension, which tends to close the keyhole, needs to be balanced by the vapour pressure, which acts as to keep the keyhole open. The geometry of the keyhole is assumed to be either conical or cylindrical, as can be seen in figure 4.28.

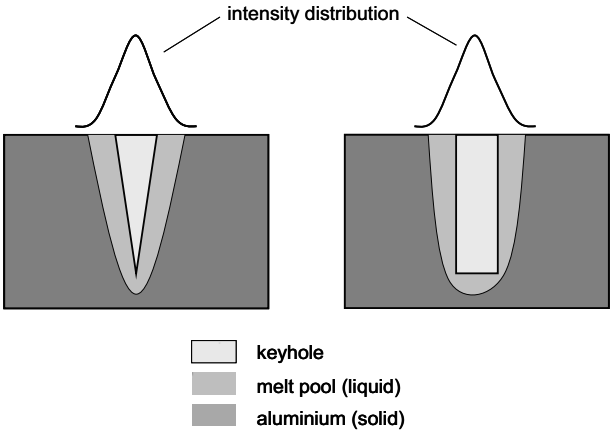

*Figure 4.29: Simplified conical and cylindrical geometry for a stationary keyhole [*DULEY *1998, p. 85;* BECK *1995, p. 130]*

The *description* of the keyhole by this model, i.e. the set of governing physical equations, implies the following assumptions:

1. The keyhole is *completely* filled with metal vapour, whose excess pressure causes a flow of vapour within the keyhole. Partly, this vapour vents through the keyhole orifice; partly, it streams within the keyhole towards the tip.

2. Keyhole geometry variations should be *symmetric,* since no directionality is contained within the pressure terms. The keyhole geometry is modelled to be cylindrically symmetric and the pressure terms causing the geometry variations of the keyhole's wall should mirror this symmetry.

Assumption 1 cannot be true, because process gas entered the keyhole, as shown by the experimental evidence in 4.1.3. Further, it was shown in this section by in-situ x-ray observation that a neck of melt originates from the rear of the melt pool and does therefore not constitute a radial symmetric geometry deformation.

Hence, a new mathematical process model is suggested in the following taking into account the *directionality* of the necking phenomena and the experimental facts, namely process gas *reaches* the keyhole bottom and process gas bubbles form *at* the bottom of the keyhole.

Although the keyhole geometries in figure 4.30 are simplified, they represent quite accurately the geometry of the keyhole in reality, c.f. figures 4.15 and 4.16. Figure 4.18 shows that the keyhole is made up in its majority of a *cylindrical* part, which is rather slim and tube-like, and a *conical* part, which is narrowing down *towards* the bottom. The necking phenomenon *distorts* the keyholes geometry. Whether the tip itself is a sharp spike or shaped more like a hemisphere, is hard to discern from experiment. It was observed in bead on plate welds that the penetration depth, i.e. the length of the keyhole, varies during welding. In cross-section macrographs those observed length variations are often termed ‘spiking’.

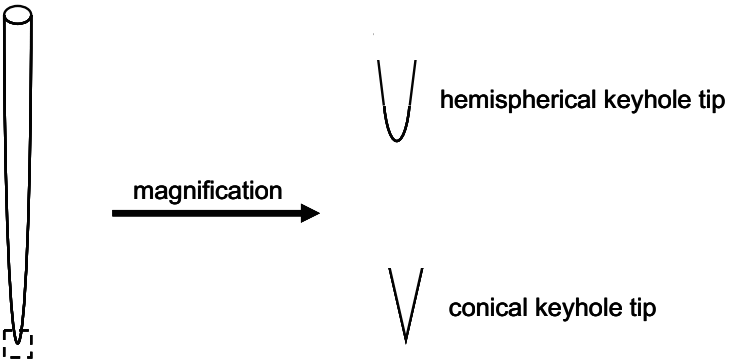

Figure 4.30: Simplified geometry for a stationary keyhole; magnification to visualize the abstraction of a hemispherical keyhole tip and an acute or conical keyhole tip

The process gas acts as to keep the keyhole open. The process gas used is argon, helium, or a mixture of these. They are considered to be almost incompressible like an *ideal* gas. These gases cannot condense on the keyhole walls, as they do not undergo phase changes. They may rather expand upon being heated up while travelling through the keyhole. Nonetheless, this expansion is considered negligible. Equation 4.8 integrates the process gas into the mathematical description:

$$p_v + p_l + p_{gas} = p_\sigma + p_g + p_{hd} \qquad \text{(Equation 4.8)}$$

where p_{gas} is the pressure term due to the dynamic or velocity pressure exerted by the process gas. The pressure of the vapour is taken to be a *static* (i.e. a scalar) pressure term, since the individual vapour particles are in constant random motion in accordance with Boltzmann's statistics (which also come into play for the derivation of u_g in equation 4.6).

The upward velocity of the vapour *in bulk* through the keyhole for venting is considered to be *relatively* small as compared to the motion of the gas-jet. Hence, the small dynamic pressure is neglected and the pressure terms associated with the vapour are treated as a scalar quantity.

A *vigorous* process gas flow, which in the following will be called jet, is *invasive* with regards to the melt pool. If such a jet of process gas hits the rear of the keyhole orifice, the rear gets displaced, as can be seen in figure 4.15 in frame 1. The gas nozzle was inclined in such a way as to direct the jet to hit the rear of the melt pool surface and cause a depression, c.f. section 4.1.3. But even if the jet is directed coaxially to the laser beam, it is only able to affect the melt at the rear of the keyhole. Only the reservoir of melt in the train of the keyhole can be substantially displaced and not the thin film of melt at the melting front. These and other effects at the melting front due to the process gas supply nozzle will be considered in chapter 5.

Subsequently to this first deceleration and *redirection* of the process gas-jet close to the keyhole orifice the flow of process gas is guided by the keyhole geometry and flows *parallel* to the keyhole wall in the direction towards the tip. A *constant* flow of process gas from the nozzle pushes it forward. In the following the leading pressure terms acting on the keyhole wall *towards* the tip of the keyhole are considered:

$$p_v + \vec{p}_{gas} \approx \vec{p}_\sigma \qquad \text{(Equation 4.10)}$$

The pressure in the vapour is an *isotropic* quantity, i.e. a *scalar,* whose magnitude is a function of position. The *scalar* pressure of the process gas adds to the vapour pressure according to Dalton's law: The total pressure of a mixture of gases or vapours is equal to the sum of the partial pressures of its components, i.e. the sum of the pressures that each component would exert if it were present alone and occupied the same volume as the mixture of gases. Strictly speaking, Dalton's law is true only for ideal gases and can be expressed as follows:

$$p_{total} = \sum_{i=1}^{N} p_i \qquad \text{(Equation 4.11)}$$

where p_{total} is the pressure in the gaseous mixture and p_i are the partial pressures in each of a number of N components.

It can be assumed that the partial *static* pressure of the process gas is *negligible* as compared to the pressure in the metal vapour. The *dynamic* pressures of the process gas are *anisotropic* and varies with direction. The dynamic pressure is closely related to the kinetic energy of a gas particle, since both quantities are proportional to the gas particle's mass (by virtue of density, in the case of the dynamic pressure p_d) and the square of the gas velocity v_{gas}:

$$p_d = \frac{1}{2}\rho_{gas} v_{gas}^2(z) \qquad \text{(Equation 4.31)}$$

In the part of the keyhole where its radius is *constant* the process gas travels *parallel* to the keyhole wall. As a result, the process gas does not exert a dynamic pressure on the keyhole wall as its component vanishes in this direction. The static pressure is assumed to be negligible and the keyhole is kept open *merely* by the recoil force exerted by the metal particles causing the vapour pressure. The surface tension needs to balance the vapour pressure term and is given by the Young-Laplace equation. It is always normal to the surface:

$$p_\sigma = \sigma\left[\frac{1}{r_1(z)} + \frac{1}{r_2(z)}\right] \qquad \text{(Equation 4.11)}$$

where σ is the coefficient of surface tension as above in equation 4.4. However, in more detail than Duley, who wrote 'keyhole radii', r_1 and r_2 are herein called the *principal* radii of curvature in *tangent* direction. In those parts of the keyhole

where the keyhole diameter is constant equation 4.11 simplifies to (c.f. equation 3.7):

$$p_\sigma = \sigma\left[\frac{1}{r(z)} + \frac{1}{\infty}\right] = \frac{\sigma}{r} \qquad \text{(Equation 4.12)}$$

where $r_1 = r$ is the radius of the keyhole at height z. Since this radius is *constant* in the stable middle part of the keyhole, r_2 in this direction tends to infinity as the keyhole is *not curved* in vertical direction.

Close to the tip of the keyhole the process gas affects the keyhole wall, because their resolved vector component is *finite* and varies according to the curvature of the keyhole wall. The contribution from the equilibrated vapour pressure does not vary and acts always *normal* to the keyhole surface. The vertical dependence of the surface tension as a function of position z close to the keyhole tip ($z = 0$) for a hemispherical keyhole tip geometry is shown in figure 4.31.

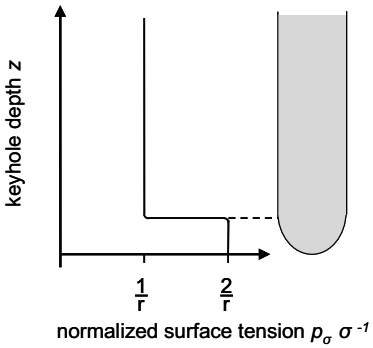

Figure 4.31: Qualitative dependence of keyhole depth on normalized surface tension for a hemispherical keyhole tip; both axes in arbitrary units

Figure 4.31 shows that for a hemispherical keyhole tip the surface tension is doubled at the tip. This finding requires the dynamical pressure exerted by the process gas to exceed the surface tension at the lowest point of the tip to inflate the keyhole to form a bubble. It should be noted that according to figure 4.31 the surface tension is *finite* for a hemispherical keyhole tip geometry.

The surface tension at the vertex N (i.e. where $t = 0$) depending on the height z of the keyhole is then given by:

$$\vec{p}_\sigma(z) = z^{-1} \cdot \underbrace{\sigma \frac{1 - \tan^2 \alpha}{(1 - \tan^4 \alpha) \sin \alpha}}_{\text{constant}} \sim z^{-1} \qquad \text{(Equation 4.13)}$$

The derivation of this formula is given in chapter 13 as appendix C.

Close to the tip of the keyhole the limit is:

$$\lim_{z \to +0} \vec{p}_\sigma(z) = \infty \qquad \text{(Equation 4.14)}$$

This *mathematical* result needs to be carefully explained and understood. The limit in equation 4.14 of the function of the surface tension does *not exist*. The asymptotic value the function approaches in the limit is *infinite*. Hence, the function has an *infinite discontinuity* **at** $z = 0$.

This *mathematical* result needs to be interpreted with regards to the *physics* governing keyhole stability. The surface tension is caused by intermolecular forces. The infinite discontinuity means in terms of physics: the surface tension exhibiting such a functional behaviour is *diverging* **at** the tip of the keyhole. This is shown in figure 4.34.

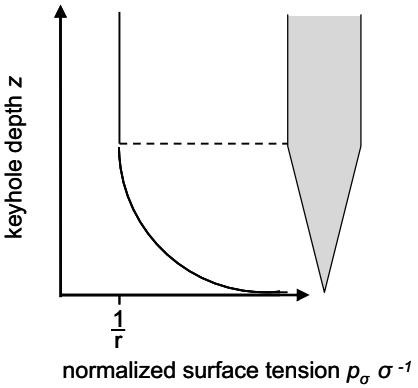

Figure 4.34: Qualitative dependence of the normalized surface tension on keyhole depth for a conical keyhole tip; both axes in arbitrary units; note the limit of the function does not exist

The gas cannot flow further down once they have reached the tip of the keyhole, and from above even more process gas is approaching. The surface tension on the wall of the keyhole towards the tip is increasing the closer to the tip the process gas particles get. For an acute keyhole tip the surface tension *diverges* in the limit, i.e. the surface tension is infinite. This means that the surface energy is increasing as well. Therefore, the wall cannot be displaced by the gas particles. They get redirected towards the tip. The surface tension is the pressure term which tries to close the keyhole. But the gas cannot flow upwards, as there is more gas pushing down from above.

Any interface is characterized by the free energy F which is proportional to its surface S_I [TABOR 1991, p. 280]:

$$F = \sigma S_I \qquad \text{(equation 4.15)}$$

where σ is the coefficient of surface tension. It is clear that expressions like equation 4.30 should be written for all surfaces of the system. At equilibrium, the free energy is minimal, so interfaces reshape in order to minimize the total free energy. Hence, the keyhole constricts at the tip and entraps the process gas as a bubble. A bubble is formed within the melt, because a gas entrapment minimizes its internal energy by forming a spherical bubble. This bubble forms at the conical keyhole tip, to relax the surface tension within the bubble formation process to a *finite* value. The energy balance will always show a minimum for bubble formation, since without bubble formation the free energy and the surface tension would diverge and become *infinite*. This can be seen in figure 4.35.

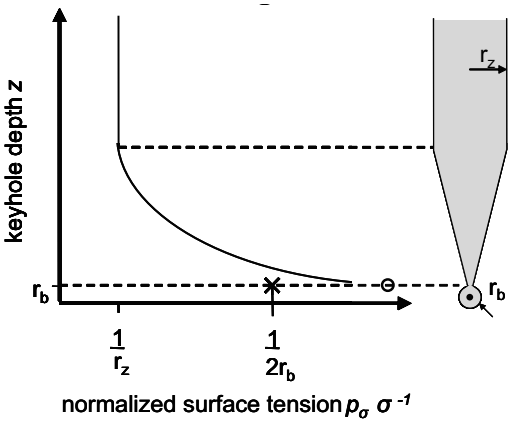

Figure 4.35: Qualitative dependence of normalized surface tension on keyhole depth for a conical keyhole with a bubble of radius r_b forming at the tip; both axes in arbitrary units;○ denotes that the limit of function does not exist, x *denotes the finite value for the spherical bubble at the former tip of the conical keyhole*

The bubble is expanding while being inflated by more process gas streaming into it. Thereby, the bubble radius r_b increases and the surface tension is decreasing. According to equation 4.30 the free energy is equally decreasing, thus, lowering the energy of the system. The bubble formation process proceeds spontaneously, as it satisfies the 2nd law of thermodynamics by energy minimization.

Once the bubble has reached a certain diameter, the upthrust and the drag forces acting on it in the melt initiate its detachment. The bubble is dragged into the melt pool in the rear of the keyhole while the keyhole itself is moving forward at the velocity of welding. The bubbles rise in the melt pool since they experience an upthrust force according to Archimedes's principle and a comparably small downward force by their weight.

The hydrodynamics of bubble formation from submerged orifices within a liquid in stagnant, cocurrent, and countercurrent flow conditions were investigated by several authors [RAMAKRISHNAN 1969, TSUGE 1986]. The models which authors develop or quote are elucidating for the following discussion. It should be noted that they always consider the formation of bubbles at a fixed or flexible orifice, which is always a *rigid* orifice. The direction of injection of the bubbles into the surrounding liquid is between vertical upward or horizontal sideward. The

condition of a *flexible* orifice represented by the keyhole surrounded by melt, i.e. a liquid not a rigid body, from which the bubbles are constricted vertically downward, is not considered in the literature. From the literature it can be gathered that the bubble size depends on detachment time, i.e. the mean time interval between the onset of the bubble's growth and its eventual detachment.

The conditions for bubble formation by argon or helium with regards to the melt pool are considered to be similar. Bubbles filled with argon should be bigger than those filled with helium. This will be experimentally shown in section 5.1.3.3. For a given volume flow rate the resulting velocity of the gas particles is the same for any gas. The density of argon is by one order of magnitude higher than that of helium, since the density of argon is 1.7837 kg m^{-3} as compared to the density of helium of 0.1785 kg m^{-3} (c.f. table 5.1). Hence, it seems reasonable that the *mean* detachment rate for helium bubbles is higher than for argon, because the constriction of the keyhole is more easily achieved if the dynamic pressure is smaller. Moreover, the buoyancy of an argon or helium bubble is practically not dependent on its gas content but only on the size of the bubble. A higher mean detachment rate leads to smaller bubbles for a fixed flow rate of process gas. As a consequence the mean size of the bubbles is smaller when helium is used as process gas instead of argon.

In this section a *self-consistent* mathematical process model for the formation of process gas porosity was developed, which is in agreement with the experimental observations in section 4.1.3. It also explains the results presented in the next chapter. Non-invasive process gas supply is unfortunately not guaranteed in most experiments in the literature, as noted by [HERMANN 2004]. Since non-invasiveness is facilitated by the coaxial double nozzle system, the results in chapter 5 show purely the influence of the particular process gas used.

5 Shielding gas nozzle for laser beam welding

The often neglected influence of process gas on the result and quality of laser welds has been demonstrated above. The caveat on process gas entrainment in section 4.2.5 sparked the development of an appropriate gas shielding nozzle. Thus, Laval nozzles, which create a supersonic flow, are not considered here. Since no system commercially available satisfied the demand of providing a non-invasive laminar gas flow with respect to the process zone, a new gas nozzle system was designed: This innovative system can perfectly shield the process zone and could therefore serve as a standard system not only for the experiments performed herein but in laser beam welding in general.

5.1 State of research and development

A consistent terminology is needed to avoid confusion within this dissertation, because a plethora of different gas shielding nozzles is documented in the literature. In a *coaxial nozzle* the laser beam propagates through the middle axis of a radial symmetric nozzle. A *lateral nozzle* provides process gas from one side at an angle to the fusion zone. This results in an angle between the direction of beam propagation and the flux normal of the gas. The term *single nozzle* refers to a nozzle geometry which guides one stream of gas or a mixture of gases. A *multiple nozzle* divides up the supply stream of gas into multiple flows of gas, which are guided independently of each other to the process zone. Each gas stream can be a pure gas or mixture of gases. A special case of this nozzle is a *double nozzle* which generates two gas flows. A fluid-dynamical advantageous design of the nozzle contour preventing boundary layer separation and turbulence is termed *laminar nozzle*.

The quotation of the absolute flow measured in litres per minute is clearly not sufficient when different nozzles are to be compared. The flux normalizes the flow with respect to the area normal to the direction of the gas flow and has units of litres per minute per unit area. Thus, it is possible to compare the amount of gas consumption of nozzles with different orifice areas.

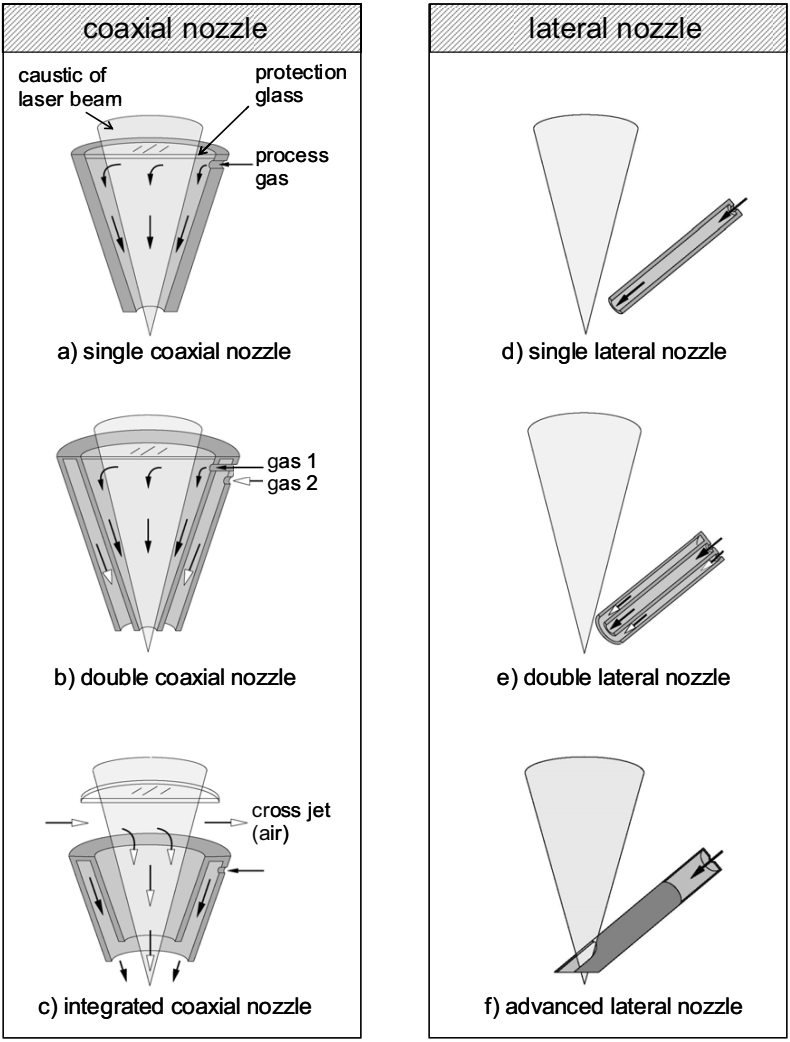

Figure 5.1: Map of nozzle concepts

New nozzles concepts developed for laser beam welding normally serve one of the following two objectives: First, by virtue of *geometry* optimization of a single nozzle a pure gas or a gas mixture shall be supplied to the process zone more efficiently than by state-of-the-art single nozzles. Second, *improvement* of gas

supply of a pure gas or a gas mixture is aimed at by various designs of multiple nozzles, be they lateral or coaxial nozzles.

Figure 5.1 maps out the concepts of lateral and coaxial gas nozzles. The bottom nozzles represent the most advanced design of the lateral and coaxial nozzle concept found in the literature.

5.1.1 Lateral nozzles

Lateral nozzles – be they single or multiple nozzles - have a significant disadvantage: they are not rotationally symmetric. Laser welding processes are normally performed by robots, because laser radiation is a security hazards for personnel in a staffed production. The programming of weld tracks is more elaborate and accessibility is reduced if the nozzles, which have to come close to the fusion zone, are not rotationally symmetric. Such lateral nozzles are generally tube-like assemblages and are therefore inherently laminar flow nozzles within the limits given by Reynolds number (c.f. equation 5.1). This has been verified by experiments. These experiments additionally show that helium makes an escape upwards before reaching the process zone. The escape of helium is caused by the upthrust it experiences, since its density is lower as compared to ambient air [SEEFELD 2005, p. 998].

It should be noted that such nozzles were tested at a pressure of 3 bar and will therefore invade the melt pool [SEEFELD 2005, p. 998]. Process gas provided in such a way is invasive and leads to increased porosity in aluminium welds. Sadly, Seefeld's paper does not quote the cross-sectional area of the nozzles' apertures. Therefore, the fluxes used cannot be calculated and no comparison of gas consumption can be made.

Caillibotte demonstrated the volatility of helium by means of simulation [CAILLIBOTTE 2004]. The gas nozzle developed by him represents a single lateral nozzle for CO_2 laser beam welding. Caillibotte's nozzle is shown in figure 5.1 f). This tube-like lateral nozzle is designed to minimize the distance between aperture and workpiece. Additionally, the nozzle is cut out in such a way as to admit the unobstructed propagation of the laser beam onto the workpiece. This meanwhile patented nozzle design supposedly provides good process gas coverage of the fusion zone. However, it suffers from a severe drawback: The rim of the nozzle is located only $1 \div 2$ mm away from the workpiece. Such a small distance makes application in production difficult, since the workpieces

need to be clamped for subsequent welding. Therefore, clamping devices need to be positioned close to the future joint. In practice, the workpieces exhibit positioning tolerances. The nozzle devised by Caillibotte would collide if not with the workpiece then with the clamping device. Additionally, Caillibotte only rendered the results of a computer simulation and did not verify this simulation by data from real welding experiments. Instead, he enumerates the problems of lateral nozzles: perturbation of the melt pool, the admixture of air into the process gas, and the positioning of the nozzle to be properly pointed at the melt pool. The inherent angle of inclination of a lateral nozzle with regards to the beam's axis causes perturbation of the melt pool inducing gas entrapment and process porosity. Hence, lateral nozzles, even of the most advanced kind, are no solution of the problem [HÄRTL 2006, p. 41].

5.1.2 Coaxial nozzles

Several coaxial nozzle systems are patented and described in the literature [JP 5050284; JP 7223086; JP 6304777; JP 6304777; JP 11058063; EP 1584406 A2]. They are either single or multiple nozzles and can for reasons of brevity not be detailed here. Some of the patents quoted render guiding mechanisms, e.g. multiple drill holes or slotted holes by which the gas is redistributed before it is blown onto the workpiece [JP 20033181676; EP 0600250].

However, all these designs feature tube-like or conic nozzle contours. They are not fluid dynamically optimized to guarantee a non-turbulent and laminar flow. This is difficult to achieve by a coaxial nozzle, since a tube-like nozzle cannot narrow down its diameter. The diameter is prescribed by the optical system necessary to focus the laser beam. Such nozzles need a high absolute flow rate to create satisfactory fluxes to effectively shield a process zone. The reduction of diameter is limited by the beam caustic for conic nozzle geometries. The conic nozzle geometry will be considered and evaluated as a benchmark for the standard nozzle presented in this dissertation. It will be shown that considerable admixture of ambient air takes place and that perfect shielding of the fusion zone can only be achieved by high fluxes, which suffer from the drawback of perturbing the melt pool.

The double nozzle described in EP 0600250 supplies argon in an outer nozzle at a higher pressure than helium in the centre nozzle. Thereby, a depression is achieved. The objective of this invention was to widen the keyhole by depression

of pressure to increase the coupling of the laser beam. This is only advantageous in CO_2 laser welding and does not seem to be applied in production at all.

Hermann, the inventor of EP 0600250, mapped out all commercially available gas nozzles [HERMANN 2004]. He concludes, "up to now *no* coaxial gas nozzle system is on the market guaranteeing a pure process gas atmosphere at the fusion melt zone".

5.1.3 Cross-jets

The laser beam propagates through the nozzle towards the workpiece. Fumes and spatter originating from the welding process move in the opposite direction. Optical components, such as focusing lenses, are very sensitive with regards to contamination by fumes and spatter. These contaminations obstruct the beam and lead to degradation of its optical properties by refraction. The energy of the beam can be released in the optical systems by such contaminations initiating damage or even destruction by over-heating. Thus, even if the optical components are separated from direct contamination by a protection glass, the contamination must be removed before reaching the optical components in order to prevent obstruction. For lateral nozzle systems the state-of-the-art remedy was a cross-jet of pressurized air rejecting particle contaminations such as fumes and spatter from the focusing lens or the protection glass. Such cross-jets were researched as to improve the air knife they generate by fluid dynamically advantageous design of their emerging unit. The best design of the emerging unit is a rectangular slit geometry instead of a line of circular Laval nozzles. A combination of such cross-jets together with a coaxial nozzle constitutes the 'integrated nozzle', shown in figure 5.1 c). This design is the most advanced design of a coaxial nozzle integrating a cross-jet to protect the optical components.

This 'integrated nozzle' patented by Fraunhofer ILT Aachen is made up of a coaxial double conic nozzle supplying the process gas through the outer nozzle, whereas the centre nozzle is void of process gas [MAIER 1999, p. 62].

The process gas is directed to the fusion zone at an angle, which is detrimental to the prevention of process pores. The cross-jet is located right above the centre nozzle. Kern showed by Schlieren optic technique that the process gas in a coaxial nozzle experiences suction towards the cross-jet. Thus, the process gas is removed from the fusion zone [KERN 1999, p. 29]. The 'integrated nozzle' does not prevent the admixture of air into the centre nozzle. Thus, expensive process

gas is removed from the fusion zone and air is admixed to the process gas and thereby reaches the fusion zone.

Kern developed a cross-jet unit, which he optimized by simulation, to create an eddy current of gas within the beam path of the laser to abolish the suction effect. He experimentally determined the average diameter of spherical spatter particles to be approximately 0.5 mm with an average speed of about 3.5 m s^{-1}. Some of the particles, however, showed peak velocities of 15 m s^{-1}. To reject those from the protection glass pressurized air throughputs exceeding 2000 L min^{-1} would be necessary. Kern concluded that such throughputs are practically not realizable. Hence, even the most favourable cross-jet design by Kern cannot remove all fumes and spatter particles.

It should be noted that the more particles are to be removed from before the optical components by increasing the throughput of pressurized air the more disadvantageously those particles are distributed throughout the production site. Fumes and spatter can give rise to many secondary hazards especially in laser beam welding, such as destruction of optics and dust explosions according to laser safety standards [DIN EN ISO 60825:1-4]. Hence, fumes and spatter should be removed.

5.2 Development of a coaxial double nozzle

A gas shielding nozzle for laser beam welding should warrant:

1. System technology for production demands rotation symmetry, a distance nozzle, low maintenance and running costs, and protection of the environment
2. Consideration of volatility of gases and propensity to admixture by turbulence with ambient air
3. Process technology of laser beam welding demands non-invasiveness of the gas flow and flow direction of the gas parallel to the laser beam

Requirement 1 necessitates a coaxial nozzle. The problems that arise when such a nozzle is combined with a cross-jet have been pointed out. In an industrial production the exchange of the protection glasses leads to costs and non-productive times. The particle emissions from the fusion zone are blown into the production site and shorten the maintenance intervals of the optics.

Requirements 2 and 3 seem to be mutually exclusive. In order to generate sufficient shielding of the fusion zone conical coaxial nozzles necessitate fluxes of up to 10 L min^{-1} cm^{-2} [TRAUTMANN 2005]. Such high fluxes perturb the melt pool. Ambient air gets entrained into the gas flow if the throughput is reduced such that no perturbation of the melt pool degrading weld quality takes place. This air reacts with the molten material and leads to a detrimental oxidation and embrittlement of the fusion zone.

5.2.1 Nozzle contour for laminar flow

Hence, a completely new approach had to be taken in order to satisfy these seemingly irreconcilable demands. An appropriate analysis of the properties of the gases and their respective flows is fundamental to this end.

The geometry of the nozzle should provide a laminar flow throughout and when leaving the nozzle. Whether a gas flow is laminar or turbulent depends on Reynolds number *Re* not exceeding a critical value of 2320:

$$\mathrm{Re} = \frac{v \cdot L \cdot \rho}{\eta} \qquad \text{(Equation 5.1)}$$

where v is the velocity of the medium, L a characteristic length, ρ the density, and η the viscosity. The ratio η/ρ is termed kinematic viscosity. Hence, *Re* should be below 2300 in all circumstances to prevent turbulence and therefore admixture of ambient air.

A tube would simplest laminar nozzle geometry. For a coaxial nozzle a continuously narrowing diameter along its length is favourable in order to reduce the absolute flow of gas while simultaneously keeping its flux *at the aperture* constant. For a non-conical geometry three methods are known:

Börger started from a given nozzle geometry and calculated the flow lines according to potential flow theory [BÖRGER 1973]. The contour of the nozzle is varied and the flow lines are iteratively calculated until an optimal flow in the nozzle is achieved. The constraints are a given contraction ratio, specific coefficients of friction at the wall of the nozzle, and the suppression of boundary layer separation. Since iterative calculations by a computer were not available at Börger's time, he made quite a few assumptions to reach a solution after nonetheless elaborate calculations. His approach does not provide a general

solution for flexible adaptation of the nozzle contour to different focal lengths. Hence, this approach is not adopted herein.

Wu, Whitehead, and Waters developed an approach where a two dimensional potential field with singularities, i.e. sources and sinks, is assumed. The position and the magnitude of the singularities are adjusted such that the flow lines show a favourable flow pattern. Subsequently, the contour of the nozzle is accordingly chosen. This approach eventually requires numerical simulation and seemed too complex to be adopted herein [WHITEHEAD 1951].

Witoszynski and Mills assumed in their optimization that a linear and uniform flow could be achieved if the nozzle contour in axial direction is continuous and the flow is incompressible and ideal. They analytically prescribed an increase of speed along a flow line starting from a low initial velocity to a high final velocity at the aperture. By virtue of the differential equations for an axis symmetric ideal fluid flow one flow line is identified with the nozzle contour. The derivation of the analytic formula can be found in appendix B [WITOSZYNSKI 1924]:

$$r(z) = \frac{r_0}{\sqrt{1-(1-\frac{r_0^2}{r_1^2})\frac{(1-\frac{3z^2}{a^2})^2}{(1+\frac{z^2}{a^2})^3}}} \qquad \text{Equation (5.2)}$$

where *r(z)* is the radius of the nozzle at height *z*, r_o is the initial radius, r_1 the radius at the aperture, *a* is the length of the nozzle, and *z* therefore varies between zero and *a*. This formula is analytic and allows flexible adaptation to the focal length of the lens. Hence, it was used to determine the nozzle contour.

The role of helium to reduce porosity in aluminium welding has been widely recognized [KATAYAMA 2007b, KUK 2004, HEIDER 2000, FARWER 1996]. Whether pure helium fed into the nozzle actually reached the fusion zone might be doubted if the volatility of helium is taken into account. The upthrust for a flow of process gas with regards to stagnant ambient air is given by:

$$F = V \cdot (\rho_{air} - \rho_{gas}) \cdot g \qquad \text{(Equation 5.3)}$$

where *F* is the upthrust, *V* is a characteristic volume, and *g* the acceleration due to gravity. The densities of helium, argon, and air are given for comparison in table 5.1.

	unit	helium	argon	air
periodic number		2	18	-
atomic mass	u	4.0026	39.948	-
density ρ (0°C, 1013 hPa)	g dm^{-3}	0.1785	1.7837	1.189
thermal conductivity λ_{th} (0°C)	W m^{-1} K^{-1}	0.146	0.0175	0.026
1st ionization engergy	eV	24.587	15.759	-
kinematic viscosity ν	10^{-6} m^2 s^{-1}	104.5	16.1	15.35

Table 5.1: Physical properties of inert gases in comparison to ambient air

From the physical properties it is obvious, and it was furthermore shown by a Schlieren optic experiment [SEEFELD, p. 998], that only a fraction of the flow of pure helium reaches the melt pool. Pure argon has a density even higher than air and therefore does not experience an upthrust, as can be seen in equation 5.3. Contrary to helium a stream of argon accumulates over the fusion zone as it is decelerated by the workpiece acting as an obstacle. Thus, a mixture of argon and helium delivers more helium to the fusion zone as compared to a jet consisting of pure helium , because separation by diffusion of a flowing gas mixture according to density is practically negligible for the distances involved here. Additionally, argon is an inert gas like helium and thus shields the melt pool from ambient air although argon is not as favourable for the prevention of porosity as is pure helium. Farwer adopts a very pragmatic approach by using a mixture consisting of 50% argon and 50% helium [FARWER 1996]. Berkmanns renders a very elaborate table in order to select an optimized mixing ratio of the two inert gases depending on the speed of welding, penetration depth, and nominal output power of the CO_2 laser [BERKMANNS 1998, p. 71]. However, these approaches represent just a compromise, because the best possible result would be attainable by *pure* helium [DILTHEY 2007]. As a matter of fact, no nozzle is currently available to effectively direct pure helium to the fusion zone. This supported the notion that the admixture of argon lead to a reduction of pores - whereas in fact - it just delivered more helium in this mixture with itself to the fusion zone, which would have otherwise escaped.

5.2.2 Design of an immerged gas flow

The double coaxial nozzle featured herein takes carefully into account all these phenomena. Pure helium is fed into the centre nozzle and emerges from it in a laminar flow like pattern. The helium flow is *guided* within a flow of argon to prevent the upthrust in stagnant ambient air described above. This argon needs to be supplied by an outer nozzle.

In order to prevent turbulence and mixing of guiding gas (argon) and main process gas (helium) both gases need to have the same speed when leaving the nozzle (c.f. equation 5.6). Hence, the nozzle was designed according to this constraint, i.e. by consideration of the continuity equation. The continuity equation for a narrowing nozzle is shown in figure 5.2.

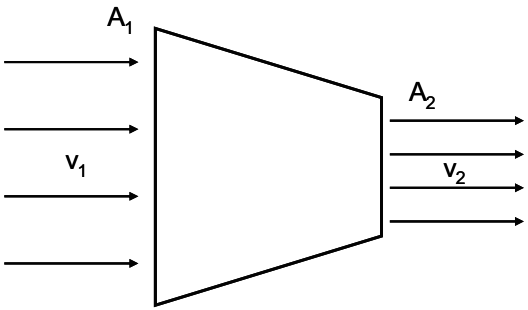

Figure 5.2: Schematic representation of flow lines before and after a narrowing nozzle to illustrate the continuity equation

$$A_1 v_1 = A_2 v_2 \qquad \text{(Equation 5.4)}$$

were A_1 is the cross-sectional area of the nozzle where the speed of the fluid is v_1 and A_2 the cross-sectional area of the nozzle where the speed of the fluid is v_2.

The guiding argon completely surrounds the helium. Helium is separated from the ambient air and is immerged in a tube of guiding gas made up from argon. This is qualitatively shown in figure 5.3.

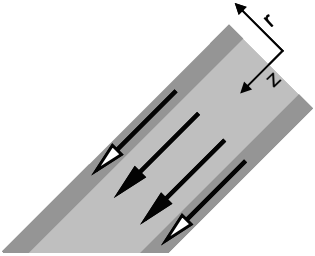

Figure 5.3: Laminar flow of helium guided by immergence within a laminar flow of argon; helium indicated by black arrows; argon indicated by white arrows

The diffusion coefficient D is defined as follows:

$$D = \frac{1}{3} \cdot l \cdot \bar{v} \qquad \text{(Equation 5.5)}$$

where l is the mean free path and $\bar{v}$ the average thermal velocity of the gas molecules. Thus, diffusion of helium into argon over the short range of parallel flow is negligible, and argon experiences no upthrust due to its higher density than the surrounding stagnant air. Since the flows of the two gases are adjusted such that they have the same velocity, turbulence is not invoked by shear stresses τ between the two layers of gases:

$$\tau = \eta \cdot \frac{\partial v}{\partial r} \qquad \text{(Equation 5.6)}$$

where η is the viscosity, v the velocity of the gas, and r is the direction perpendicular to the flow direction. Hence, pure helium is effectively delivered to the fusion zone and the nozzle aperture can be kept a fair distance away from the workpiece. This design according to theory will be scrutinized by verifying experiments further down.

5.2.3 Gas injection unit

In order to obtain a laminar flow at the apertures of the nozzles the gas must be injected in such a way as to prevent turbulence upon entering the nozzles. This is achieved by a two stage injection plate with round and slotted holes, which are orientated to minimize turbulences. The lower injection plate is shown in figure 5.4.

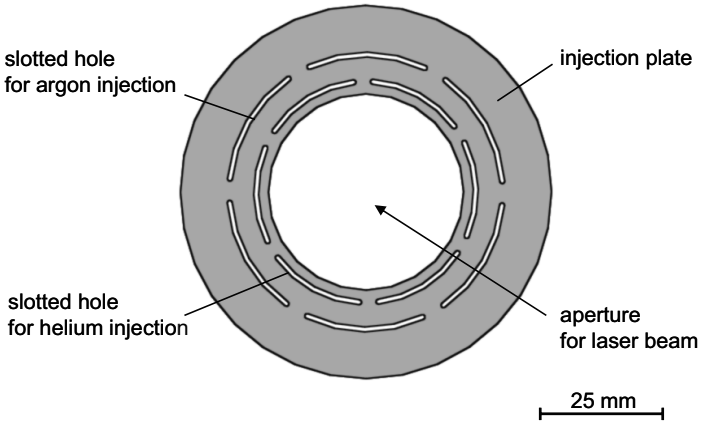

Figure 5.4: Lower injection plate

The upper plate has circular drill holes right above the dividing part of adjacent slotted holes in order to achieve an optimal dispersion of gas. The gases are supplied to the injection plate by hoses attached to the injection plate unit from one side. Hence, due to frictional losses the pressure and velocity of the gas is not homogeneous but varies as the gas flows through the injection plate to reach the drill holes on the opposite side of the hose's connection. As the associated turbulences are difficult to calculate, the condition of equal velocities upon emerging from the aperture of the two gas species is invoked. If a gas emerges from a nozzle at a different pressure than the ambient medium, the flow will diverge and the gas molecules will disperse. Therefore, argon and helium should emerge at atmospheric pressure.

The pressure losses are calculated for helium and argon at a maximal flow of 20 L min^{-1} and a minimal flow of 10 L min^{-1}. The first pressure drop is associated with a drop of potential energy within the length of the nozzle. For the centre nozzle the change in velocity needs to be taken into account. Bernoulli's theorem is used to calculate this pressure drop:

$$\frac{v^2}{2} + \frac{p}{\rho} + gh = const. \qquad \text{(Equation 5.7)}$$

where v is the velocity of the gas, p the pressure of the gas, ρ the density of the gas, g the gravitational acceleration, and h the relative height.

No standard formula is available to calculate the pressure losses of the gases in the channels of the injection plate. The ratio of cross-sectional areas β can be employed to estimate the pressure loss by virtue of tabled loss or resistance numbers ζ [SIGLOCH, p. 401]:

$$\beta = \frac{n \cdot A_{hole}}{A_{slot}} \qquad \text{(Equation 5.8)}$$

where n is the number of round holes over one slotted hole, A_{hole} is the cross-sectional area of the circular hole, and A_{slot} the cross-sectional area of the slotted hole.

The loss or resistance number ζ is inserted into the formula for grating-losses [WAGNER, p. 57]:

$$\Delta p = \zeta \frac{\rho}{2} v^2 \qquad \text{(Equation 5.9)}$$

where Δp is the pressure loss. The deflection loss calculated below is due to the deflection of the gases by 90° upon entering the groove of the injection plate. The resistance number in this case is $\zeta = 4$ according to [WAGNER 1991].

Additionally, the gas' pressure losses in the hoses accumulating on the its way from the gas bottle to the nozzle needs to be considered. The pressure loss is calculated:

$$\Delta p = \frac{\rho \cdot v^2}{2} \frac{\mu \cdot L}{d} \qquad \text{(Equation 5.10)}$$

where v is the speed of the gas, L is the length, and d is the diameter of the gas hose. If the gas flow is laminar, the friction number μ is given by:

$$\mu = \frac{64}{\mathrm{Re}} \qquad \text{(Equation 5.11)}$$

where Re is the Reynolds' number, as defined in equation 5.1.

The total pressure loss Δp_{total} owed to changes of cross-sectional area of the nozzle is independent of local pressure. Hence, the total pressure loss is the sum of the individual pressure losses Δp_i within the nozzle system:

$$\Delta p_{total} = \Sigma \Delta p_i \qquad \text{(Equation 5.12)}$$

Table 5.2 gives the calculated total pressure drops in the double coaxial nozzle system. The pressure losses in the double nozzle system are rated as negligible, because the losses in the hoses are clearly dominant. The pressure set at the hygrometers, which are located close to the nozzle, does translate to the nozzle without need for pressure loss compensation.

	helium (inner nozzle)		**argon** (outer nozzle)	
	max. flow	min. flow	max. flow	min. flow
hoses	0.149 bar	0.0745 bar	0.228 bar	0.114 bar
grating	$1.35 \cdot 10^{-7}$ bar	$2.5 \cdot 10^{-7}$ bar	$1.5 \cdot 10^{-7}$ bar	$2.8 \cdot 10^{-7}$ bar
deflection	$4.7 \cdot 10^{-4}$ bar	$8.5 \cdot 10^{-4}$ bar	$3.6 \cdot 10^{-4}$ bar	$6.6 \cdot 10^{-3}$ bar
total loss	0.149 bar	0.0753 bar	0.228 bar	0.120 bar

Table 5.2: Calculated pressure losses for the double coaxial nozzle system and the hoses

The flow line diagram indicating the respective velocities of the gas flows within and behind the orifice of the double coaxial nozzle is shown in figure 5.5.

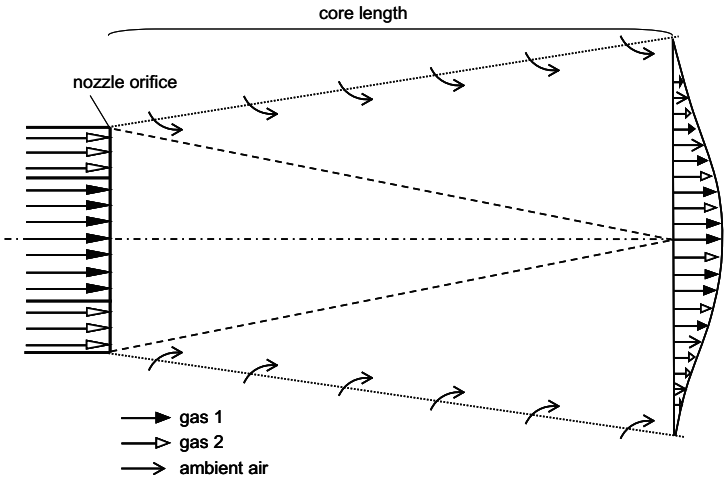

Figure 5.5: Diagram of flow lines and velocity distribution, triangles indicate the mixing fronts; helium is the gas in the inner nozzle and is indicated by black arrows; argon is the gas in the outer nozzle and is indicated by white arrows [mod. acc. to HACKSTEIN 1987, p. 147]

Figure 5.6 shows an elevation of the double coaxial nozzle system:

Figure 5.6: Exploded drawing of the double coaxial nozzle system and the injection plate; the outer nozzle was made transparent to show the inner nozzle

The complete nozzle system with associated flow of gas is shown in figure 5.7:

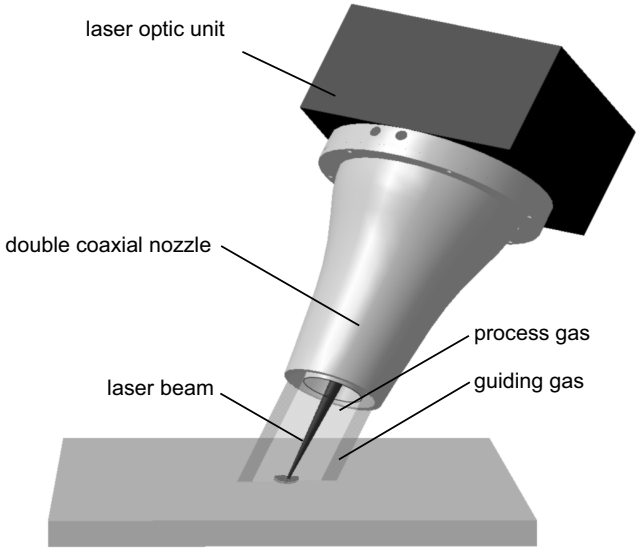

Figure 5.7: Double coaxial nozzle system

5.3 Merits of the double coaxial nozzle: experiments and results

In sections 5.1.1 and 5.1.2 several state-of-the-art nozzle systems were discussed. However, to *fully* assess a particular nozzle system and compare its merits to other competing nozzle systems two benchmarks or criteria need to be considered: merit of gas coverage and non-invasiveness.

The merit of gas coverage concerns the system technology of the gas nozzle: How *effective* is the nozzle system in delivering expensive process gases onto the melt pool surface to *shield* it from the influences of the ambient environment and *assist* the welding process in a desired way? Depending on perspective, the *process* gases used are sometimes termed *shielding* or *assist* gas in the literature. To qualify the effectiveness of the process gas supply it is not enough to assure that all the process gas reaches the process zone without escaping beforehand, but additionally that the process gas is not contaminated with ambient air. As a consequence, the effectiveness is also related to the economics of the nozzle

system. Unfortunately, no standard of effectiveness is established for most nozzles presented in the literature. In the following section 5.3.2 an indirect method to measure the effectiveness will be introduced.

The non-invasiveness of the gas supply concerns the process technology of the nozzle *and* the welding technique. As described in section 4.1.3 the porosity in aluminium is to a great extent induced by process gas. Hence, a nozzle system that is non-invasive with regard to the melt pool should prevent process gas porosity. In order to assess and measure non-invasiveness a suitable standard for comparison needs to be established. A chamber completely filled with the process gas at ambient pressure is a setup in which the process gas is *least* invasive. Any nozzle will fall short of this standard. The results for such a chamber filled with process gas are presented in the next section.

5.3.1 Influence of means of process gas supply

The influence of how the process gas is supplied to the fusion zone is generally acknowledged. Ion noticed, "a small change in, for example, the shielding gas flow rate is sufficient to produce a dramatic effect on the geometry of the weld bead" [ION, p. 435]. Kern showed that perturbations in the fusion zone by the process gas should not be underestimated [KERN 1999, p. 35]. He shielded the fusion zone from ambient air. He deployed a nozzle within a chamber-setup. He used an even He/Ar mixture supplied at 33 L min^{-1}. A bead on plate weld was performed on AlMgSi1 by a 4 kW-CO_2 laser welding at a speed of 4 m min^{-1}. Kern demonstrated that the visual quality of the bead's surface was *notably* improved when welding with a nozzle in a chamber-setup as compared to a nozzle which permitted air to access the fusion zone. Kern's work was primarily concerned with the optimization of the cross-jet in a twofold way: First, he tried to improve the effectiveness of cross-jets of pressurized *air* for spatter removal. To this end he created high dynamic pressures of the air molecules to divert the spatter particles. Second, he tried to fight the consequences of a strong cross-jet, i.e. to minimize the admixture of its air particles to the process gas. He showed that a conventional cross-jet design led to a very perturbed bead [KERN 1996]. This is an important experimental *proof* of the detrimental effect of process gas supply if not taken care of. Kern's chamber was *purely* a laboratory setup, because it was attached to the workpiece and did not allow accessibility. Kern himself admits that it could not be used in industrial applications [KERN 1996; KERN 1999, p. 35].

The same perturbations of the bead are induced if the orientation of a gas nozzle is changed. Figure 5.8 shows a sequence of pictures taken by high-speed photography for which a single lateral nozzle was used. The pictures in figure 5.8 show spatter and ejections from the keyhole. The bead is perturbed and the welding process is agitated.

The best shielding conditions, i.e. perfect gas coverage and least invasiveness, are provided by a process gas chamber. To qualify the merit of a nozzle it has to be compared to a process gas chamber. A gas chamber serves as a measuring rod to which any nozzle can hardly live up to. Figure 5.9 shows a sequence of pictures taken by high-speed photography in a process gas chamber.

The sequence displayed in figure 5.9 shows the sedation of the melt pool. Note the difference to figure 5.8. The weld bead shows a very clean chevron pattern and spatter droplets occur very rarely. Since the conditions and parameters of welding are otherwise equal to those in figure 5.8, it is obvious how invasive the process gas can become and thus affects the seam quality.

The research within this dissertation is focused on BHLW. The technology of BHLW exhibits a greater robustness than single spot laser beam welding. This advantage of BHLW, i.e. the increase of robustness by a sedation of weld pool dynamics in BHLW, is detailed in paragraph 7.1. BHLW *by itself* also reduces spatter and other defects, as shown in paragraph 6.3. The double coaxial nozzle system developed in this chapter could merely marginally improve the robustness and reduce spatter and other defects in BHLW. Obvious improvements for single spot laser welding by virtue of the double coaxial nozzle systems are not considered within the scope of this dissertation for reasons of brevity.

BHLW can *reduce* process gas porosity by prolonging the solidification time of the melt pool, thus allowing more process gas bubbles to escape. If the process gas supply is non-invasive with regards to the melt pool, *no* bubbles should form and the seam should be *free* of porosity. In BHLW the double coaxial nozzle system is potentially the critical *enabling* factor for the *prevention* of porosity. This is carefully considered in section 5.3.3.

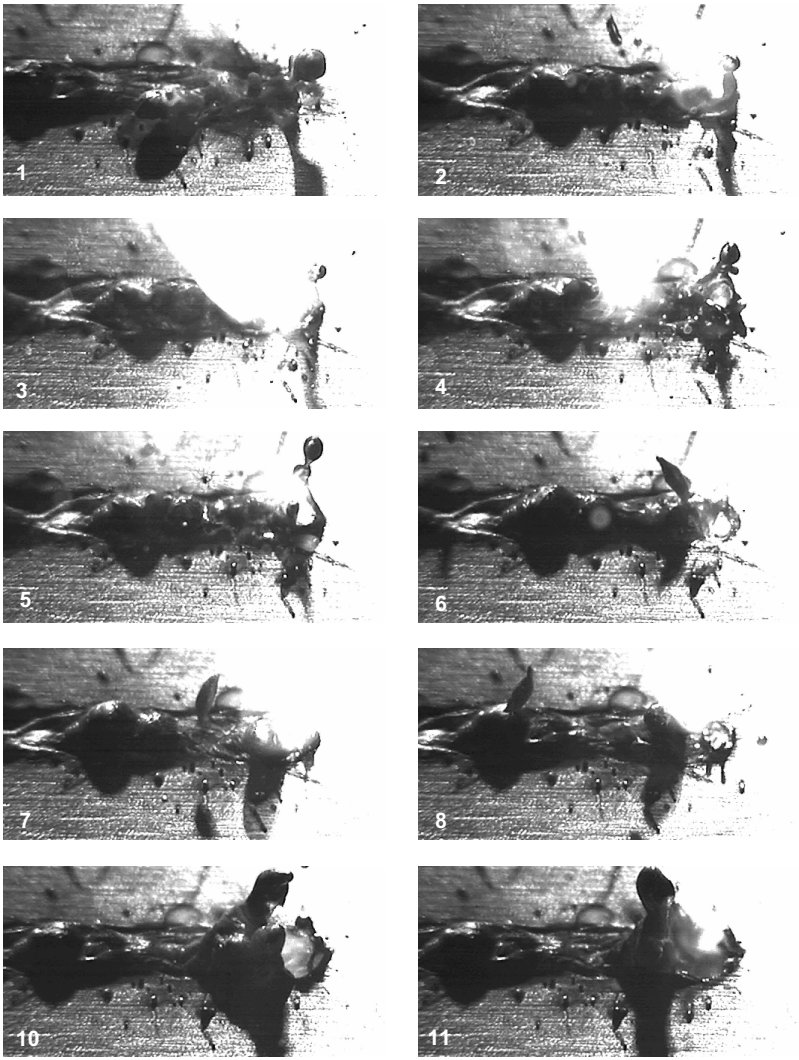

Figure 5.8: *Sequence of high-speed pictures of fibre laser welding; 1000 fps; P_{fibre} = 6 kW; φ = 6°; laser specifications as in figure 4.17; v_w= 3 m min^{-1}; argon flow 25 L min^{-1}; argon flux 50 L min^{-1} cm^{-2}; nozzle inclination angle 45° leading the laser beam axis; EN AW-50831; bead on plate*

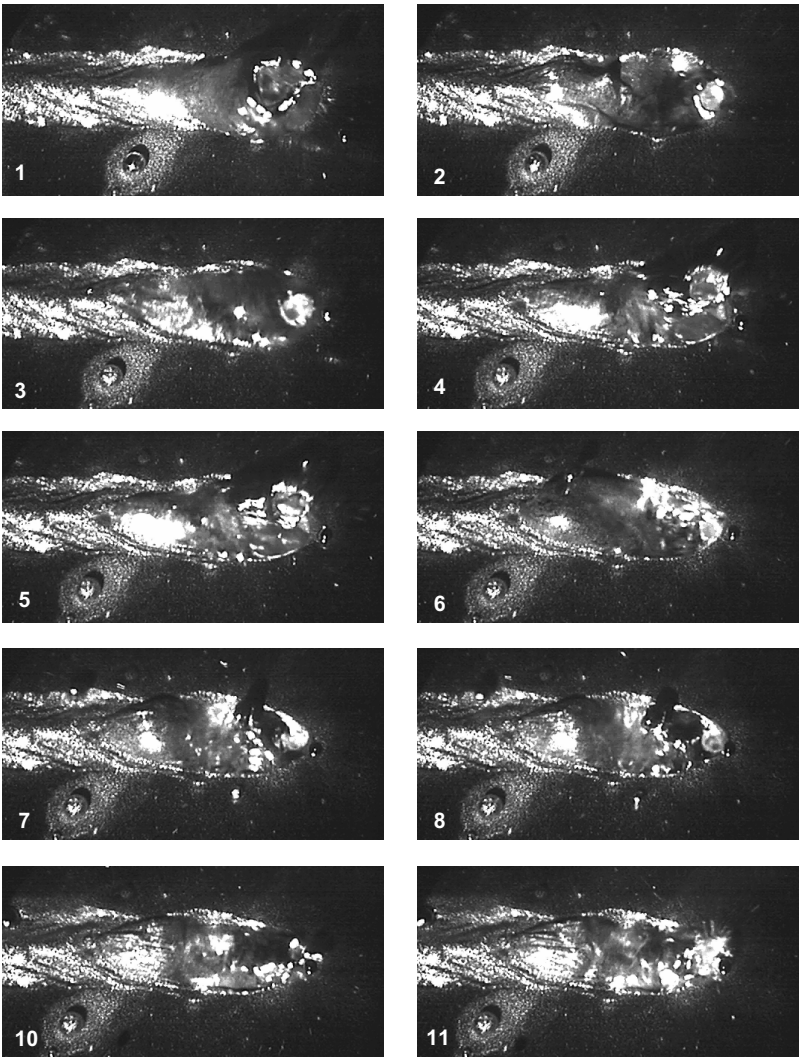

Figure 5.9: Sequence of high-speed pictures of fibre laser welding; 1000 fps; P_{fibre} = 6 kW; φ = 6°; laser specifications as in figure 4.17; v_w= 3 m min^{-1}; chamber rinsed with argon before welding; EN AW-50831; bead on plate

5.3.2 Merit of process gas supply

Many investigations present gas nozzles without ever proving their merit of gas coverage. Herein, a novel, *indirect* method is deployed to demonstrate the merit of inert gas shielding. The elevated temperature at the free surface of the melt pool or in the vapour cavity leads to the formation of NO_x in the *presence* of air. NO_x designates nitric oxide, i.e. colourless NO, which in contact with air forms reddish brown fumes of nitrogen dioxide NO_2. In experiments it turned out that the concentration of NO_x increased during welding. Once the laser radiation ceased, the NO_x-concentration subsequently levelled off.

The NO_x-concentration is measured with a probe originally designed to assess emissions of household heating systems. The probe is intended to take measurements in the funnel of the heating system. The probe displays the value of NO_x in parts per million (ppm) after this value settled for more than 0.5 s. In order to determine the merit of gas shielding of a nozzle a collection vessel was used to guide the fumes towards the probe to replace the funnel. The setup is shown in figure 5.10.

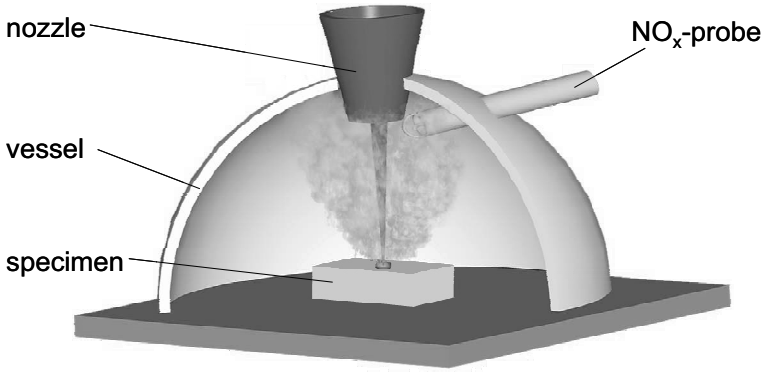

Figure 5.10: Diagram of experimental setup for indirect measurement of the merit of gas shielding

The relative maximum ppm-concentration of NO_x is recorded, because the vessel integrates the emissions over the laser emission time. Perfect shielding by inert gas of the fusion zone is identified with an NO_x-concentration of 0 ppm, since only the complete exclusion of air from the fusion zone results in a suppression

of NO_x-formation. This value is reliable, as any formation of NO_x during welding would have resulted in a reading of the probe.

The other values displayed in the following figures have to be considered cognisant of the following caveat: The probe renders a measurement once the ppm value settles for more than 1 s. The reading shows the average amount of NO_x at the beginning of welding. The increase of NO_x-concentration at subsequent instants was not measured, as this would have required the probe to be initialized *during* welding. The time of welding was too short to remove the probe from the vessel for zeroing and to initialize it again for measurements at later instants. Hence, low readings of ppm values indicate that NO_x formed and would surely have increased over time had a later measurement been possible. A zero measurement of ppm can be trusted, as in this case no NO_x developed during the *whole* time interval of welding. These values are highlighted in the following graphs.

In figures 5.12 to 5.14 the necessary absolute flows and fluxes to guarantee perfect shielding are shown for the pertinent nozzle geometry. The consumption of inert gas of the conical nozzle was compared to the consumption of the double coaxial nozzle system. In the literature on conical nozzles an angle of inclination between 10° and 20° to the axis of symmetry is recommend to minimize turbulence. Cizungu regards an inclination angle of 12° as optimal to delay eddy formation [CIZUNGU 2003].

It should be noted that the conical nozzle used for the following experiments satisfied this condition und therefore represents to the *most* advantageous conical nozzle.

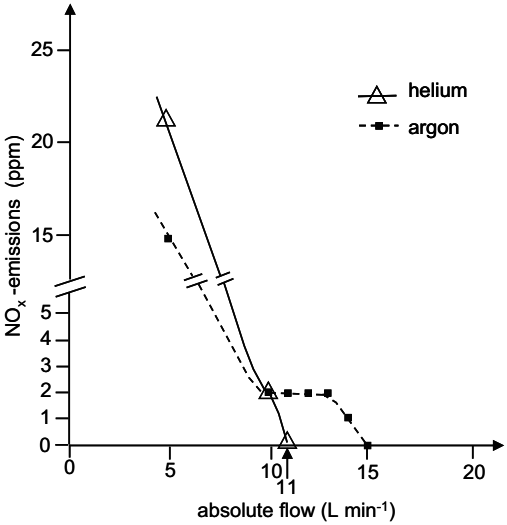

Figure 5.11: NO_x -emissions versus gas flow rates of argon and helium in single spot Nd:YAG laser welding with a conical nozzle; $P_{Nd:YAG}$ = 3 kW

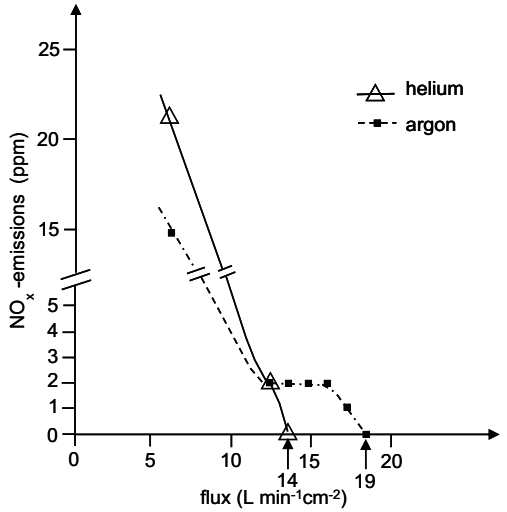

Figure 5.12: NO_x -emissions versus gas fluxes of argon and helium in single spot Nd:YAG laser welding with a conical nozzle; $P_{Nd:YAG}$ = 3 kW

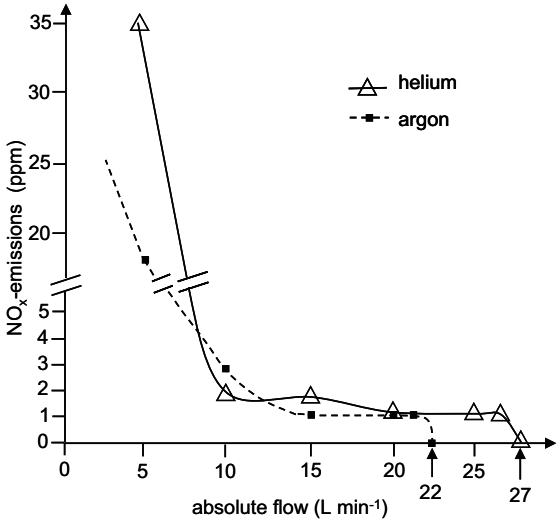

Figure 5.13: NO_x -emissions versus gas flow rates with a conical nozzle in BHLW; P_{BHLW} = 3 kW+3 kW

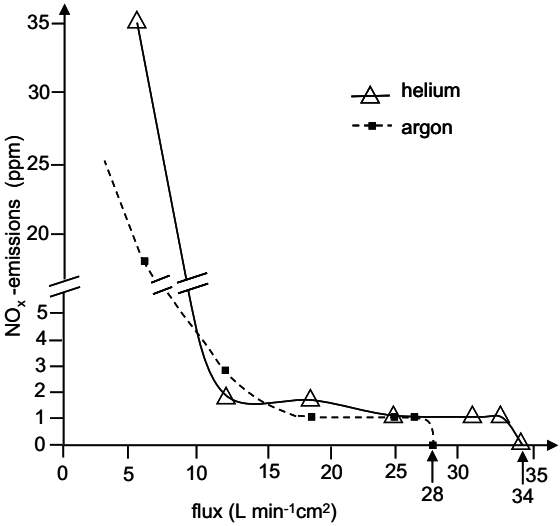

Figure 5.14: NO_x -emissions versus gas fluxes of argon and helium with a conical nozzle in BHLW; P_{BHLW} = 3 kW+3 kW

To explain the difference in consumption of inert gas the flow needs to be visualized. Schlieren photography cannot be used in these circumstances as this technique utilizes the change of the refractive index with density being made apparent under a special type of illumination. Argon in the outer guiding nozzle can unfortunately not be discriminated against the ambient air by Schlieren photography. Hence, in this dissertation the flow lines of the respective gas species are visualized by injecting tracer particles. These particles stem from a reaction of hydrochloric acid (HCl) and ammonium (NH_3). The reaction is:

$$NH_3 + HCl \rightarrow NH_4Cl\uparrow$$

The resulting thick smoke of NH_4Cl is lead into the nozzle. The respective flow at least necessary to guarantee perfect coverage, as determined above, was used for the conical as well for the double coaxial nozzle. The geometry of the conical nozzle is shown in figure 5.15. The result of the smoke tracer particle experiment to visualize the flow is displayed in figure 5.16.

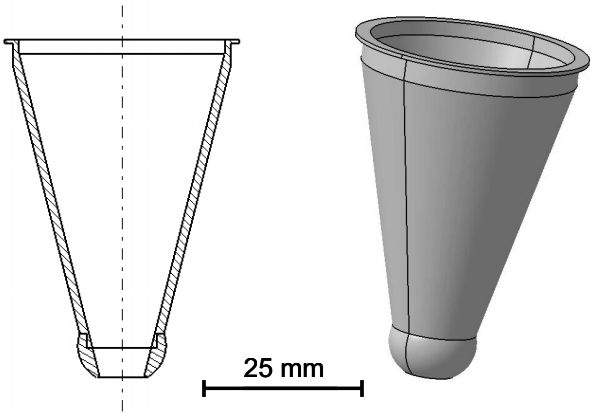

Figure 5.15: Conical nozzle geometry for least turbulence

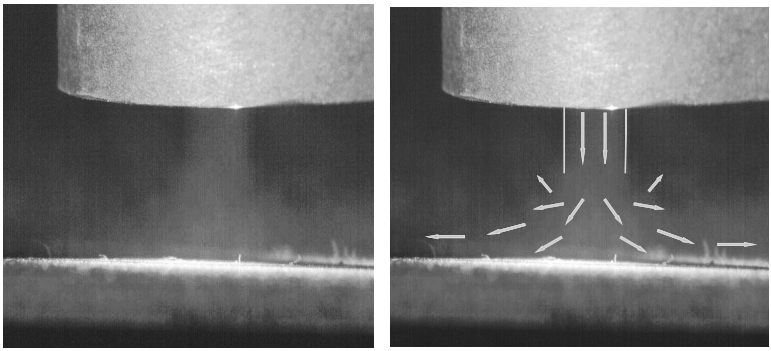

Figure 5.16: Flow lines of a conical nozzle; pictures are identical, added arrows in the right picture indicate the motion of the smoke tracer particles, which can be more easily seen in a high-speed film; flow of argon 30 L min^{-1}; flow of helium 30 L min^{-1}; gases are supplied at 1 bar; NH_4Cl smoke particles; 200 fps; diameter of nozzle 8 mm

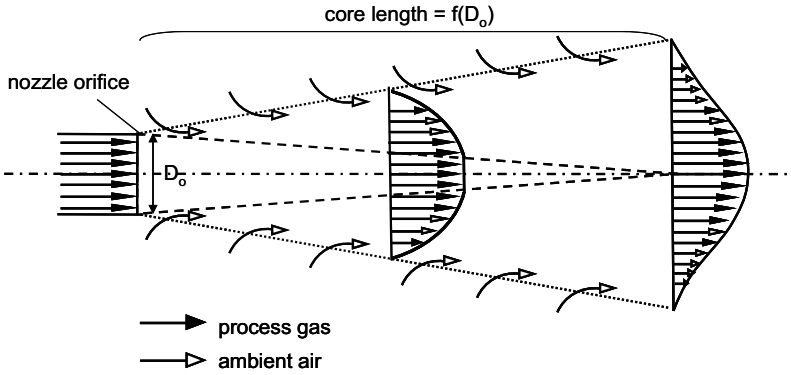

Figure 5.17: Diagram of flow lines for a single nozzle orifice; the unperturbed area with laminar flow forms a wake, the wake is indicated by dashed lines;D_o is the diameter of the nozzle at its orifice; process gas in the nozzle is indicated by black arrows; admixture of ambient air to the process gas is indicated by white arrows [mod. acc. to ECK *1991, p. 120]*

The velocity distribution displayed in figure 5.17 shows that the regime of laminar flow narrows down the farther the gas travels from the nozzle's orifice. Beyond the core length the laminar flow vanishes. The distribution spreads out by accelerating gas molecules in the vicinity. This broadening of the flow of gas emerging from the nozzle can clearly be seen in figure 5.17. This leads to an admixture of ambient gas, i.e. air. Thus, air contaminates the inert gas coverage. By increasing the absolute flow more process gas reaches the interaction zone to promote shielding and reduce the relative admixture of air. The welder is caught in a cleft stick as elevated flows of shielding gas are invasive with regards to sensitive melt pool dynamics especially when welding aluminium [HÜGEL 1992, p. 288]. On the other hand, if the welder reduces the flow as not to perturb the melt pool the inert gas coverage is not perfect and air reaches the fusion zone.

The following describes a nozzle system addressing this problem. The double coaxial nozzle provides a laminar, non-invasive flow at the fusion zone, as can be seen in figures 5.18 to 5.22. In figure 5.18 the tracer smoke particles were *only* introduced to the inner flow of helium. The flow of argon in the outer nozzle is transparent and therefore invisible. But the argon flow is present. It can clearly be seen despite the volatility of helium. Helium is contained within the circumferential guiding flow of argon. Thus, helium is effectively and exhaustively delivered to the fusion zone. The double coaxial nozzle can claim to *really* provide a pure gas to the process zone. For most of the gas nozzle systems described above it is feared that most of the helium was lost on its way to the fusion zone. Although helium entered the nozzle at a given absolute flow, it escaped during its travel towards the fusion zone due to its volatility.

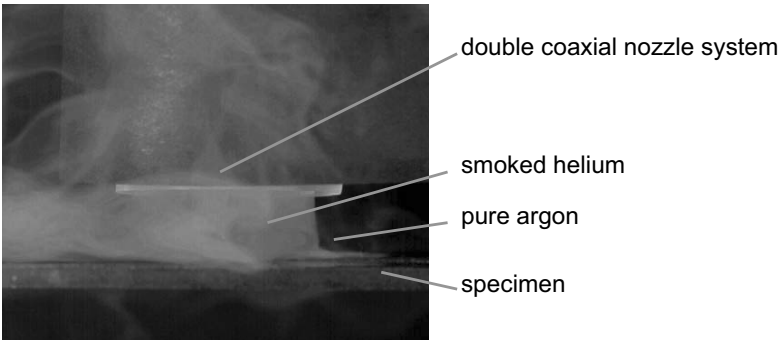

Figure 5.18: Snapshot from a sequence of high-speed photographs; flow of helium is smoked in the inner nozzle; in the outer nozzle the flow of argon is present but not smoked; double coaxial nozzle system is covered by a card board to prevent glares by reflection; 1000 fps

In figure 5.19 the argon flow in the outer nozzle was marked with tracer particles. As can be seen, no boundary layer separation or turbulence arises during the travel of the gas flow to the workpiece.

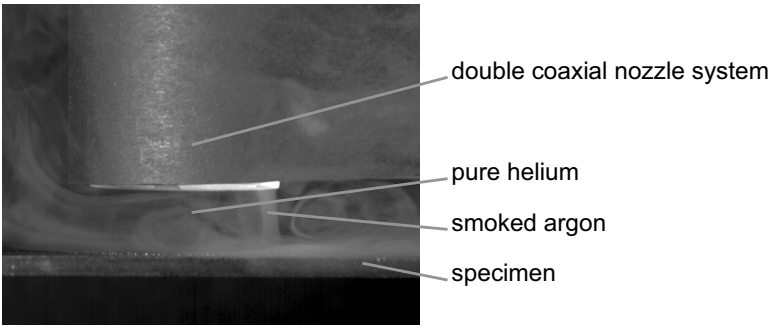

Figure 5.19: Snapshot of a sequence of high-speed photographs; flow of helium in the inner nozzle is present but not smoked; flow of argon in the outer nozzle smoked; double coaxial nozzle system is covered by a card board to prevent glares by reflection; 1000 fps

The flow of gas remains non-turbulent upon deflection by the workpiece, as can be seen in figure 5.20. The transparent flow of helium is embedded in the smoked flow of argon and forms spirally shaped eddie-like structures.

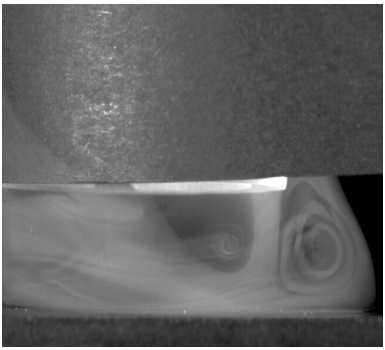

Figure 5.20: Boundary layer embedment of helium and argon and formation of spiral eddies

But even at distances farther than where the workpiece would normally be placed, the flow of helium is constrained and laminar, as can be seen in figure 5.20.

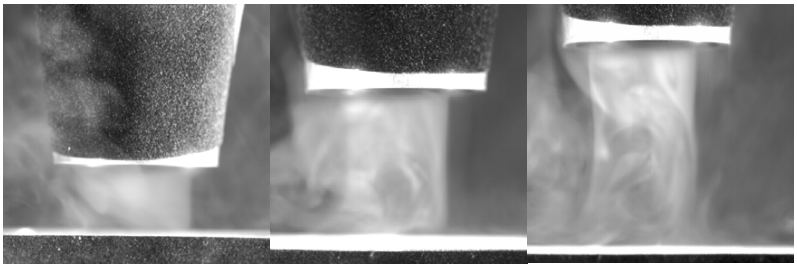

Figure 5.21: Laminar gas flow of the coaxial nozzle system for travel distances from the nozzle's orifice to the workpiece:1.5 cm, 2.5 cm, and 3 cm

Figure 5.22 shows that the flow is laminar even if the double coaxial nozzle is inclined with respect to the surface of the workpiece to be welded. The volatility of helium causes the flow to be slightly bent upwards. However, all the helium reaches the surface of the workpiece, c.f. figure 5.22. Helium would escape and not reach the workpiece without the guiding gas.

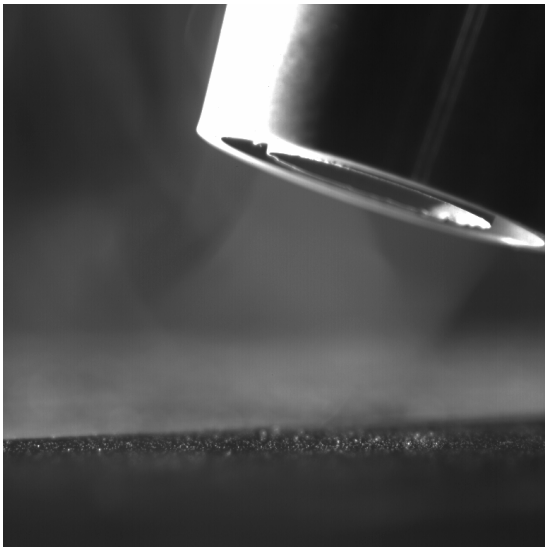

Figure 5.22: High-speed photography snapshot of the double coaxial nozzle inclined with respect to the workpiece, angle of inclination $\varphi = 20°$; helium in the inner nozzle is smoked; argon in the outer nozzle is present but not smoked

The coaxial nozzle system underwent the experimental procedure described above to determine perfect shielding conditions. The results are shown in figures 5.23 and 5.24.

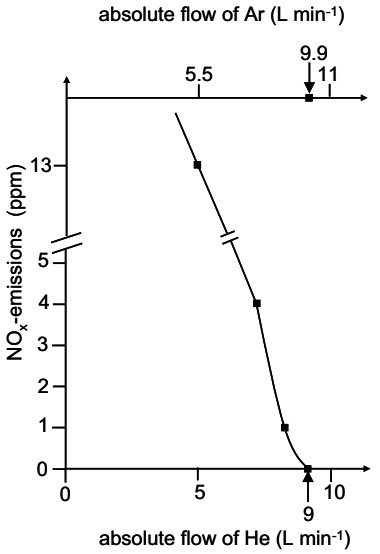

Figure 5.23: Absolute flows of argon and helium and resulting NO_x-formation for the double coaxial nozzle system

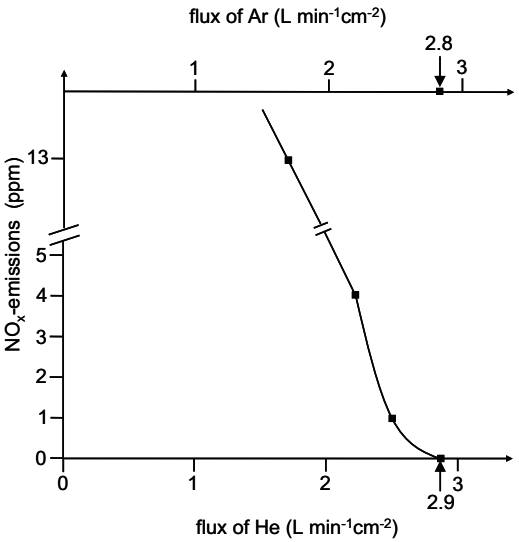

Figure 5.24: Fluxes of argon and helium and resulting NO_x-formation for the double coaxial nozzle system

Inert gas shielding by the double coaxial nozzle was proven to be effective and laminar. The admixture of air is prevented and all the process gas reaches the fusion zone. This nozzle is the first coaxial system that guarantees a pure process gas atmosphere at the fusion melt zone. Thus, the requirements of industry as formulated by Hermann are fulfilled [HERMANN 2004]. The nozzle is radial symmetric and provides a laminar flow up to approximately 3.5 cm beyond the nozzle's orifice as shown in figure 5.21.

5.3.3 Prevention of process gas porosity

So far, the effectiveness of gas coverage was presented. The demonstration of non-invasiveness of the process gas was observed by high-speed x-ray imaging at Katayama Laboratory of Osaka University, as described in section 4.1.3. A lateral nozzle system, the conical nozzle in figure 5.15, and the previous double coaxial nozzle system were used in single spot fibre laser welding. In order to assess BHLW in Japan the HPDL and fibre laser available at Katayama Laboratory were employed to *rebuild* an intensity distribution *similar* to BHLW as custumarily available in Germany for this dissertation. The laser system parameters are compared in table 5.3 for the solid state lasers, i.e. Nd:YAG laser in Germany and fibre laser in Japan.

	Germany	**Japan**
laser system	Nd:YAG	fibre
wavelength	1064 nm	1070 nm
BPP	25 mm*mrad	4.5 mm*mrad
maximum output power	3000 W	10 000W
diameter of focal spot (for f = 150 mm)	450 µm	130 µm
beam guide	fibreoptic cable (Ø 600 µm)	fibreoptic cable (Ø 100 µm)

Table 5.3: Comparison of solid state laser parameters of laser systems used in Germany and in Japan

The caustic and intensity distribution for the Nd:YAG laser in Germany is shown in figures 4.10 and 4.11. The caustic of the fibre laser in Japan is displayed in figure 4.17. Both solid state lasers were set to a maximum output power of 3 kW

to make the results comparable. The focal spot size is the only difference of experimental relevance between those two setups. The spot size diameter of the Nd:YAG laser is three times the spot size diameter of the fibre laser. Defocusing of the fibre laser in Japan to match the spot size of the Nd:YAG laser in Germany was not feasible for space restrictions of the grid within the high-speed x-ray apparatus in Japan.

The HPDL used in Japan and Germany where both a 3kW-Laserline LDL 160-3000 with a beam parameter product (BPP) of 85 x 200 mm*mrad. The wavelengths of the HPDL are centred on 808 & 940 ± 10 nm (FWHM). The qualitative intensity distribution of this laser system is shown in figure 4.3. In Germany and Japan the laser was directly irradiating the specimen through a focal lens of f = 150 mm. Due to different forming lenses within the HPDL head the German laser had a rectangular focal spot of 1.658 x 3.820 mm^2, whereas the laser in Japan had a focal spot of 2.120 x 3.152 mm^2. This difference in focal spot area is considered negligible for the results presented in the following. Hence, it is assumed that the rebuild of the German system by the components available in Japan secures transferable results.

In the experiments described in the following the gas flows are not arbitrary. For the lateral nozzle they are adjusted such that the flux of the lateral nozzle is *equal* to the flux of the conical nozzle. Thereby the influence of direction of the gas flow could be studied. The flow for the respective process gas or process gas mixture was selected as to guarantee perfect coverage according to the findings shown in figures 5.12 and 5.13. The flows of the double coaxial nozzle system were fixed to assure perfect shielding according to figures 5.23 and 5.24. It should be noted that a variation of the helium flow in the inner nozzle necessitates an adjustment of the argon flow in the outer nozzle to prevent turbulence between the guiding gas argon and the immersed gas flow consisting of helium. The laser power, the alloy, and other parameters were chosen as to enable a comparison of results within this dissertation.

Bubble formation was observed *during* welding with the Japanese x-ray apparatus. The x-ray snapshots in the following figures were taken subsequently to welding. Transmission was surface-on through the specimens. The size and the relative amount of pores are made visible for the reader. The bubbles can be seen in the high-speed films. But to observe them needs an accommodated eye. Single snapshots from those films suffered from low resolution and their quality does unfortunately not permit their reproduction in a printed dissertation.

First, the influence of the gas nozzle system in single spot fibre laser welding was studied. Figure 5.25 employed a lateral nozzle and shows a thread of pores in the middle of the sample along a horizontal line.

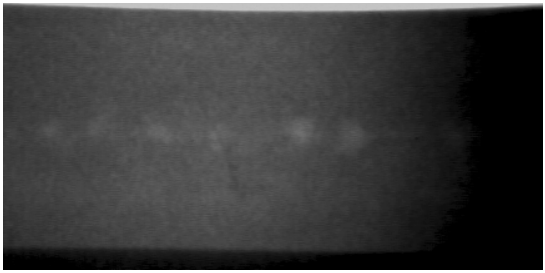

Figure 5.25: Surface-on x-ray transmission photograph of a fibre laser bead with a lateral nozzle; P_{fibre} = 3 kW; f = 150 mm; φ = 6°; v_w= 4.0 m min^{-1}; bead on plate; EN AW-6060, argon flow 30 L min^{-1}; argon flux 36 L min^{-1} cm^{-2}; lateral nozzle diameter = 8 mm; angle of inclination of lateral nozzle 45° to the surface normal of the specimen's surface; leading position of the nozzle

In figure 5.26 the result for the conical nozzle is displayed. Although the flux of argon was slightly lowered, the gas obviously bubbled more easily into the melt pool, since the direction of the gas flow is *coaxial* to the laser beam and thus the keyhole axis. This leads to comparably bigger pores than in figure 5.25.

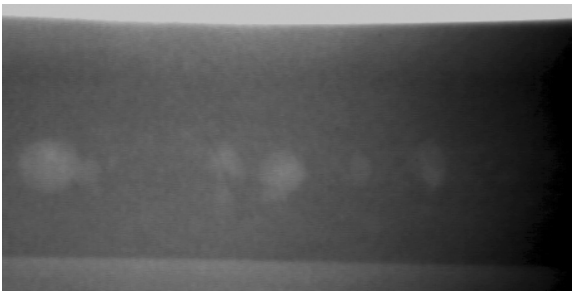

Figure 5.26: Surface-on x-ray transmission photograph of a fibre laser bead with a coaxial conical nozzle; P_{fibre} = 3 kW; f = 150 mm; φ = 6°; v_w= 3.0 m min^{-1}; bead on plate; EN AW-6060; argon flow 25 L min^{-1}; argon flux 30 L min^{-1} cm^{-2}; conical nozzle diameter = 10.3 mm

The influence of using helium instead of argon can be seen in figure 5.27. A thread of very small pores is visible. In the literature it is widely reported that the use of helium reduces the *magnitude* of porosity, c.f. equation 6.1. The definition of this magnitude of porosity will be critically discussed in section 6.2. In figure 5.27 it looks as if the absolute number of pores decreased. This is in agreement with the forecasts based on the mathematical process model in section 4.3.

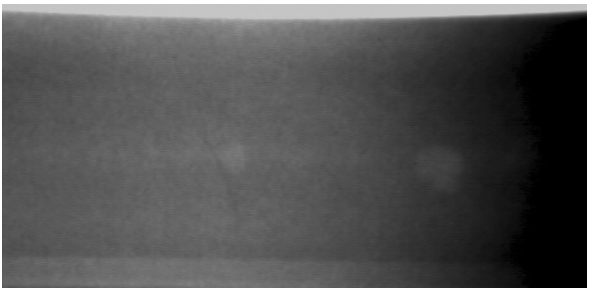

Figure 5.27: Surface-on x-ray transmission photograph of a fibre laser bead with a coaxial conical nozzle; P_{fibre} = 3 kW; f = 150 mm; φ = 6°; v_w= 4.0 m min^{-1}; bead on plate; EN AW-6060; helium flow 30 L min^{-1}; helium flux 36 L min^{-1} cm^{-2}; conical nozzle diameter = 10.3 mm

The influence of the double coaxial nozzle system was also studied, as shown in figure 5.28. There are still pores present. But due to the reduced flow rate of helium it seems that they are smaller. Thus, they are hopefully less malignant in dynamical loading of the workpiece.

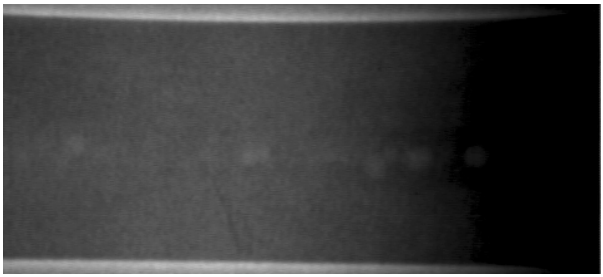

Figure 5.28: Surface-on x-ray transmission photograph of a fibre laser bead with the double coaxial nozzle system; P_{fibre} = 3 kW; f = 150 mm; φ = 6°; v_w= 3.0 m min^{-1}; bead on plate; EN AW-6060; inner nozzle: helium flow 9 L min^{-1}; helium flux 2.9 L min^{-1} cm^{-2}; outer nozzle for guiding gas: argon flow 10 L min^{-1}; argon flux 2.8 L min^{-1} cm^{-2}

The influence of those nozzles on porosity of BHLW seams was analogously examined using the system rebuilt in Japan. The x-ray photograph in figure 5.29 was taken with the lateral nozzle.

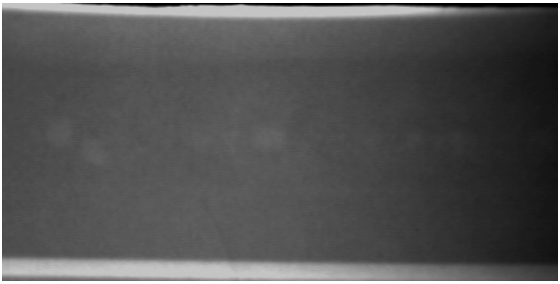

Figure 5.29: Surface-on x-ray transmission photograph of fibre laser bead with a lateral nozzle; P_{BHLW} = 3 kW + 3 kW; f = 150 mm; φ = 6°; v_w= 4.0 m min^{-1}; bead on plate; EN AW-6060; argon flow 30 L min^{-1}; argon flux 36 L min^{-1} cm^{-2}; lateral nozzle diameter = 8 mm; angle of inclination of lateral nozzle 45° to the surface normal of the specimen's surface; leading position of the nozzle

The conical nozzle was studied with argon as process gas, c.f. figure 5.30.

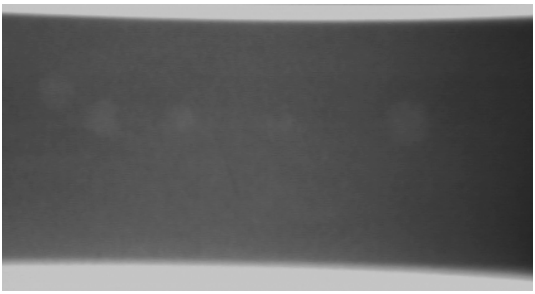

Figure 5.30: Surface-on x-ray transmission photograph of fibre laser bead with a coaxial conical nozzle; P_{BHLW} = 3 kW + 3 kW; f = 150 mm; φ = 6°; v_w= 4.0 m min^{-1}; bead on plate; EN AW-6060, argon flow 25 L min^{-1}; argon flux 30 L min^{-1} cm^{-2}; conical nozzle diameter = 10.3 mm

The double coaxial nozzle system showed **no** visible pores, as can be seen in figure 5.31.

Figure 5.31: Surface-on x-ray transmission photograph of BHLW bead with the double coaxial nozzle system; P_{BHLW} = 3 kW + 3 kW; f = 150 mm; φ = 6°; v_w= 3.0 m min^{-1}; bead on plate; EN AW-6060; inner nozzle: helium flow 9 L min^{-1}; helium flux 2.9 L min^{-1} cm^{-2}; outer nozzle for guiding gas: argon flow 10 L min^{-1}; argon flux 2.8 L min^{-1} cm^{-2}

Thereby, the non-invasiveness of the double coaxial nozzle system is successfully proven. This is a very important finding validating the empirical process model developed in section 4.2. The double coaxial nozzle system *together* with BHLW enables porosity-free seams in aluminium, which is a notable result with regards to DIN EN ISO 13919-2. This standard defines how to judge and categorize irregularities for electron and laser beam welding by assignment of quality groups. In this standard the quality group B is awarded to

seams of the highest quality, but even quality group B allows for porosity. A porosity-free quality group A was not standardized. This is most probably owed to the fact that for fusion welding of aluminium alloys porosity can *practically* not be avoided by all state-of-the-art technologies. BHLW *together* with the double coaxial nozzle system offers a solution, and standardization may be adjusted accordingly.

5.4 Economic and environmental case

The indiscriminate NO_x molecules used above to evaluate the merit of shielding gas coverage originate from NO-formation. European regulations currently permit 25 ppm of NO [98/24/EG 1998]. However, this exposure limit is under review and in 2003 the general directory recommended a value as low as 0.2 ppm. This means a reduction of 99.2% of NO-emissions [STEINHAGE 2005]. The nitric oxide is quite stable, however, reacts in the presence of humidity to nitric acid HNO_3. This causes irritations of mucous membranes, and long term exposure can lead to occupational diseases.

The double coaxial nozzle easily satisfies the proposed maximum exposure limit of 0.2 ppm. Hence, the double coaxial nozzle is a sustainable system. Alterations of this nozzle system could be employed in *autogenous* joining, cutting, and cladding where molecular nitrogen is naturally oxidized to NO. Should this maximum exposure limit of 0.2 ppm passed and enacted as law in the European member states autogenous industrial applications need to be fitted with inert or NO_x-suppressing gas nozzle systems. The double coaxial nozzle system is ready to take on this challenge.

The consumption of commodities such as process gases contribute to the running costs of a welding production. Flows of helium of up to 50 L min^{-1} are regularly reported in the literature [KATAYAMA 2000a & b; TSUKAMOTO 2004; LANDOLT BÖRNSTEIN 2004, p. 43-46]. The conical nozzle described above in figure 5.15 required a flux of helium of up to 34 L min^{-1} cm^{-2} although it had the best possible angle of inclination to prevent turbulence. The optical system used with a focal length of f = 150 mm permitted the design of a continuous contour of the nozzle and to keep the orifice of the conical nozzle rather small. Optical systems with a smaller f-number need wider orifices, thus, increasing the amount of gas consumed, as a change of inclination angle or a discontinuous reduction of the contour diameter would invariably lead to turbulence. The nozzle concept by

Caillibotte uses at least a flux of 6.63 L min^{-1} cm^{-2} although his data is purely theoretical and does not allow for comparison as his nozzle almost touches the workpiece [CAILLIBOTTE 2004]. For the 'integrated nozzle' no values of flows or fluxes are rendered in the literature [PETRING 2004]. The information provided for lateral nozzles by Seefeld does not allow inferring the flux [SEEFELD 2005]. The inert gas consumptions of these nozzles are assumed to be of the same order of magnitude.

The coaxial double nozzle consumes 2.9 L min^{-1} cm^{-2} of helium in the inner nozzle. The outer nozzle needs a flux of guiding gas as low as 2.8 L min^{-1} cm^{-2}. This guiding gas, i.e. a gas which has equal or higher density than ambient air, needs not necessarily be argon; air can be used for the same effect. In Nd:YAG laser welding the fusion zone is smaller than in BHLW. Thus, it might not be necessary even to use expensive argon.

The so-called Linde-process cannot economically produce helium by liquefying air. Technical helium is a 'fossil' commodity, as it is obtained from oil and gas deposits. Its availability will eventually cease if these deposits are exhausted. When using helium for the inner and argon for the outer nozzle a total reduction of gas flux of 60% is possible as compared to Caillibotte's nozzle. Calculating the consumption from the fluxes displayed in figures 5.11 to 5.14 shows that the savings of gas are impressive.

The cost savings can be estimated as helium is four times as expensive as argon in Europe. Average prices for helium are 40 € m^{-3} and for argon about 15 € m^{-3}. Hence, besides many environmental and occupational safety aspects the economical case for the double coaxial nozzle system is extremely persuasive.

6 Synergies of Bifocal Hybrid Laser Welding

6.1 Introduction to synergies in laser beam welding

This chapter gives an account of synergies in BHLW as compared to its constituent processes, i.e. keyhole welding by an Nd:YAG laser and CMW by an HPDL, in comparison to other state-of-the-art laser beam welding techniques. For a synergy two propositions have to be fulfilled:

1. Two or more processes interact such that their combined effect is greater than the *sum* of their individual effects.
2. The behaviour of the whole system is not predictable from the behaviour of its separate parts.

The first proposition requires *quantitative* analysis of each of the contributing processes as a prerequisite to demonstrate a synergy according to this definition. Although individual processes *act in* the same process zone, as e.g. in laser augmented MIG welding, they do not nonetheless not synergistically interact if their superpositioned effect *equals* the sum of their respective contributions. The second proposition calls for *theoretical* analysis, as one can only speak of a synergy if experimental results well surpass what could be induced and expected form experimental data already known. Process or system technology advantages of BHLW are not treated in this chapter, because mere advantages do not satisfy these propositions to be termed synergy. These advantages, which are especially important for production engineering, are dealt with in the next chapter.

6.2 Increase of welding efficiency

Superior process efficiency manifests itself in an increase of the correlated parameters, e.g. welding speed or penetration depth. The synergies of BHLW are demonstrated by presentation of direct measurements of the energy input efficiency η_{EI} and melting efficiency η_M. In the literature there are definitions of 'process efficiency' and 'melting efficiency' in terms of the power of the laser employed [LANDOLT-BÖRNSTEIN 2004, p.62; HÜGEL 1992, p. 245]. Others resort to the energies released and introduce the 'energy transfer efficiency' as a further figure of merit [FUERSCHBACH 1996]. In this dissertation the following terminology and definitions are adopted: The energy input efficiency η_{EI} is the

ratio of the radiation energy emitted by the laser and the energy released as heat within the workpiece. The melting efficiency η_M is the ratio of the energy released as heat within the workpiece and the amount of energy for melting a part of the workpiece, i.e. the total enthalpy of melting to create the seam.

It should be noted that this definition of melting efficiency is different form that encountered in the literature [LANDOLT-BÖRNSTEIN 2004]. The definition of melting efficiency adopted in this dissertation is necessary to establish the results presented in this paragraph. Although it is potentially confusing to reuse the term melting efficiency in the context of this dissertation, this could not be avoided for lack of an alternative apt term. This dissertation is free to adopt any terminology as it pleases.To measure these figures of merit, η_{EI} and η_M, a new experiment was designed. The power of the laser and the energy absorbed within the workpiece were determined by a calorimetric measurement. The experiment was conducted in a calorimeter, which was designed like a chamber and was filled with process gas during the experiment. For the measurement the reference alloy EN AW-6060 and argon as process gas was used. The welding speed corresponded to 4 m min^{-1}.

For the HPDL η_{EI} was experimentally determined to be 35.6% with a standard deviation of 2.5%. This value of η_{EI} is higher as the absorptivity of aluminium, which is 0.13 for the centre wavelengths of the HPDL, would seem to allow for. The Nd:YAG laser emitting 3 kW gave a mean energy per unit length of the seams of 262.5 Joule cm^{-1} with a standard deviation of 32.9 J cm^{-1}. This corresponds to a standard error in the mean of 14.7%. For the 3 kW-HPDL the mean energy per unit length is 129.8 Joule cm^{-1} with a standard deviation of 32.9 Joule cm^{-1}. For BHLW at 6 kW, i.e. the Nd:YAG and the HPDL are equally emitting their maximum output power of 3 kW, the experimental value is 389.8 Joule cm^{-1} with a standard deviation of 26.3 Joule cm^{-1}.

For the Nd:YAG laser η_{EI} is 65% with a standard deviation of 9.2%. This greatly surpasses the absorbtivity of aluminium, which is 0.07 for the wavelength of the Nd:YAG laser. Multiple reflections on the wall within the keyhole can account for this result. The *theoretical* combination (i.e. purely mathematical by calculating the weighted arithmetic mean) of these figures of η_{EI} renders a nominal value for η_{EI} of 50.3% for BHLW. It should be noted that the *measured* value of η_{EI} for BHLW is 48% with a standard deviation of 1.99% and a standard error in the mean of 0.9%. The theoretical value of η_{EI} agrees with the measured

value within the limits of experimental error. These measurements show that for η_{El} no synergy could be found according to proposition 1 in paragraph 6.1.

The melting efficiency η_M of Nd:YAG laser welding is 12.6% with a standard deviation of 1.3%. For the HPDL it is 3.5% with a standard deviation of 0.7%. The *mathematical* combination (again by calculating the weighted arithmetic mean) of those values suggests a *theoretically* expected value for the hybrid process of both lasers of 8.05%. In the experiment η_M of BHLW was found to be 15.2% with a notably small standard deviation of 0.048%. This corresponds *nearly* to a **doubling** of melting or process efficiency. This clearly indicates a true synergy of BHLW, because the beam quality of the HPDL is up to two orders of magnitude inferior to that of the Nd:YAG laser. Additionally, this elucidates the *nature* of the synergy as well. The HPDL does not affect the energy input of the Nd:YAG laser. Instead, the *creation* of melt is synergistically enhanced.

The *doubling* of the melting efficiency is a very significant result for industrial production. This can be proven by virtue of the speeds of welding: Unsurprisingly, the speed of welding still enabling root fusion rises from the benchmark speed set by the Nd:YAG laser of around $2 \div 3$ m min^{-1} to 5.5 m min^{-1} in BHLW, i.e. the speed of welding is nearly doubled. This is in agreement with this measurement of melting efficiency. As described above, the melting efficiency nearly doubled as well. The melting efficiency η_M is connected to the Rykalin number *Ry*

The melting efficiency η_M is connected to the Rykalin number *Ry* according the Fuerschbach's definition: [FUERSCHBACH 1996]:

$$Ry = \frac{E_a \cdot v_w}{\alpha^2 \Delta H_m} \qquad \text{(Equation 6.1)}$$

E_a is the energy absorbed by the workpiece, α is the thermal diffusivity of the workpiece at the liquidus temperature, ΔH_m the enthalpy of melting. Although *Ry* predicts a rise of melting efficiency upon increasing v_w, the doubling of η_M observed for the BHLW system must be a synergetic effect.

This result can also be more easily appreciated by an experiment of mind: The maximum welding speed of a 3-kW Nd:YAG laser to guarantee root fusion in the reference specimen laser is $2 \div 3$ m min^{-1}. If one wanted to approximately double this welding speed, an Nd:YAG laser of 6 kW output power would be

necessary. However, in the case of BHLW just an HPDL of 3 kW output power was used. The HPDL emitting 3 kW could *not* create a proper weld in the reference specimen, since the energy input efficiency and melting efficiency of this HPDL are much lower than those of the Nd:YAG laser. However, teaming up those two laser sources in BHLW enables a synergistic result, which could not be predicted from combining those two lasers in *mind*. This experiment of mind will be explained more carefully in the following.

The assessment of welding techniques for industrial applications is normally centred on welding speed. An increase of welding speed allows reducing cycle times. Reduced cycle times translate to cost reductions per unit by improved productivity. As explained in paragraph 4.1 CMW by the HPDL could not create stable welds in aluminium. Beyond a certain threshold in HPDL welding an increase of HPDL power does not lead to deeper penetration but only to a broadening of the seam width (c.f. figure 6.1).

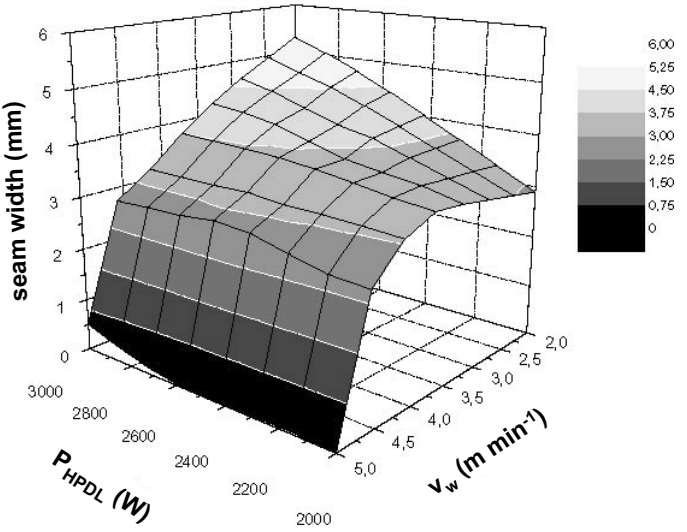

Figure 6.1: Width of the weld seam versus velocity of welding and power of the HPDL

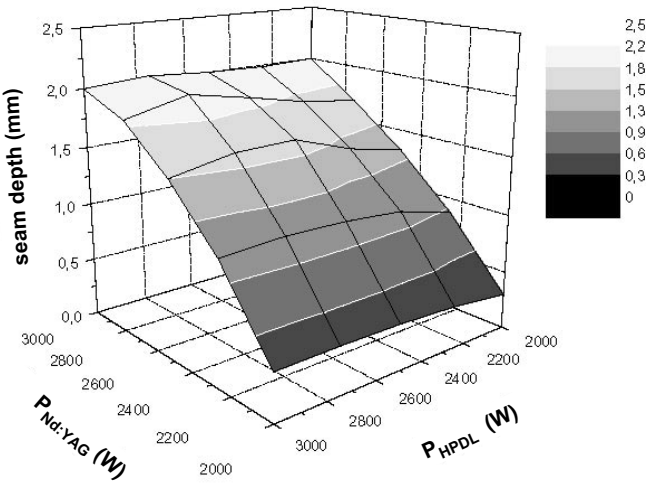

Figure 6.2: Depth of the weld seam versus laser powers in BHLW

Welding solely by an Nd:YAG laser enables a maximum speed for the reference specimen of approximately 2 to about 3 m min^{-1}. However, the quality of such welds is inferior, and root fusion cannot be guaranteed due to variations of the welding depth. For welding at a constant velocity of 4 m min^{-1} the variation of depth dependent on the individual powers of the two laser sources is shown in figure 6.2.

The maximum speed for robust welding without solidification cracking is v_w = 5.5 m min^{-1}, as is shown in detail in paragraph 8.2. Such seams exhibit robust root fusion without variation of depth and no porosity. The weld easily satisfies all requirements of quality group B as standardized in DIN EN ISO 13919-2. 6 kW-BHLW allows for more than doubling of the speed of welding although the 3 kW-HPDL alone could not generate satisfactory welds. The BPP of the HPDL is by *one* order of magnitude inferior to that of the 3 kW-Nd:YAG laser employed in BHLW. This increase of welding speed could not be extrapolated and therefore constitutes a true synergy of BHLW.

BHLW was put to the test. An industrial application for paper machinery necessitated a weld in thick sheets to be liquid proof. No established laser welding technology could be found by the paper machinery company satisfying the requirements as to penetration depth and seam quality. To solve this problem the following alloys were considered in a study: EN AW-5083, EN AW-5754,

EN AW-7020, and EN AW-6082. BHLW showed increased penetration depth as compared to Nd:YAG laser welding and produced the required quality. In figure 6.3 a characteristic weld is shown.

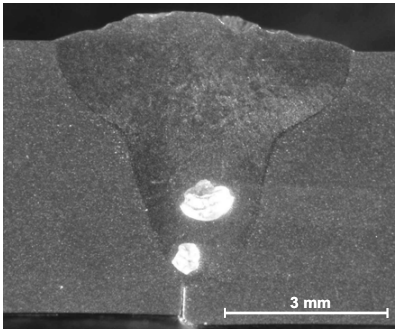

Figure 6.3: P_{BHLW} *= 3 kW + 3 kW; f = 150 mm; φ = 20°; argon 25 L* min^{-1}*;* v_w*= 2.0 m* min^{-1}*;* v_f*= 2.0 m* min^{-1}*; butt joint; EN AW-6082;* ***conical*** *gas nozzle*

6.3 Reduction of porosity

Porosity in aluminium is rife in classical arc welding as well as laser welding. The analytical treatment of porosity is ambiguous. The *magnitude* of porosity x_p is defined as:

$$x_p = \frac{A_p}{A} \qquad \text{(Equation 6.1)}$$

Here A_p is the cross-sectional area of the pores and A the cross-sectional area of the weld seam. This ratio does not provide any information on number and average cross-sectional area of the pores. Instead, in many papers the *number* of pores per unit length is counted. The failure risk in dynamical loading of workpieces that contain pores depends on the distribution of sizes as well as the position of those pores within the fusion zone. Pores close to free surfaces or interfaces of the base material are assumed to be especially detrimental to the properties of the welded piece in dynamical loading. These pores act as kerfs promoting failure in dynamical loading. Additionally, the average size and the distribution of sizes of the pores provide important information on the origin of these pores. Such information is hard to convey by a representation as a graph or a chart. Thus, typical *photographs* of porosity are displayed in this dissertation.

Photograph representing the *best* source of evaluation and judgement for the reader's eye.

Macroporosity is well reported in fusion welding of aluminium alloys. Macroporosity comprises all pores that can be resolved by the naked eye, i.e. as small as 0.1 mm in diameter, because the resolution limit of the human eye is approximately a tenth of a millimetre. Macroporosity in extruded EN AW-6060 has the following major causes:

1. The extrusion process contaminates the base metal and the surfaces. Upon fusion welding *contamination* pores arise.

2. The solubility of hydrogen in aluminium melts is 6.5 10^{-3} ml g^{-1}. The solubility drops sharply to 0.34 10^{-3} ml g^{-1} upon solidification: *Hydrogen* pores precipitate in the fusion zone close to free surfaces.

3. The nozzle systems to supply process gas promote entrapment of gas bubbles during keyhole welding. These artefacts will subsequently be called *process* pores.

Contamination pores are randomly distributed throughout the base metal, and should be rather small for quality controlled aluminium profiles. Hydrogen can enter the fusion zone via free surfaces as it is a constituent of the ambient atmosphere. Proper shielding of these surfaces by hydrogen free process gas can counteract formation of process pores. Contaminations on the edges of the workpiece with organic material can release hydrogen upon sublimation during welding. Figure 6.4 shows a nest of pores located in the vicinity of the former dividing edge and close to the lower free surface at the bottom, because the root was not protected by shielding gas. Thorough cleaning and degreasing can prevent these pores.

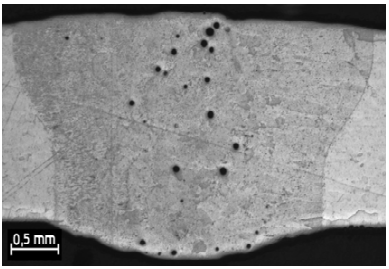

Figure 6.4: Hydrogen pores; P_{BHLW} = 3 kW + 3 kW; f = 150 mm; φ = 20°; argon flow 25 L min^{-1}; v_w= 3.75 m min^{-1}; butt joint; EN AW-6060

Process pores in aluminium are caused by a straw effect as described in the gas entrapment caveat in section 4.1.3. The resultant entrapments within the solidifying train of the melt pool form characteristically extended pores, as can be seen in figure 6.5.

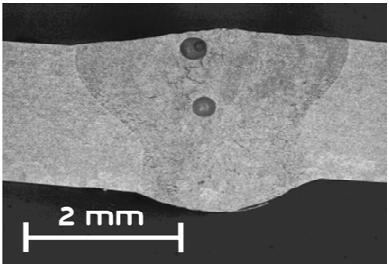

Figure 6.5: Process pores; P_{BHLW} = 3 kW + 3 kW; f = 150 mm; φ = 20°; argon flow 25 L min^{-1}; v_w= 4.0 m min^{-1}; butt joint; EN AW-6060

The parameters in laser augmented MIG-Hybrid-Welding are affected by a change in gas composition, because the voltage has to be adjusted in order to ionize the *specific* gases used. Laser beam propagation is independent of process gas, and thereby the variables of BHLW welding are not affected by a change in gas composition. The individual influence of different gas mixtures on porosity can be studied ideally in a laser welding process. For EN AW-6060 porosity is significantly reduced in BHLW as compared to Nd:YAG laser welding irrespective of gas. In figure 6.6 the porosity is shown for different gas mixtures.

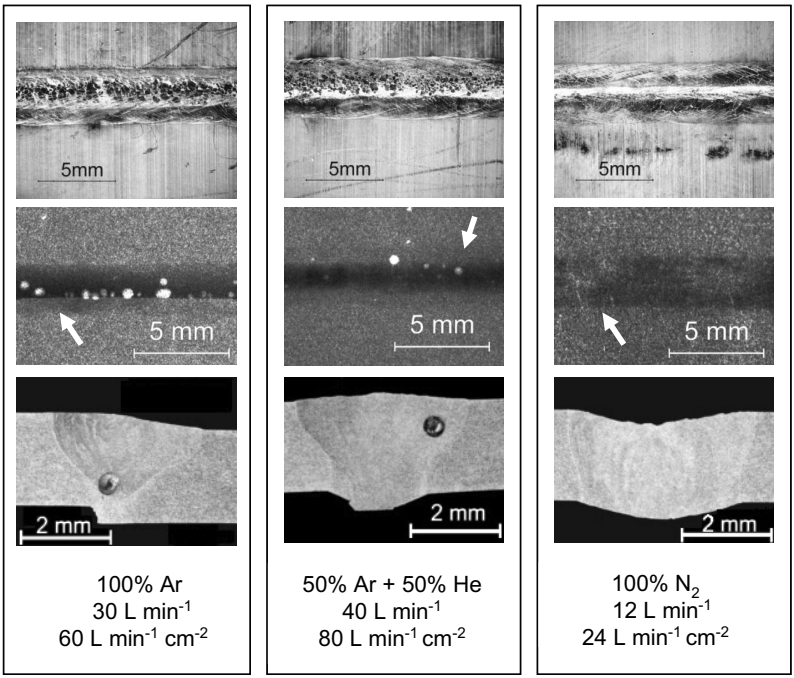

Figure 6.6: Dependence of porosity on process gas mixtures; top: surface photograph, middle: x-ray transmission photograph; bottom: cross-section macrograph; P_{BHLW} = 3 kW + 3 kW; f = 150 mm; φ = 20°; v_w= 3.0 m min^{-1}; v_f = 1.7 m min^{-1}, butt joint; EN AW-6060; filler Al4047 A; single conical nozzle was used, it should be noted that spots of soot stained the overbead in the surface photograph, those spots are do not affect the bead quality; note also the filler wire enters the melt pool at an angle with regard to the direction of welding; the arrows indicate filler wire position

The porosity clearly correlates to the filler wire supply position in this case. The sharp, dark rim where the wire was fed into the melt pool is a predominant site of pore formation. The pores in the macrographs of figure 6.6 are due to all the causes detailed above. The wire is a potential source of contamination inducing contamination pores. The wire was supplied for the specimens in figure 6.6 at an angle of 50° to the surface normal, i.e. not an acute angle alongside the beam axis, which leads to a *discontinuous* transfer of filler wire. The design and filler

wire transfer properties of BHLW taking heed of these findings are described in paragraph 8.2. BHLW seams show no process porosity at all apart from a few remnant hydrogen pores in paragraph 8.2. The positive effect of an admixture of helium has been reported for classical arc welding [FARWER 1996; DILTHEY 2007] and could be reproduced for BHLW within this dissertation. Seams completely free of process porosity could be produced with the double coaxial nozzle system described in chapter 5.

It should be noted that the standard gas shielding nozzle was not used for the welds displayed in figure 6.6. The positive effect of nitrogen on porosity obviation in BHLW, which is obvious from figure 6.6, would otherwise, i.e. by virtue of the coaxial double nozzles system, not have been discernable. This result requires careful discussion: Katayama demonstrated that welding *steels* with an Nd:YAG laser with nitrogen as process gas leads to porosity free welds. Others reported similar findings [BACHHOFER 1997; KATAYAMA 2000b; ZÄH & TRAUTMANN 2004b]. The welding of *aluminium* with an Nd:YAG laser using nitrogen as process gas did not yield porosity free welds in Katayama's investigations. Figure 6.6 shows that the bead is free of porosity if it is welded with BHLW and using nitrogen as process gas. Katayama showed that the suppression of porosity in *steels* was possible by an increase of welding speed with He/Ar-mixtures acting as process gas. Conversely, suppression could be shown for lower welding speeds and using N_2 as process gas. The equivoque result was achieved for *aluminium* with BHLW, as described above.

From the results of the Japanese researchers it can be deduced that the key to porosity free welds lies in an increase of total laser power of BHLW while keeping the overall intensities low. If in the desired process window for BHLW an increase in energy input per unit length can be achieved, the nitrogen, which reacts to form AlN in an overall exothermal reaction (c.f. section 4.1.4), could be replaced by inert gases. The best way to realize this objective is the deployment of an HPDL with a higher nominal output power than the Nd:YAG laser in the specific setup of BHLW. Another possibility is the use of the double coaxial nozzle system.

AlN degrades the mechanical loading properties of a weld and should therefore be carefully evaluated for applications where the mechanical properties of the welded structures need to meet highest standards, e.g. most aeronautic applications. Hence, the use of nitrogen is problematic. KATAYAMA lately showed that AlN did form when welding aluminium with a CO_2 laser. AlN also

formed when aluminium was welded with a fibre laser. However, with an Nd:YAG laser *no* AlN-formation in aluminium seams could be found by [KATAYAMA 2007a].

These results require careful interpretation: The formation of AlN is exothermal, as shown in the energy balance in section 4.1.2. The *activation* energy for this exothermal reaction, however, needs to be provided by the irradiated laser energy released as heat. If the heat flow is high enough to create temperatures within the workpiece above a threshold temperature, the AlN-formation reaction is initiated. In figure 1.1 three laser sources, namely fibre laser, CO_2 laser, and Nd:YAG laser and their system parameters are shown. A comparison of the intensities attainable by those lasers reveals that the intensity of the Nd:YAG laser is by one order of magnitude smaller than those of the fibre and CO_2 laser. The intensities of the fibre and CO_2 laser are of the same order of magnitude. It can be concluded that the temperature generated on the walls of the keyhole by a conventional Nd:YAG laser is not high enough to initiate AlN-formation. The intensities arising in BHLW are dominated by the Nd:YAG laser. The contribution of the HPDL to the intensity in the focal spot is negligible, as can be easily seen in figure 4.23. Hence, the formation of process porosity can be avoided by the usage of nitrogen as process gas in BHLW if one is aware of the risk of embrittlement by AlN-formation. A decision as to which process gas is permissible depends on economic considerations, health and safety requirements, and other constraints of the application.

6.4 Superior surface quality

The mechanical properties of the weld are decisive for most applications in naval, aeronautic, or plant construction. In automotive applications and specifically chassis joining resistance spot welding (RSW) was dominant over the last decades. RSW induces distortion at the point of contact. RSW inherently creates an overlap joint and requires the top and the bottom side to be accessible for the RSW clamp to reach the point of contact. Hence, these welds are located within the chassis and required flanges.

The Nd:YAG laser was employed in automotive production to weld the roof to the car body. It replaced a roll weld seam where the flanges were overlapped in such a way as to stick out to the outside, c.f. figure 10.1. Such a joint geometry cannot be welded with RSW, as RSW creates punctual joints, whereas Nd:YAG

laser welding enables a continuous seam. The cross-sectional area of welded joint is larger for a continuous laser seam as compared to a resistance spot weld. Yet, an Nd:YAG laser seam, which was welded from the outer side of the chassis, exhibited an inferior surface quality. It had to be covered by a plastic overlay. Laser brazing by an HPDL allowed closing the roof seam of the chassis without having to resort to a disguising plastic cover, because the brazed surface showed a high surface quality. This technique championed by Volkswagen necessitated support by resistance spot welds located inside of the chassis to make up for the lower strength of the brazed seam as compared to an Nd:YAG laser deep penetration weld.

So why was the laser brazed seam introduced in the first place? Nowadays, aesthetic welding is an issue, as e.g. modern exterior automotive design is more than ever determined by customer expectations rather than the feasibilities of joining technologies. This demands welds that can be processed without costly reworking, e.g. for immediate lacquering. For lacquering weld surfaces should also be smooth and free of spatter. For the following experiments the amount of Al 4047 A was normalized with respect to the welding speed. The surface roughness R_t is defined according to DIN EN ISO 4287. The roughness of beads solely welded with an Nd:YAG laser is R_t= 85.0 µm, c.f. figure 6.7. The surface roughness topography was determined transverse to the direction of welding. Generally, the addition of filler wire decreases surface roughness, as can be seen in figure 6.8.

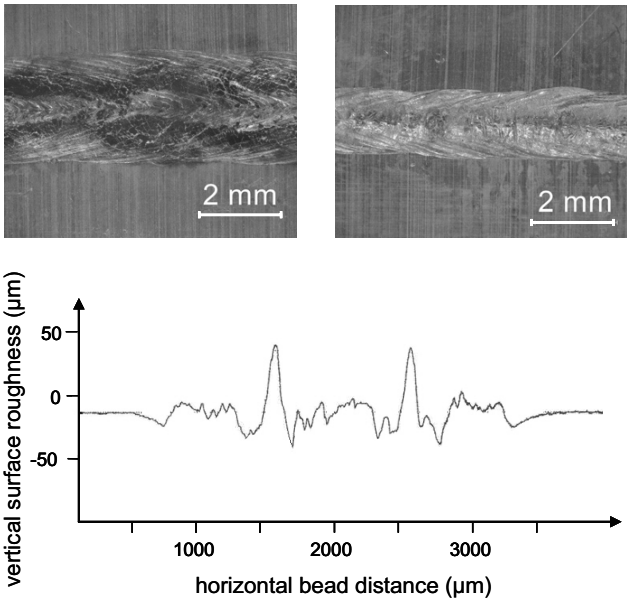

Figure 6.7: *Nd:YAG laser bead; top left: without filler wire: surface photograph; top right: root face photography ; bottom: surface roughness graph; R_t= 85 µm; P_{YAG} = 3 kW; f = 150 mm; φ = 20°; argon flow 25 L min^{-1}; v_w= 4.5 m min^{-1}; butt joint; EN AW-6060*

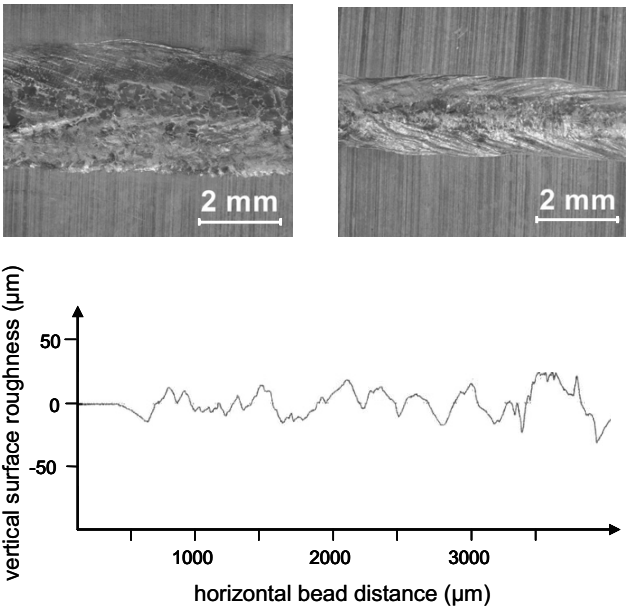

Figure 6.8: Nd:YAG laser bead with filler wire; top left: surface photograph; top right: root face; bottom: surface roughness graph; R_t= 58.4 µm; $P_{Nd:YAG}$ = 3 kW; f = 150 mm; φ = 20°; argon flow 25 L min^{-1}; v_w= 4.0 m min^{-1}; v_f= 3 m min^{-1}; butt joint; EN AW-6060 (AlMgSi0.5) T66; filler Al4047 A (SG-AlSi12); $Ø_f$ = 1 mm

Although CMW welding with the HPDL could not create a stable coalescence of the workpieces, this process sets the benchmark for surface roughness. Bead on plate welds done by the HPDL exhibited R_t = 9.6 µm in the region of the horizontal bead distance between approximately 1000 to 3500 µm in figure 6.9.

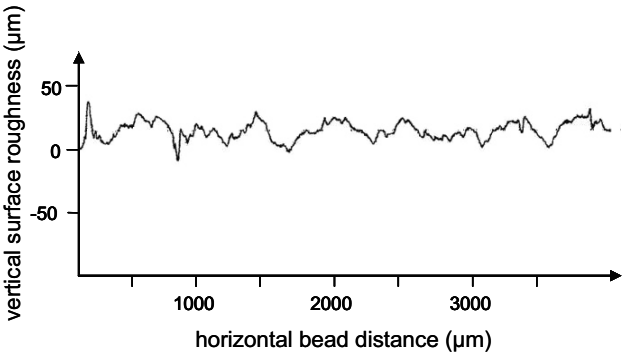

Figure 6.9: HPDL graph of surface roughness of a bead on plate weld; R_t= 9.6 µm; P_{HPDL} = 3 kW; f = 150 mm; φ = 20°; argon flow 25 L min^{-1}; v_w= 0.5 m min^{-1}; v_f= 0 m min^{-1}; bead on plate; EN AW-6060 (AlMgSi0.5) T66; without filler wire

In figure 6.10 a butt joints with R_t= 19.3 µm is shown. The increase of roughness is due to the oxide layer on the abutted edges. Hence, there is a spike in roughness in the middle of the weld at 2000 µm on the x-axis. The surface oxide layer on the abutted edges could not be dispersed by HPDL welding. This layer appears dark in the surface photograph in figure 6.10.

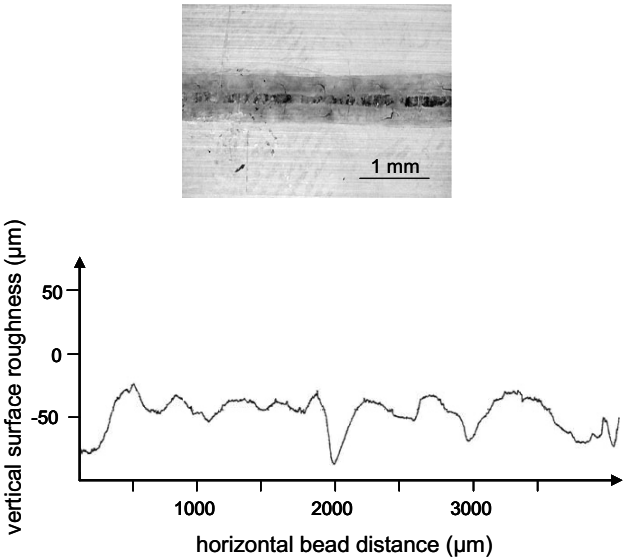

Figure 6.10: Top: surface photograph; bottom: HPDL surface roughness graph of a butt joint; R_t= 19.3 µm; P_{HPDL} = 3 kW; f = 150 mm; φ = 20°; argon flow 25 L min^{-1}; v_w= 0.5 m min^{-1}; v_f = 0 m min^{-1}; butt joint; EN AW-6060 (AlMgSi0.5) T66; without filler wire

The BHLW butt weld had a surface roughness as small as R_t= 6.3 µm in most areas in figure 6.11. BHLW obviously makes full use of the sedation of the weld pool surface by the convectional fluid flow within the train of the melt pool subsequent to the keyhole. This constitutes a synergy of Nd:YAG laser and HPDL. Figure 6.11 shows a spike at around 3500 µm pointing downwards on the side where the filler wire was fed into the melt pool and a spike upwards around 2000 µm where the Nd:YAG keyhole went through.

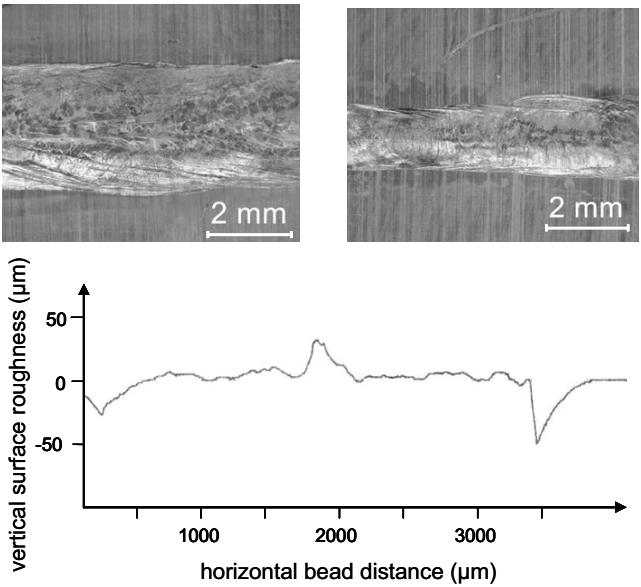

Figure 6.11: HPDL bead; top left: surface photograph; top right: root face photograph; bottom: surface roughness graph; R_t= 6.3 µm neglecting middle spike and underfilling at the edges; P_{BHLW} = 3 kW+ 3kW; f = 150 mm; φ = 20°; argon flow 25 L min^{-1}; v_w= 5.5 m min^{-1}; v_f= 5.5 m min^{-1}; butt joint; EN AW-6060 (AlMgSi0.5) T66; filler Al4047 A (SG-AlSi12); $Ø_f$ = 1 mm

These spikes can be overcome by an HPDL of higher nominal output power, i.e. an HPDL that can increase the seam energy per unit length. These spikes were absent at a welding speed of 3 m min^{-1}. The reference speed of welding of v_w = 5.5 m min^{-1} is set in this dissertation to guarantee root fusion of the reference specimen of 2 mm thickness. When welding at 5.5 m min^{-1} as compared to 3 m min^{-1} the heat energy generated per unit length by a 3 kW-HPDL has to melt the wire at the same feed rate. Hence, not enough energy is available for perfect smoothening of the surface in the train of the weld pool. Moreover, the experimental optic setup did not allow focusing the HPDL on the surface, as its focal plane of the HPDL lies 1 mm above the focal plane of the Nd:YAG laser, which is actually focused on the surface; c.f. paragraph 4.1 and the constraints of the experimental optic setup detailed in paragraph 8.1. It is

obvious that a beam shape of the HPDL, which facilitates further CMW of the surface behind the keyhole, could easily remove those spikes. These demands can be satisfied by the prototype optic presented in paragraph 8.1. To verify this claim welds were assayed for roughness welded at a speed of 3 m min^{-1} with less filler than customary used for previous welds. Those welds showed a surface roughness of R_t = 6.8 µm over the *whole* of the weld surface, i.e. the spikes had been smoothed out by the higher energy per unit area. Hence, it can be safely stated that BHLW can achieve welds that feature a surface quality comparable to a brazed seam, which were brazed with an HPDL alone.

7 Advantages of Bifocal Hybrid Laser Welding

In this chapter the advantages of BHLW are outlined and discriminated against the synergies described in the previous chapter. This distinction between synergies and advantages is important to fully comprehend their nature. Any improvement might be termed as an advantage however small it might be. But only those advantages where the whole is more than the sum of its constituent parts should deservedly be called a synergy. This is specifically important as it seems common place to designate mere advantages of various welding techniques as synergies. The advantages of BHLW do not fall short of the synergies as far as their improvements of aluminium welding are concerned.

7.1 Robustness

In BHLW the increase of process robustness is tangible if the instabilities induced by the process gas supply system are excluded, since the gas is invasive with regards to the melt pool, as shown in chapter 4. A chamber, which was thoroughly rinsed and was therefore exclusively filled with process gas, was used for welding experiments with different laser sources. Such a chamber excludes all possible external sources of disturbance and allows studying the robustness of the welding technique *for itself*.

The beads in the following figures 7.1 to 7.3 were all made in such a sealed gas chamber. HPDL and Nd:YAG laser welding are each considered on their own. In figure 7.3 the result of their combination in BHLW is shown for comparison.

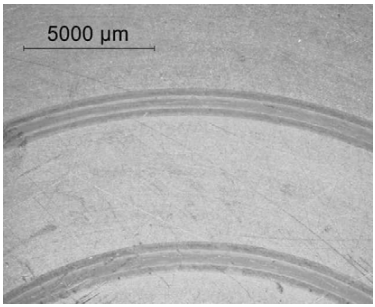

Figure 7.1: Top surface photograph of HPDL welding; seam is bent because the gas chamber did not permit a linear seam; chamber was filled with argon; P_{HPDL} = 3 kW; v_w = 4 m min^{-1}; bead on plate; EN AW-6060; angle φ = 6°

The HPDL does not penetrate the specimen to a great depth. The surface was melted by CMW, as can be seen in figure 7.1.

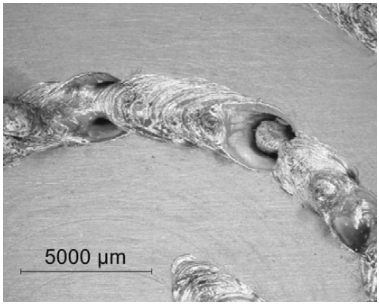

Figure 7.2: Top surface photograph of Nd:YAG laser welding; seam is bent because the gas chamber did not permit a linear seam; chamber was filled with argon; $P_{Nd:YAG}$ = 3 kW; v_w = 4 m min^{-1}; bead on plate; EN AW-6060; angle φ = 6°

The seam generated by the Nd:YAG laser is a deep penetration weld by virtue of a keyhole. The instabilities in Nd:YAG laser welding are obvious. Instabilities arose although a gas supply system was absent and the seam was produced in the gas chamber.

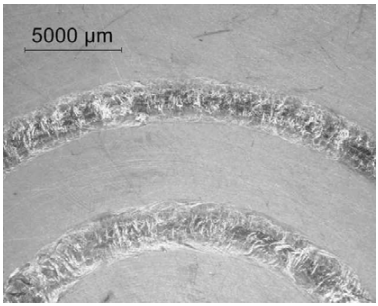

Figure 7.3: Top surface photograph of BHLW; seam is bent because the gas chamber did not permit a linear seam; chamber was filled with argon; P_{BHLW} = 3 kW + 3 kW; v_w = 9 m min^{-1}; bead on plate; EN AW-6060; angle φ = 6°

BHLW seams were produced at a normalized energy per unit length. The speed of welding had to be doubled for normalization, because the two lasers used emitted each 3 kW. As can be clearly seen in figure 7.3, the seam is free of instabilities proving the robustness of BHLW in *itself*.

It should be noted that in some cases it is a major challenge to guarantee process robustness for comparably *low* speeds of welding. Even thin sheets can be welded to high seam quality by accordingly reducing the power of the HPDL and the Nd:YAG laser. For thin sheets the speed of welding with BHLW is *low* as compared to Nd:YAG laser welding. This is desirable as high speeds necessitate high accelerations of the kinematical systems moving the workpiece or the optic system. These motions lead to inaccuracies and strain the kinematics. A high welding speed inhibits the segmentation of seams or reorientation of the welding direction. For thin sheet welding with an Nd:YAG laser the power of the laser cannot be lowered beneath a certain threshold if deep penetration by keyhole welding is to be sustained. For BHLW this threshold can be lowered since the material is melted by the HPDL. The Nd:YAG laser subsequently needs less energy to induce vaporization, which is a prerequisite for keyhole welding. This demonstrates the robustness of BHLW.

7.2 Reduction of relative crack length

Aluminium alloys exhibit a propensity to cracking in fusion welding depending on the distribution of their alloying contents. The details of cracking and cracking susceptibility are dealt with in section 8.2.1. To *completely* counteract cracks in welds of the reference alloy EN AW-6060 filler material cannot be forgone. A standardized experiment needs to be conducted to assess the merits of a given laser welding technology to reduce the propensity to cracking. The experiment must be designed such that external influences are excluded from affecting the result. This would otherwise lead to systematic errors. The experimental chamber employed in the preceding paragraph 7.1 to generate the results displayed in figures 7.1 to 7.3 was used again. The speed of welding was kept constant at 4 m min^{-1}. The macrographs for Nd:YAG laser and BHLW are shown in figure 7.4.

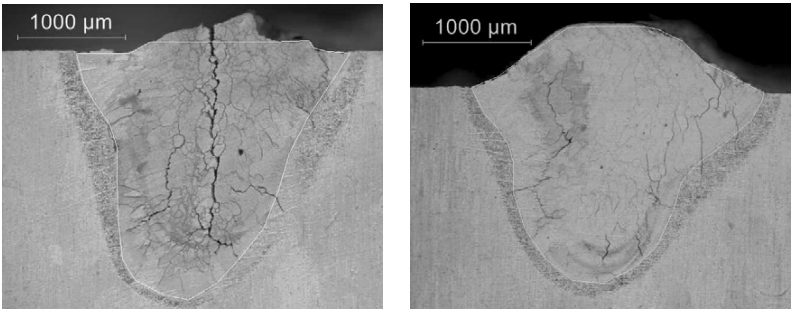

Figure 7.4: Cross-section macrograph for v_w = 4 m min^{-1}; left: Nd:YAG laser welding; $P_{Nd:YAG}$ = 3 kW; right: BHLW; P_{BHLW} = 3 kW + 3 kW; chamber was filled with argon; bead on plate; EN AW-6060; angle φ = 6°

As can be clearly seen by the naked eye the relative crack lengths are greatly reduced in BHLW in comparison to Nd:YAG laser welding. The mean energy per unit length is doubled in BHLW compared to Nd:YAG laser welding for the parameters in figure 7.4. BHLW exhibits an in-line “post-heating” effect, which is very difficult to achieve by other state-of-the-art laser welding technologies. The penetration depth of the HPDL is negligible as compared to the penetration of the Nd:YAG laser displayed in figure 7.1. The HPDL does not act at depth, but rather at the surface. The Nd:YAG laser induced a deep reaching crack, as can be seen left in figure 7.4. In BHLW the HPDL obviated this prominent crack,

c.f. right macrograph of figure 7.4. Additionally, the lengths and breadths of the cracks are mitigated and the absolute number of cracks is reduced. In figure 7.5 magnifications of the macrographs of figure 7.4 are shown and typical breadths of cracks are measured. For this impartial, random selection of measurement point the absolute length L was found to be 23.7 µm in Nd:YAG laser welding and approximately 8 µm in BHLW.

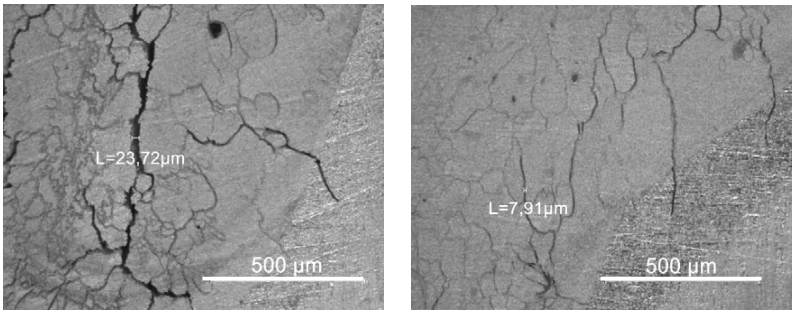

Figure 7.5: Magnification of cross-section macrographs of figure 7.4 for v_w = 4 m min^{-1}; left: Nd:YAG laser welding, $P_{Nd:YAG}$ = 3 kW; right: BHLW; P_{BHLW} = 3 kW + 3 kW; chamber was filled with argon; bead on plate; EN AW-6060; angle φ = 6°

The *mere* reduction of relative crack lengths in BHLW as compared to Nd:YAG laser welding is important for production engineering, since one can suspect that the amount of filler material necessary to *completely* prevent cracking is reduced in BHLW as compared to classical Nd:YAG laser welding. In a laser production process the filler wire needs to be melted on the expense of the laser's capacity to melt the material. Thereby the necessity to dilute more filler material per unit time decreases the process efficiency of the *welding* process, since in laser welding it is the amount of base material melted which contributes to the process efficiency and not the amount of molten filler material as in classical GMAW processes. The problems encountered in the system technology to feed filler to the melt pool and how to forecast the filler supply rate for a given welding process is dealt with in paragraph 8.2.

The final upshot of this section is the reduction of crack propensity in BHLW as compared to Nd:YAG laser welding, which allows decreasing the dilution ratio. Dilution is dealt with in paragraph 8.2.

7.3 Prevention of stop crater cracks

In most investigations in the literature researchers seemed to have concentrated only on the properties of the bead. However, every seam exhibits a starting and a stop crater, which are much more prone to solidification cracking than the seam itself, as the temperature gradients are steepest at the start and the end point of the seam. This is an often overlooked issue for the application of laser beam welding in production, as these craters represent singularities with respect to the weld. The onset of the bead is generally well behaved, as it is formed by successive solidification fronts. The end point, however, is correlated to the shape of the weld pool. The end part develops when the laser stops moving through the plate. The depletion of material together with the thermal stresses induced by the removal of the heat source do rarely allow relaxing those stresses. Hence, solidification cracking is a common phenomenon even in materials that exhibit otherwise little susceptibility to solidification cracking. Typical cracks are widely reported in the literature [MATHERS 2002, p. 27]. Typical stop crater cracks in the reference alloy are shown in figure 7.6.

Solidification cracking in the stop crater is a major challenge for state-of-the-art aluminium welding technologies. In most cases these cracks are a notorious point for failure of an otherwise well behaved seam [DILTHEY 2005, p. 234]. Otto reports, "a crack on the face and the root side of the workpiece developed despite of measures for process optimization, such as filler wire supply and usage of forming gas" [OTTO 1997, p. 81]. This result was for a seam in EN AW-6082, which is comparable to the reference alloy EN AW-6060.

Other methods described in the literature to overcome stop crater cracks are defocusing or ramping down the laser power in order to avoid this transient effect. Yet, these measures – which are only moderately successful anyway to reduce stop crater cracks - inhibit the supply of filler wire, which is indispensable for alloys with high susceptibility to solidification cracking due to their chemical composition. If the optical system is defocused, the filler wire tip formerly adjusted to feed wire to the focal plane of the laser is shifted accordingly preventing proper supply of wire to the focal spot. A ramp of laser power does not only reduce the magnitude of the thermal stresses but also the power available for melting the wire. Yet, filler wire supply to the stop crater is particularly indispensable, since otherwise cracks originate from those craters.

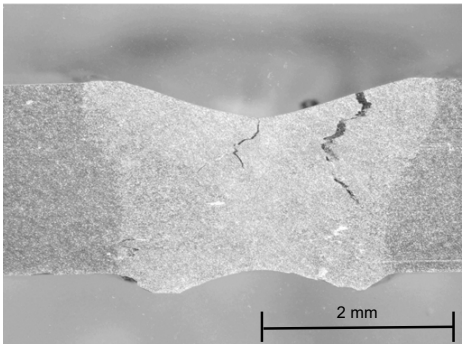

Figure 7.6: Solidification cracking in a stop crater of an Nd:YAG laser weld; butt joint; EN AW-6060 (AlMgSi0.5) T66; $P_{Nd:YAG}$ = 3 kW; angle φ =20°; argon flow 25 L min^{-1}; v_w = 2.5 m min^{-1}

BHLW can make full use of the possibility to independently trigger the two laser sources. Twin- and multiple spot laser welding techniques normally employ only one laser source. The beams in multiple spot techniques cannot be triggered individually, because they all emerge from one laser system, which can either be switched on or off.

Several strategies for parameter variation to avoid stop crater cracks were devised for BHLW and experimentally compared. It proved to be best practice to mitigate stop craters and their associated cracks to switch off the Nd:YAG laser shortly before the end of the seam was reached. Subsequently keeping the HPDL stationary until the crater was filled up by wire material. The wire feed speed of the wire supply warranted short reaction times and high accuracy and reliability.

The results of this strategy for the prevention of stop crater cracks are shown in figures 7.7 ÷ 7.10. The craters which formed without the strategy are displayed for comparison. Figures 7.7 and 7.8 show the face and root weld in the vicinity of the stop crater. A small offset from the line through the abutted edges of the specimen plates was intentionally introduced to clearly demonstrate that the longitudinal crack originated from the stop crater and is not a continuation of the plates' edges into the fusion zone. In practice, a seam which is satisfactory and of good quality for the major part of its length is often destroyed by such cracks at its very end.

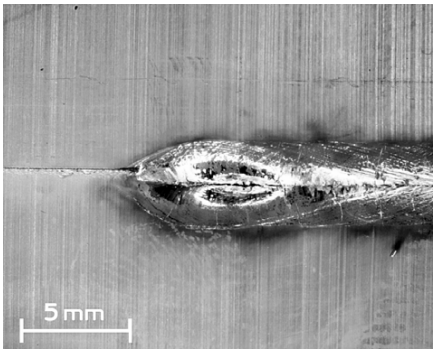

Figure 7.7: Longitudinal crack in the stop crater, face surface view; P_{BHLW} = 3 kW + 3 kW; f = 150 mm; φ = 20°; argon flow 25 L min^{-1}; v_w= 4.0 m min^{-1}; v_f = 3.0 m min^{-1}; butt joint; EN AW-6060; filler Al4047 A; Ø$_f$ = 1 mm

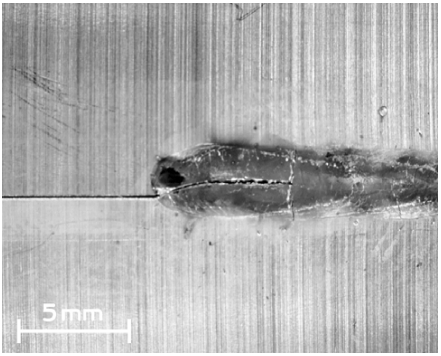

Figure 7.8: Longitudinal and transverse crack in the stop crater, root surface view; P_{BHLW} = 3 kW + 3 kW; f = 150 mm; φ = 20°; argon flow 25 L min^{-1}; v_w= 4.0 m min^{-1}; v_f = 3.0 m min^{-1}; butt joint; EN AW-6060; filler Al4047 A; Ø$_f$ = 1 mm

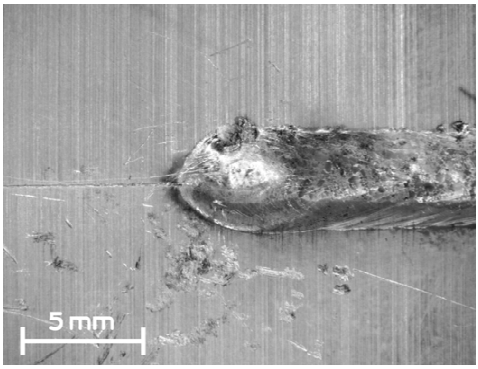

Figure 7.9: Optimized stop crater, face surface view; P_{BHLW} = 3 kW + 3 kW; f = 150 mm; φ = 20°; argon flow 25 L min^{-1}; v_w= 4.0 m min^{-1}; v_f = 3.0 m min^{-1}; butt joint; EN AW-6060; filler Al4047 A; $Ø_f$ = 1 mm

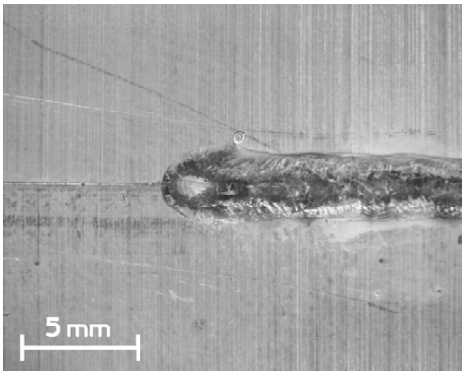

Figure 7.10: Optimized stop crater, root surface view; P_{BHLW} = 3 kW + 3 kW; f = 150 mm; φ = 20°; argon flow 25 L min^{-1}; v_w= 4.0 m min^{-1}; v_f = 3.0 m min^{-1}; butt joint; EN AW-6060; filler Al4047 A; $Ø_f$ = 1 mm

The ramifications of this result for manufacturing technology are obvious if the constraints of robots as standard kinematics for laser beam welding are considered. A weld seam in aluminium could hardly ever be segmented, because every stop crater posed the potential danger of such malignant stop crater cracks, as shown in figure 7.6. Seams segmented by multiple-pass welding suffer from increased porosity and face the danger of reheat cracking in the part of the seam

passed twice. This demanded continuous and closed seams in profiles to be welded in 'one go'. The general problem remains: for any seam *one* stop crater must lie somewhere!

BHLW allows *deliberate* segmentation of the seam making welding of complex geometrical structures feasible. In space frame structures circular or rectangular profiles are commonly used. Welding around an edge on a rectangular profile necessitates extreme accelerations for reorientation of the axes of the robot if the speed of welding on the seam has to stay constant. Although for circumferential welds on rounded profiles this seems easier to achieve, this is in fact not the case. The space frame reduces accessibility and the inclination of the seam with respect to the direction of gravitational acceleration needs to be kept within certain limits for the melt not to drop out downward. A reorientation of the frame structures is unavoidable for a closed weld seam. Hence, *segmentation* is a critical enabling factor for the joining of space frames, because it is impossible to weld most seams in 'one go' owing to the limits of kinematic systems such as robots. In addition, the possibility of segmentation allows processes which were originally designed for cooperating robots to weld profiles of steels, e.g. exhaust pipes, to be transferred to aluminium alloys.

The beam forming of BHLW facilitates bead shape design according to need. The width of the HPDL focal spot predetermines the width of gaps that can be robustly bridged by BHLW. The details of the gap bridging ability of BHLW are dealt with in section 8.2.3. Gaps up to 1 mm can be securely bridged. BHLW has the potential to bridge even broader gaps by increasing the width of the HPDL focal spot. For the exemplary application in paper machinery, mentioned above, the weld needs to be liquid proof. A broadened weld face and a rather reduced penetration depth are advantageous to create liquid proof seams. In BHLW the two laser beams can be independently focused on distinct focal planes, as detailed in the next paragraph. This is an important feature of BHLW to weld zinc-coated steels. The *bifocality* of BHLW is the key for the following.

7.4 Zinc-coated steels

Zinc-coated steels reduce corrosion wear and gain an ever increasing application in vehicle manufacturing. Thin sheet welding by classical arc-augmented techniques and by laser beam welding of such materials is demanding due to the vaporization of zinc, because zinc-coated steels are typically welded in an overlap joint geometry. State-of-the-art process technologies, which were considered in this dissertation in section 3.2, are briefly reviewed with regards to zinc-coated steels. This background allows the merits of BHLW to be fully appreciated.

It was thought that enlarging the keyhole would enable zinc vapour to exit the capillary without creating blow holes. The process technologies of *multiple spot* and *oscillation beam* laser welding were designed to this end. By multiple spot laser welding several spots are positioned on the workpiece as to enlarge the keyhole by generation of an advantageous intensity distribution. In multiple spot laser welding the zinc layers on the surface *and* in the gap are *simultaneously* intersected by the same laser beam. Generally, the isotherms of melting and vaporization lie very close to each other at the melting front in keyhole welding. In the case of an overlap joint they also lie on top of each other in the overlap gap.

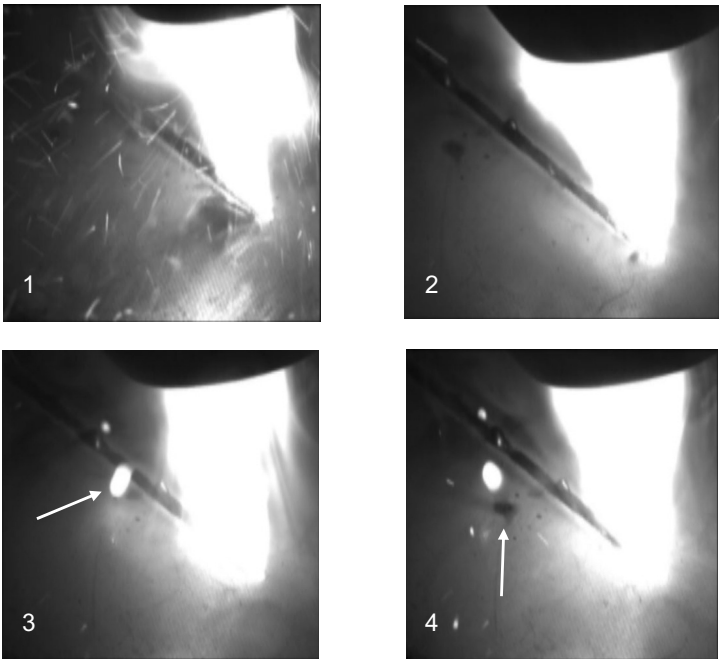

Figure 7.11: Zinc-coated steel DX56D; thickness 1.5 mm; overlap joint; $P_{Nd:YAG}$ = 3 kW; argon flow 25 L min^{-1}; v_w = 3 m min^{-1}; high-speed photography at 1000 fps; note the flying sparks accompanying a burst of vapour in frame 1, in frame 2 the bright flame of zinc is noteworthy, in frame 3 a drop of molten metal ejected from the melt pool is indicated by an arrow, in frame 4 the mark left by the droplet after bouncing off from the metal surface is arrowed.

At first, the laser power is absorbed by the top zinc layer leading to its immediate vaporization. *Thereafter*, the melt film of the vapour capillary touches the two layers in the overlap. The zinc there evaporates while being covered by a film of molten steel. Rapid volume expansion of vaporizing zinc causes the blows described above. Zinc is soluble within steel melts. The potential of multiple spot CO_2 laser welding to increase process robustness and weld quality was evaluated by [MEIER 2005]. Hohenberger held that the uninhibited venting of the metal vapour from the vapour cavity is fundamental for a robust and stable welding process [HOHENBERGER 2003; p. 45-48]. Hohenberger tried to facilitate venting

by a dual spot optic system. The final study in this succession was conducted in 2005. Therein dual, triple, and quadruple spot setups were deployed to weld aluminium and zinc-coated steels with Nd:YAG and disc lasers [GREF 2005]. In some specific alloys and joint geometries pores could be eliminated and generally be reduced as compared to single spot laser welding. Eventually, it is admitted that dual spot disc laser welding of zinc-coated steels by "widening of the vapour cavity could not create welds free of pores and expulsions" [GREF 2005, p. 114]. The empirical process model according to which multiple spot laser welding was designed did not guide it to success. It was obviously expected from the beam's diffraction angle that a widening of the cavity could be achieved. However, it seems more likely that beam *channelling* took place [ALLMEN 1995, p. 38]. The concept of stabilization and influence of the keyhole geometry by oscillation and laser stir welding or other manipulation of the beam is based on the same process model as multiple or twin spot laser welding. The instabilities are to be prevented by widening of the keyhole. The process was originally invented and patented for gap bridging and for tailored welded blanks where the workpieces to be joined differ in thickness [COSTE 1997, RUBBEN 1997, STOL & MARTUKANITZ 2004]. It has recently been researched for aluminium and zinc-coated steels. Meier developed an advanced optical setup which generated oscillations up to 1500 Hz by virtue of a scanner mirror [MEIER 2005]. These results are reproduced in figure 7.12 to remind the reader of figure 3.19.

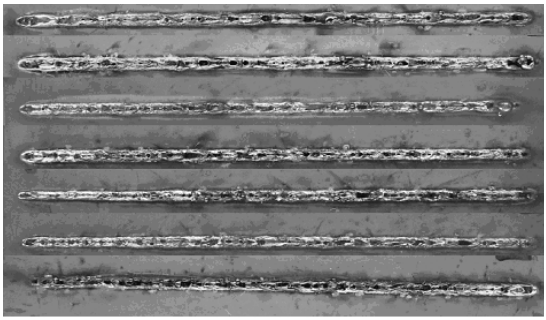

Figure 7.12: Surface photograph of zinc-coated steel welded with oscillation Nd:YAG laser welding; $P_{Nd:YAG}$ = 3 kW; v_w =2 m min^{-1}; frequency of oscillation 1500 Hz; a is the amplitude of oscillation; specifics of zinc coating not given in the reference [from MEIER 2005]

There is *no* positive effect of oscillation on weld quality, as can be clearly seen in figure 7.12. In sum, state-of-the-art laser welding technologies do not produce seams of satisfactory quality in zinc-coated steels. In the following the merits of BHLW are presented.

The strata proposition is an integral part of the empirical process model for *coated* materials, c.f. section 4.2.3. In the same section the model was specified for zinc-coated steels. The experimental results to support this empirical model are given in the following.

For automotive applications the width of fusion in the overlap gap should be equal to or exceed the thickness of a single sheet. The best result with an Nd:YAG laser fulfilling this requirement serves as a benchmark. It is compared to the best result with BHLW. Three exemplary zinc-coated steels of general interest in automotive manufacturing were considered: DX56C + Z, HXT700D, and DC04 + Z.

DC04 + Z is a cold formed, normally dipped zinc-coated steel according to DIN EN 10327. This zinc-coated steel is laser weldable with an Nd:YAG laser and with BHLW. Either technology can achieve welds of good visual quality. BHLW enables to double maximum welding speed as compared to Nd:YAG laser welding. Overlap fusion widths are comparable (c.f. figure 7.13), but the BHLW weld has a more pointed shape (c.f. figure 7.14).

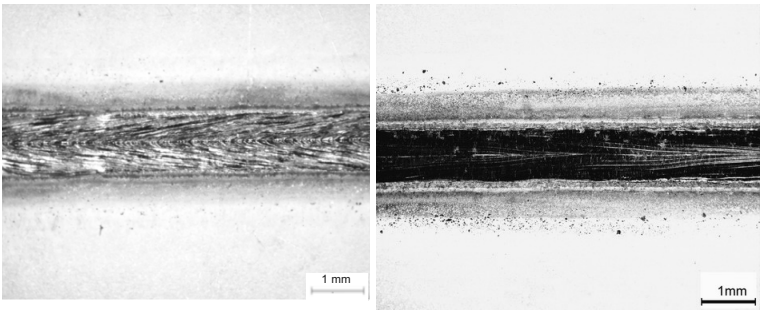

Figure 7.13: DC04 + Z; overbead of overlap joint; left: $P_{Nd:YAG}$ = 3 kW; argon flow 35 L min^{-1}; v_w = 5.5 m min^{-1}; right: P_{BHLW} = 3 kW + 3 kW; argon flow 30 L min^{-1}; v_w = 12 m min^{-1}; z axis defocusing = 0 mm

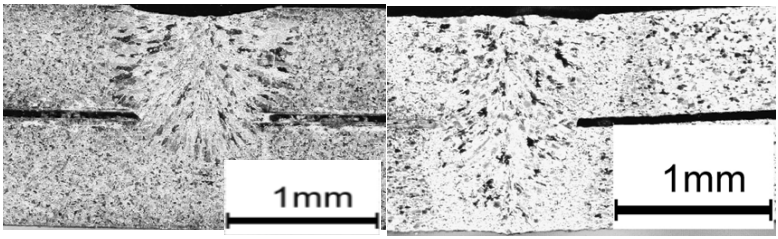

Figure 7.14: DC04 + Z; overlap joint; thickness 0.9 mm; left: $P_{Nd:YAG}$ = 3 kW; argon flow 35 L min^{-1}; v_w = 6 m min^{-1}; fusion width in overlap joint = 0.9 mm; right: P_{BHLW} = 3 kW + 3 kW; argon flow 30 L min^{-1}; v_w = 12 m min^{-1}; z axis defocusing = 0 mm; fusion width in overlap joint = 0.9 mm

HXT700D is a novel zinc coating which shows good weldability with an Nd:YAG laser and likewise with BHLW. BHLW enables higher welding speeds and increased fusion widths in the overlap.

The apparent difference of robustness of BHLW as compared to Nd:YAG laser welding can be best demonstrated for DX56D + Z. DX56D + Z is a dipped zinc-coated steel according to DIN EN 10327. This method for zinc coating is cost effective. A dipped coating is, however, notorious in laser welding and regarded as not weldable in most cases. In figure 7.15 the most stable weld in DX56D + Z with an Nd:YAG laser is shown. Massive spatter and expulsions from the fusion zone are obvious. Due to these expulsions the top sheet is cut through rather then joined by laser beam treatment. Such beads are completely defective.

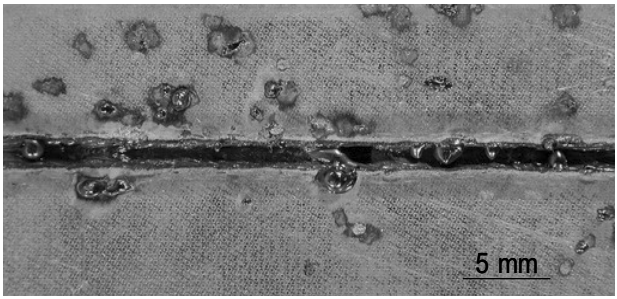

Figure 7.15: DX56D + Z; overlap joint; $P_{Nd:YAG}$ = 3 kW; argon flow 35 L min^{-1}; z axis defocusing = 0 mm

Microscopic inspection reveals that these expulsions originate from the zinc layer in the overlap zone. The reason is that the temperature of vaporization of zinc is below the liquidus temperature of aluminium. The associated mechanism is discussed in section 4.2.3. These microscopic magnifications are shown in figure 7.16.

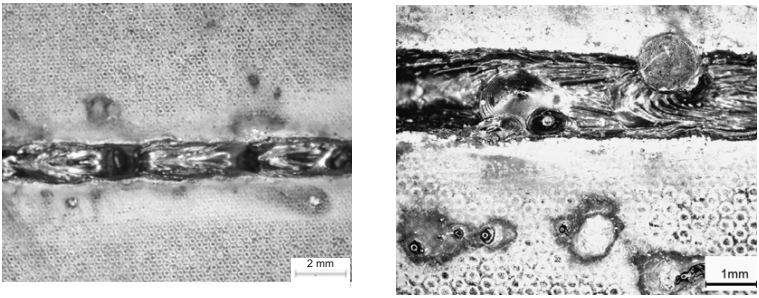

Figure 7.16: Microscopic magnification of the surface of an overlap joint in DX56D + Z; $P_{Nd:YAG}$ = 3 kW; argon flow 35 L min^{-1}; v_w = 2 m min^{-1}; z axis defocusing = 0 mm

The following results are based on the strata proposition expounded in section 4.2.3 for zinc-coated steels. By adjusting the focal planes in BHLW such that the HPDL is focused on the top surface layer and the Nd:YAG on the zinc layers in the overlap, a flawless and defect-free seam can be generated, c.f. figure 7.17.

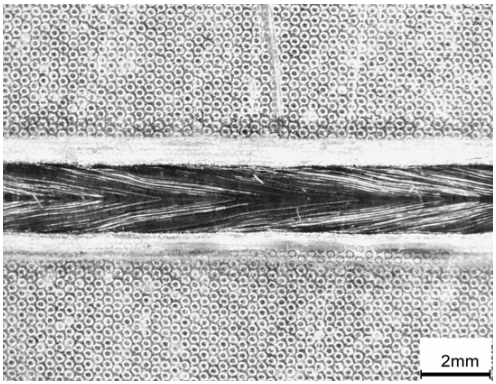

Figure 7.17 Defect-free weld face achieved with BHLW in DX56D + Z; overbead of overlap joint; P_{BHLW} = 3 kW + 3 kW; argon flow 30 L min^{-1}; v_w = 12 m min^{-1}; z axis defocusing = -1.5 mm

The cross-section macrographs shown in figure 7.18 exemplify this result. The expulsions lead to a substantial underfilling in the top part of the weld. The way taken by evaporates through the melt is stamped into the grain structure. For BHLW such a trace is not visible and there is no deposited zinc in the overlap gap in the Nd:YAG laser weld. This clearly indicates that the coating has been 'burned out' by massive beam material interaction exactly in the focal plane of the Nd:YAG laser, which was adjusted to be congruent with the two layers of zinc coating in the overlap. Hence, these results validate the strata proposition of the empirical process model of BHLW.

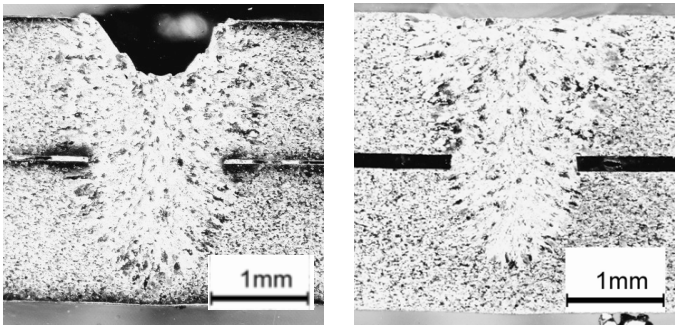

Figure 7.18: Cross-section macrograph; overlap joint; thickness 1.5 mm; left: $P_{Nd:YAG}$ = 3 kW; argon flow 35 L min^{-1}; v_w = 3.25 m min^{-1}; fusion width in overlap joint = 1.4 mm; right: P_{BHLW} = 3 kW + 3 kW; argon flow 30 L min^{-1}; v_w = 4 m min^{-1}; z axis defocusing = -1.5 mm; fusion width in overlap joint = 1.3 mm; gap in overlap joint = 0.1 mm

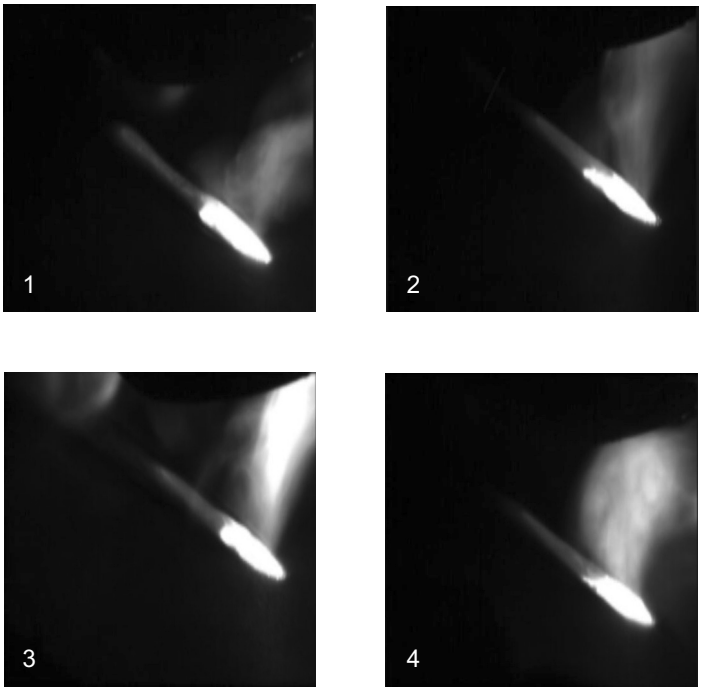

Figure 7.19: Zinc-coated steel DX56D; P_{BHLW} = 3 kW + 3 kW; thickness 1.5 mm; overlap joint; argon flow 25 L min^{-1}; v_w = 3 m min^{-1}; high-speed photography at 1000 fps; note the brightness of the plume and the sedation of the weld pool in comparison to figure 7.11

In figure 7.19 it can be seen that the melt pool in BHLW appears to be sedated considerably as compared to Nd:YAG laser welding, c.f. figure 7.11. Defects did not arise. The vapour plume is not as bright in BHLW as in Nd:YAG laser welding indicating that most of the zinc was removed by the diode laser. At times a bulge appears in the melt pool and the plume gets brighter, but no defect is induced.

It is an overall very important achievement for laser manufacturing technology in industrial application to weld zinc-coated steels without defects. Zinc-coated steels can satisfactorily be resistance spot welded. The zinc, however, degrades the contact tips of the RSW-clamp after several welds. Cleaning or replacement of those tips necessitates undesirable non-productive times. Additionally, the

strength in the overlap is reduced by the zinc coating. Classical arc and Nd:YAG laser welding require a gap of a few tenths of a millimetre in the overlap to allow the zinc vapour to escape from within the overlap fusion zone. Elaborate and very accurate clamping devices are necessary in production lines to create gaps which are neither too big to constitute a malignant kerf initiating failure in dynamical loading nor too small for the zinc to escape. For BHLW the sheets can be contact clamped, because a gap of zero technical width can be tolerated.

8 System Technology

8.1 Laser optic system

8.1.1 Experimental optic setup

An experimental setup was assembled to investigate the fundamentals of the combination of HPDL and Nd:YAG laser. The HPDL stack was directly integrated into the optical head. Its beam passes through a dichroic mirror orientated at an angle of 45° with respect to the beam's direction of propagation. The coating of the mirror transmits the radiation of the HPDL to a very high degree. The Nd:YAG laser beam is guided to the optical head via a fibreoptic cable, in which its beam is enlarged by a water-cooled collimator to a diameter of 44 mm. The beam is subsequently deflected by 90° with regards to the direction of propagation of the HPDL and is reflected at the bottom surface of the dichroic mirror. The Nd:YAG laser radiation is deflected into the beam path of the HPDL such that both beams are propagating parallel to each other. Both beams are focused by a spherical lens of f = 150 mm. Before the rays impinge on the workpiece they transgress the filter glass that protects the lens from spatter. Subseqently, they propagate coaxially within a gas nozzle. The experimental optical head is shown in figure 8.1.

All the welding results presented herein were generated with this experimental optical head. A number of drawbacks became obvious during operation of the experimental head. These drawbacks are forgone in the prototype optic system, which is consequently ready for industrial applications.

In the experimental optic setup the share of radiation of both lasers, which is not deflected towards the lens, falls onto a black anodized water-cooled beam trap. Thereby, heating up of the head is prevented. In practice, the sum of radiation power of 6 kW emitted by both lasers heated up the optic, since a fraction of the laser power impinged on the mount. This is the reason that the length of a continuous weld seam was limited to about 20 cm. Otherwise, the beam trap overheated and time had to be allowed for it to cool down. The gimbal mount of the dichroic mirror utilized four screws which did not permit a repeatedly accurate and retrievable adjustment of the dichroic mirror. Moreover, the rotational axes of the mirror mount were unsupported. This lead to a complicated

and time consuming routine for varying the relative focal positions of the two beams. Reflections of radiation from the workpiece could re-enter the HPDL stack via the optical components. This radiation burned into the diodes of the HPDL resulting in a gradual reduction of output power of the HPDL stack. Particle and thermal emissions from the welding process did affect the experimental setup. Particles degraded the lenses and process radiation heated up the cavity, as the outer walls were blackened and therefore highly absorbent.

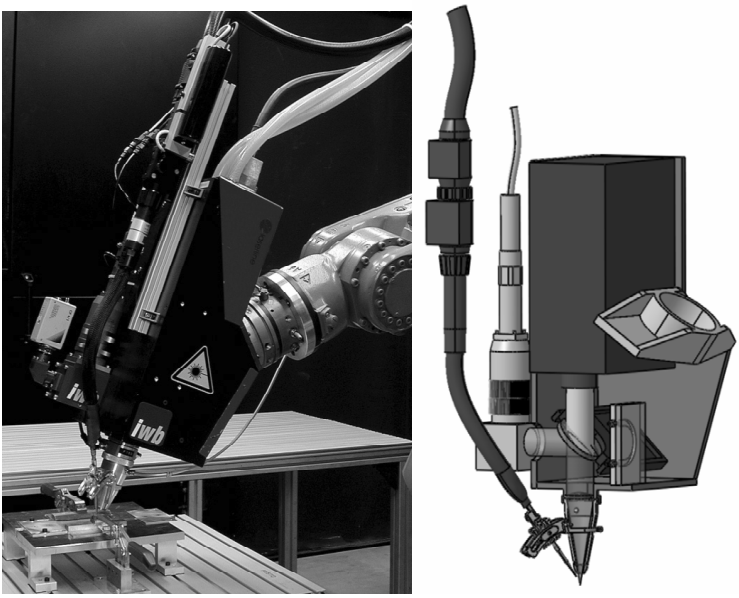

Figure 8.1: Experimental setup of the optical head; left: HPDL stack integrated into the head; right: headlong elevation of the experimental optic setup

The filler wire tube batch and the deflecting optic for the Nd:YAG laser are located on the same side of the HPDL. The wire could only be fed by torsion of the batch to the plane of longitudinal motion, as the plane itself was occupied by the Nd:YAG laser optic. The optic system is not mirror symmetric with respect to the direction of motion. This reduces accessibility and makes welding of T-joint geometries of extended parts impossible.

8.1.2 Optical engineering of the beam path

The beam path of the experimental optical setup was modelled by optical engineering software. All indispensable optical components and constraints were encoded and allowed abstract planning and optimization of the beam path and the optical components. All practical possibilities were evaluated. The final result of the components' arrangement is shown in figure 8.2.

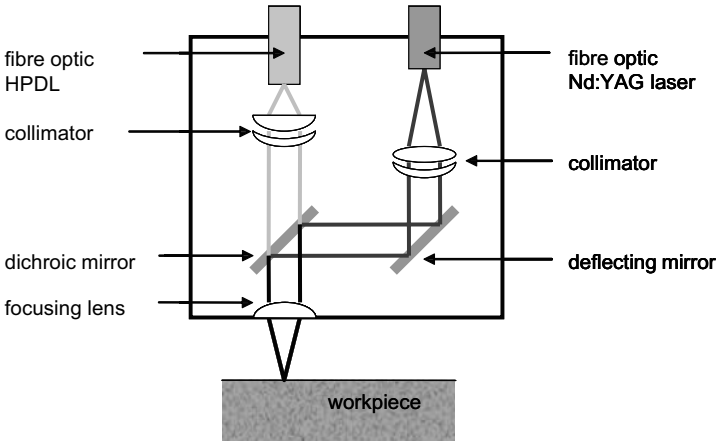

Figure 8.2: Sequence of optical components of the optimized optical beam path

The encoding of the specific optical components revealed several shortcomings of the mirrors and lenses used in the experimental setup. It turned out that the experimental optic setup's *diffraction limit* is set by the apertures of the dichroic mirror and the focusing lens, as shown in figure 8.3. The footprint in figure 8.3 shows the image of the HPDL emerging after the experimental optic setup.

The objective was to design the optical components such that the optic is diffraction limited by the apertures of the optical components. The Rimray aberration plot (RIM) shows the magnitude of spherical aberration on the ordinate, whereas the abscissa renders the position of the rays in the aperture on entry of the optical system. Refraction is not accounted for by the RIM. The line spread function (LSF) gives the intensity distribution of the beam within the focal spot. Refraction and all wavelengths according to their individual weight are accounted for. The LSF shows the one-dimensional distribution of the

intensity along the x-axis defined horizontally and transverse to the direction of propagation. The RIM and LSF for the HPDL and the Nd:YAG laser are displayed in figures 8.4 and 8.5 respectively.

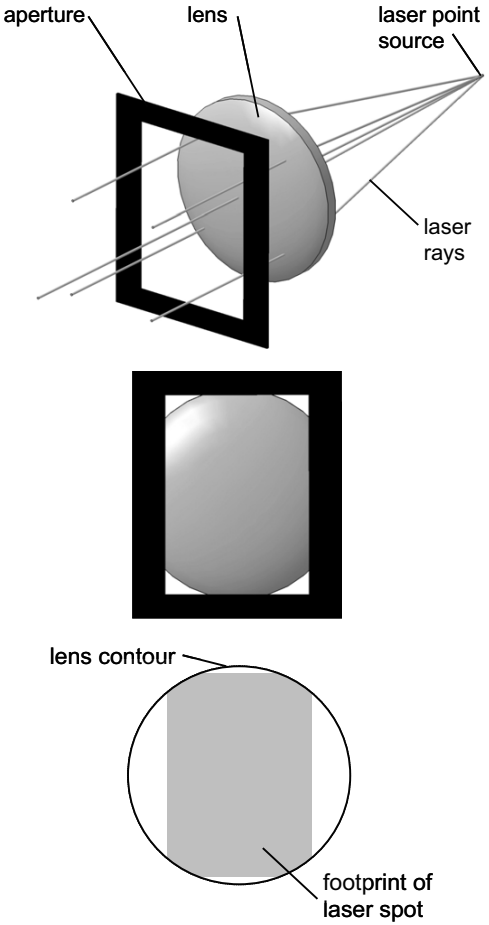

Figure 8.3: *Top: elevation of beam path; middle: aperture represented by the gimbal mount of the dichroic mirror; bottom: footprint-analysis of the resultant trimmed rectangular beam of the HPDL emerging after the experimental optical setup*

The LSF can therefore be used to determine refraction effects and secondary maxima. A new dichroic mirror was designed accordingly. The fibre optic systems of the two lasers are standard components of the lasers' manufacturers and had therefore to be accepted as the diffraction limit of the prototype optic.

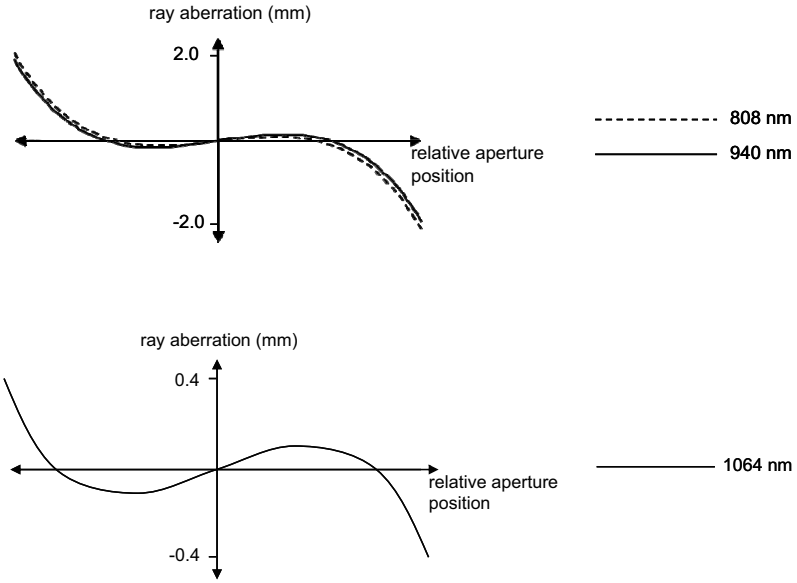

Figure 8.4: Rimray aberration plot of both lasers employed in BHLW; top: HPDL according to dominant wavelengths; bottom: Nd:YAG laser for its single wavelength

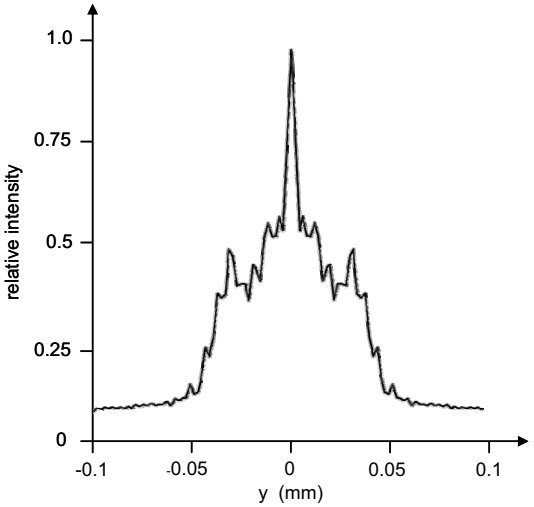

Figure 8.5: Line spread function of the Nd:YAG laser

The optical simulation showed that an aspheric lens can reduce aberrations. The improvements by virtue of an aspherical lens are given for completeness. Figure 8.6 shows the RIM and LSF as generated by the optical engineering software. Such an aspheric lens could not readily be obtained from manufacturers. Therefore in the prototype optic system an achromatic duplet was used instead.

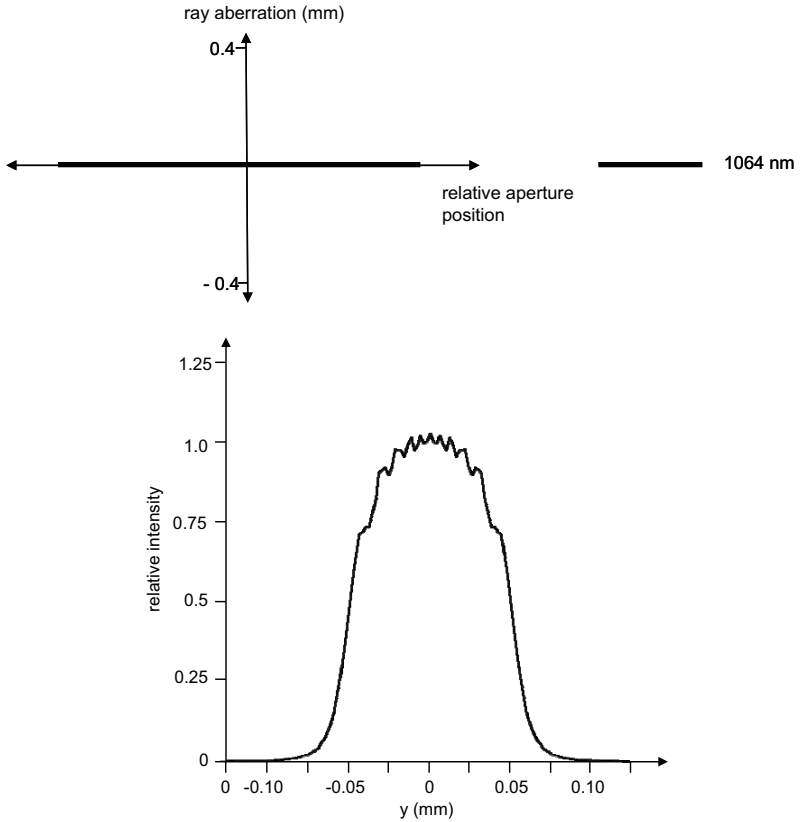

Figure 8.6: Improvements by an aspherical lens: top: Rimray aberration plot of the Nd:YAG laser; bottom: line spread function of the Nd:YAG laser

8.1.3 Prototype optic system

The fundamentals of BHLW had been revealed, studied, and optimized with the experimental setup described above. In order to apply the welding technique of BHLW to workpieces with complex geometry and to allow demanding joint geometries to be welded, the optical head needs to be improved and the lessons learned from the experimental head to be heeded. The objective of the new design was to reduce weight and increase accessibility by fibreopitc deliverance of the HPDL's radiation. The thermo-optical efficiency of the components had to be improved in order to allow for higher nominal output powers of recent HPDL systems.

The dichroic mirror which is a dielectric multiple-coated mirror was designed for the wavelengths employed. The dichroic mirror should uninhibitedly transmit the beam of the HPDL, whereas the radiation of the Nd:YAG laser is desired to be most fully reflected. For an angle of irradiance of 45° the reflection coefficient for S-polarised radiation of 1064 nm is above 99.8% and for P-polarised radiation still 99.5%. The Nd:YAG laser emits radiation of both polarisations. Conversely, for the HPDL the transmission coefficient for a wavelength of 808 nm is 92% or 98% for S- or P-polarisation. Radiation of 940 nm is transmitted analogously with 80% or 90% respectively, c. f. figure 8.7. Graph and values measured by courtesy of mirror manufacturer.

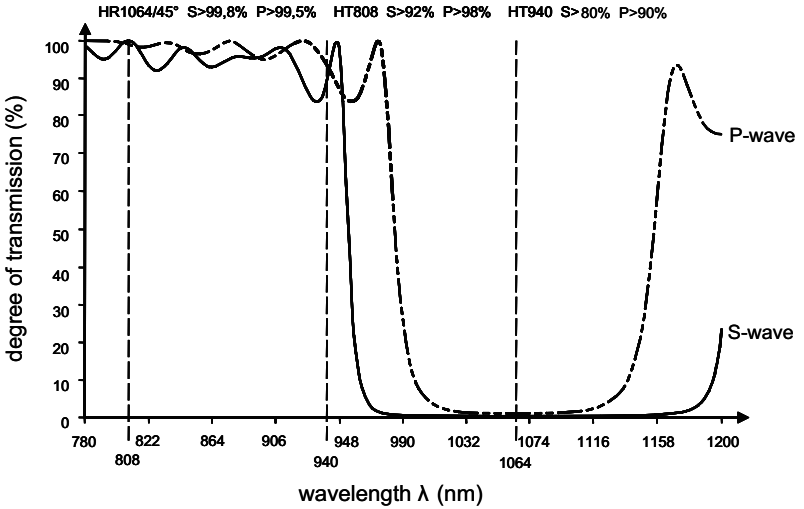

Figure 8.7: Degree of transmission of the dichroic mirror for different wavelengths; top line gives the exact transmission degree values from the graph for S-waves and P-waves according to wavelength of the Nd:YAG (i.e. 1064 nm) incident at 45° and for the dominant wavelengths of the HPDL (i.e. 808 nm and 940 nm)

The substrate of the mirror is boron crown glass. It has a specific transmission coefficient τ_i defined for standard thickness. In this case τ_i[10 mm] = 0.999 for 1064 nm and τ_i[10 mm] = 0.997 for 700 nm. The gimbal mount of the mirror is necessary to accurately position the Nd:YAG laser above the focusing lens. The mount allows varying the angle of irradiance of the Nd:YAG laser with regards to the optical axis of the focusing lens. This enables a horizontal shift of the back focal plane of the Nd:YAG spot. This results in a z-offset with regards to the focal spot of the HPDL on the workpiece. The collimated beam of the HPDL for whose wavelengths the mirror is not reflective is not affected by the mount's adjustment. The direction of the HPDL beam is always parallel to the optical axis of the focusing lens. A change of mirror inclination leads to a relative horizontal shift of the focal spot of the Nd:YAG laser within the larger focal spot of the HPDL. The refraction of 27.92° of the HPDL beam within the dielectric mirror is displayed in figure 8.8. This double refraction leads to a horizontal offset of 4.22 mm of the two beams. The optical axes of the collimator of the HPDL and of the focusing lens were designed accordingly.

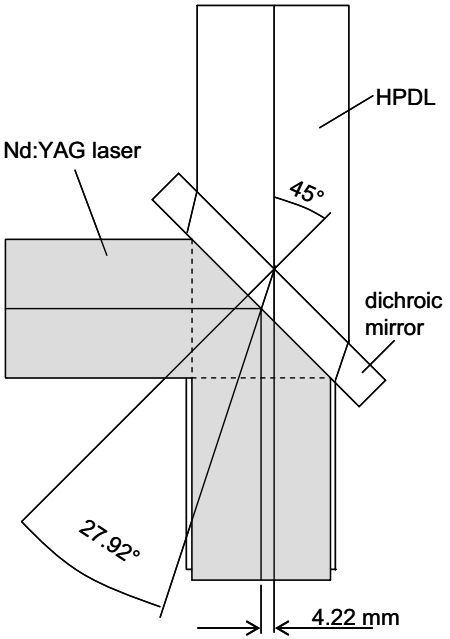

Figure 8.8: Offset of beams due to refraction in the dichroic mirror substrate

The gimbal mount is adjusted by micrometer heads which allow for deliberate mirror inclinations to be *accurately* and *repeatedly* adjusted. The mount itself consists of two integrated frames. The frames are supported by brass axes in anti-friction bearings, which do not need additional lubrication. These axes lie on the bottom side of the dichroic mirror and cross each other in the middle of the mirror plane. The gimbal mount is shown in figure 8.9.

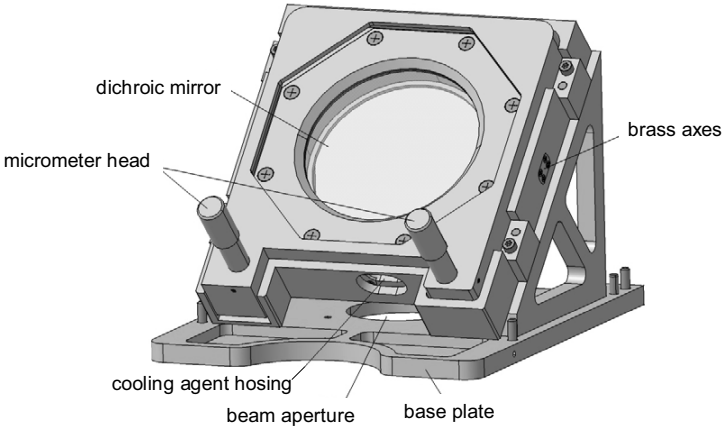

Figure 8.9: Gimbal mirror mount of the prototype optic setup

The length of the optical path of the Nd:YAG laser between its collimator and the focal lens remains constant upon mirror adjustment and the vertical focal position stays put as previously adjusted. It should be noted that the rotations around two axes at right angles are brought about by a frame-in-frame design reducing the number of screws from *four* to only *two* to adjust the gimbal mount. The two micrometer heads are positioned at the front of the mount for easy access. The mirror is water-cooled to prevent it from heating up when radiation is impinging on the frames. The absorbed radiation power by the dichroic mirror is as low as 15 W in BHLW for the combined power of its lasers of 6 kW. For this prototype head a sustainable beam trap of high merit is necessary to allow for technological progress of nominal output powers of HPDLs.

Although the multiple coating layers of the dielectric mirror give superior coefficients of reflection and transmission, complete reflection of Nd:YAG laser radiation and full transmission of HPDL radiation cannot be achieved simultaneously for technical restrictions of the mirror coating. The coefficient of transmission for the major wavelengths of the HPDL, i.e. 92% for λ= 808 nm and 80% for λ= 940 nm, lead to a considerable amount of heat that needs to be removed from the prototype head. For the current 3 kW experimental system the radiation power incident on the beam trap totals 435 W, and for a future 6 kW-HPDL would correspond to 855 W. Therefore, the beam trap of the prototype is manufactured from copper instead of aluminium. The cooling water channel's

surface area for heat exchange is more than tripled from $2.5 \cdot 10^3$ mm^2 to $8.51 \cdot 10^3$ mm^2. The new beam trap is coated by a material much superior to a black-chromium coating. The absorption spectrum of the coating, displayed as figure 8.10, shows 93% absorption of the lasers' wavelengths. This absorption is equal to a black coating. However, the diagram shows the greatly reduced emission of heat as compared to a black body. This leads to less heating-up of the mirror chamber and is therefore a critical enabling factor for its compact design.

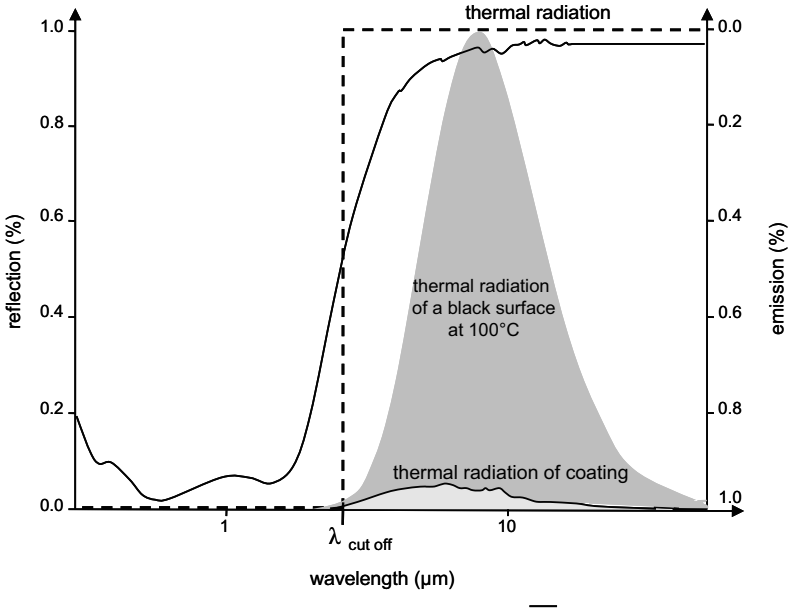

Figure 8.10: Absorption spectrum of the coating of the beam trap;
—— indicates the reflection from an ideal absorber and
----- indicates the reflection of the special coating used

The real focusing lens in the prototype head is an achromatic doublet. This lens system consists of a convex and a concave lens made from different glasses. The lenses are closely connected and puttied. The glasses are selected so that the dispersion of the components is inversely proportional to their refractive index. Since the specific curvatures of the single lenses do not degrade the suppression of chromatic aberrations, spherical aberrations can be additionally overcome by appropriate form design [PEDROTTI et al. 2002, p. 155].

The achromatic lens system used for the prototype head has a focal length of $f = 150$ mm. Achromatic aberrations are corrected in the range of 700 to 1100 nm and achromatic lens design utilizes the additional degree of freedom of curvature in the intermediate layer to greatly reduce spherical aberrations up to wavelengths of 2 µm. Such an achromatic lens system is ideal for BHLW since three distinct wavelengths have to be taken care of. Due to the collimation of the beam the total diameter of the lens is irradiated, which would lead to noticeable spherical aberration without correction. To achieve a high degree of transmission the achromatic lens is anti-reflectance coated. This reduced reflectivity in the spectral range form 700 to 1550 nm to less than 1%.

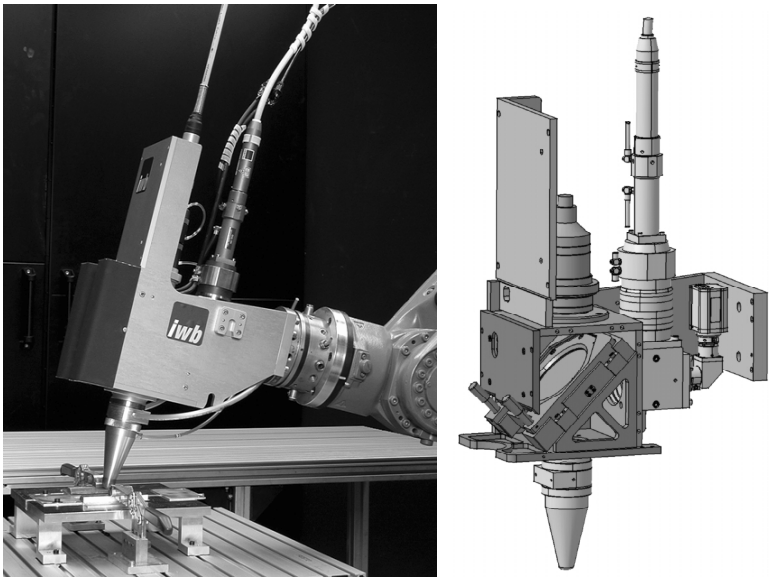

Figure 8.11: Prototype optic: left: photograph of the optic mounted on the robot; right: side elevation of the optic

Figure 8.11 shows the prototype head. The chamber with the dichroic mirror is dust proof, compact, and completely closed. It can be easily disassembled for cleaning and maintenance. The beam trap and the mirror face each other to prevent contamination from unintentional touching. Easy access to the screws of the micrometer heads is enabled. The prototype has reflective surfaces to minimize heat absorption from the surroundings. The Nd:YAG laser fibre optic was placed opposite to its position in the experimental head. This makes room

for the tube batch of the filler wire supply. In this arrangement the filler wire unit can be more flexibly adjusted without torsion. The prototype head is mirror symmetric with regards to the direction of welding and it allows for T-joint geometries to be easily accessible, because its width is reduced by 190 mm as compared to the experimental optic setup. Its overall weight is half the weight of the experimental head. A weaker robot can accurately move the prototype head. In sum, the prototype constitutes a stable and robust optic head ready for application in industrial circumstances. Table 8.1 compares the major measures of the experimental to the prototype head.

	units	**experimental head**	**prototype head**
weight	kg	41	22
width	mm	320	190
height	mm	710	650
breadth	mm	450	380
surface beam trap	mm^2	$2.5 \cdot 10^3$	$8.1 \cdot 10^3$
heat conductivity	$W\ m^{-1}\ K^{-1}$	230	385
reproducibility of mirror inclination		no	yes
T-joint accessibility		no	yes

Table 8.1: Comparison of the experimental optic setup to the prototype optic head

8.2 Filler material supply

8.2.1 Introdcution to hot cracks in aluminium

The restrained contraction of a weld during cooling sets up tensile stresses in the joint and may cause cracking, one of the most serious weld defects. There are two kinds of hot cracking: Cracking that occurs in the fusion zone during solidification of the weld metal is known as *solidification cracking*. Whereas cracking that takes place in the partially melted zone due to liquation of low melting point components of the alloy is known as *liquation cracking*. Aluminium alloys are generally susceptible to both cracking mechanisms. Due to the low heat input and small HAZ of laser welds as compared to classical arc welding techniques liquation cracking has hardly been reported [HUANG 2003]. Solidification cracking is dominant in aluminium alloys.

Most alloys pass through a brittle temperature range (BTR) upon solidification. Weld solidification cracking is related to the extent of the BTR of the alloy. Cracking occurs when the thermal tensile strains induced by thermal contraction and external displacement exceed the ductility of the weld metal in the BTR [ZHAO 1999]. Various theories of solidification cracking are effectively identical and embody the concept of the formation of a coherent interlocking solid network that is separated by essentially continuous thin liquid films and thus ruptured by the tensile stresses upon solidification. These theories are not further considered herein and can be found elsewhere [KOU 2002, p. 263, BORLAND 1960, SINGER 1947, FLEMINGS 1974, BISHOP 1957].

This chapter concentrates on a robust system technology for filler wire supply to avoid solidification cracking. Type 5xxx alloys are usually not susceptible to solidification cracking due to their high magnesium content. 2xxx and 6xxx alloys have higher solidification crack susceptibility due to their chemical composition. It was observed that aluminium alloys have the highest solidification crack susceptibility if their chemical composition consists of 0.6% Si content in Al-Si binary alloys for arc welding, c.f. figure 8.12 [BRENNER 1967].

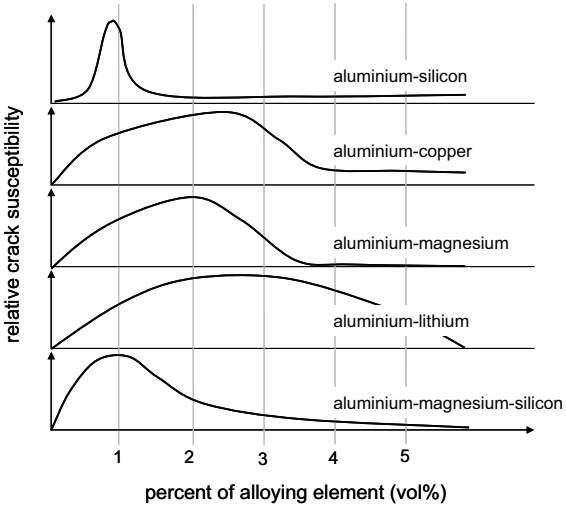

Figure 8.12: Relative crack susceptibility depending on volume percent of alloying elements [MATHERS, p. 28]

The experimental data shown in figure 8.13 is obtained from solidification crack testing by ring casting. Ring casting is a method to estimate the relative susceptibility to solidification cracking, i.e. to illustrate the influence of alloying variation by comparison of the *relative* length of the cracks generated in ring casting. The crack lengths obtained do not represent *absolute* lengths of cracks in laser beam welding [JENNINGS 1948].

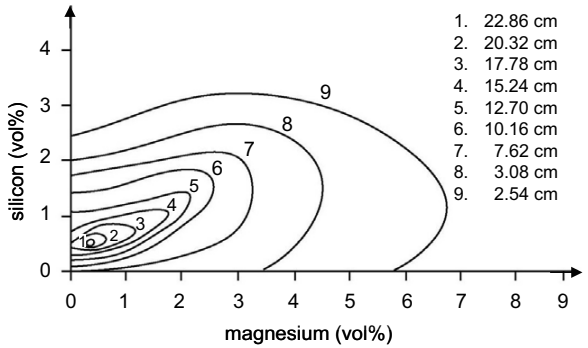

Figure 8.13: Crack length for 6xxx alloy depending on major alloying elements [mod. acc. to KOU, p. 287]

The chemical composition of EN AW-6060 is given in table 8.2. It shows that the reference alloy used in this dissertation exhibits the highest susceptibility to solidification cracking within the 6xxx alloy group. Thus, it poses the most challenging task to weld it free of cracks.

Si	Mg	Fe	Cu	Mn	Cr	Zn	Ti	Al
0.3-0.6	0.3-0.6	0.1-0.3	0.1	0.1	0.05	0.15	0.1	remainder

Table 8.2: Chemical composition of EN AW-6060 in vol% according to element

The solidification crack susceptibility of other binary alloys can be estimated: Empirical solidification crack indices (SCI) have been developed for binary (and ternary) alloys, based on laser welds [ION 2005, p. 427]:

$$SCI_{binary} = 15.32 - (\%Si - 0.7)^2 - 0.25(\%Cu - 2.0)^2 - 0.04(\%Mg - 1.5)^2$$

For EN AW-6060 the SCI is 14.33 and therefore among the highest in 6xxx alloys. Note that the maximum crack length observed doubles from 0.4 mm to 0.8 mm with an increase in SCI from 13.7 to 14.5. Arc welding practice reflected in figure 8.13 recommends that the silicon content of the weld metal in Al-Mg-Si alloys is kept above 2% to prevent solidification cracking [GUITERREZ 1996].

In alloys with critical Si content this can be achieved by addition of filler material with elevated Si content. Filler wire Al4047 A (SG-AlSi12), i.e. with 12% Si content, is apprehensively used to compensate for excess vaporization of Si, because Si is more volatile than Al. The remedy for solidification cracking is straightforward as far as material science is concerned. However, in laser beam welding the continuous and robust supply of filler wire poses a challenge to process technology. In the following only the supply of filler material in form of wire will be considered as the general case.

8.2.2 State of research and technology of filler material supply

Several attempts can be found in the literature to determine the amount of filler material needed in aluminium welding:

DILTHEY calculates the feed rate V_w of wire necessary to bridge a given gap in between abutted plates:

$$V_w = \frac{\pi \cdot d_w^2 \cdot v_f}{4 \cdot v_w} = A_{gap} \qquad \text{(Equation 8.1)}$$

where V_w is the wire deposition, i.e. the volume of filler wire per unit length in $mm^3\ mm^{-1}$, A_{gap} is the cross-sectional area of the gap in mm^2, d_w is the diameter of the wire in mm, v_f is the speed of the wire in m min^{-1}, and v_w the speed of welding in m min^{-1} [DILTHEY 2000].

However, the formula does not correlate the quantities involved to the alloying content in vol% of Si in the fusion zone, which is pivotal to prevent solidification cracking. Berkmanns renders a formula that correlates the desired alloying content in vol% of Si in the fusion zone of the weld c_w to the Si content in the base material c_b to the content of Si in the filler wire c_f:

$$c_w = \frac{A_{gap} \cdot c_f + (A - A_{gap}) \cdot c_b}{A} \qquad \text{(Equation 8.2)}$$

where A is the cross-sectional area of the fusion zone [BERKMANNS 1998, p. 87]. This formula - though mathematically correct - is not helpful to the welder to adjust or *anticipate* the process *variables*, i.e. velocity of welding and wire feed speed, to attain a desired content of Si in the fusion zone c_{fz} *prior* to welding. This formula represents the formula for the *dilution ratio* in abutted plates with a continuous gap. The dilution formula appears in various disguises. Huang introduces the cross-sectional area of the filler wire:

$$c_w = c_b \cdot \frac{A}{A + A_f} + c_{fz} \cdot \frac{A_f}{A + A_f} \qquad \text{(Equation 8.3)}$$

where $\frac{A}{A + A_f}$ is the dilution ratio.

A is the cross-sectional area of the base material and A_f is the cross-sectional area of the filler wire [HUANG 2003]. Although A_f is a *variant* of the process, it stays *constant* during welding and it cannot be varied at will, as only specific diameters of wire are commercially available. Hence, this formula - or any alteration of it depending only on the dilution ratio - is not sufficient to purposely adjust the process variables to achieve a desired Si content in the fusion zone. This is exactly what is needed to guide welding experiments to the end of crack-free welds.

Objective:

A formula that relates the in-line adjustable process variables, namely velocity of welding v_w and feed speed of the filler wire v_f, to the resultant, namely cross-sectional area of the fusion zone A.

To satisfy this objective a novel formula is presented in this dissertation. The filler dilution formula (FDF) fulfils these requirements. The derivation of the FDF and the associated errors can be found in appendix A.

The formula makes the following assumptions, whose validity will be scrutinized in due course:

1. Homogeneous mixture of base material and filler wire in the fusion zone
2. No excess vaporization or precipitation of alloying elements, especially of silicon

The FDF is:

$$c_{fz} = \frac{v_f}{v_w} \cdot c_f \cdot \frac{A_f}{A} + c_b \cdot \left(1 - \frac{A_f}{A}\right) \qquad \text{(Equation 8.4)}$$

where

c_{fz} is the Si content in vol% in the fusion zone (desired magnitude)

v_w is the velocity of welding (variable)

v_f is the feed speed of the wire (variable)

A_f is the cross-sectional area of the filler wire (known)

A is the cross-sectional area of the weld seam (resultant)

c_f is the Si content in vol% in the filler wire (known)

c_b is the Si content in vol% in the base material (known)

The FDF employs the ratio of v_f/v_w. This ratio represents a dimensionless group. Such groups are used in dimensional analysis. Dimensional analysis is, however, much deeper than simple consistency of formulas and can help to solve complicated problems without having to solve complicated equations. In some cases, where the equations describing a problem are not known, they can be guessed at by dimensional analysis. For this aim, a remarkable theorem enunciated by Edgar Buckingham in 1914 and an accompanying procedure is introduced:

Buckingham Π theorem:

A system described by n variables, built from r independent dimensions, is described by n - r independent dimensionless groups.

Procedure:

1. Guess at what are the important quantities in the problem
2. Apply the Buckingham Π theorem
3. Form from the important quantities all the simplest n - r possible dimensionless groups
4. The most general solution to the problem can be written as a function of the n - r independent dimensionless groups

As there are three independent variables in this problem, i.e. v_w, v_f, and A, and merely two independent dimensions, namely length and time, only one dimensionless group can be formed. This is the velocity ratio of v_f/v_w. The power of this approach becomes clear if the FDF is used to solve for the cross-sectional area A, c.f. equation 8.5. The variation of A versus the velocity ratio is shown in the plot in figure 8.14.

$$A = \frac{A_f}{c_{fz} - 0.005}\left(\frac{v_f}{v_w} \cdot 0.12 - 0.005\right) \qquad \text{(Equation 8.5)}$$

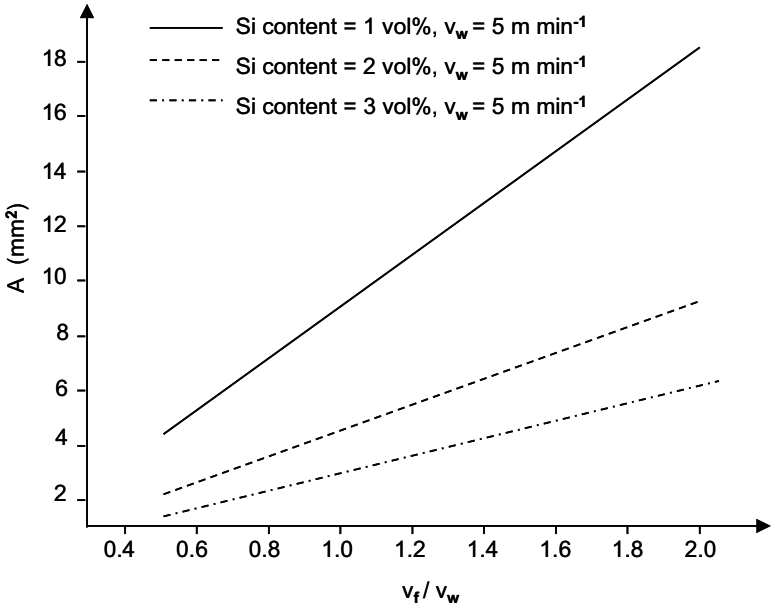

Figure 8.14: Plot of the cross-sectional area of the weld versus the velocity ratio for a constant velocity of welding and a desired dilution; A_f = ¼ π mm^2 (for diameter of filler wire of 1 mm as used within this dissertation)

The merit of this approach is to guarantee a desired dilution within the constraints set by the welding process. In many cases the cross-sectional area of the weld is dependent on the welding speed. *A* can be determined from any cross-section macrograph exhibiting cracks. The diagram in figure 8.14 guides the experimenter as to which feed speed of wire is most probably successful in generating crack-free welds. The experimenter needs to know the Si content necessary to reduce the susceptibility to solidification cracking. In many cases it might turn out that further experimental attempts are in vain as the magnitude of the velocity ratio is practically limited, because stick out of wire at the root occurs beyond a certain threshold velocity. The experimenter has to increase the melting efficiency or the diameter of the filler wire. An increase of melting efficiency can be achieved by virtue of other laser systems or more efficient laser welding techniques. In other words: the process *technology* itself must be improved to widen the accessible process window. Without sufficient

improvements new welding experiments assaying distinctive points in too small a process window do not make sense.

The FDF allows *forecasting* whether parameter settings could be potentially successful in experiments. The results can be analyzed by visualization of the figures obtained from welds in a graph incorporating the FDF. This graph is presented at the end of the next section. The following section describes the system technology to robustly feed filler wire to the fusion zone of the weld, which is a prerequisite for the assumptions (see above) on which the FDF is based.

8.2.3 Robust integration of filler material supply for BHLW

Customary filler wires have a diameter of 1 mm or 0.8 mm. The focal spot generated by the Nd:YAG laser has a diameter of 0.45 mm for a focal length of $f = 150$ mm. For any customary wire its diameter exceeds the diameter of the focal spot, which to a good approximation translates into the diameter of the keyhole. Hence, the positioning of the filler wire with respect to the focal spot of the Nd:YAG laser is cumbersome, and wire supply can in many cases not be robustly maintained. Common problems include drop formation, wire stick out at the root, and discontinuous filler transfer. If the wire feed speed is too high, a single Nd:YAG laser beam cannot completely melt the wire. As a result, part of the wire sticks to the surface and forms drops. If the feed speed is too high in thin sheet welding, the wire pins through the weld pool and sticks out at the root. If the feed speed is too low, the wire does not even reach the melt pool since a drop forms at the tip of the wire. This drop is sustained by surface tension. The drop falls onto the workpiece when its size and therefore its weight cannot any longer be balanced by surface tension. These problems can be overcome by proper adjustment of the filler wire positioning unit and selection of an appropriate feed speed. The process window concerning the feed speed of the wire had been the subject of modelling as well as experiment. The scope of these investigations was to determine the minimal feed speed preventing drop formation at the tip. An energy balance of laser power models the energy to melt the wire [BINROTH 1993, p. 30]. The minimal threshold velocity is, however, not checked for satisfactory dilution of alloying elements. It should be noted that excess filler may necessitate weld preparation such as slants to prevent excess filling, which is detrimental to mechanical loading properties [BINROTH 1993, p. 27-33].

Even if the filler wire is delivered to the melt pool, the transfer is not continuous in Nd:YAG laser welding. The wire tip gets sputtered into the keyhole upon successively obstructing the laser beam, as can be seen in high-speed imaging. This is a potential source of instabilities and inhomogeneous dilution. In sum, the supply of filler wire has to be painstakingly adjusted and imposes restrictions to the parameters of welding. Robust and continuous filler wire supply in *laser* beam welding cannot be regarded as state-of-the-art of technology. Only one industrial application has come to the attention of the author. For welding steels BMW and Mitsubishi created a welding head. In this application the wire is fed coaxially to the laser beam [EP 1 020 249 A2]. Otherwise, the supply of filler wire can still be regarded as not satisfactorily solved.

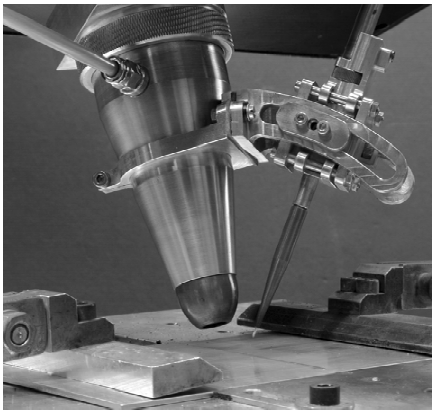

Figure 8.15: Filler wire supply unit mounted to a conical gas nozzle on the bottom of the experimental optic setup

In order to position the filler wire tip, a supply unit was designed allowing for the tip position to be repeatedly and accurately adjusted. The tip can be moved through a hemispherical volume centred on the focal spot of the Nd:YAG laser. To facilitate fine adjustment the tip location can be changed in normal direction to the hemisphere and sweep through an angle transverse to the direction of travel of the head. The supply unit attached to the conical gas nozzle is displayed in figure 8.15. By virtue of this supply unit the filler wire tip can be finely adjusted and varied to find the most robust filler wire tip position. This position was subsequently fixed and retained for further experiments. The leading position of the filler wire with respect to the Nd:YAG laser was assayed and compared to the trailing position. For the FDF to hold, the filler wire has to be

homogeneously distributed to secure continuous Si alloying throughout the weld fusion zone (assumption 1; c.f. p. 215). Whether the filler wire is supplied leading or trailing to the Nd:YAG laser's focus with respect to the welding direction significantly influences the dilution and distribution of the filler material within the fusion zone. In figures 8.15 and 8.16 the difference between a leading and a trailing filler wire position can be seen. The homogeneity of dilution of the leading position is obvious from the cross-section macrographs.

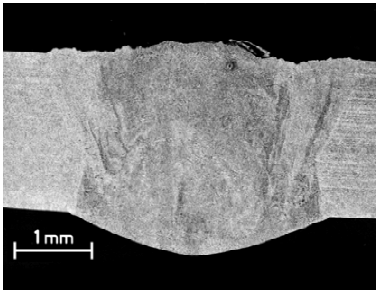

Figure 8.15: Dilution of filler material, trailing position of the wire; P_{BHLW} = 3 kW + 3 kW; f = 150 mm; φ = 20°; EN AW-6082 T66; filler Al4047 A (SG-AlSi12); $Ø_f$ = 1 mm; argon flow 25 L min^{-1}; v_w= 4.0 m min^{-1}; v_f = 3.0 m min^{-1}; butt joint

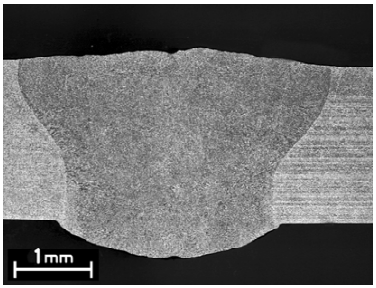

Figure 8.16: Dilution of filler material, leading position of the wire; P_{BHLW} = 3 kW + 3 kW; f = 150 mm; φ = 20°; EN AW-6082 T66, filler Al4047 A (SG-AlSi12); $Ø_f$ = 1 mm; argon flow 25 L min^{-1}; v_w= 4.0 m min^{-1}; v_f = 3.0 m min^{-1}; butt joint

When laser beam welding is integrated into a production line, e.g. in the automotive industry, the welding process should be able to tolerate misalignment between the edges of the pieces to be joined. The addition of filler wire combined with the extended spot of the HPDL measuring approximately 2 mm across

enables the bridging of wider gaps than could be tolerated by the Nd:YAG laser alone. Twin Spot technology allowed a gap of 0.4 mm with a 4 kW-Nd:YAG laser. The gap could be enlarged to 1.0 mm for two lasers with a total power of 5 kW [HOHENBERGER 2003, p. 94]. BHLW enables equally 1.0 mm of gaps to be tolerated and robustly bridged.

The addition of filler material does not affect the measured tensile properties of the weld. This could be the case, because the tensile strength of the filler wire is less than that of the base metal, as can be seen in table 8.3. The base metal was received in T6 temper, i.e. solution heat treated and artificially aged. The HAZ invokes the strengths of T4 as the material was melted but not heat treated, i.e. solution heat treated and naturally aged.

	unit	**EN AW-6060**	**EN AW-6060**	**S Al 4047 A**
temper		T6	T4	
density ρ	kg dm^{-3}	2.7	2.7	2.7
tensile strength R_m	N mm^{-2}	245	160	130
yield $R_{p0,2}$	N mm^{-2}	215	90	60
elongation	%	13	20	5
thermal conductivity λ_{th}	W m^{-1} K^{-1}	209	187	200 - 220

Table 8.3: Mechanical properties of base metal and filler material

Figure 8.17 shows the stop crater of a seam with a gap of 0.8 mm. The feed speed of the wire was accordingly adjusted to fill the gap as to create an overbead and root without undercut. Quasi-static loading tests showed no substantial trend towards lower tensile strengths as characteristic for T4, c.f. figure 8.19. Thus, proper dilution (assumption 1; c.f. p. 215) can again be demonstrated. For the graphs in figures 8.19 to 8.22 v_f was individually adjusted to fill the gap. Error bars are displayed whenever they could be resolved within the scale of the ordinate.

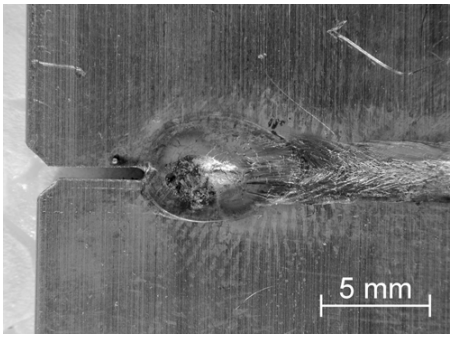

Figure 8.18: Gap bridging ability for 0.8 mm gap at the stop crater; butt joint; P_{BHLW} = 3 kW+ 3 kW; EN AW-6082 T66; filler Al4047 A; $Ø_f$ = 1 mm; argon flow 25 L min^{-1}; v_w = 5.5 m min^{-1}; v_f = 6.5 m min^{-1}

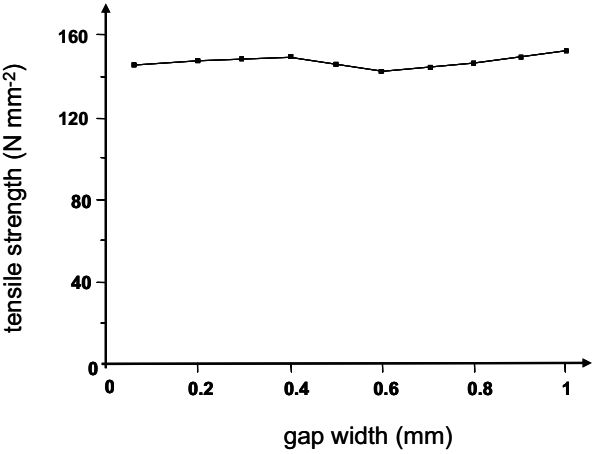

Figure 8.19: Influence of filler wire: tensile strength versus gap width; leading position of the filler wire; P_{BHLW} = 3 kW + 3 kW; argon flow 25 L min^{-1}; v_w= 4.0 m min^{-1}; EN AW-6082 T66; filler Al4047 A; $Ø_f$= 1 mm

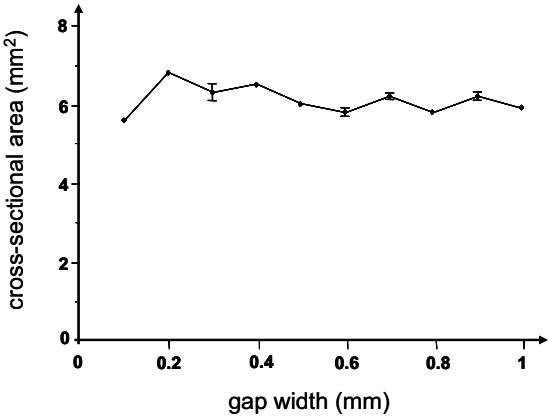

Figure 8.20: Influence of filler wire: cross-sectional area versus gap width; leading position of the filler wire; P_{BHLW} = 3 kW + 3 kW; argon flow 25 L min^{-1}; v_w= 4.0 m min^{-1}; EN AW-6082 T66; filler Al4047 A; $Ø_f$= 1 mm

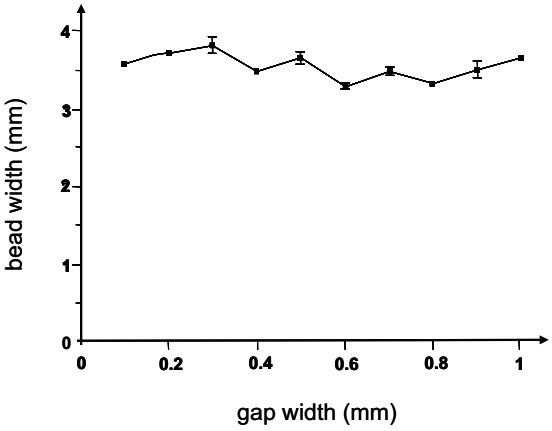

Figure 8.21: Influence of filler wire: bead width versus gap width; leading position of the filler wire; P_{BHLW} = 3 kW + 3 kW; argon flow 25 L min^{-1}; v_w= 4.0 m min^{-1}; EN AW-6082 T66, filler Al4047 A; $Ø_f$= 1 mm

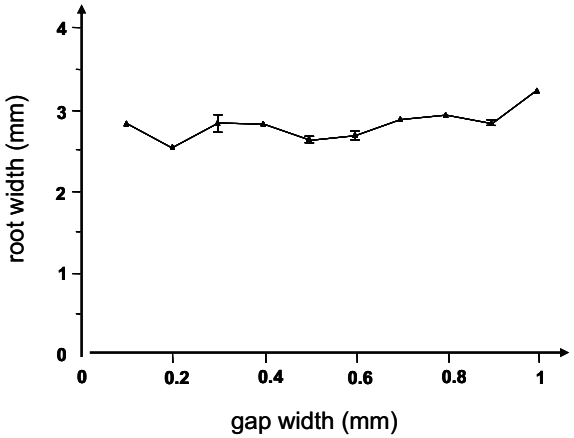

Figure 8.22: Influence of filler wire: root width versus gap width; leading position of the filler wire; P_{BHLW} = 3 kW + 3 kW; argon flow 25 L min^{-1}; v_w= 4.0 m min^{-1}; EN AW-6082 T66, filler Al4047 A; $Ø_f$= 1 mm

As discussed in paragraph 6.3 for porosity, the supply of cold filler material affects porosity due to the restrictions set by the experimental optic head. The experimental head did not allow for the wire to be fed in the plane defined by the workpiece, surface normal, and the direction of welding. Since the cold wire is positioned on one side of the weld pool of the HPDL the pertinent side of the bead shows an increased temperature gradient since the wire is supplied at ambient temperature. This leads to some perturbation of this side of the weld pool. The filler material supply batch allows preheating of the wire. A high charge at a voltage below threshold for arc ignition heats up the wire by the Peltier effect. Preheating was not considered within this dissertation.

The dilution of filler wire can be seen in surface cross-section macrographs of figures 8.23 and 8.24. For filler feed speeds far below the necessary dilution, solidification cracks span across seams welded with BHLW. For increased filler supply rates the cracks are limited to the areas at the edges, where the Nd:YAG laser did not properly dilute the melt by keyhole motion, as can be seen in figure 8.24. The corollary is that for convectional mixing a higher dilution is necessary in those parts of the melt pool which are induced by the HPDL.

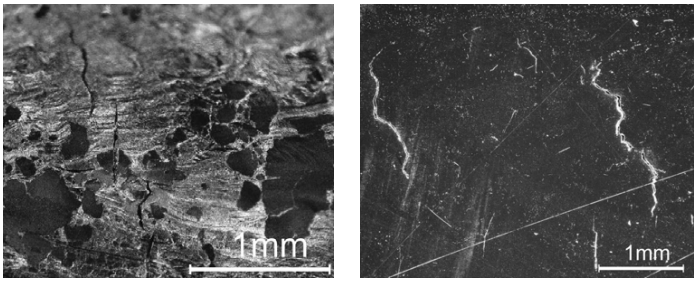

Figure 8.23: Dilution of filler material for v_f = 1.5 m min^{-1}; left: surface photograph; right; surface macrograph; v_w= 4.0 m min^{-1}; P_{BHLW} = 3 kW + 3 kW; f = 150 mm; φ = 20°; argon flow 25 L min^{-1}; EN AW-6082 T66; filler Al4047 A (SG-AlSi12); Ø$_f$ = 1 mm; butt joint

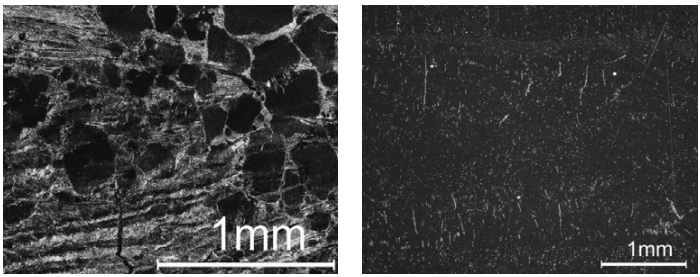

Figure 8.24: Dilution of filler material for v_f = 3.0 m min^{-1}; left: surface photograph; right: surface macrograph; v_w= 4.0 m min^{-1}; P_{BHLW} = 3 kW + 3 kW; f = 150 mm; φ = 20°; argon flow 25 L min^{-1}; EN AW-6082 T66; filler Al4047 A (SG-AlSi12); Ø$_f$ = 1 mm; butt joint, note the fine transverse cracks close to edge

The dilution ratio and therefore the solidification crack susceptibility depend on the ratio of v_f / v_w and the absolute magnitude of v_w. For ratios of v_f/v_w > 1, i.e. filler feed rates *exceeding* the speed of welding, the filler wire tends to get pushed out on the root side or to get stuck to the edge of the weld pool on the surface leading to sputter marks obvious to the naked eye, c.f. top row in figure 8.25. In etched surface section macrographs this results in a wavy edge of the melt pool where the wire was positioned in, c. f. picture in the second row in the middle column in figure 8.25. This in turn affects the overall process robustness reducing homogeneity of mixing and the melting efficiency. Figure 8.25 shows

that hot cracks are only absent for $v_f / v_w \geq 1$, i.e. filler feed rate exceeding or *equalling* the speed of welding.

Henceforth, the stable ratio for v_f/v_w mirroring both constraints is:

$$v_f/v_w = 1$$

This makes further experimental investigations easier, because these two parameters are not varied independently since the variation of one fixes the other. Figure 8.25 proves how the ratio v_f/v_w was constrained to a fixed value.

The dilution of the filler wire does not only rely on homogeneous mixing but also on the amount of molten material, i.e. the melting efficiency. Figure 8.14 displays the inversion of the FDF to read off the calculated dilution for a given cross-sectional area. This graph 8.14 being termed a *diagram* implies that the underlying melting efficiency stays *constant*. However, the FDF renders a graph, which is in fact a *chart*, as the real values from experiment show that the melting efficiency varies according to how much filler material is supplied. This is due to the fact that the melting of the filler wire reduces the energy available for melting of the base metal. Hence, the cross-section macrographs of the seam are not symmetric, as can be seen in the bottom row in figure 8.25. The fusion zone boundary of the melt pool is much steeper at the side where the wire was fed into the melt pool.

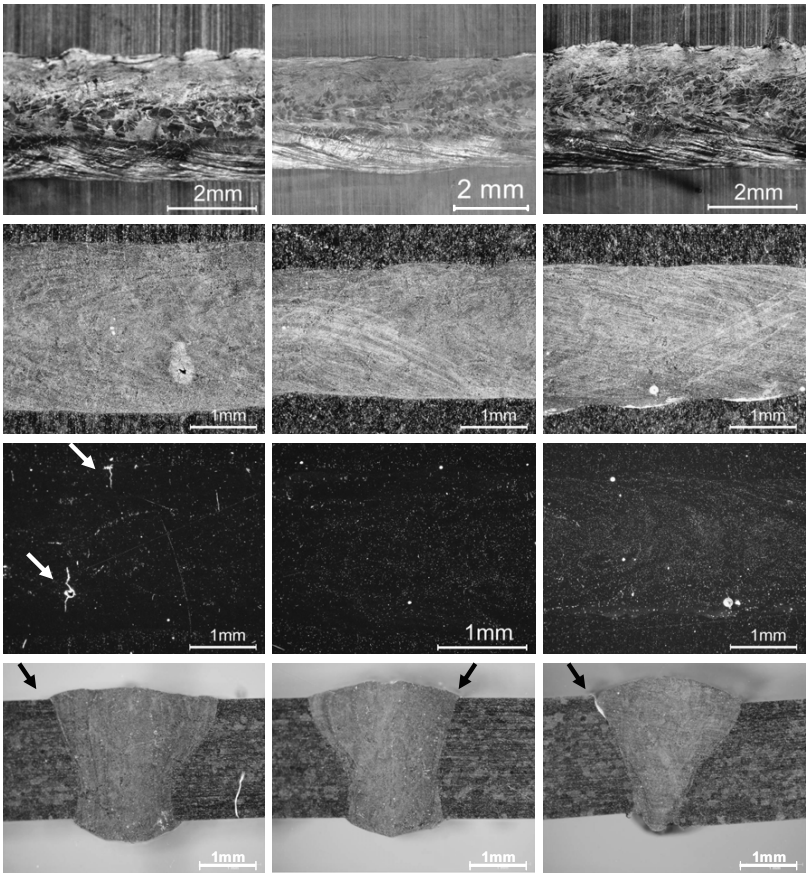

Figure 8.25: Dilution of filler material; left: v_w= 5 m min^{-1}; v_f = 4 m min^{-1}; middle: v_w= 5.5 m min^{-1}; v_f = 5.5 m min^{-1}; right: v_w= 6 m min^{-1}; v_f = 7 m min^{-1}; 1st row: top surface photograph, 2nd row: etched horizontal cross-section macrograph; 3rd row: horizontal cross-section to visualize cracks and pores indicated by white arrows; 4th row: cross-section macrograph, black arrows designate position of filler wire supply; P_{BHLW} = 3 kW + 3 kW; f = 150 mm; φ = 20°; argon 25 l min^{-1}; Ø$_f$= 1 mm; butt joint; EN AW-6060

The influences of the wire can be qualitatively seen in the FDF chart shown as figure 8.26. The FDF chart resolves the ratio of speeds by displaying the speed of welding to create a 3D-representation.

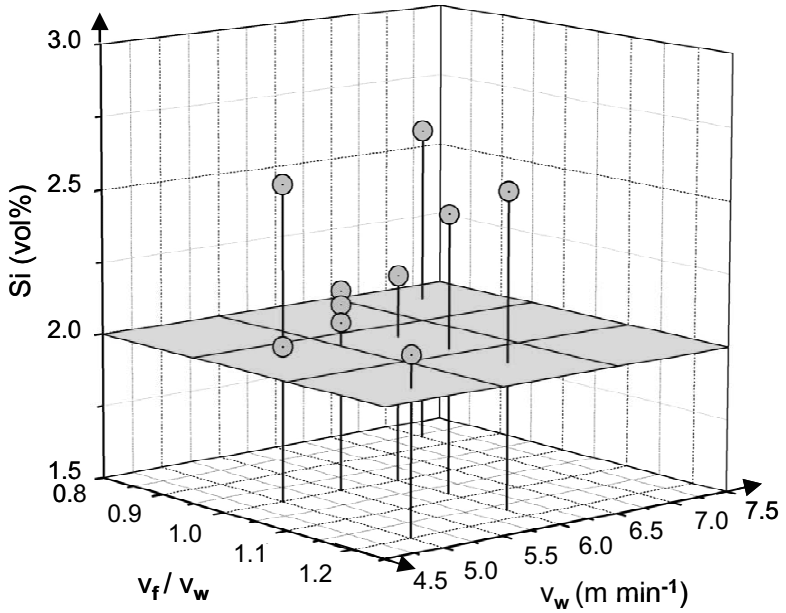

Figure 8.26: Filler dilution chart according to the filler dilution formula (FDF)

The FDF chart depicts the Si content as calculated according to the filler dilution formula. To clearly show that the values stem from experiment, bullets are displayed instead of a continuous area fitted by some customary regression method. For each point five samples were assayed. For clarity, errors are not shown in the chart. The errors in the cross-section are calculated in appendix A. They are very small, i.e. below 10%, and are therefore not displayed by error bars. If the cross-sectional area of the fusion zone is small, the Si content is increased for a given feed rate of filler wire. At first blush, this might seem to be a desired result with regards to hot crack susceptibility. However, for ratios of $v_f / v_w > 1$ this has to do with the inhibition of convectional fluid flow within the HPDL melt pool resulting in a higher nominal dilution according to the FDF. This trend can be seen in figure 8.26 where an incremental increase of welding

speed in individual steps of 0.5 m min^{-1} leads to an over-proportional decrease of the cross-sectional area. As stated above, only the ratio $v_f / v_w = 1$ is of interest. In the FDF chart in figure 8.26 the results for this ratio demonstrate clearly that for $v_f = v_w = 5.5$ m min^{-1} the most robust result could be achieved. Three sets of values, each of which is drawn from five samples, allowed comparable result. This point, i.e. $v_f = v_w = 5.5$ m min^{-1}, was the starting point (1st value at this point) for the following experiments, because this point was selected according to the rules of statistical planning and design of experiments.

The speed was decreased and gave the lower value for $v_f = v_w = 5.0$ m min^{-1}. The experiment was repeated at $v_f = v_w = 5.5$ m min^{-1} (2nd value at this point). The speed was then raised to $v_f = v_w = 6.0$ m min^{-1}. The value obtained showed the largest error in the mean of A, namely 7%, indicating a less robust process. Even minute adjustments of the supply unit tip to support the feed of the wire by another position did nothing to the better. The starting point was redone giving the 3rd value again to good agreement with the previous results notwithstanding the adjustment of the supply unit beforehand. Thus, its robustness was clearly demonstrated. Finally, the speed was decreased to $v_f = v_w = 5.0$ m min^{-1}. Due to the previous adjustment this resulted in yet a different value as before. Hence, it could be established that $v_f = v_w = 5.5$ m min^{-1} is a very robust set of parameters for crack free and robust welds and had a favourable Si content of 2.19 % ± 0.20 vol% in the fusion zone (calculated according to the FDF). This set of parameters could be easily established for those samples with the FDF.

BHLW is advantageous for robust supply of filler wire. The wire can be stuck into the rectangular focal spot of the HPDL, which measures about 1 mm along its fast and 4 mm along its slow axis. This is a major advantage as compared to welding solely with the Nd:YAG laser for which the size of the keyhole is smaller than the diameter of the filler wire to be fed into it. Berkmanns showed that it was not permissible for the wire tip in Nd:YAG laser welding to be farther away from the focal spot than 0.4 mm [BERKMANNS 1998, p. 83]. This constraint significantly reduces accessibility. The wire feed tip in BHLW was as far as 15 mm distanced from the workpiece surface, thereby, guaranteeing highest *accessibility* and *robustness* of filler wire supply during welding.

In addition, high-speed imaging reveals that in BHLW the filler wire is not sputtered into the keyhole when struck by the laser beam as in Nd:YAG laser welding. On the contrary, the intensity within the spot of the HPDL is not high enough to instantly melt the filler wire. The wire gets melted upon being stuck

into the melt pool of the HPDL. The molten filler wire is diluted within the melt pool by convectional fluid flow and subsequently stirred downwards by the rapid motion of melt around the keyhole. This results in a decreased demand for fit-up of the filler wire supply, as the keyhole is notably unstable in welding of aluminium with the Nd:YAG laser alone. The introduction of filler wire to a laser welding process often leads to more problems [GREF 2005, p. 105].

In BHLW the filler wire is introduced to the calm CMW melt pool of the HPDL, thus not affecting keyhole welding of the Nd:YAG laser. In addition, the Nd:YAG laser can be switched off without affecting the continuous melt down of filler wire. The strategy described in paragraph 7.2 allows easy prevention of stop craters. This strategy is *exclusively* feasible by BHLW. The transfer of filler is therefore *non-invasive* and moreover *continuous*. The continuity of wire transfer is an enabling factor for the measures of quality control of filler wire supply outlined in the following section.

The properties of the welds with filler wire were tested in quasi-static tensile loading. The tests curves render the static mechanical properties, as shown in figure 8.27. The weld properties of BHLW with filler wire are above those of an Nd:YAG laser weld with filler and as expected well above those of Nd:YAG laser welding without filler material. In figure 8.28 the absence of filler material leads to a failure within the seam. BHLW seams did fail in the HAZ provided the wire feed rate was chosen to guarantee sufficient dilution.

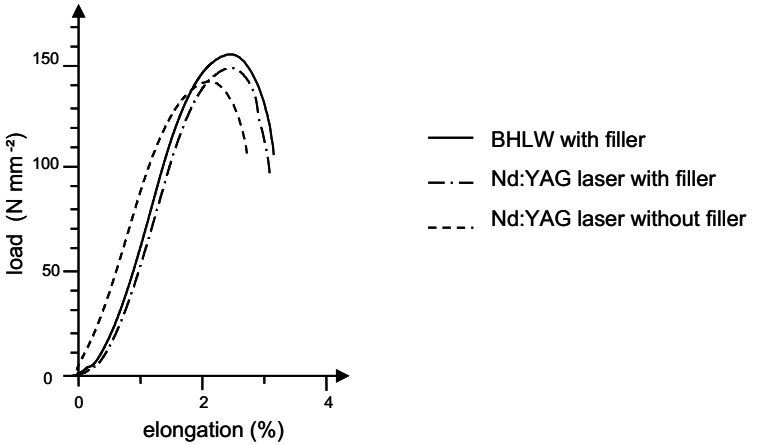

Figure 8.27: Load elongation curve for quasi-static transverse tensile tests of EN-AW 6060 welded with BHLW as compared to an Nd:YAG laser seam with and without filler, transverse tensile test according to DIN EN 10002 and specimen according to DIN EN 895

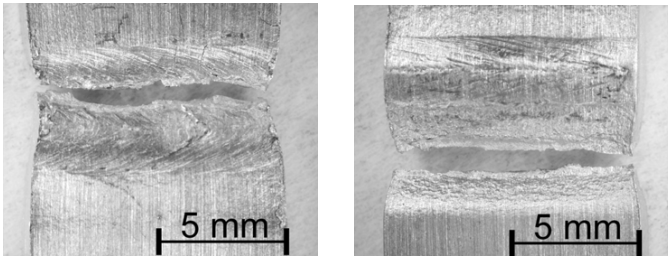

Figure 8.28: Left: failure in the fusion zone of the test specimen; $P_{Nd:YAG}$ = 3 kW; v_w = 3 m min^{-1}; right: failure in the HAZ of the test specimen; P_{BHLW} = 3 kW + 3 kW; v_w = 5 m min^{-1}; v_f = 5 m min^{-1}

The loading tests were performed according to DIN EN 10002-1. In this standard the testing procedure and the rules for quasi-static tensile loading tests of metallic materials are defined. The testing apparatus was calibrated according to DIN EN 10002-2 and the testing speed set to 50 mm min^{-1}. The dimensions of the test specimens were chosen according to DIN EN 895 [DIN EN 10002, DIN EN 895].

8.3 Quality control of filler wire supply

The continuity and robustness of the filler wire supply are enabling factors for easy and affordable means of quality control. The state of research and technology of laser seam inspection is given by Landolt and will not be detailed here [LANDOLT-BÖRNSTEIN 2004, p. 243-275].

Quality control of filler wire supply is, if done at all, integrated into the optical sensors' signal analysis. The inspection of the seam and keyhole control by processing an optical signal for brightness is a demanding task for calibration and data analysis. The systems available are expensive to purchase and their integration into the process is a challenge and differs according to the process' characteristics and tolerance bands in the signal. For example, whether the wire forms a drop above the weld pool upon transecting the beam of the laser is difficult to securely detect by a shift of brightness alone.

In arc welding filler is always transferred to the fusion zone in form of droplets. In GMAW the detachment rate can be controlled by the AC current settings. Filler wire transfer, however, is always discontinuous in Nd:YAG laser welding as was shown by high speed photography. When the filler wire intersects the beam path small droplets are detached. In some cases this does not take place and a larger drop accumulates at the end of the filler wire tip. The drop is detached once it has grown too big to be sustained by surface tension. This causes distinctive drops on the surface of the seam, c.f. figure 3.17. The challenge of filler wire integration for some state-of-the-art technologies was detailed in paragraph 3.2. While a droplet is growing to become a drop no filler material is transferred to the fusion zone and micro cracks do frequently arise. A distinction between drops and droplets is elucidating, and those species are defined in this dissertation as follows: *Droplets* are continuously detached and thus transferred to the weld pool, whereas the formation of a *drop* indicates that the transfer is disturbed. It is notoriously difficult to calibrate a sensor system to discriminate between droplets and drops.

In BHLW the filler wire runs continuously into the melt pool. Thus, formation of drops, or droplets, or sputtered supply of filler can equally be regarded as perturbation. This allows direct controlling of the continuity of the contact between the wire and melt pool by an indicator current. The variation of filler wire velocity controlled by the wire feed unit is shown in figure 8.29.

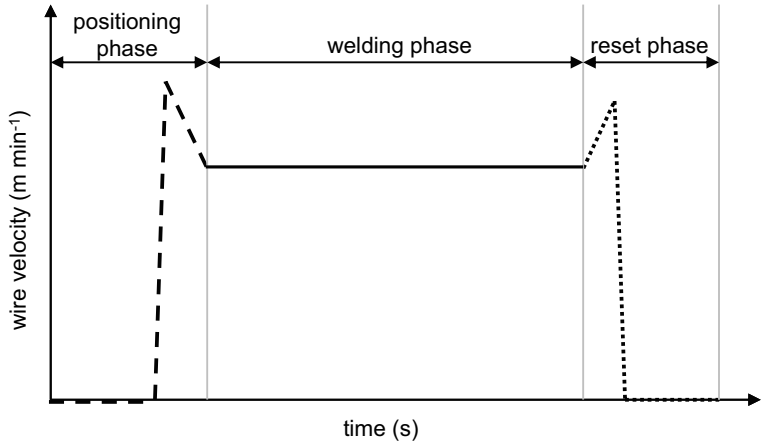

Figure 8.29: Velocity of filler wire for specific welding phases

The variation of the indicator current is shown in figure 8.30:

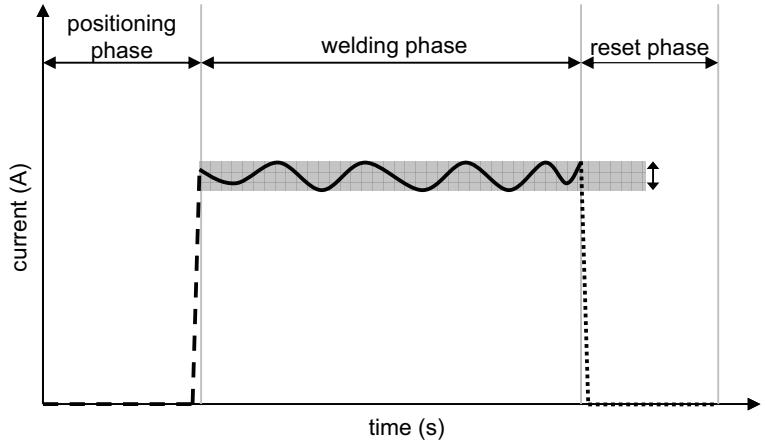

Figure 8.30: Variation of indicator current of filler wire for specific welding phases

The current signal can be fed into a system for continuous data monitoring and processing based on Boolean algebra. This can be executed by a LabVIEW routine. The time intervals of positioning, welding, and reset phase are defined

by time instants that are determined by signals provided by the programmable logic controller (PLC) of the filler wire supply unit.

Three steps can be monitored and assayed:

1. The current rise upon positing of the wire must take place in the respective time interval, as otherwise the wire did not touch the workpiece.

2. The indicator current may fluctuate within a tolerance band in the welding phase but must not cease, as otherwise droplet formation occurred.

3. The current fall upon withdrawal of the wire must take place in the respective time interval, as otherwise the wire was not melted by the beam and scratches on the workpiece's surface.

These three stages can be tabulated in a truth table and connected by a logical conjunction: i.e. a Boolean AND operator. Logical conjunction is an operation on logical values, typically the values of propositions, that produces a value of *true* if and only if all of its operands are true. Thus, the weld is only accepted if all three propositons are simulateneously true. Or otherwise, the weld is rejected if only one of them is false. On the quality monitoring display this can be shown by a binary quality signal. However, a complete misalignment was never observed with the filler wire end unit shown in figure 8.30.

8.4 Summary of system technology

In this chapter the improvements on system technology for BHLW were described. Appropriate system technology is a critical enabling factor for transfer of a welding technology form the laboratory to a production line in industry. Some technologies inherently lack the possibility for an adequate system technology to be developed, since their requirements for cleanliness, space, and accessibility cannot be satisfied in a workshop-like production plant, which is in most cases not a cleanroom.

The experimental optic setup suffered from several drawbacks, which were overcome by the prototype optic head. The accessibility of the head mounted on a robot was as good as a conventional Nd:YAG laser head with filler wire supply or in fact any conventional RSP-weld-clamp, which today still enjoys a widespread use in manufacturing. The beam path and its optical components

were improved compared to the experimental optic setup by optical engineering. Optical engineering software allowed planning and testing of several components without actually building yet another experimental optic setup to accommodate those components. This saved a lot of time and money.

Moreover, some system technologies in laser welding, c.f. paragraph 3.2, are so involved that only *scientists* could ever adjust, maintain, and operate them. A process that runs satisfactorily every now and then in the laboratory for a reference sample geometry might run aground if a reliable *repeat* accuracy needs to be guaranteed by *technicians* for variable workpieces at a high piece number per unit time in industry.

The prototype head, therefore, was an integrated and closed system for easy adjustment by technicians. As it was sealed off from external influences, such as dust, it needed little maintenance by technicians, thus avoiding non-productive times. Actually, the head was put to the test by letting students of either sex, which were considered to be knowledgeable proband people, act as proxy for technicians. The students were all able to adjust and handle the system within a day of training. The gimbal mount of the mirror and the wire feed system was easy to manipulate. The FDF allowed calculating the filler feed rate for a desired dilution. It turned out that the necessary dilution to achieve welds free of cracks was lower for BHLW as compared to Nd:YAG laser welding. The wire supply unit was easy to operate. The quality control allowed checking whether the settings guaranteed continuous filler wire transfer to the melt pool. If the filler wire transfer was interrupted, those parts were separated out. Hence, the system technology of BHLW is fit to be integrated into an industrial manufacturing process. In the future an optical setup creating a similar intensity distribution and the virtues of bifocality will be developed that relies on one laser source only.

9 Economic Case

In the proverbial chapter on the economic case, its authors facilely demonstrate the case by reliance on reduced unit costs. These calculations are normally based on assumptions which make them at best idealized or at worst fatally flawed. Each individual case has its own applications and needs, meaning that each one has unique circumstances and financial constraints. In current industry, dependant as it is on welders to apply hand-held techniques, difficulties in staffing make reaching production goals difficult. Welders are exposed to noxious emissions, which necessitate sophisticated equipment to satisfy health and occupational safety standards. Welding is regarded as heavy labour, and recruitment suffers from a shortage of applicants [MIKLOS 2004; BRAT 2006].

For reasons of laser safety and process velocities, laser beam welding is normally accomplished by standard kinematics such as robots or machining centres. Resistance spot welding has traditionally been applied by robots in the automotive industry. However, in ship and aircraft building, automation regarding welding has not taken place to a high degree as batch sizes are very small. In small-sized businesses hand-held welding is prevalent. This is not about to change – in handicraft enterprises the investment for laser sources is normally too high to amortise. Nonetheless attempts for hand-held laser welding systems have been made. It is dubious that they have conformed to laser safety standards. Whereas classical arc welding technologies cannot be automated, as they require a welder for good quality, laser welding is capable of being readily automated. Thus, laser safety standards do not only *necessitate* automation, but laser welding is *appropriate* for automation.

In small and medium-sized businesses (SMB) the application of robots and machining centres is increasing. Thus, laser welding applications can be readily adapted. In vehicle production enterprises laser welding applications are commonplace. Clearly then, the circumstances dictate whether a robot is needed. One suitable for welding costs approximately € 35.000.

Industrial experts are welcome to make their own cost estimates based on the following economic vertices of BHLW. The market launch of novel laser sources, such as fibre laser and HPDL of up to 10 kW output power, will substantially effect the prices of other high power cw-lasers such as Nd:YAG and CO_2 lasers. For BHLW, a conventional lamp pumped 3 kW-Nd:YAG laser was used for which one kilowatt of laser power cost approximately € 100.000. One

kilowatt of HPDL power comes at half this price: € 50.000. However, using BHLW, the velocity of welding could be doubled or more as compared to single spot welding with the same power of an Nd:YAG laser alone. This represents a cost saving of 25%. As compared to multiple or Twin Spot laser welding, BHLW results in even greater cost savings, as a considerable fraction of the beam power is used only for 'process stabilization' and does not contribute to the welding process, that is, penetration depth and velocity of welding. These important parameters for production engineering are set by the power attributed to the major spot. As described in section 3.2.3, the auxiliary laser spot in multiple or Twin Spot laser welding is often intentionally defocused, thus degrading beam quality. This beam, however, comes from an otherwise superior laser source with good BPP which enables the welding process by the focused major spot. This amounts to wasting the BPP product in the auxiliary spot. In BHLW the BPP of the HPDL is not inherently inferior to an Nd:YAG laser. However, as shown above, the BPP of the HPDL is sufficient to achieve the necessary results, such as the melting of the zinc or oxide layer on the surface and distancing out the isotherms of melting and vaporization to satisfy proposition I and II (c.f. p. 85 f. and 89 f.) of the new empirical process model. Moreover, the HPDL provides a rectangular spot and can be focused independently onto different planes in and on top of the workpiece. In multiple or Twin Spot laser welding the auxiliary spot is defocused to attain focal spot sizes of the order of magnitude of the HPDL in BHLW. In this case, however, the beam does not interact with the material in its focal plane where the beam material interactions are strongest. Although the HPDL has inferior beam quality compared to the Nd:YAG laser, it is most efficiently utilized in BHLW.

Currently there seems to be a market developing for second-hand lasers for applications such as cutting and cladding, the improved BPP of fibre and disc lasers being very advantageous. The conventional Nd:YAG laser systems formerly employed are on the market and quite affordable.

Other technologies, such as laser stir and laser augmented MIG welding, can achieve welds of comparable quality in aluminium and allow integration of filler wire. An advanced filler wire supply unit costs approximately € 30.000. Quality control is ensured by BHLW as the continuity of filler wire transfer allows for robust, inexpensive, and secure monitoring utilizing an indicator current processed and evaluated by Boolean algebra. State-of-the-art welding technologies have to resort to optical sensor signal analysis of drop formation at the tip of the filler wire. Systems available are expensive and in some case

prohibitively so, and their calibration for a specific process is elaborate and represents only a single solution. Currently, the formation of an excessively large drop indicating delay of droplet detachment is not a plug-and-play solution for any sensor system found in the literature. The filler wire in BHLW is not detached in droplets but runs evenly and continuously into the melt pool. Thus, by virtue of a steady indicator current it can be monitored and processed irrespective of process specifics such as the drop's size and the brightness of the surroundings. It is an easy solution that can be transferred even if the parameters or the setup for welding are changed. These sensor systems can easily cost at least € 100.000. Calibration is bound to create further expenses.

Laser augmented MIG and Laser Stir Welding (LSW) are less flexible regarding other peripheral technology. The coaxial nozzle system detailed in chapter 5 cannot be used for LSW. Gas consumption in laser augmented MIG welding is higher since the interaction zone of an arc welding process is extended as compared to a laser welding process. The savings in gas consumption are impressive, as shown in section 5.1.4. The reduction of gas consumption greatly affects a welding application's running costs.

For welding of zinc-coated steels BHLW is the only realistic choice. In laser augmented MIG welding spatter could not be eliminated even by the expediency of leaving out one of the zinc layers in the overlap. The spatter is flung far from the seam and is deposited on the structure. This requires additional workers for scraping it off who would not be needed if BHLW were used. Moreover, it appears that adapting the process calls for relatively modest skills. The new empirical process model encoded in proposition I and II (c.f. p. 85 f. and 89 f.) and the gas entrainment caveat are relatively simple to understand and the adjustments are easily made for new tasks, such as a different thickness of zinc-coated steel sheets or the like. There are just two micrometer heads and the result can be anticipated from tabulated values. This optic is hardly used in production lines because the adjustment of the Twin Spot head used in the benchmark study is complex. This head's use is confined to researchers at a number of industrial laboratories. The technicians who run BHLW are not unduly taxed by it because it is easily explained and its results are predictable.

Finally, BHLW is a technology by which *all* aluminium alloys and zinc-coated steels can be welded to the highest quality using the same optical head, process, and system technology; for those alloys it is indeed the most flexible.

At first blush, the two laser systems used in BHLW appear cost intensive. However, the superiority of results as compared to any other state-of-the-art technology makes BHLW inimitable if aluminium and zinc-coated steels are to be welded to highest quality. Cost savings by doubling the speed of welding, by reduction of expensive, scarce helium by the double coaxial nozzle system, and easy and inexpensive continuous quality control are cogent economic arguments for BHLW if peripheral and running costs are fully taken into account.

10 Vision

Several applications are envisaged for BHLW. Consider chronologically the development of joining technology regarding the seam joining the roof to the body frame in car body manufacturing. First, resistance spot welds (RSW) followed by a rolled pressure-weld seam were used, which required a double-flanged seam as the fusion zone needed to be accessed by the resistance spot clamp. The joint geometry is displayed in figure 10.1.

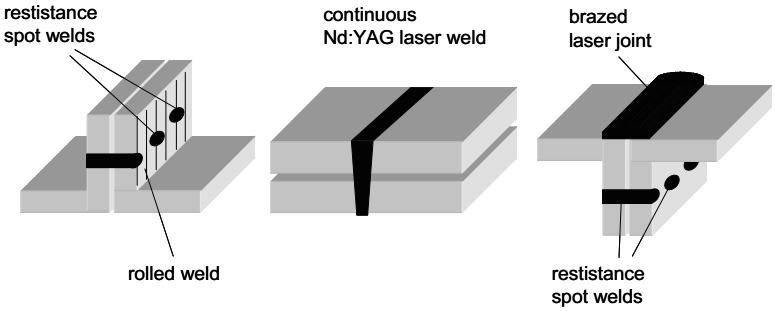

Figure 10.1: Joint geometries and associated welds and welding techniques for a roof-body-seam; left: roll and RSW; middle: Nd:YAG laser welding; right: brazing and RSW

Second, a continuous Nd:YAG laser seam was used in an overlap joint. For Nd:YAG laser welding only optical accessibility is required. However, the seam needs a cover to conceal or disguise its unsightliness. Currently, the most advanced form of this seam is achieved by laser brazing. The brazed seam is distinguished by its high surface quality and can be directly lacquered. Yet this seam needs to be supported by spot welds for stability at flanges pointing towards the interior. Hence, the demands on accessibility are more than those of Nd:YAG laser welding. A seam done by BHLW unites the strength of a continuous deep penetration laser weld with a surface quality equal to a brazed seam. Thus, RSW could be made redundant for this joint geometry. Even zinc-coated steels in an overlap joint, as in figure 10.1 in the middle, can be generated to the highest quality by BHLW. Other applications include thick-section welding for paper machinery. Such a seam needs liquid-proof welds to safely contain cooling agent fluids.

Magnesium welding, which poses a major challenge, will undoubtedly be undertaken in the near future. Magnesium is extremely difficult to fusion weld at all due to its magnesium oxide layer. However, an enhanced version of BHLW could be promising and is worth researching.

11 Conclusion

This dissertation has presented the process innovation of BHLW. While researching the fundamentals of LBW of aluminium, it became obvious that most state-of-the-art empirical process models suffered from seeming antinomies which ultimately could not be reconciled with the experimental evidence. This evidence was often documented in the literature with a paucity that forbade comparison. This necessitated benchmark studies under *ceteris paribus* conditions. This dissertation endeavours to state fully the process parameters needed to compare different process technologies. To do so, the merit of process efficiency specifically is the focus when comparing the various processes. Even the best wall-plug efficiency of the laser systems employed does not make up for reduced process efficiency. Thus, a new the welding efficiency was measured by a calorimetric measurement. The results allowed the accounting for the synergies of BHLW. In order to do justice to matters only those results have been called a synergy that have exceeded the mere sum of the processes constituting the hybrid process, a designation scheme to be borne in mind given that synergies are insouciantly claimed by other technologies but are rarely proven to exist.

State-of-the-art technology of gas shielding, filler wire supply, and quality control was shown to be insufficient. Thus, each was not only improved but harmonized and integrated into BHLW. A complete system technology together with auxiliary technology was developed. This appears to have been hitherto neglected. Good results had been achieved in laboratories but whenever they were to be transferred to industry problems had arisen. Generally this discredited laser technology, and, within industry, much trust dissipated. A number of manufacturers have reacted to this vigorously, even to the extent of replacing those laser processes by conventional technologies, and they have offered bonuses to their employees to replace ill-conceived laser processes. The once new-fangled laser has lost its innocence and has to face the realities and constraints of industrial manufacturing. Innovations dawn one upon another. They need to be simplified in order to be understood, taught, and applied by technicians. Thus, researchers should scrupulously assess their findings and ask themselves point-blank whether they have done enough research on *application* in its multitudinous aspects. In engineering a result that cannot be really applied can be put to one use only: *non sequitur.* The dissertation's author has striven to do otherwise.

12 Bibliography

AICHELE 2005
Aichele, G.: Herodot und der erste Schweißer der Weltgeschichte. In: Schweissen und Schneiden; 10/2005, p. 561-566.

ALLMEN 1995
Allmen, M.; Blatter, A.: Laser-Beam Interactions with Materials, Physical Principles and Applications. Springer 1995.

ANDREWS & ATTHEY 1976
Andrews, J. G.; Atthey, D. R.: Hydrodynamic limit to penetration of a material by a high-power beam. In: J. Phys. D.: Appl. Phys., Vol. 9, No. 15, 1976, p. 2181-2194.

ARATA 1978
Arata, Y.; Maruo, H.; Miyamoto, I.: Application of laser material processing - Heat flow in laser hardening. IIW Doc. IV-241-78, IIW Doc. 212-436-78, 1978.

BACHHOFER 1997
Bachhofer, A.; Rapp, J.; Schinzel, C.; Heimerdinger, C.; Hügel, H.: Laserstrahlschweißen von Aluminiumlegierungen unter reaktiver Schutzgasatmosphäre; Teil I: Energieeinkopplung und Prozessstabilität; [Part II was never published, remark by the author] In: Aluminium, International Journal for Industry, Research and Application, 73 (1997) 11, p. 790-795.

BECK 1996
Beck, M.: Modellierung des Lasertiefschweißens, Laser in der Materialbearbeitung. Forschungsberichte des ISFW; doctoral dissertation. Univ. of Stuttgart. Stuttgart: Teubner 1996.

BECK & BERGER & HÜGEL 1992
Beck, M.; Berger, P.; Hügel, H.: Keyhole Modelling during Laser Welding. In: Proc. of European Conference on Laser Treatment 1992 (ECLAT'92), Mordike, B. L. (ed.), (DGM Informationsgesellschaft, 1992), p. 693-99.

BENTER 2003
Benter, C.; Seme, B.; Petring, D.; Poprawe, R.: Application of new diode laser tools for cutting and welding. In: LIM 2003. Proc. WLT conference, Munich 2003, p. 85-95.

BERKMANNS et al. 1992
Berkmanns, J.; Behler, K.; Beyer, E.: Schweißen von Aluminiumwerkstoffen der Legierungssysteme AlMg und AlMgSi. In: VDI Technologiezentrum Physikalische Technologien (ed.): Broschüre zur Abschlußpräsentation des vom BMFT geförderten Verbundprojektes "Fügen mit CO_2-Hochleistungslasern". Düsseldorf 1992, p. 37-47.

BERKMANNS 1998
Berkmanns, J.: Steigerung der Prozeßstabilität beim Laserstrahlschweißen von Aluminiumwerkstoffen mit Strahlleistungen bis 6 kW und Tragverhalten der Verbindungen; doctoral dissertation, Aachen: Shaker 1998.

BESKE 1991
Beske, E. U.; Meyer-Kobbe, C.: Prozeßdiagnose beim Laserstrahlschweißen. In: Laser und Optoelektronik (1991) 23 (3), p. 134-140.

BESKE 1992
Beske, E. U.: Untersuchungen zum Schweißen mit kW Nd:YAG-Laserstrahlung, doctoral dissertation, Univ. Hanover. Hanover 1992.

BEYER 1995,
Beyer, E.: Schweißen mit Laser: Grundlagen. Berlin: Springer 1995.

BEYER 1987
Beyer, E.: Schweißen nmit CO2-Hochleistungslasern. In: Cleemann, L. (ed.): Technologie Aktuell; Reports · Analysen · Prognosen; VDI Verlag, Düsseldorf 1987.

BIBEAU 2006
Bibeau, C.; Rhodes, M. A.; Atherton, L. J.: Innovative Technology Enables a New Architecture for the World's Largest Laser. In: Photonics Spectra. 06/2006, p. 50-60.

BINROTH 1993
Binroth, C.: Das Abschmelzen von drahtförmigem Zusatzwerkstoff durch einen fokussierten Laserstrahl - Experiment und Modellierung-. Grundlegende Untersuchungen zur Wechselwirkung zwischen Strahl, Zusatzdraht und Aluminiumgrundwerkstoff beim Laserstrahlschweißen. In: Geiger, M.; Hollmann, F. (ed.): Strahl-Stoff-Wechselwirkung bei der Lasermaterialbearbeitung. Meisenbach, Bamberg 1993, p. 27-33.

BISHOP 1957
Bishop, H. F.; Ackerlind, C. G.; Pellini, W. S.: Investigation of Metallurgical and Mechanical Effects in Development of Hot Tearing. In: Tans. AFS (1957) Vol. 65, p. 247.

BONSS 2001
Bonss, S.; Brenner, B.; Beyer, E.: Innovations in laser hybrid technology. In: Industrial Laser solutions. 01/ 2001, p. 29-32.

BÖRGER 1973
Börger, L.; Götz, G.: Optimierung von Windkanaldüsen für den Unterschallbereich. F. f. Maschinenbau u. konstruktiven Ingenieurbau, doctoral dissertation, Univ. Bochum, Bochum 1973.

BORLAND 1960
Borland, J. C.; Younger, R. N.: Some aspects of cracking in welded Cr-Ni austenitic steels. In: Br. Weld. J. (1960) 7, p. 22-60.

BRAT 2006
Brat, I.: Where Have All the Welders Gone, As Manufacturing and Repair Boom? In: Wall Street Journal Online, 15.08.2006.

BRENNER 1967
Brenner, P.: Entwicklung von Aluminiumlegierungen mit hoher Festigkeit im geschweißten Zustand. In: Aluminium 43 (1967) 4, p. 225-238.

CAILLIBOTTE 2004
Caillibotte, G.; Briand, F.; Kharim, C.; Verna, E.; Caristan, C.: Study of Shielding Nozzles for CO_2 Laser Welding. In: Proc. of the 23rd International Congress of Applications of Lasers & Electro-Optics (ICALEO) 2004, p. 121-128.

CHANDRASEKHAR 1961
Chandrasekhar, S.: Hydrodynamic and Hydromagnetic Stability. Oxford: Claredon Press 1961.

CIZUNGU 2003
Cizungu, K. I.: Modellierung und Optimierung von Ein- und Zweiphasen-Strahlverdichtern im stationären Betrieb, doctoral dissertation, Univ. Stuttgart. Stuttgart 2003.

COSTE 1997
Coste, F.; Fabbro, R.; Sabatier, L.: Applications of Visions to Laser Welding: Increase of Operatine Tolerances Using Beam-Oscillation and Filler, Proc. of 17th International Congress on Application of Lasers and Electro-Optics, (ICALEO) 1997, LIA 21-29, 1997.

DAUSINGER & SHEN 1993
Dausinger, F.; Shen, J.: Energy Coupling Efficiency in Laser Surface Treatment. In: ISIJ (Iron and Steel Institute of Japan) International, (1993) Vol. 9, p. 925-933.

DAUSINGER 1995
Dausinger, F.: Strahlwerkzeug Laser: Energieeinkopplung und Prozesseffektivität, doctoral dissertation, Univ. Stuttgart. Stuttgart: Teubner 1995.

DAUSINGER & MATSUNAWA 2000
Iwase, T; Shibata, K; Sakamoto, H; Dausinger, F; Hohenberger, B; Muller, M; Matsunawa, A; Seto, N.: Real time X-ray observation of dual focus beam welding of aluminum alloys. In: ICALEO 2000: Laser Materials Processing Conference, Dearborn, MI, USA. 2.10 -5.10.2000, p. C26-C34.

DAVÉ 2003
Davé, V. R. et al.: The Financial Impact of Weld Process Modeling. In: Weld. J. (2003) Vol. 83, p. 24-27.

DE: 40 24 299 A1
DE: 40 24 299 A1: Vorrichtung zum Fokussieren eines Lichtstrahls in wenigstens zwei Fokuspunkten.

DE 197 51 195 C1
DE 197 51 195 C1: Vorrichtung zum Fokussieren eines Lichtstrahles in zwei Fokuspunkten.

DE 196 19 339 B4
DE 196 193 39 B4 Laserstrahl-Bearbeitungsvorrichtung mit zwei Teilstrahlen.

DILTHEY 2000
Dilthey, U.: Laserstrahlschweißen: Prozesse, Werkstoffe, Fertigung und Prüfung. Düsseldorf: DVS-Verlag GmbH 2000.

DILTHEY 2005
Dilthey, U.: Schweißtechnische Fertigungsverfahren 2. Berlin: Springer 2005.

DILTHEY 2007
Dilthey, U.; Woeste, K.; Wagner, N.: Laserstrahl-MIG-Hybridschweißen von Aluminium- und Magnesiumlegierungen. In: Schweißen und Schneiden, 1/2007, p. 16-21.

DIN EN 10002
DIN EN 10002 – 1. 2001-12: Metallische Werkstoffe - Zugversuch - Teil 1: Prüfverfahren bei Raumtemperatur; Deutsche Fassung EN 10002-1:2001. Metallic materials - Tensile testing – Part 1: Method of testing at ambient temperature; German version EN 10002-1:2001.

DIN EN 60825:1-4
DIN EN 60825:1-4 Sicherheit von Laser-Einrichtungen - Teil 1: Klassifizierung von Anlagen, Anforderungen und Benutzer-Richtlinien.

DIN EN 895
DIN EN 895: 1999-05: Zerstörende Prüfung von Schweißverbindungen an metallischen Werkstoffen - Querzugversuch; Deutsche Fassung EN 895:1995. Destructive tests on welds in metallic materials - Transverse tensile test; German version EN 895:1995.

DIN EN 10327
DIN EN 10327: Kontinuierlich schmelztauch-veredelte Flacherzeugnisse aus Stahl - Technische Lieferbedingungen. German version prEN 10346:2007 as replacement of DIN EN 10292 (2007-06), DIN EN 10326 (2004-09), DIN EN 10327 (2004-09), DIN EN 10336 (2007-07).

DIN EN ISO 13919-2
DIN EN ISO 13919-2: Elektronenstrahl- und Laserstrahl-Schweißverbindungen, Richtlinie für Bewertungsgruppen für Unregelmäßigkeiten, Teil 2: Aluminium und seine schweißgeeigneten Legierungen, German version 2001.

DOWDEN et al. 1987
Dowden, J.; Postacioglu, N.; Davis, M.; Kapadia, P.: A keyhole model in penetration welding with a laser. In: J. Phys. D: Appl. Phys., Vol. 20, No. 1, 1987, p. 36-44.

DUBBEL 1990
Dubbel, H.; Beitz, W. (ed.); Küttner, K.-H. (ed.): Taschenbuch für den Maschinenbau. Berlin: Springer 1990.

DULEY 1998
Duley, W. W.: Laser Welding, Wiley-Interscience publication, New York 1998.

EAGAR 1986
Hundington, C. A.; Eagar, T. W.: Laser welding of aluminium and aluminium alloys. In: J. Weld. (1986) 62 (4), p. 105 -107.

ECK 1991
Eck, B.: Technische Strömungslehre. Berlin: Springer 1991.

EINSTEIN 1905
Einstein, A.: Über einen die Erzeugung und Verwandlung des Lichtes betreffenden heuristischen Gesichtspunkt. In: Ann. Phys,. 17. Leipzig 1905, p. 132-148.

EP 0600250
EP 0600250: Procedure of welding work pieces by a laser beam and laser welding nozzle; Linde AG.

EP 1020249 A2
EP 1020249 A2: Laser beam machining head; Mitsubishi motor company.

EP 1584406 A2
EP 1584406 A2: A gas shielding method and a gas shielding apparatus for laserwelding; Hokkaido University.

FABBRO 1990
Dionisio, B.; Fabbro, R.; Sabatier, L.; Leprince, L.; Orza, J. M.: Spectroscopic studies of iron plasmas induced by continuous high power CO_2 laser. In: SPIE (1990) Vol. 1279, p. 118-126.

FABBRO 2007
Fabbro, R. (1997) The contribution of Prof. Akira Matsunawa to understanding of laser welding processes, In: Proc. of 26th International Congress on Applications of Lasers & Electro-Optics (ICALEO) 2007, Orlando, FL, USA, p. 372-375.

FARWER 1996
Farwer, A.: Recent investigations on MIG and TIG aluminium welding with different shielding gases. In: Proc. of Comission XII. Budapest (1996) IIW-Document XII-1436-96, p. 25-48.

FRANZ 1998
Franz, T.: Laserstrahlschweißen mit Nd:YAG-Laser unter Wasser. In: Bericht aus dem Bremer Institut für Strahltechnik. Strahltechnik Bremen Vol. 8, doctoral dissertation, Univ. Bremen. Bremen 1998.

FLEMINGS 1974
Flemings, M. C.: Solidifications Processing. New York: McGraw-Hill 1974.

FUNK 1994
Funk, M.: Absorption von CO_2-Laserstrahlung beim Laserstrahlscheißen von Grobblech, doctoral disseration, RWTH Aachen. Aachen 1994.

FUERSCHBACH 1999
Fuerschbach, P.W.; Eisler, G.R.: Effect of very high travel speeds on melting efficiency in laser beam welding. In: SAE Transactions: Journal of Material and Manufacturing (1999) Vol. 108.

GLUMANN 1996
Glumann, C.: Verbesserte Prozeßsicherheit und Qualität durch Strahlkombination beim Laserschweißen. In: Hügel, H. (ed.): Laser in der Materialbearbeitung. Forschungsberichte des IFSW. Stuttgart: Teubner 1996.

GOD
God, F. A.: Genesis book 1. In: Spirit, H. (ed.): The Holy Bible.

GRAF 2002
Graf, T., Staufer, H.: LaserHybrid at Volkswagen, IIW-Doc. XII-1730-02, 2002.

GREF 2005
Gref, W.: Laserstrahlschweißen von Aluminiumwerkstoffen mit der Fokusmatrixtechnik. In: Hügel, H. (ed.): Laser in der Materialbearbeitung. Forschungsberichte des IFSW. München: Herbert Utz Verlag 2005.

GUITERREZ 1996
Guiterrez, L.; Neye, G.; Zschech, E.: Microstructure, hardness profile and tensile strength in welding of 6013 T6 extrusions. In: Weld. J. (1996) 75 (4), p. 115-121.

GUGGENHEIMER 1977
Guggenheimer, H.W.: Differential Geometry. New York: Dover 1977.

HACKSTEIN 1987
Hackstein, J. H.: Strömungsmechanische und akustische Untersuchungen an Koaxialstrahlen unterschiedlicher Profilierung. In: Forschungsberichte VDI Reihe 15 Nr. 48, doctoral dissertation, RWTH Aachen. Aachen: VDI Verlag 1987.

HÄNSCH 2006
Hänsch, T. W.: Nobel Lecture: Passion for Precision, Reviews of Modern Physics 78, 2006, p. 1297- 1309.

HÄRTL 2006
Härtl, J.: Prozessgaseinflus beim Schweissen mit Hochleistungsdiodenlasern. In: *iwb*-Forschungsbericht 197. München: Herbert Utz 2006.

HEIDER 2000
Heider P.: Lasergerechte Konstruktion und lasergerechte Fertigungsmittel zum Schweißen großförmiger Aluminium Strukturbauteile. Diss. Reihe 2, Nr. 326. VDI Verlag, 2000.

HERMANN 2004
Hermann, J.: Düsenparameter und Prozessgase für einen optimierten Laserschweißprozess. In: Lasertagung 2004 DVS 230, p. 149-159.

HERMANN 2004
Hermann, J.: Prozessgase beim Laserschweißen: Kostenfaktor oder Garant für wirtschaftliche, stabile und hochwertige Schweißverbindungen. In: Lasertechnik – neue Entwicklungen und Anwendungen, DVS-Bericht 241, Lasertagung 2006, p. 133-142.

HOHENBERBER 2003
Hohenberger, B.: Laserstrahlschweißen mit der Nd:YAG-Doppelfokustechnik - Steigerung von Prozeßstabilität, Flexibilität und verfügbarer Strahlleistung. In: Hügel, H. (ed.): Laser in der Materialbearbeitung. Forschungsberichte des IFSW. München: Herbert Utz 2003.

HUANG 2003
Huang, C.; Kou, S.: Liquation Cracking in Partial-Penetration Aluminum Welds: Effect of Penetration Oscillation and Backfilling. In: Welding Journal 07/2003, p. 187-194.

HÜGEL 1992
Hügel, H.: Strahlwerkzeug Laser, Teubner 1992.

HÜGEL 2008
Personal conversation with Prof. Dr.-Ing. H. Hügel, quoting from at the time of writing unpublished work of the IFSW .

HÜGEL & DAUSINGER 2002
Hügel, H.; Dausinger, F.: Laserstrahlschweißen von Aluminiumwerkstoffen – Probleme, Lösungsansätze und Anwendungspotenziale. In: Laserstrahlfügen: Prozesse, Systeme, Anwendungen, Trends; Sepold, G.; Seefeld, T. (ed.): Strahltechnik Band 19, BIAS Verlag, Bremen, 2002, p. 201-214.

INTERNET 1
Proposed New Federal Motor Vehicle Safety Standard for Motor Vehicle Side Impact Protection (FMVSS 214).
www.ita.doc.gov/td/auto/domestic/staffreports/NHTSA%20Side%20Impact%203.pdf.

ION 2005
Ion, J. C.: Laser Processing of Engineering Materials. Elsevier Butterworth-Heinemann 2005.

ISO TR 20172
ISO TR 20172:2006: Welding - Grouping systems for materials - European materials.

JENNINGS 1948
Jennings, P. H.; Singer, A. R. E.; Pumphrey, W. I.: Hot-shortness of some high-purity alloys in the systems aluminium-copper-silicon and aluminum-magnesium-silicon. In: J. Inst. Metals. (1948) 74, p. 227.

JP 11058063
JP 11058063: Gas nozzle for laser beam welding; Kawasaki Steel.

JP 20033181676
JP 20033181676: Laser welding gas shielded nozzle; Hokkaido Technology.

JP 5050284
JP 5050284: Shielding gas nozzle for laser beam welding; Nissan Motor Company.

JP 6304777
JP 6304777: Gas nozzle for welding sealing plate of battery on armor can by laser beam; Sanyo Electronic.

JP 7223086
JP 7223086: Assist gas nozzle for laser beam welding; Nissan Motor Company.

DE 196 19 339 A1
DE 196 19 339 A1: Laserstrahl-Bearbeitungsvorrichtung mit zwei Teilstrahlen.

KÄGELER et al. 2007
Kägeler, C.; Albert, F.; Mys, I.; Grimm, A.; Urmoneit, U.: Observation of Process Oscillations during High Power Laser Welding. In: Proc. of 7th LANE 2007, Conference on Laser Assisted Net Shape Engineering, Erlangen 25.–28.09.2007, Meisenbach, Bamberg, p. 123-135.

KALWA 2005
Kalwa, J.: Neue Esskultur? Homaro Cantu ist der Daniel Düsentrieb der Haute Cuisine. Mit LASER und HELIUM krempelt der Koch aus Chicago alle Konventionen des Kochens um. Whynot, Lifestile im Handelsblatt, Nr. 5, Oktober 2005, p. 38-42.

KANT 1787
Kant, I.: Kritik der reinen Vernunft (KrV). In: Sämtliche Werke. Ed. Preußische (Dt.) Akademie der Wissenschaften. Berlin 1910.

KAPLAN 1994
Kaplan, A.: A model of deep penetration laser welding based on calculation of the keyhole profile. In: J. Phys. D.: Appl. Phys., Vol. 27, No. 9, 1994, p. 1805-1815.

KATAYAMA 1999
Seto, N.; Katayama, S.; Matsunawa A.: High-Speed simultaneous observation of plasma and keyhole behaviour during high power CO_2 laser welding. In: Proc. of International Congress on Applications of Lasers & Electro-Optics (ICALEO) 1999, San Diego, USA, 15.11 -18.11.1999, p. E19-27.

KATAYAMA 2000a
Matsunawa, A.; Kim, J. D.; Seto, N.; Mitzutani, N.; Katayama, S.: Dynamics of keyhole and molten pool in laser welding. In: J. Laser Appl. (2000) Vol. 10, p. 247-254.

KATAYAMA 2000b
Katayama, S.; Seto, N.; Mizutani, M.; Matsunawa, A.: Formation Mechanism of Porosity in High Power YAG Laser welding. In: Proc. of International Congress on Applications of Lasers and Electro-Optics (ICALEO) 2000, Vol. 89, Dearborn, USA, 2.10 -5.10.2000, p. C16-25.

KATAYAMA 2001
Katayama, S.; Kobayashi, Y.; Mitzutani, M; Matsunawa, A.: Effect of vacuum on penetration and defects in laser welding. In: Journal of Laser Applications, October 2001, Vol. 13, Issue 5, p. 187-192.

KATAYAMA 2006
Katayama, S.; Uchiumi, S.; Briand, F.: Production of sound Deep-Penetration Hybrid Weld in Aluminum Alloy with YAG Laser and MIG Arc. In: Proc. of 25th International Congress on Applications of Lasers & Electro-Optics (ICALEO) 2006, Scottsdayle, USA, 30.10.-2.11.2006, p. 953-959.

KATAYAMA 2007a
Personal conversation between Prof. Dr. Seiji Katayama and the author during his research fellowship at Osaka University from 19.06.07 – 20.09.2007. Some of those results were published by Professor Katayama in internal research reports in Japanese and will be published in papers for international conferences in due course.

KATAYAMA 2007b
Katayama, S.; Kawahito, Y.; Mizutani, M. (2007) Collaboration of physical and metallurgical viewpoints for understanding and process development of laser welding, In: Proc. of 26th International Congress on Applications of Lasers & Electro-Optics (ICALEO) 2007, Orlando, FL, USA, p. 360-369.

KERN 1996
Kern, M.; Berger, P.; Hügel, H.: Optimiertes Querjetkonzept zur effizienten Sprizerablenkung und gesicherten Schutzgaszufuhr beim Laserschweißen. In: Laser und Optoelektronik, Vol. 28, Issue 4, 1996, p. 62-66.

KERN 1999
Kern, M.: Gas- und magnetofluiddynamische Maßnahmen zur Beeinflussung der Nahtqualität beim Laserstrahlschweißen, doctoral dissertation, Univ. Stuttgart. Stuttgart: Teubner 1999.

KLASSEN 2000
Klassen, M.: Prozeßdynamik und resultierende Prozeßinstabilitäten beim Laserstrahlschweißen von Aluminiumlegierungen. In: Bericht aus dem Bremer Institut für Strahltechnik. Strahltechnik Bremen, Vol. 13, doctoral dissertation, Univ. Bremen, Bremen, BIAS Verlag 2000.

KLEIN 1993
Klein, T.; Kroos, J.; Vicanek, F.; Simon, G.; Decker, I.: Eigenschwingungen und Rayleigh-Instability der Dampfkappillare. In: Geiger, M.; Hollmann, F. (ed.): Texte zum Berichtskolloquium der DFG im Rahmen des Schwerpunkt-programms "Strahl-Stoff-Wechselwirkung bei der Laserstrahlbearbeitung". Erlangen 1993. Bamberg: Meisenbach 1993, p. 155-160.

KLEMEANS 1976
Klemens, P. G.: Heat balance and flow conditions for electron beam and laser welding. In: J. Appl. Phys. (1976), Vol. 47, No. 5, p. 2165-2174.

KOU 2002
Kou, S.: Welding Metallurgy. Wiley Interscience John Wiley & Sons, 2002.

KROOS & GRATZKE & SIMON 1993a
Kroos, J.; Gratzke, U.; Simon, G.: Towards a self-consistent model of the keyhole in penetration laser beam welding. In: J. Phys. D.: Appl. Phys., Vol. 26, No. 3, 1993, p. 474-481.

KROOS et al. 1993b
Kroos, J.; Gratzke, U.; Vicanek, M.; Simon, G.: Dynamic behaviour of the keyhole in laser welding. In: J. Phys. D.: Appl. Phys., Vol. 26, No. 3, 1993, p. 481-487.

KUHN 1962
KUHN, T. S.: The Structure of Scientific Revolutions, University of Chicago Press, 1962.

KUK 2004
Kuk, J. M.; Jang, K. C.; Lee, D. G.; Kim, I. S.: Effects of temperature and shielding gas mixture on fatigue life of 5083 alluminium alloy. In: Journal of Materials Processing Technology (2004), Vol. 155-156, p. 1408-1414.

LANDOLT-BÖRNSTEIN 2004
Landolt-Börnstein: Numerical data and functional relationships in science and technology. New Series. Editor in Chief: Martienssen, W.; Group VIII Vol. 1C: Laser physics and applications. Subvolume C: Laser Applications: Hügel, H, Dausinger, F.: Fundamentals of laser-induced processes, edited by Poprawe, R.; Weber, H.; Herzinger, G.; Berlin: Springer 2004, p. 1-68.

LONGAIR 2003
Longair, M.: Theoretical Concepts in Physics. Cambridge University Press 2003.

MAIER 1999
Maier C.: Laserstrahl- Lichtbogen- Hybridschweißen von Aluminiumwerstoffen, doctoral dissertation, RWTH Aachen. Aachen: Shaker Verlag 1999.

MAIMAN 1961
Maiman, T. H.; Hoskins, R. H.; D'Haenens, I. J.; Asawa, C. K.; Evtuhov, V.: Stimulated Optical Emission in Fluorescent Solids. II. Spectroscopy and Stimulated Emission. In: Ruby Phys. Rev. 123. 1961, p. 1151-1157.

MATHERS 2002
Mathers, G.: The welding of aluminium and its alloys. Cambridge: Woodhead Publishing Ltd. 2002.

MARTUKANITZ 2005
Martukanitz, R. P; Stol, I.; Tressler, J. F.; Warren, C. J.: Development of the Laser Stir Welding process for Aluminum Laser Beam Welding. In: Proc. of 24th International Congress on Applications of Lasers and Electro-Optics (ICALEO) 2005, Miami, USA, 31.10.-3.11.2005, p. 712-718.

MATSUHIRO & INABA & OHJI 1994
Matsuhiro, Y; Inaba, Y.; Ohji, T.: Mathematical modelling of laser welding with a keyhole: modelling of laser welding. Welding International (UK), Vol. 8, No. 4, 1994, p. 479-483.

MATSUNAWA 1997
Matsunawa, A.; Semak, V.: The Simulation of Front Keyhole Wall Dynamics During Laser Wedling, J. Phys. D., 1997, Vol. 30, p. 798-809.

MAZUMDER 1987
Mazumder, J.; Rockstroh, T. J.: Spectroscopic studies of plasma during cw laser materials interaction. In: J. Appl. Phys. (1987), Vol. 61 (1), p. 917-923.

MEADOWS 1972
Meadows, Dennis; Meadows, Donella; Zahn, E.; Milling, P.: Die Grenzen des Wachstums. Bericht des Club of Rome zur Lage der Menschheit. Stuttgart: Deutsche Verlags-Anstalt 1972, UB A 8047.

MEADOWS 1974
Meadows, D. et al.: Dynamics of growth in a finite world. Cambridge, Mass.: Wright-Allen 1974, SAI wiw 87/959.

MEIER 2005
Meier O.: Hochfrequentes Strahlpendeln zur Erhöhung der Prozessstabilität beim Laserstrahlschweißen mit hoher Schmelzbaddynamik; Zwischenbericht AiF 13.600 N / DVS-Nr.: 6.049; 2005; http://www.dvs-forschungsvereinigung.de

MIKLOS 2004
Miklos, E.: Europen trends and developments in Gas-shielded Arc Welding, Linde AG, Consolda Rio de Janairo 2004.

MONGE 1900
Monge, G.: Darstellende Geometrie von Gaspard Monge (1798) mit zahlreichen Figuren in dem Texte und in den Anmerkungen. By: Haussner, R. K. H. (ed. and tr.) 1863. Published by: Engelmann, W.; Leipzig 1900.
http://name.umdl.umich.edu/ABN3249.0001.001.

MÜLLER 1994
Mueller, R.: A model for predicting keyhole and fusion zone depths in blind keyhole welding. In: Proc. of International Congress on Applications of Lasers & Electro-Optics (ICALEO) 1994, Orlando, FL, USA, 17.10 - 20.10.1994, p. 509-518.

OTTO 1997
Otto, A.: Transiente Prozesse beim Laserstrahlscheißen. In: Geiger, M.; Feldman, K. (ed.): Fertigungstechnik-Erlangen, Vol. 65, Bamberg 1997.

PEDROTTI et al. 2002
Pedrotti, F. L.; Pedrotti, L. S.; Bausch, W.; Schmidt; H.: Optik für Ingeniuere - Grundlagen. Berlin, Heidelberg, New York: Springer 2002.

POPPER 1959
Popper, K.: Logik der Forschung, Tübigen 1959.

POPRAWE 2005
Poprawe, R.: Lasertechnik für die Fertigung. Berlin: Springer 2005.

RÅDE & WESTERGREN 1997
Råde, L.; Westergren, B.: Springers mathematische Formeln: Taschenbuch für Ingenieure, Naturwissenschaftler, Wirtschaftswissenschaftler. Berlin: Springer 1997.

RAMAKRISHNAN 1969
Ramakrishnan, S.; Kumar, S.; Kuloor, N. R.: Studies in bubble formation – I Bubble formation under constant flow conditions. In: Chemical Engineering Science, Vol. 24, 1969, p. 731-747.

RAPP 1996
RAPP, J.: Laserschweißeignung von Aluminiumwerkstoffen für Anwendungen im Leichtbau, doctoral dissertation, IFSW Stuttgart. Stuttgart 1996.

RAYLEIGH 1892
Lord Rayleigh: On the instability of Cylindrical Fluid Surfacces. In: The London, Edinburgh and Dublin Philosophical Magazine 34 (1892), p. 177.

REUTZEL 2005
Reutzel, E. W.; Mikesic, D. A; Tressler, J. F.; Crue, R. A.; Gwinn, E. A.; Sullivan, M. J.: Laser Pipe Welding: Technology Evaluation and Cost Analysis, ARL Penn State Technical Report No. 04-014, February 2005.

ROEREN & TRAUTMANN 2005
Roeren, S.; Trautmann, A.; Zaeh, M. F.: Modelling of Transient Clamping Conditions during Laser Beam Welding. In: Proceedings of the Third International WLT-Conference on Lasers in Manufacturing 2005, Munich, Germany, p. 95-10.

RUBBEN 1997
Rubben, K; Mohrbacher, M.; Leirman, E.: Andvantages of Using and Oscillating Laser Beam for the Production of Tailored Blanks. In: Laser in Materials Processing, SPIE, Vol. 3097, 1997, p. 228-243.

RYKALIN 1988
Rykalin, N. N.; Ugalov, A.; Zuev, I.; Kokara, A.: Laser and electron beam material processing: handbook. Moscow: Mir Publishers 1988.

SATOH 1997
Satoh, S. et al.: Journal of Light Metal Welding and Construction (1997), Vol. 35, No. 9, p. 1-8 (in Japanese).

SCHULZ et al. 1996
Schulz, W.; Fürst, B.; Kaierle, S.; Turichin, G.; Kreutz, E. W.; Poprawe, R.: Powerful features for LBW including theoretical aspects. In: Proc. of International Congress on Applications of Lasers and Electro-Optics (ICALEO) 1996, Orlando, Florida, USA, p.1-9.

SEEFELD 2005
Neumann, S.; Thomy, C.; Seefeld; T.; Vollertsen, F.: Distortion Minimization and Shielding Gas Flow Optimisation in CO_2- Laser Remote Welding of Steel. ICAELO 2005, p. 992-1000.

SEPOLD 1976
Sepold, G.; Bödecker, V.; Jüptner, W.; Steffen, H.-D.: The Influence of Electron- and Laser Beam Distribution on Weld Seam Formation. In: Paper 1-1-(3)(S) Japan Weld. Soc. 1976, Vol.1, p. 9-14.

SHEN 1994
Shen, J.: Optimierung von Verfahren der Laseroberflächenbehandlung bei gleichzeitiger Pulverzufuhr, doctoral dissertation, Univ. Stuttgart. Stuttgart: Teubner-Verlag 1994.

SIGLOCH 1995
Sigloch, H.: Technische Fluidmechanik, Düsseldorf: VDI Verlag 1995.

SINGER 1947
Singer, A. R. E.; Jennings, P. H.: In: J. Inst. Metals (1947) 73, p. 273.

STAUFER 2003
Staufer, H.; Rührmößl, M.; Miessbacher, G.: LaserHybrid welding and Laser Brazing: state of the art in technology and practice by the examples of the Audi A8 and VW-Phaeton, Fronius International GmbH, 2003.

STEEN 1980
Steen, W. M.: Arc augmented laser processing of materials, Journal of Applied Physics, Vol. 51, No. 11, November 1980, p. 5636-5641.

STEINHAGE 2005
Steinhage, M.; Jerzembeck, J.: Festlegung eines Arbeitsplatzgrenzwertes für Stickstoffmonoxid. In: Der Praktiker 4/2005, p. 99-102.

STOL & MARTUKANITZ 2004
Stol, I.; Martukanitz, R. P.: Laser Welding with Beam Osillation, U.S. Patent No. 6,740,845; 2004.

SWIFT 1973
Swift-Hook, D. T.; Gick, A. E. F.: Penetration Welding with Lasers. In: Welding J. (1973) 52, p. 492-499.

TABOR 1991
Tabor, D.: Gases, liquids, and solids and other states of matter. 3rd edition. Cambridge: University Press 1991.

TRAUTMANN 2005a
Hornfeck, T.; Trautmann, A.: Laserschutzgasschweißen im Spannungsfeld Prozessbeeinflussung und Emissionsschutz. In: *iwb* Newsletter Jahrgang 13, Nr. 3, ISSN 1434-324X, p. 5-6.

TRAUTMANN 2005b
Trautmann, A.; Zaeh, M. F.: Hybrid Bifocal Laser Welding of Aluminum, Proc. of ICALEO, 24th International Congress on Applications of Lasers and Electro-Optics, 2005, Miami, USA, 31.10.-3.11.2005, p. 153-162.

TSUGE 1986
Tsuge, H.: Hydrodynamics of bubble formation from submerged orifices. In: Encyclopedia of Fluid Mechanics, Gulf Publishing, Houston, Texas, Vol. 3, p. 191-232.

TSUKAMOTO 2004
Tsukamoto, S; Kawaguchi, I.; Arakane, G.; Honda, H.: Prevention of weld defect by power modulation in high power laser welding, In: Geiger, M.; Otto, A. (ed.), Proc. of 4th LANE 2004, Conference on Laser Assisted Net Shape Engineering, Erlangen 21.–24.09.2004, Meisenbach, Bamberg, p. 119-130.

WAGNER 1991
Wagner, W.: Lufttechnische Anlagen. Vogel Verlag 1991.

WHITEHEAD 1951
Whitehead, L. G.; Wu, L. Y.; and Waters, M. H. L.: Contracting Ducts of Finite Length. In: Aeronautical Quarterly (1951) Vol. 2, Pt. 4, p. 254-271.

WITOSZYNSKI 1924
Witoszynski, E.: Über Strahlerweiterung und Strahlablenkung. In: Vorträge aus dem Gebiet der Hydro- und Aerodynamik. Berlin: Springer 1924, p. 248-251.

WRIED 1986
Wried, H. A.: The Al-N (Aluminum–Nitrogen) System. In: Bulletin of Alloy Phase Diagrams 7, Vol. 7, 1986, p. 329-333.

ZÄH & TRAUTMANN 2004a
Zäh, M. F.; Trautmann, A. et al.: Den Vorsprung sichern. In: Blech in Form (2004) Vol. 5, p. 23-27.

ZÄH & TRAUTMANN 2004b
Zäh, M. F.; Trautmann, A.: Vergleich des hybriden, bifokalen Laserschutzgasschweißens mit Laser-MIG-Hybridverfahren; In: Aluminium, International Journal for Industry, Research and Application, 80 (2004) 12, p. 1387-1391.

ZÄH & TRAUTMANN 2005
Zäh, M. F.; Trautmann, A. et al.: Forschung als Motor der Leichtbau-Fügetechnik. In: Blech in Form. (2005) Vol. 2, p. 32-34.

ZHAO 1999
Zhao, H.; White, D. R.; Debroy, T.: Current issues and problems in laser welding of automotive aluminium alloys. In: Int. Mat. Rev. (1999), Vol. 44, No. 6, p. 238-266.

98/24/EG 1998
Richtlinie 98/24/EG des Rates vom 7. April 1998 zum Schutz von Gesundheit und Sicherheit der Arbeitnehmer vor der Gefährdung durch chemische Arbeitsstoffe bei der Arbeit.

Other publications by the author:

Stimming, U.; Trautmann, A.; Wagner, U. et al.: Brennstoffzelle und Verkehr; In: Energieversorgung im 21. Jahrhundert – Globale Herausforderung, Lokale Verantwortung, Bayerische EliteAkademie, Projektarbeiten 3. Jahrgang, München 2002, p. 198-232.

Ulrich, C.; Trautmann, A.: Methodische Wissensaufbereitung zur Planung von Fügeaufgaben. In: Industriekolloquium Sonderforschungsbereich 582, Marktnahe Produktion individualisierter Produkte, München 2004, p. 11.1-10.

Zäh, M. F.; Trautmann, A. et al.: Forschung als Motor der Leichtbau-Fügetechnik. In: Blech in Form 2 (2004), p. 32-34.

Zäh, M. F.; Trautmann, A. et al. , Forschungstrends in der Leichtbau-Fügetechnik. In: Fügetechnik im Leichtbau, 16.-17.03.2004, Stuttgart, Carl Hanser Verlag München.

Zäh, M. F.; Hornfeck, T.; Trautmann, A.: Den Vorsprung sichern. In: Blech in Form 5 (2004), p. 23-27.

Zäh, M. F.; Trautmann, A.: Vergleich des hybriden, bifokalen Laserschutzgasschweißens mit Laser-MIG-Hybridverfahren; In: Aluminium, International Journal for Industry, Research and Application, 80 (2004) 12, p. 1387-1391.

Zäh, M. F.; Trautmann, A.; Roeren S.: Fügetechnik-Trends: Leichtbau puscht alternative Verfahren. Produktion Technik, 36 (2005), p. 1.

Zäh, M. F.; Trautmann, A. et al.: Trends in der Fügetechnik: Innovative Fügeverfahren für neue Produkte, 19. Deutscher Montagekongress, München, 18.-20.10.2005, p. 31-28.

Trautmann, A.; Siviour, C. R.; Walley, S. M., Field, J. E.: Lubrication of polycarbonate at cryogenic temperatures in the split Hopkinson pressure bar. In: International Journal of Impact Engineering 31 (2005), p. 523-544.

Trautmann, A.; Zaeh, M. F.: Hybrid Bifocal Laser Welding of Aluminum. In: Proc. of 24th International Congress on Applications of Lasers & Electro-Optics (ICALEO) 2005, Miami, FL, USA 31.10.-3.11.2005, p. 153-162.

Oefele, F.; Munzert, U.; Trautmann, A.: Startschuss für RoFaLas, Remotelaserstrahlschweißen mit dem Faserlaser, *iwb* Newsletter, Jahrgang 13, Nr. 3, 2006, ISSN 1434-324X, p. 4-5.

Hornfeck, T.; Trautmann, A.: Laserschutzgasschweißen im Spannungsfeld zwischen Prozessbeeinflussung und Emissionsschutz, Newsletter, Jahrgang 13, Nr. 3, 2006, ISSN 1434-324X, p. 5-6 .

Trautmann, A.; Zaeh, M. F.: Laser Bifocal Hybrid Welding of Aluminum. In: Advanced Materials Research: Flexible Manufacture of Lightweight Frame Structures, Vol. 10 (2006), p. 65-79.

Trautmann, A.: Hybride Bifokaltechnik aus Nd:YAG- und Hochleistungsdiodenlaser, 8. Münchener Kolloquium, Tagungsband, München 9.-10.03.06, p. 321-322.

Hornfeck, T.; Trautmann, A.; Oefele, F.: Laserstrahlumformen von Aluminiumlegierungen für die Luft- und Raumfahrt, 8. Münchener Kolloquium, Tagungsband, München 9.-10.03.06, p. 323-324.

Trautmann, A.: Mobile Laserkabinen und Sicherheitstechnik für Hochleistungslaser der neusten Generation, Bayern Photonics, Kompetenznetz Optische Technologien, Newsletter 01/06, p. 8.

Zäh, M. F.; Trautmann, A. et. al.: Innovative Schweißverfahren in der Produktion. Schweißtagung 2006 - Innovative Schweißfahren in der Produktion 28. -29. Juni 2006, Neu-Ulm, Carl Hanser Verlag, p. 1-15.

Trautmann, A.; Zäh, M. F.: Prozesssicheres Fügen von Aluminium-Tragwerkstrukturen mit einem hybriden, bifokalen Lasersystem. In: Kleiner M.; Baier H.; Fleischer J.; Löhe D.; Weinert K.; Zäh M.; Schikorra M. (ed.): Integration von Umformen, Trennen und Fügen für die flexible Fertigung von leichten Tragwerkstrukturen, Fortschritt-Berichte VDI: Ergebnisbericht der Phase 1, Jan. 2003 – Dez. 2006, Düsseldorf, Germany, Reihe 2, p. 153 – 181.

Huber, S.; Trautmann, A.; Zäh, M. F.: Bifocal Hybrid Laser Welding of Aluminium. In: Geiger, M.; Otto, A.; Schmidt, M. (ed.), Proc. of 7th LANE 2007, Conference on Laser Assisted Net Shape Engineering, Erlangen 25.–28.09.2007; Meisenbach, Bamberg, p. 151-162.

Trautmann, A.; Zäh, M. F.: Increase of Process Robustness of Zinc-Coated Steels in Bifocal Hybrid Laser Welding. In: Geiger, M.; Otto, A.; Schmidt, M. (ed.), Proc. of 7th LANE 2007, Conference on Laser Assisted Net Shape Engineering, Erlangen 25.–28.09.2007; Meisenbach, Bamberg, p. 197-208.

13 Appendices

Appendix A: Derivation of the filler dilution formula (FDF)

Magnitudes given or regarded as constants during the welding process:

v_w velocity of welding

v_f velocity of the filler wire

P_L power emitted by the laser

A_f cross-sectional area of the filler wire

d_f diameter of the filler wire

c_f silicon content of the filler wire (for Al 4047 A the Si content is 12%)

c_b silicon content in the base alloy (for EN-AW6060 the Si content is 0.5%)

Magnitude measured:

The cross-sectional area of the fusion zone A needs to be determined form cross-sections macrographs:

$$A = f(v_w, P_L)$$

The Si content in the fusion zone represents the desired magnitude c_{fz}, i.e. the dilution in the fusion zone. This dilution depends on the filler wire dilution. The determination of the FDF proceeds as follows:

$$V = V_f + V_b \qquad \text{(Equation 11.1)}$$

where V is the volume of the fusion zone, V_f the volume of filler wire, and V_b the volume of the base metal per unit time t.

$$V = A \cdot v_w \cdot t \qquad \text{(Equation 11.2)}$$

$$V_f = A_f \cdot v_f \cdot t = \frac{\pi \cdot d_f^2}{4} \cdot v_f \cdot t \qquad \text{(Equation 11.3)}$$

The partial seam volumes can be expressed as:

$$V_f = \frac{A_f}{A} \cdot A \cdot v_f \cdot t \qquad \text{(Equation 11.4)}$$

$$V_b = \left(1 - \frac{A_f}{A}\right) \cdot A \cdot v_w \cdot t \qquad \text{(Equation 11.5)}$$

Thus, the values for the Si-content c_{fz} in the fusion zone are:

$$c_{fz} \cdot V = c_f \cdot V_f + c_b \cdot V_b \qquad \text{(Equation 11.6)}$$

Rearrange:

$$c_{fz} \cdot V - c_b \cdot V_b = c_f \cdot V_f \qquad \text{(Equation 11.7)}$$

$$\frac{c_{fz} \cdot V}{c_b \cdot V_b} - 1 = \frac{c_f \cdot V_f}{c_b \cdot V_b} \qquad \text{(Equation 11.8)}$$

$$\frac{c_{fz} \cdot A \cdot v_w}{c_b \cdot \left(1 - \frac{A_f}{A}\right) \cdot A \cdot v_w} - 1 = \frac{c_{fz} \cdot \frac{A_f}{A} \cdot A \cdot v_f}{c_b \cdot \left(1 - \frac{A_f}{A}\right) \cdot A \cdot v_w} \qquad \text{(Equation 11.9)}$$

$$\frac{c_{fz}}{c_b \cdot \left(1 - \frac{A_f}{A}\right)} - 1 = \frac{v_f}{v_w} \cdot \frac{c_f \cdot \frac{A_f}{A}}{c_b \cdot \left(1 - \frac{A_f}{A}\right)} \qquad \text{(Equation 11.10)}$$

The filler dilution formula is (c.f. Equation 8.4):

$$c_{fz} = \frac{v_f}{v_w} \cdot c_f \cdot \frac{A_f}{A} + c_b \cdot \left(1 - \frac{A_f}{A}\right) \qquad \text{(Equation 11.11)}$$

Inserting c_f and c_b for the reference alloy:

$$c_{fz} = \frac{v_f}{v_w} \cdot 0.12 \cdot \frac{A_f}{A} + 0.005 \cdot \left(1 - \frac{A_f}{A}\right) \qquad \text{(Equation 11.12)}$$

In order to achieve a desired dilution the parameters of welding need to be adjusted such that the cross-section of the weld satisfies:

$$A = f\left(v_w, P_L\right)$$

Starting from the FDF: $$c_{fz} = \frac{v_f}{v_w} \cdot c_f \cdot \frac{A_f}{A} + c_b \cdot \left(1 - \frac{A_f}{A}\right)$$ (Equation 11.13)

$$c_{fz} \cdot A = \frac{v_f}{v_w} \cdot c_f \cdot A_f + c_b \cdot A - c_b \cdot A_f$$

$$A \cdot \left(c_{fz} - c_b\right) = \frac{v_f}{v_w} \cdot c_f \cdot A_f - c_b \cdot A_f$$

$$A = \frac{1}{c_{fz} - c_b} \cdot \left(\frac{v_f}{v_w} \cdot c_f \cdot A_f - c_b \cdot A_f\right)$$ (Equation 11.14)

For the reference alloy (c.f. Equation 8.5):

$$A = \frac{A_f}{c_{fz} - 0.005} \cdot \left(\frac{v_f}{v_w} \cdot 0.12 - 0.005\right)$$ (Equation 11.15)

The error of the Si content in the FDF is calculated according to Gaussian error propagation.

$$c_{fz} = \frac{v_f}{v_w} \cdot 0.12 \cdot \frac{A_f}{A} + 0.005 \cdot \left(1 - \frac{A_f}{A}\right)$$ (Equation 11.16)

The errors in v_w, v_f, A_f, and the Si contents c_f and c_b are regarded to be negligible. Thus, the error Δc_{fz} is:

$$\Delta c_{fz} = \sqrt{\left(\frac{dc_{fz}}{dA}\right)^2 \cdot (\Delta A)^2 \cdot 2}$$ (Equation 11.17)

$$\frac{dc_{fz}}{dA} = -0.12 \cdot \frac{v_f}{V_w} \cdot \frac{A_f}{A^2} + 0.005 \cdot \frac{A_f}{A^2}$$ (Equation 11.18)

where ΔA is the standard deviation of the cross-sectional area.

Hence, the errors for the measurements displayed in table 11.1 are:

v_f (m min^{-1})	v_w (m min^{-1})	mean value of A (mm^2)	standard deviation in A (mm^2)	error in the mean of A (mm^2)	mean value of Si content (vol%)	error in Si content (vol%)
5	5	5.90	0.30	0.15	2.03	0.11
6	6	5.29	0.81	0.47	2.12	0.36
5.5	5.5	5.51	0.52	0.26	2.14	0.21
5.5	5.5	5.34	0.39	0.20	2.19	0.17

Table 11.1: Calculus of errors

Appendix B: Derivation of Witoszynski's formula

The formula (c.f. equation 5.2) can be deduced as follows:

Witoszynski assumed that a laminar flow can be achieved by a nozzle contour. This flow is continuous in axial direction and without sudden changes presupposing that the flow is ideal and incompressible. To solve this problem Witoszynski started from the differential equation of an ideal fluid which flows radial symmetric and free of a vortex. In cylindrical coordinates:

$$\frac{\mathrm{d}^2\psi}{\mathrm{d}r^2} - \frac{1}{r}\frac{d\psi}{dr} + \frac{d^2\psi}{dz^2} = 0 \qquad \text{(Equation 11.19)}$$

The following series solution is considered:

$$\psi = \mathrm{r}^2 f(\mathrm{z}) - \frac{r^4}{2\cdot 4}\frac{d^2 f(z)}{dz^2} + \frac{r^6}{2\cdot 4^2\cdot 6}\frac{d^4 f(z)}{dz^4} - \ldots \qquad \text{(Equation 11.20)}$$

f(z) is chosen such that in the series $f(\infty) = 1$. Additionally, the other terms of the series, e.g. $\mathrm{d}^2\mathrm{f}/\mathrm{dz}^2$ and $\mathrm{d}^4\mathrm{f}/\mathrm{dz}^4$, vanish at infinity and the differential quotients of f(z) converge.

An exemplary function f(z) :

$$f(\mathrm{z}) = 1 + \frac{f_1(z)}{(z^2 + a^2)^n} \qquad \text{(Equation 11.21)}$$

where a is a constant and f_1(z) is a rational function of low order.

Inserting f(z) into equation 11.20 leads to a series which converges for all values of z and a except for $r = a$ and $z = 0$.

Selecting for example:

$$f_1(\mathrm{z}) = \mathrm{C}\,\frac{(1-\frac{3z^2}{a^2})^2}{(1+\frac{z^2}{a^2})^3} \qquad \text{(Equation 11.22)}$$

Taking into account small values of r only, e.g. $r < 0.2$, a it is sufficient to consider the first term of the series in equation 11.19:

$$\psi = r^2 \left[1 + C \frac{(1-\frac{3z^2}{a^2})^2}{(1+\frac{z^2}{a^2})^3} \right] \qquad \text{(Equation 11.23)}$$

For the constant C the following ansatz is used:

$$C = 1 - \frac{r_0^2}{r_1^2} \qquad \text{(Equation 11.24)}$$

Inserting C into the equation gives for the flow line:

$$r(z) = \frac{r_0}{\sqrt{1-(1-\frac{r_0^2}{r_1^2})\frac{(1-\frac{3z^2}{a^2})^2}{(1+\frac{z^2}{a^2})^3}}} \qquad \text{(Equation 11.25)}$$

Hence, the contour of any desired nozzle can be calculated.

Appendix C: Derivation of surface tension at a conical keyhole tip

As described in section 4.3, a 'spike-like' geometry of a conical keyhole is to a very good degree in agreement with experimental evidence. In the following a conical keyhole tip is shown to account for the experimentally proven behaviour of bubble formation. To determine the surface tension in a conically tipped keyhole the curvature at the keyhole wall needs to be evaluated. The ellipse sought after is formed by the intersection of a plane with a right circular cone. The plane is inclined to the axis of the cone at an angle which *equals* half the apex angle of the cone, i.e. the ellipse is *normal* to the surface of the cone. This conic section can be seen in figure 11.1.

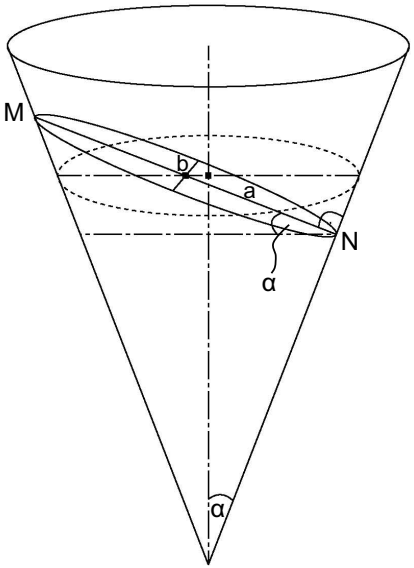

Figure 11.1: Diagram of a conic section, the ellipse is normal to the cone's surface at the vertices N and M; a *is half the major axis;* b *is half the minor axis; α is half the cone's apex angle; for later reference in figure 11.2 a circle whose area is perpendicular to the axis of rotation symmetry and intercepting the centre point of the ellipse is shown*

The tangent through the vertex N and the apex is a straight line, i.e. its curvature is zero. To determine the curvature at this vertex N only the curvature of the ellipse in the conic section needs to be considered. The simplified version of the Young-Laplace equation 4.12 applies. A plane curve in a right-handed Cartesian coordinate system in parameterized form is given by:

$$x = x(t), y = y(t) \qquad \text{(Equation 11.26)}$$

where t is the parameter describing the angle on the curve as seen from the centre.

The curvature $\kappa(t)$is given by the following formula:

$$\kappa(t) = \frac{x'y'' - y'x''}{\sqrt{(x')^2 + (y')^2}^3} \qquad \text{(Equation 11.27)}$$

where $(\ )' = \frac{d(\ )}{dt}$ and $(\ )'' = \frac{d^2(\ )}{dt^2}$.

An ellipse taking values of t, which are increasing anticlockwise from the vertex N, is suitably parameterized by:

$$x(t) = a\cos t, y(t) = b\sin t \qquad \text{(Equation 11.28)}$$

Using this parameterization in equation 11.27 gives the curvature κ:

$$\kappa(t) = \frac{ab}{\sqrt{a^2\sin^2 t + b^2\cos^2 t}^3} \qquad \text{(Equation 11.29)}$$

Hence, the curvature at the vertex N, i.e. $t = 0$, is:

$$\kappa(0) = \frac{a}{b^2} \qquad \text{(Equation 11.30)}$$

In figure 11.2 a diagram is given to determine a and b. The circle shown in dashed lines in figure 11.1 is mirrored into the plane of the paper.

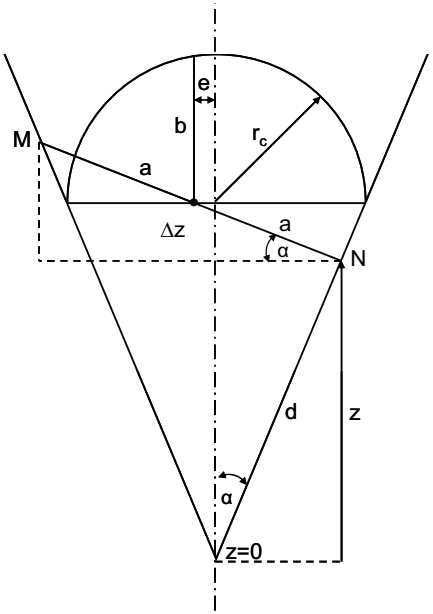

Figure 11.2: Diagram of conic section in the plane defined by the centre point of the ellipse, vertices N and M of the ellipse, and the apex of the cone; the circle around the centre point of the ellipse is mirrored into the paper plane

The triangle given by the apex of the cone and the two vertices N and M is considered to determine *a* by *elementary* geometry. In the triangle:

$$\tan(2\alpha) = \frac{2a}{d}, \cos\alpha = \frac{z}{d} \qquad \text{(Equation 11.31)}$$

using:

$$\tan(2\alpha) = \frac{2\tan\alpha}{1-\tan^2\alpha} \qquad \text{(Equation 11.32)}$$

gives:

$$a = \frac{z\tan\alpha}{(1-\tan^2\alpha)\cos\alpha} \qquad \text{(Equation 11.33)}$$

Descriptive geometry is invoked to determine *b*. The method of descriptive geometry was introduced by Monge in his book "Géométrie descriptive" published in 1798. For ease of citation from a historic book the German translation of 1900 done by Haussner is referred to. According to descriptive

geometry [MONGE 1900, p. 103] a circle of latitude around the centre point of the ellipse with radius r_C is used:

The circle of latitude is at height $z + \Delta z$. Δz can be found from:

$$\sin\alpha = \frac{\Delta z}{a} \qquad \text{(Equation 11.34)}$$

The radius r_C is determined by:

$$\tan\alpha = \frac{r_C}{z + \Delta z} \qquad \text{(Equation 11.35)}$$

The distance e of the normal onto the major axis of the ellipse intersecting the circle of latitude is given by:

$$e = a\cos\alpha - z\tan\alpha \qquad \text{(Equation 11.36)}$$

Using Pythagoras' theorem in the circle with radius r_C taken from equation 11.35 gives:

$$b^2 + \left(a\cos\alpha - z\tan\alpha\right)^2 = \left(z + \Delta z\right)^2 \tan^2\alpha \qquad \text{(Equation 11.37)}$$

Insert the expression for a of equation 11.33 and simplify:

$$b^2 = z^2 \tan^2\alpha \frac{1 - \tan^4\alpha}{(1 - \tan^2\alpha)^2} \qquad \text{(Equation 11.38)}$$

Use equation 4.17 to find the desired curvature at the vertex N:

$$\kappa(0) = \frac{a}{b^2} = z^{-1} \underbrace{\frac{1 - \tan^2\alpha}{(1 - \tan^4\alpha)\sin\alpha}}_{\text{constant}} \qquad \text{(Equation 11.39)}$$

Rewriting equation 4.12 in terms of the curvature $\kappa(t)$ renders the surface tension:

$$\vec{p}_\sigma = \sigma\left[\kappa(t) + \frac{1}{\infty}\right] = \sigma \cdot \kappa(t) \qquad \text{(Equation 11.40)}$$

The surface tension at the vertex N (i.e. where $t = 0$) depending on the height z of the keyhole is then given by:

$$\vec{p}_\sigma(z) = z^{-1} \cdot \underbrace{\sigma \frac{1 - \tan^2\alpha}{(1 - \tan^4\alpha)\sin\alpha}}_{\text{constant}} \sim z^{-1} \qquad \text{(Equation 11.41)}$$

iwb Forschungsberichte Band 1–121

Herausgeber: Prof. Dr.-Ing. J. Milberg und Prof. Dr.-Ing. G. Reinhart, Institut für Werkzeugmaschinen und Betriebswissenschaften der Technischen Universität München

Band 1–121 erschienen im Springer Verlag, Berlin, Heidelberg und sind im Erscheinungsjahr und den folgenden drei Kalenderjahren erhältlich im Buchhandel oder durch Lange & Springer, Otto-Suhr-Allee 26–28, 10585 Berlin

1 *Streifinger, E.*
Beitrag zur Sicherung der Zuverlässigkeit und Verfügbarkeit moderner Fertigungsmittel
1986 · 72 Abb. · 167 Seiten · ISBN 3-540-16391-3

2 *Fuchsberger, A.*
Untersuchung der spanenden Bearbeitung von Knochen
1986 · 90 Abb. · 175 Seiten · ISBN 3-540-16392-1

3 *Maier, C.*
Montageautomatisierung am Beispiel des Schraubens mit Industrierobotern
1986 · 77 Abb. · 144 Seiten · ISBN 3-540-16393-X

4 *Summer, H.*
Modell zur Berechnung verzweigter Antriebsstrukturen
1986 · 74 Abb. · 197 Seiten · ISBN 3-540-16394-8

5 *Simon, W.*
Elektrische Vorschubantriebe an NC-Systemen
1986 · 141 Abb. · 198 Seiten · ISBN 3-540-16693-9

6 *Büchs, S.*
Analytische Untersuchungen zur Technologie der Kugelbearbeitung
1986 · 74 Abb. · 173 Seiten · ISBN 3-540-16694-7

7 *Hunzinger, I.*
Schneiderodierte Oberflächen
1986 · 79 Abb. · 162 Seiten · ISBN 3-540-16695-5

8 *Pilland, U.*
Echtzeit-Kollisionsschutz an NC-Drehmaschinen
1986 · 54 Abb. · 127 Seiten · ISBN 3-540-17274-2

9 *Barthelmeß, P.*
Montagegerechtes Konstruieren durch die Integration von Produkt- und Montageprozeßgestaltung
1987 · 70 Abb. · 144 Seiten · ISBN 3-540-18120-2

10 *Reithofer, N.*
Nutzungssicherung von flexibel automatisierten Produktionsanlagen
1987 · 84 Abb. · 176 Seiten · ISBN 3-540-18440-6

11 *Diess, H.*
Rechnerunterstützte Entwicklung flexibel automatisierter Montageprozesse
1988 · 56 Abb. · 144 Seiten · ISBN 3-540-18799-5

12 *Reinhart, G.*
Flexible Automatisierung der Konstruktion und Fertigung elektrischer Leitungssätze
1988 · 112 Abb. · 197 Seiten · ISBN 3-540-19003-1

13 *Bürstner, H.*
Investitionsentscheidung in der rechnerintegrierten Produktion
1988 · 74 Abb. · 190 Seiten · ISBN 3-540-19099-6

14 *Groha, A.*
Universelles Zellenrechnerkonzept für flexible Fertigungssysteme
1988 · 74 Abb. · 153 Seiten · ISBN 3-540-19182-8

15 *Riese, K.*
Klipsmontage mit Industrierobotern
1988 · 92 Abb. · 150 Seiten · ISBN 3-540-19183-6

16 *Lutz, P.*
Leitsysteme für rechnerintegrierte Auftragsabwicklung
1988 · 44 Abb. · 144 Seiten · ISBN 3-540-19260-3

17 *Klippel, C.*
Mobiler Roboter im Materialfluß eines flexiblen Fertigungssystems
1988 · 86 Abb. · 164 Seiten · ISBN 3-540-50468-0

18 *Rascher, R.*
Experimentelle Untersuchungen zur Technologie der Kugelherstellung
1989 · 110 Abb. · 200 Seiten · ISBN 3-540-51301-9

19 *Heusler, H.-J.*
Rechnerunterstützte Planung flexibler Montagesysteme
1989 · 43 Abb. · 154 Seiten · ISBN 3-540-51723-5

20 *Kirchknopf, P.*
Ermittlung modaler Parameter aus Übertragungsfrequenzgängen
1989 · 57 Abb. · 157 Seiten · ISBN 3-540-51724-3

21 *Sauerer, Ch.*
Beitrag für ein Zerspanprozeßmodell Metallbandsägen
1990 · 89 Abb. · 166 Seiten · ISBN 3-540-51868-1

22 *Karstedt, K.*
Positionsbestimmung von Objekten in der Montage- und Fertigungsautomatisierung
1990 · 92 Abb. · 157 Seiten · ISBN 3-540-51879-7

23 *Peiker, St.*
Entwicklung eines integrierten NC-Planungssystems
1990 · 66 Abb. · 180 Seiten · ISBN 3-540-51880-0

24 *Schugmann, R.*
Nachgiebige Werkzeugaufhängungen für die automatische Montage
1990 · 71 Abb. · 155 Seiten · ISBN 3-540-52138-0

25 *Wrba, P.*
Simulation als Werkzeug in der Handhabungstechnik
1990 · 125 Abb. · 178 Seiten · ISBN 3-540-52231-X

26 *Eibelshäuser, P.*
Rechnerunterstützte experimentelle Modalanalyse mittels gestufter Sinusanregung
1990 · 79 Abb. · 156 Seiten · ISBN 3-540-52451-7

27 *Prasch, J.*
Computerunterstützte Planung von chirurgischen Eingriffen in der Orthopädie
1990 · 113 Abb. · 164 Seiten · ISBN 3-540-52543-2

28 *Teich, K.*
Prozeßkommunikation und Rechnerverbund in der Produktion
1990 · 52 Abb. · 158 Seiten · ISBN 3-540-52764-8

29 *Pfrang, W.*
Rechnergestützte und graphische Planung manueller und teilautomatisierter Arbeitsplätze
1990 · 59 Abb. · 153 Seiten · ISBN 3-540-52829-6

30 *Tauber, A.*
Modellbildung kinematischer Strukturen als Komponente der Montageplanung
1990 · 93 Abb. · 190 Seiten · ISBN 3-540-52911-X

31 *Jäger, A.*
Systematische Planung komplexer Produktionssysteme
1991 · 75 Abb. · 148 Seiten · ISBN 3-540-53021-5

32 *Hartberger, H.*
Wissensbasierte Simulation komplexer Produktionssysteme
1991 · 58 Abb. · 154 Seiten · ISBN 3-540-53326-5

33 *Tuczek, H.*
Inspektion von Karosseriepreßteilen auf Risse und Einschnürungen mittels Methoden der Bildverarbeitung
1992 · 125 Abb. · 179 Seiten · ISBN 3-540-53965-4

34 *Fischbacher, J.*
Planungsstrategien zur stömungstechnischen Optimierung von Reinraum-Fertigungsgeräten
1991 · 60 Abb. · 166 Seiten · ISBN 3-540-54027-X

35 *Moser, O.*
3D-Echtzeitkollisionsschutz für Drehmaschinen
1991 · 66 Abb. · 177 Seiten · ISBN 3-540-54076-8

36 *Naber, H.*
Aufbau und Einsatz eines mobilen Roboters mit unabhängiger Lokomotions- und Manipulationskomponente
1991 · 85 Abb. · 139 Seiten · ISBN 3-540-54216-7

37 *Kupec, Th.*
Wissensbasiertes Leitsystem zur Steuerung flexibler Fertigungsanlagen
1991 · 68 Abb. · 150 Seiten · ISBN 3-540-54260-4

38 *Maulhardt, U.*
Dynamisches Verhalten von Kreissägen
1991 · 109 Abb. · 159 Seiten · ISBN 3-540-54365-1

39 *Götz, R.*
Strukturierte Planung flexibel automatisierter Montagesysteme für flächige Bauteile
1991 · 86 Abb. · 201 Seiten · ISBN 3-540-54401-1

40 *Koepfer, Th.*
3D-grafisch-interaktive Arbeitsplanung - ein Ansatz zur Aufhebung der Arbeitsteilung
1991 · 74 Abb. · 126 Seiten · ISBN 3-540-54436-4

41 *Schmidt, M.*
Konzeption und Einsatzplanung flexibel automatisierter Montagesysteme
1992 · 108 Abb. · 168 Seiten · ISBN 3-540-55025-9

42 *Burger, C.*
Produktionsregelung mit entscheidungsunterstützenden Informationssystemen
1992 · 94 Abb. · 186 Seiten · ISBN 3-540-55187-5

43 *Hoßmann, J.*
Methodik zur Planung der automatischen Montage von nicht formstabilen Bauteilen
1992 · 73 Abb. · 168 Seiten · ISBN 3-540-5520-0

44 *Petry, M.*
Systematik zur Entwicklung eines modularen Programmbaukastens für robotergeführte Klebeprozesse
1992 · 106 Abb. · 139 Seiten · ISBN 3-540-55374-6

45 *Schönecker, W.*
Integrierte Diagnose in Produktionszellen
1992 · 87 Abb. · 159 Seiten · ISBN 3-540-55375-4

46 *Bick, W.*
Systematische Planung hybrider Montagesysteme unter Berücksichtigung der Ermittlung des optimalen Automatisierungsgrades
1992 · 70 Abb. · 156 Seiten · ISBN 3-540-55377-0

47 *Gebauer, L.*
Prozeßuntersuchungen zur automatisierten Montage von optischen Linsen
1992 · 84 Abb. · 150 Seiten · ISBN 3-540-55378-9

48 *Schrüfer, N.*
Erstellung eines 3D-Simulationssystems zur Reduzierung von Rüstzeiten bei der NC-Bearbeitung
1992 · 103 Abb. · 161 Seiten · ISBN 3-540-55431-9

49 *Wisbacher, J.*
Methoden zur rationellen Automatisierung der Montage von Schnellbefestigungselementen
1992 · 77 Abb. · 176 Seiten · ISBN 3-540-55512-9

50 *Garnich, F.*
Laserbearbeitung mit Robotern
1992 · 110 Abb. · 184 Seiten · ISBN 3-540-55513-7

51 *Eubert, P.*
Digitale Zustandesregelung elektrischer Vorschubantriebe
1992 · 89 Abb. · 159 Seiten · ISBN 3-540-44441-2

52 *Glaas, W.*
Rechnerintegrierte Kabelsatzfertigung
1992 · 67 Abb. · 140 Seiten · ISBN 3-540-55749-0

53 *Helml, H.J.*
Ein Verfahren zur On-Line Fehlererkennung und Diagnose
1992 · 60 Abb. · 153 Seiten · ISBN 3-540-55750-4

54 *Lang, Ch.*
Wissensbasierte Unterstützung der Verfügbarkeitsplanung
1992 · 75 Abb. · 150 Seiten · ISBN 3-540-55751-2

55 *Schuster, G.*
Rechnergestütztes Planungssystem für die flexibel automatisierte Montage
1992 · 67 Abb. · 135 Seiten · ISBN 3-540-55830-6

56 *Bomm, H.*
Ein Ziel- und Kennzahlensystem zum Investitionscontrolling komplexer Produktionssysteme
1992 · 87 Abb. · 195 Seiten · ISBN 3-540-55964-7

57 *Wendt, A.*
Qualitätssicherung in flexibel automatisierten Montagesystemen
1992 · 74 Abb. · 179 Seiten · ISBN 3-540-56044-0

58 *Hansmaier, H.*
Rechnergestütztes Verfahren zur Geräuschminderung
1993 · 67 Abb. · 156 Seiten · ISBN 3-540-56053-2

59 *Dilling, U.*
Planung von Fertigungssystemen unterstützt durch Wirtschaftssimulationen
1993 · 72 Abb. · 146 Seiten · ISBN 3-540-56307-5

60 *Strohmayr, R.*
Rechnergestützte Auswahl und Konfiguration von Zubringeeinrichtungen
1993 · 80 Abb. · 152 Seiten · ISBN 3-540-56652-X

61 *Glas, J.*
Standardisierter Aufbau anwendungsspezifischer Zellenrechnersoftware
1993 · 80 Abb. · 145 Seiten · ISBN 3.540-56890-5

62 *Stetter, R.*
Rechnergestützte Simulationswerkzeuge zur Effizienzsteigerung des Industrierobotereinsatzes
1994 · 91 Abb. · 146 Seiten · ISBN 3-540-56889-1

63 *Dirndorfer, A.*
Robotersysteme zur förderbandsynchronen Montage
1993 · 76 Abb. · 144 Seiten · ISBN 3-540-57031-4

64 *Wiedemann, M.*
Simulation des Schwingungsverhaltens spanender Werkzeugmaschinen
1993 · 81 Abb. · 137 Seiten · ISBN 3-540-57177-9

65 *Woenckhaus, Ch.*
Rechnergestütztes System zur automatisierten 3D-Layoutoptimierung
1994 · 81 Abb. · 140 Seiten · ISBN 3-540-57284-8

66 *Kummetsteiner, G.*
3D-Bewegungssimulation als integratives Hilfsmittel zur Planung manueller Montagesysteme
1994 · 62 Abb. · 146 Seiten · ISBN 3-540-57535-9

67 *Kugelmann, F.*
Einsatz nachgiebiger Elemente zur wirtschaftlichen Automatisierung von Produktionssystemen
1993 · 76 Abb. · 144 Seiten · ISBN 3-540-57549-9

68 *Schwarz, H.*
Simulationsgestützte CAD/CAM-Kopplung für die 3D-Laserbearbeitung mit integrierter Sensorik
1994 · 96 Abb. · 148 Seiten · ISBN 3-540-57577-4

69 *Viethen, U.*
Systematik zum Prüfen in flexiblen Fertigungssystemen
1994 · 70 Abb. · 142 Seiten · ISBN 3-540-57794-7

70 *Seehuber, M.*
Automatische Inbetriebnahme geschwindigkeitsadaptiver Zustandsregler
1994 · 72 Abb. · 155 Seiten · ISBN 3-540-57896-X

71 *Amann, W.*
Eine Simulationsumgebung für Planung und Betrieb von Produktionssystemen
1994 · 71 Abb. · 129 Seiten · ISBN 3-540-57924-9

72 *Schöpf, M.*
Rechnergestütztes Projektinformations- und Koordinationssystem für das Fertigungsvorfeld
1997 · 63 Abb. · 130 Seiten · ISBN 3-540-58052-2

73 *Welling, A.*
Effizienter Einsatz bildgebender Sensoren zur Flexibilisierung automatisierter Handhabungsvorgänge
1994 · 66 Abb. · 139 Seiten · ISBN 3-540-580-0

74 *Zetlmayer, H.*
Verfahren zur simulationsgestützten Produktionsregelung in der Einzel- und Kleinserienproduktion
1994 · 62 Abb. · 143 Seiten · ISBN 3-540-58134-0

75 *Lindl, M.*
Auftragsleittechnik für Konstruktion und Arbeitsplanung
1994 · 66 Abb. · 147 Seiten · ISBN 3-540-58221-5

76 *Zipper, B.*
Das integrierte Betriebsmittelwesen · Baustein einer flexiblen Fertigung
1994 · 64 Abb. · 147 Seiten · ISBN 3-540-58222-3

77 *Raith, P.*
Programmierung und Simulation von Zellenabläufen in der Arbeitsvorbereitung
1995 · 51 Abb. · 130 Seiten · ISBN 3-540-58223-1

78 *Engel, A.*
Strömungstechnische Optimierung von Produktionssystemen durch Simulation
1994 · 69 Abb. · 160 Seiten · ISBN 3-540-58258-4

79 *Zäh, M. F.*
Dynamisches Prozeßmodell Kreissägen
1995 · 95 Abb. · 186 Seiten · ISBN 3-540-58624-5

80 *Zwanzer, N.*
Technologisches Prozeßmodell für die Kugelschleifbearbeitung
1995 · 65 Abb. · 150 Seiten · ISBN 3-540-58634-2

81 *Romanow, P.*
Konstruktionsbegleitende Kalkulation von Werkzeugmaschinen
1995 · 66 Abb. · 151 Seiten · ISBN 3-540-58771-3

82 *Kahlenberg, R.*
Integrierte Qualitätssicherung in flexiblen Fertigungszellen
1995 · 71 Abb. · 136 Seiten · ISBN 3-540-58772-1

83 *Huber, A.*
Arbeitsfolgenplanung mehrstufiger Prozesse in der Hartbearbeitung
1995 · 87 Abb. · 152 Seiten · ISBN 3-540-58773-X

84 *Birkel, G.*
Aufwandsminimierter Wissenserwerb für die Diagnose in flexiblen Produktionszellen
1995 · 64 Abb. · 137 Seiten · ISBN 3-540-58869-8

85 *Simon, D.*
Fertigungsregelung durch zielgrößenorientierte Planung und logistisches Störungsmanagement
1995 · 77 Abb. · 132 Seiten · ISBN 3-540-58942-2

86 *Nedeljkovic-Groha, V.*
Systematische Planung anwendungsspezifischer Materialflußsteuerungen
1995 · 94 Abb. · 188 Seiten · ISBN 3-540-58953-8

87 *Rockland, M.*
Flexibilisierung der automatischen Teilbereitstellung in Montageanlagen
1995 · 83 Abb. · 168 Seiten · ISBN 3-540-58999-6

88 *Linner, St.*
Konzept einer integrierten Produktentwicklung
1995 · 67 Abb. · 168 Seiten · ISBN 3-540-59016-1

89 *Eder, Th.*
Integrierte Planung von Informationssystemen für rechnergestützte Produktionssysteme
1995 · 62 Abb. · 150 Seiten · ISBN 3-540-59084-6

90 *Deutschle, U.*
Prozeßorientierte Organisation der Auftragsentwicklung in mittelständischen Unternehmen
1995 · 80 Abb. · 188 Seiten · ISBN 3-540-59337-3

91 *Dieterle, A.*
Recyclingintegrierte Produktentwicklung
1995 · 68 Abb. · 146 Seiten · ISBN 3-540-60120-1

92 *Hechl, Chr.*
Personalorientierte Montageplanung für komplexe und variantenreiche Produkte
1995 · 73 Abb. · 158 Seiten · ISBN 3-540-60325-5

93 *Albertz, F.*
Dynamikgerechter Entwurf von Werkzeugmaschinen - Gestellstrukturen
1995 · 83 Abb. · 156 Seiten · ISBN 3-540-60608-8

94 *Trunzer, W.*
Strategien zur On-Line Bahnplanung bei Robotern mit 3D-Konturfolgesensoren
1996 · 101 Abb. · 164 Seiten · ISBN 3-540-60961-X

95 *Fichtmüller, N.*
Rationalisierung durch flexible, hybride Montagesysteme
1996 · 83 Abb. · 145 Seiten · ISBN 3-540-60960-1

96 *Trucks, V.*
Rechnergestützte Beurteilung von Getriebestrukturen in Werkzeugmaschinen
1996 · 64 Abb. · 141 Seiten · ISBN 3-540-60599-8

97 *Schäffer, G.*
Systematische Integration adaptiver Produktionssysteme
1996 · 71 Abb. · 170 Seiten · ISBN 3-540-60958-X

98 *Koch, M. R.*
Autonome Fertigungszellen - Gestaltung, Steuerung und integrierte Störungsbehandlung
1996 · 67 Abb. · 138 Seiten · ISBN 3-540-61104-5

99 *Moctezuma de la Barrera, J.L.*
Ein durchgängiges System zur computer- und rechnergestützten Chirurgie
1996 · 99 Abb. · 175 Seiten · ISBN 3-540-61145-2

100 *Geuer, A.*
Einsatzpotential des Rapid Prototyping in der Produktentwicklung
1996 · 84 Abb. · 154 Seiten · ISBN 3-540-61495-8

101 *Ebner, C.*
Ganzheitliches Verfügbarkeits- und Qualitätsmanagment unter Verwendung von Felddaten
1996 · 67 Abb. · 132 Seiten · ISBN 3-540-61678-0

102 *Pischeltsrieder, K.*
Steuerung autonomer mobiler Roboter in der Produktion
1996 · 74 Abb. · 171 Seiten · ISBN 3-540-61714-0

103 *Köhler, R.*
Disposition und Materialbereitstellung bei komplexen variantenreichen Kleinprodukten
1997 · 62 Abb. · 177 Seiten · ISBN 3-540-62024-9

104 *Feldmann, Ch.*
Eine Methode für die integrierte rechnergestützte Montageplanung
1997 · 71 Abb. · 163 Seiten · ISBN 3-540-62059-1

105 *Lehmann, H.*
Integrierte Materialfluß- und Layoutplanung durch Kopplung von CAD- und Ablaufsimulationssystem
1997 · 96 Abb. · 191 Seiten · ISBN 3-540-62202-0

106 *Wagner, M.*
Steuerungsintegrierte Fehlerbehandlung für maschinennahe Abläufe
1997 · 94 Abb. · 164 Seiten · ISBN 3-540-62656-5

107 *Lorenzen, J.*
Simulationsgestützte Kostenanalyse in produktorientierten Fertigungsstrukturen
1997 · 63 Abb. · 129 Seiten · ISBN 3-540-62794-4

108 *Krönert, U.*
Systematik für die rechnergestützte Ähnlichteilsuche und Standardisierung
1997 · 53 Abb. · 127 Seiten · ISBN 3-540-63338-3

109 *Pfersdorf, I.*
Entwicklung eines systematischen Vorgehens zur Organisation des industriellen Service
1997 · 74 Abb. · 172 Seiten · ISBN 3-540-63615-3

110 *Kube, R.*
Informations- und kommunikationstechnische Integration von Menschen in der Produktion
1997 · 77 Abb. · 155 Seiten · ISBN 3-540-63642-0

111 *Kaiser, J.*
Vernetztes Gestalten von Produkt und Produktionsprozeß mit Produktmodellen
1997 · 67 Abb. · 139 Seiten · ISBN 3-540-63999-3

112 *Geyer, M.*
Flexibles Planungssystem zur Berücksichtigung ergonomischer Aspekte bei der Produkt- und Arbeitssystemgestaltung
1997 · 85 Abb. · 154 Seiten · ISBN 3-540-64195-5

113 *Martin, C.*
Produktionsregelung - ein modularer, modellbasierter Ansatz
1998 · 73 Abb. · 162 Seiten · ISBN 3-540-64401-6

114 *Löffler, Th.*
Akustische Überwachung automatisierter Fügeprozesse
1998 · 85 Abb. · 136 Seiten · ISBN 3-540-64511-X

115 *Lindermaier, R.*
Qualitätsorientierte Entwicklung von Montagesystemen
1998 · 84 Abb. · 164 Seiten · ISBN 3-540-64686-8

116 *Koehrer, J.*
Prozeßorientierte Teamstrukturen in Betrieben mit Großserienfertigung
1998 · 75 Abb. · 185 Seiten · ISBN 3-540-65037-7

117 *Schuller, R. W.*
Leitfaden zum automatisierten Auftrag von hochviskosen Dichtmassen
1999 · 76 Abb. · 162 Seiten · ISBN 3-540-65320-1

118 *Debuschewitz, M.*
Integrierte Methodik und Werkzeuge zur herstellungsorientierten Produktentwicklung
1999 · 104 Abb. · 169 Seiten · ISBN 3-540-65350-3

119 *Bauer, L.*
Strategien zur rechnergestützten Offline-Programmierung von 3D-Laseranlagen
1999 · 98 Abb. · 145 Seiten · ISBN 3-540-65382-1

120 *Pfob, E.*
Modellgestützte Arbeitsplanung bei Fertigungsmaschinen
1999 · 69 Abb. · 154 Seiten · ISBN 3-540-65525-5

121 *Spitznagel, J.*
Erfahrungsgeleitete Planung von Laseranlagen
1999 · 63 Abb. · 156 Seiten · ISBN 3-540-65896-3

Seminarberichte iwb

herausgegeben von Prof. Dr.-Ing. Gunther Reinhart und Prof. Dr.-Ing. Michael Zäh,
Institut für Werkzeugmaschinen und Betriebswissenschaften
der Technischen Universität München

Seminarberichte iwb sind erhältlich im Buchhandel oder beim
Herbert Utz Verlag, München, Fax 089-277791-01, info@utz.de

1 Innovative Montagesysteme - Anlagengestaltung, -bewertung und -überwachung
115 Seiten · ISBN 3-931327-01-9

2 Integriertes Produktmodell - Von der Idee zum fertigen Produkt
82 Seiten · ISBN 3-931327-02-7

3 Konstruktion von Werkzeugmaschinen - Berechnung, Simulation und Optimierung
110 Seiten · ISBN 3-931327-03-5

4 Simulation - Einsatzmöglichkeiten und Erfahrungsberichte
134 Seiten · ISBN 3-931327-04-3

5 Optimierung der Kooperation in der Produktentwicklung
95 Seiten · ISBN 3-931327-05-1

6 Materialbearbeitung mit Laser · von der Planung zur Anwendung
86 Seiten · ISBN 3-931327-76-0

7 Dynamisches Verhalten von Werkzeugmaschinen
80 Seiten · ISBN 3-931327-77-9

8 Qualitätsmanagement · der Weg ist das Ziel
130 Seiten · ISBN 3-931327-78-7

9 Installationstechnik an Werkzeugmaschinen · Analysen und Konzepte
120 Seiten · ISBN 3-931327-79-5

10 3D-Simulation - Schneller, sicherer und kostengünstiger zum Ziel
90 Seiten · ISBN 3-931327-10-8

11 Unternehmensorganisation · Schlüssel für eine effiziente Produktion
110 Seiten · ISBN 3-931327-11-6

12 Autonome Produktionssysteme
100 Seiten · ISBN 3-931327-12-4

13 Planung von Montageanlagen
130 Seiten · ISBN 3-931327-13-2

14 Nicht erschienen – wird nicht erscheinen

15 Flexible fluide Kleb/Dichtstoffe · Dosierung und Prozeßgestaltung
80 Seiten · ISBN 3-931327-15-9

16 Time to Market - Von der Idee zum Produktionsstart
80 Seiten · ISBN 3-931327-16-7

17 Industriekeramik in Forschung und Praxis - Probleme, Analysen und Lösungen
80 Seiten · ISBN 3-931327-17-5

18 Das Unternehmen im Internet - Chancen für produzierende Unternehmen
165 Seiten · ISBN 3-931327-18-3

19 Leittechnik und Informationslogistik - mehr Transparenz in der Fertigung
85 Seiten · ISBN 3-931327-19-1

20 Dezentrale Steuerungen in Produktionsanlagen - Plug & Play - Vereinfachung von Entwicklung und Inbetriebnahme
105 Seiten · ISBN 3-931327-20-5

21 Rapid Prototyping - Rapid Tooling - Schnell zu funktionalen Prototypen
95 Seiten · ISBN 3-931327-21-3

22 Mikrotechnik für die Produktion - Greifbare Produkte und Anwendungspotentiale
95 Seiten · ISBN 3-931327-22-1

24 EDM Engineering Data Management
195 Seiten · ISBN 3-931327-24-8

25 Rationelle Nutzung der Simulationstechnik - Entwicklungstrends und Praxisbeispiele
152 Seiten · ISBN 3-931327-25-6

26 Alternative Dichtungssysteme - Konzepte zur Dichtungsmontage und zum Dichtmittelauftrag
110 Seiten · ISBN 3-931327-26-4

27 Rapid Prototyping · Mit neuen Technologien schnell vom Entwurf zum Serienprodukt
111 Seiten · ISBN 3-931327-27-2

28 Rapid Tooling · Mit neuen Technologien schnell vom Entwurf zum Serienprodukt
154 Seiten · ISBN 3-931327-28-0

29 Installationstechnik an Werkzeugmaschinen · Abschlußseminar
156 Seiten · ISBN 3-931327-29-9

30 Nicht erschienen – wird nicht erscheinen

31 Engineering Data Management (EDM) · Erfahrungsberichte und Trends
183 Seiten · ISBN 3-931327-31-0

32 Nicht erschienen – wird nicht erscheinen

33 3D-CAD · Mehr als nur eine dritte Dimension
181 Seiten · ISBN 3-931327-33-7

34 Laser in der Produktion · Technologische Randbedingungen für den wirtschaftlichen Einsatz
102 Seiten · ISBN 3-931327-34-5

35 Ablaufsimulation · Anlagen effizient und sicher planen und betreiben
129 Seiten · ISBN 3-931327-35-3

36 Moderne Methoden zur Montageplanung · Schlüssel für eine effiziente Produktion
124 Seiten · ISBN 3-931327-36-1

37 Wettbewerbsfaktor Verfügbarkeit · Produktivitätsteigerung durch technische und organisatorische Ansätze
95 Seiten · ISBN 3-931327-37-X

38 Rapid Prototyping · Effizienter Einsatz von Modellen in der Produktentwicklung
128 Seiten · ISBN 3-931327-38-8

39 Rapid Tooling · Neue Strategien für den Werkzeug- und Formenbau
130 Seiten · ISBN 3-931327-39-6

40 Erfolgreich kooperieren in der produzierenden Industrie · Flexibler und schneller mit modernen Kooperationen
160 Seiten · ISBN 3-931327-40-X

41 Innovative Entwicklung von Produktionsmaschinen
146 Seiten · ISBN 3-89675-041-0

42 Stückzahlflexible Montagesysteme
139 Seiten · ISBN 3-89675-042-9

43 Produktivität und Verfügbarkeit · ...durch Kooperation steigern
120 Seiten · ISBN 3-89675-043-7

44 Automatisierte Mikromontage · Handhaben und Positionieren von Mikrobauteilen
125 Seiten · ISBN 3-89675-044-5

45 Produzieren in Netzwerken · Lösungsansätze, Methoden, Praxisbeispiele
173 Seiten · ISBN 3-89675-045-3

46 Virtuelle Produktion · Ablaufsimulation
108 Seiten · ISBN 3-89675-046-1

47 Virtuelle Produktion · Prozeß- und Produktsimulation
131 Seiten · ISBN 3-89675-047-X
48 Sicherheitstechnik an Werkzeugmaschinen
106 Seiten · ISBN 3-89675-048-8
49 Rapid Prototyping · Methoden für die reaktionsfähige Produktentwicklung
150 Seiten · ISBN 3-89675-049-6
50 Rapid Manufacturing · Methoden für die reaktionsfähige Produktion
121 Seiten · ISBN 3-89675-050-X
51 Flexibles Kleben und Dichten · Produkt-& Prozeßgestaltung, Mischverbindungen, Qualitätskontrolle
137 Seiten · ISBN 3-89675-051-8
52 Rapid Manufacturing · Schnelle Herstellung von Klein- und Prototypenserien
124 Seiten · ISBN 3-89675-052-6
53 Mischverbindungen · Werkstoffauswahl, Verfahrensauswahl, Umsetzung
107 Seiten · ISBN 3-89675-054-2
54 Virtuelle Produktion · Integrierte Prozess- und Produktsimulation
133 Seiten · ISBN 3-89675-054-2
55 e-Business in der Produktion · Organisationskonzepte, IT-Lösungen, Praxisbeispiele
150 Seiten · ISBN 3-89675-055-0
56 Virtuelle Produktion – Ablaufsimulation als planungsbegleitendes Werkzeug
150 Seiten · ISBN 3-89675-056-9
57 Virtuelle Produktion – Datenintegration und Benutzerschnittstellen
150 Seiten · ISBN 3-89675-057-7
58 Rapid Manufacturing · Schnelle Herstellung qualitativ hochwertiger Bauteile oder Kleinserien
169 Seiten · ISBN 3-89675-058-7
59 Automatisierte Mikromontage · Werkzeuge und Fügetechnologien für die Mikrosystemtechnik
114 Seiten · ISBN 3-89675-059-3
60 Mechatronische Produktionssysteme · Genauigkeit gezielt entwickeln
131 Seiten · ISBN 3-89675-060-7
61 Nicht erschienen – wird nicht erscheinen
62 Rapid Technologien · Anspruch – Realität – Technologien
100 Seiten · ISBN 3-89675-062-3
63 Fabrikplanung 2002 · Visionen – Umsetzung – Werkzeuge
124 Seiten · ISBN 3-89675-063-1
64 Mischverbindungen · Einsatz und Innovationspotenzial
143 Seiten · ISBN 3-89675-064-X
65 Fabrikplanung 2003 – Basis für Wachstum · Erfahrungen Werkzeuge Visionen
136 Seiten · ISBN 3-89675-065-8
66 Mit Rapid Technologien zum Aufschwung · Neue Rapid Technologien und Verfahren, Neue Qualitäten, Neue Möglichkeiten, Neue Anwendungsfelder
185 Seiten · ISBN 3-89675-066-6
67 Mechatronische Produktionssysteme · Die Virtuelle Werkzeugmaschine: Mechatronisches Entwicklungsvorgehen, Integrierte Modellbildung, Applikationsfelder
148 Seiten · ISBN 3-89675-067-4
68 Virtuelle Produktion · Nutzenpotenziale im Lebenszyklus der Fabrik
139 Seiten · ISBN 3-89675-068-2
69 Kooperationsmanagement in der Produktion · Visionen und Methoden zur Kooperation – Geschäftsmodelle und Rechtsformen für die Kooperation – Kooperation entlang der Wertschöpfungskette
134 Seiten · ISBN 3-98675-069-0
70 Mechatronik · Strukturdynamik von Werkzeugmaschinen
161 Seiten · ISBN 3-89675-070-4
71 Klebtechnik · Zerstörungsfreie Qualitätssicherung beim flexibel automatisierten Kleben und Dichten
ISBN 3-89675-071-2 · vergriffen
72 Fabrikplanung 2004 Ergfolgsfaktor im Wettbewerb · Erfahrungen – Werkzeuge – Visionen
ISBN 3-89675-072-0 · vergriffen
73 Rapid Manufacturing Vom Prototyp zur Produktion · Erwartungen – Erfahrungen – Entwicklungen
179 Seiten · ISBN 3-89675-073-9
74 Virtuelle Produktionssystemplanung · Virtuelle Inbetriebnahme und Digitale Fabrik
133 Seiten · ISBN 3-89675-074-7
75 Nicht erschienen – wird nicht erscheinen
76 Berührungslose Handhabung · Vom Wafer zur Glaslinse, von der Kapsel zur aseptischen Ampulle
95 Seiten · ISBN 3-89675-076-3
77 ERP-Systeme - Einführung in die betriebliche Praxis · Erfahrungen, Best Practices, Visionen
153 Seiten · ISBN 3-89675-077-7
78 Mechatronik · Trends in der interdisziplinären Entwicklung von Werkzeugmaschinen
155 Seiten · ISBN 3-89675-078-X
79 Produktionsmanagement
267 Seiten · ISBN 3-89675-079-8
80 Rapid Manufacturing · Fertigungsverfahren für alle Ansprüche
154 Seiten · ISBN 3-89675-080-1
81 Rapid Manufacturing · Heutige Trends – Zukünftige Anwendungsfelder
172 Seiten · ISBN 3-89675-081-X
82 Produktionsmanagement · Herausforderung Variantenmanagement
100 Seiten · ISBN 3-89675-082-8
83 Mechatronik · Optimierungspotenzial der Werkzeugmaschine nutzen
160 Seiten · ISBN 3-89675-083-6
84 Virtuelle Inbetriebnahme · Von der Kür zur Pflicht?
104 Seiten · ISBN 978-3-89675-084-6
85 3D-Erfahrungsforum · Innovation im Werkzeug- und Formenbau
375 Seiten · ISBN 978-3-89675-085-3
86 Rapid Manufacturing · Erfolgreich produzieren durch innovative Fertigung
162 Seiten · ISBN 978-3-89675-086-0
87 Produktionsmanagement · Schlank im Mittelstand
102 Seiten · ISBN 978-3-89675-087-7
88 Mechatronik · Vorsprung durch Simulation
134 Seiten · ISBN 978-3-89675-088-4
89 RFID in der Produktion · Wertschöpfung effizient gestalten
122 Seiten · ISBN 978-3-89675-089-1

Forschungsberichte iwb

herausgegeben von Prof. Dr.-Ing. Gunther Reinhart und Prof. Dr.-Ing. Michael Zäh,
Institut für Werkzeugmaschinen und Betriebswissenschaften
der Technischen Universität München

Forschungsberichte iwb ab Band 122 sind erhältlich im Buchhandel oder beim
Herbert Utz Verlag, München, Fax 089-277791-01, info@utz.de

122 Schneider, Burghard
Prozesskettenorientierte Bereitstellung nicht formstabiler Bauteile
1999 · 183 Seiten · 98 Abb. · 14 Tab. · broschiert · 20,5 x 14,5 cm · ISBN 3-89675-559-5

123 Goldstein, Bernd
Modellgestützte Geschäftsprozeßgestaltung in der Produktentwicklung
1999 · 170 Seiten · 65 Abb. · broschiert · 20,5 x 14,5 cm · ISBN 3-89675-546-3

124 Mößmer, Helmut E.
Methode zur simulationsbasierten Regelung zeitvarianter Produktionssysteme
1999 · 164 Seiten · 67 Abb. · 5 Tab. · broschiert · 20,5 x 14,5 cm · ISBN 3-89675-585-4

125 Gräser, Ralf-Gunter
Ein Verfahren zur Kompensation temperaturinduzierter Verformungen an Industrierobotern
1999 · 167 Seiten · 63 Abb. · 5 Tab. · broschiert · 20,5 x 14,5 cm · ISBN 3-89675-603-6

126 Trossin, Hans-Jürgen
Nutzung der Ähnlichkeitstheorie zur Modellbildung in der Produktionstechnik
1999 · 162 Seiten · 75 Abb. · 11 Tab. · broschiert · 20,5 x 14,5 cm · ISBN 3-89675-614-1

127 Kugelmann, Doris
Aufgabenorientierte Offline-Programmierung von Industrierobotern
1999 · 168 Seiten · 68 Abb. · 2 Tab. · broschiert · 20,5 x 14,5 cm · ISBN 3-89675-615-X

128 Diesch, Rolf
Steigerung der organisatorischen Verfügbarkeit von Fertigungszellen
1999 · 160 Seiten · 69 Abb. · broschiert · 20,5 x 14,5 cm · ISBN 3-89675-618-4

129 Lulay, Werner E.
Hybrid-hierarchische Simulationsmodelle zur Koordination teilautonomer Produktionsstrukturen
1999 · 182 Seiten · 51 Abb. · 14 Tab. · broschiert · 20,5 x 14,5 cm · ISBN 3-89675-620-6

130 Murr, Otto
Adaptive Planung und Steuerung von integrierten Entwicklungs- und Planungsprozessen
1999 · 178 Seiten · 85 Abb. · 3 Tab. · broschiert · 20,5 x 14,5 cm · ISBN 3-89675-636-2

131 Macht, Michael
Ein Vorgehensmodell für den Einsatz von Rapid Prototyping
1999 · 170 Seiten · 87 Abb. · 5 Tab. · broschiert · 20,5 x 14,5 cm · ISBN 3-89675-638-9

132 Mehler, Bruno H.
Aufbau virtueller Fabriken aus dezentralen Partnerverbünden
1999 · 152 Seiten · 44 Abb. · 27 Tab. · broschiert · 20,5 x 14,5 cm · ISBN 3-89675-645-1

133 Heitmann, Knut
Sichere Prognosen für die Produktionsptimierung mittels stochastischer Modelle
1999 · 146 Seiten · 60 Abb. · 13 Tab. · broschiert · 20,5 x 14,5 cm · ISBN 3-89675-675-3

134 Blessing, Stefan
Gestaltung der Materialflußsteuerung in dynamischen Produktionsstrukturen
1999 · 160 Seiten · 67 Abb. · broschiert · 20,5 x 14,5 cm · ISBN 3-89675-690-7

135 Abay, Can
Numerische Optimierung multivariater mehrstufiger Prozesse am Beispiel der Hartbearbeitung von Industriekeramik
2000 · 159 Seiten · 46 Abb. · 5 Tab. · broschiert · 20,5 x 14,5 cm · ISBN 3-89675-697-4

136 Brandner, Stefan
Integriertes Produktdaten- und Prozeßmanagement in virtuellen Fabriken
2000 · 172 Seiten · 61 Abb. · broschiert · 20,5 x 14,5 cm · ISBN 3-89675-715-6

137 Hirschberg, Arnd G.
Verbindung der Produkt- und Funktionsorientierung in der Fertigung
2000 · 165 Seiten · 49 Abb. · broschiert · 20,5 x 14,5 cm · ISBN 3-89675-729-6

138 Reek, Alexandra
Strategien zur Fokuspositionierung beim Laserstrahlschweißen
2000 · 193 Seiten · 103 Abb. · broschiert · 20,5 x 14,5 cm · ISBN 3-89675-730-X

139 Sabbah, Khalid-Alexander
Methodische Entwicklung störungstoleranter Steuerungen
2000 · 148 Seiten · 75 Abb. · broschiert · 20,5 x 14,5 cm · ISBN 3-89675-739-3

140 Schliffenbacher, Klaus U.
Konfiguration virtueller Wertschöpfungsketten in dynamischen, heterarchischen Kompetenznetzwerken
2000 · 187 Seiten · 70 Abb. · broschiert · 20,5 x 14,5 cm · ISBN 3-89675-754-7

141 Sprenzel, Andreas
Integrierte Kostenkalkulationsverfahren für die Werkzeugmaschinenentwicklung
2000 · 144 Seiten · 55 Abb. · 6 Tab. · broschiert · 20,5 x 14,5 cm · ISBN 3-89675-757-1

142 Gallasch, Andreas
Informationstechnische Architektur zur Unterstützung des Wandels in der Produktion
2000 · 150 Seiten · 69 Abb. · 6 Tab. · broschiert · 20,5 x 14,5 cm · ISBN 3-89675-781-4

143 Cuiper, Ralf
Durchgängige rechnergestützte Planung und Steuerung von automatisierten Montagevorgängen
2000 · 168 Seiten · 75 Abb. · 3 Tab. · broschiert · 20,5 x 14,5 cm · ISBN 3-89675-783-0

144 Schneider, Christian
Strukturmechanische Berechnungen in der Werkzeugmaschinenkonstruktion
2000 · 180 Seiten · 66 Abb. · broschiert · 20,5 x 14,5 cm · ISBN 3-89675-789-X

145 Jonas, Christian
Konzept einer durchgängigen, rechnergestützten Planung von Montageanlagen
2000 · 183 Seiten · 82 Abb. · broschiert · 20,5 x 14,5 cm · ISBN 3-89675-870-5

146 Willnecker, Ulrich
Gestaltung und Planung leistungsorientierter manueller Fließmontagen
2001 · 175 Seiten · 67 Abb. · broschiert · 20,5 x 14,5 cm · ISBN 3-89675-891-8

147 Lehner, Christof
Beschreibung des Nd:Yag-Laserstrahlschweißprozesses von Magnesiumdruckguss
2001 · 205 Seiten · 94 Abb. · 24 Tab. · 20,5 x 14,5 cm · ISBN 3-8316-0004-X

148 Rick, Frank
Simulationsgestützte Gestaltung von Produkt und Prozess am Beispiel Laserstrahlschweißen
2001 · 145 Seiten · 57 Abb. · 2 Tab. · 20,5 x 14,5 cm · ISBN 3-8316-0008-2

149 Höhn, Michael
Sensorgeführte Montage hybrider Mikrosysteme
2001 · 171 Seiten · 74 Abb. · 7 Tab. · 20,5 x 14,5 cm · ISBN 3-8316-0012-0

150 Böhl, Jörn
Wissensmanagement im Klein- und mittelständischen Unternehmen der Einzel- und Kleinserienfertigung
2001 · 179 Seiten · 88 Abb. · 20,5 x 14,5 cm · ISBN 3-8316-0020-1

151 Bürgel, Robert
Prozessanalyse an spanenden Werkzeugmaschinen mit digital geregelten Antrieben
2001 · 185 Seiten · 60 Abb. · 10 Tab. · 20,5 x 14,5 cm · ISBN 3-8316-0021-X

152 Stephan Dürrschmidt
Planung und Betrieb wandlungsfähiger Logistiksysteme in der variantenreichen Serienproduktion
2001 · 914 Seiten · 61 Abb. · 20,5 x 14,5 cm · ISBN 3-8316-0023-6

153 Bernhard Eich
Methode zur prozesskettenorientierten Planung der Teilebereitstellung
2001 · 132 Seiten · 48 Abb. · 6 Tabellen · 20,5 x 14,5 cm · ISBN 3-8316-0028-7

154 Wolfgang Rudorfer
Eine Methode zur Qualifizierung von produzierenden Unternehmen für Kompetenznetzwerke
2001 · 207 Seiten · 89 Abb. · 20,5 x 14,5 cm · ISBN 3-8316-0037-6

155 Hans Meier
Verteilte kooperative Steuerung maschinennaher Abläufe
2001 · 162 Seiten · 85 Abb. · 20,5 x 14,5 cm · ISBN 3-8316-0044-9

156 Gerhard Nowak
Informationstechnische Integration des industriellen Service in das Unternehmen
2001 · 203 Seiten · 95 Abb. · 20,5 x 14,5 cm · ISBN 3-8316-0055-4

157 Martin Werner
Simulationsgestützte Reorganisation von Produktions- und Logistikprozessen
2001 · 191 Seiten · 20,5 x 14,5 cm · ISBN 3-8316-0058-9

158 Bernhard Lenz
Finite Elemente-Modellierung des Laserstrahlschweißens für den Einsatz in der Fertigungsplanung
2001 · 150 Seiten · 47 Abb. · 5 Tab. · 20,5 x 14,5 cm · ISBN 3-8316-0094-5

159 Stefan Grunwald
Methode zur Anwendung der flexiblen integrierten Produktentwicklung und Montageplanung
2002 · 206 Seiten · 80 Abb. · 25 Tab. · 20,5 x 14,5 cm · ISBN 3-8316-0095-3

160 Josef Gartner
Qualitätssicherung bei der automatisierten Applikation hochviskoser Dichtungen
2002 · 165 Seiten · 74 Abb. · 21 Tab. · 20,5 x 14,5 cm · ISBN 3-8316-0096-1

161 Wolfgang Zeller
Gesamtheitliches Sicherheitskonzept für die Antriebs- und Steuerungstechnik bei Werkzeugmaschinen
2002 · 192 Seiten · 54 Abb. · 15 Tab. · 20,5 x 14,5 cm · ISBN 3-8316-0100-3

162 Michael Loferer
Rechnergestützte Gestaltung von Montagesystemen
2002 · 178 Seiten · 80 Abb. · 20,5 x 14,5 cm · ISBN 3-8316-0118-6

163 Jörg Fährer
Ganzheitliche Optimierung des indirekten Metall-Lasersinterprozesses
2002 · 176 Seiten · 69 Abb. · 13 Tab. · 20,5 x 14,5 cm · ISBN 3-8316-0124-0

164 Jürgen Höppner
Verfahren zur berührungslosen Handhabung mittels leistungsstarker Schallwandler
2002 · 132 Seiten · 24 Abb. · 3 Tab. · 20,5 x 14,5 cm · ISBN 3-8316-0125-9

165 Hubert Götte
Entwicklung eines Assistenzrobotersystems für die Knieendoprothetik
2002 · 258 Seiten · 123 Abb. · 5 Tab. · 20,5 x 14,5 cm · ISBN 3-8316-0126-7

166 Martin Weißenberger
Optimierung der Bewegungsdynamik von Werkzeugmaschinen im rechnergestützten Entwicklungsprozess
2002 · 210 Seiten · 86 Abb. · 2 Tab. · 20,5 x 14,5 cm · ISBN 3-8316-0138-0

167 Dirk Jacob
Verfahren zur Positionierung unterseitenstrukturierter Bauelemente in der Mikrosystemtechnik
2002 · 200 Seiten · 82 Abb. · 24 Tab. · 20,5 x 14,5 cm · ISBN 3-8316-0142-9

168 Ulrich Roßgoderer
System zur effizienten Layout- und Prozessplanung von hybriden Montageanlagen
2002 · 175 Seiten · 20,5 x 14,5 cm · ISBN 3-8316-0154-2

169 Robert Klingel
Anziehverfahren für hochfeste Schraubenverbindungen auf Basis akustischer Emissionen
2002 · 164 Seiten · 89 Abb. · 27 Tab. · 20,5 x 14,5 cm · ISBN 3-8316-0174-7

170 Paul Jens Peter Ross
Bestimmung des wirtschaftlichen Automatisierungsgrades von Montageprozessen in der frühen Phase der Montageplanung
2002 · 144 Seiten · 38 Abb. · 38 Tab. · 20,5 x 14,5 cm · ISBN 3-8316-0191-7

171 Stefan von Praun
Toleranzanalyse nachgiebiger Baugruppen im Produktentstehungsprozess
2002 · 250 Seiten · 62 Abb. · 7 Tab. · 20,5 x 14,5 cm · ISBN 3-8316-0202-6

172 Florian von der Hagen
Gestaltung kurzfristiger und unternehmensübergreifender Engineering-Kooperationen
2002 · 220 Seiten · 104 Abb. · 20,5 x 14,5 cm · ISBN 3-8316-0208-5

173 Oliver Kramer
Methode zur Optimierung der Wertschöpfungskette mittelständischer Betriebe
2002 · 212 Seiten · 84 Abb. · 20,5 x 14,5 cm · ISBN 3-8316-0211-5

174 Winfried Dohmen
Interdisziplinäre Methoden für die integrierte Entwicklung komplexer mechatronischer Systeme
2002 · 200 Seiten · 67 Abb. · 20,5 x 14,5 cm · ISBN 3-8316-0214-X

175 Oliver Anton
Ein Beitrag zur Entwicklung telepräsenter Montagesysteme
2002 · 158 Seiten · 85 Abb. · 20,5 x 14,5 cm · ISBN 3-8316-0215-8

176 Welf Broser
Methode zur Definition und Bewertung von Anwendungsfeldern für Kompetenznetzwerke
2002 · 224 Seiten · 122 Abb. · 20,5 x 14,5 cm · ISBN 3-8316-0217-4

177 Frank Breitinger
Ein ganzheitliches Konzept zum Einsatz des indirekten Metall-Lasersinterns für das Druckgießen
2003 · 156 Seiten · 20,5 x 14,5 cm · ISBN 3-8316-0227-1

178 Johann von Pieverling
Ein Vorgehensmodell zur Auswahl von Konturfertigungsverfahren für das Rapid Tooling
2003 · 163 Seiten · 88 Abb. · 20,5 x 14,5 cm · ISBN 3-8316-0230-1

179 Thomas Baudisch
Simulationsumgebung zur Auslegung der Bewegungsdynamik des mechatronischen Systems Werkzeugmaschine
2003 · 190 Seiten · 67 Abb. · 8 Tab. · 20,5 x 14,5 cm · ISBN 3-8316-0249-2

180 Heinrich Schieferstein
Experimentelle Analyse des menschlichen Kausystems
2003 · 132 Seiten · 20,5 x 14,5 cm · ISBN 3-8316-0251-4

181 Joachim Berlak
Methodik zur strukturierten Auswahl von Auftragsabwicklungssystemen
2003 · 244 Seiten · 20,5 x 14,5 cm · ISBN 3-8316-0258-1

182 Christian Meierlohr
Konzept zur rechnergestützten Integration von Produktions- und Gebäudeplanung in der Fabrikgestaltung
2003 · 181 Seiten · 84 Abb. · 20,5 x 14,5 cm · ISBN 3-8316-0292-1

183 Volker Weber
Dynamisches Kostenmanagement in kompetenzzentrierten Unternehmensnetzwerken
2004 · 210 Seiten · 64 Abb. · 20,5 x 14,5 cm · ISBN 3-8316-0330-8

184 Thomas Bongardt
Methode zur Kompensation betriebsabhängiger Einflüsse auf die Absolutgenauigkeit von Industrierobotern
2004 · 170 Seiten · 40 Abb. · 20,5 x 14,5 cm · ISBN 3-8316-0332-4

185 Tim Angerer
Effizienzsteigerung in der automatisierten Montage durch aktive Nutzung mechatronischer Produktkomponenten
2004 · 180 Seiten · 67 Abb. · 20,5 x 14,5 cm · ISBN 3-8316-0336-7

186 Alexander Krüger
Planung und Kapazitätsabstimmung stückzahlflexibler Montagesysteme
2004 · 197 Seiten · 83 Abb. · 20,5 x 14,5 cm · ISBN 3-8316-0371-5

187 Matthias Meindl
Beitrag zur Entwicklung generativer Fertigungsverfahren für das Rapid Manufacturing
2005 · 222 Seiten · 97 Abb. · 20,5 x 14,5 cm · ISBN 3-8316-0465-7

188 Thomas Fusch
Betriebsbegleitende Prozessplanung in der Montage mit Hilfe der Virtuellen Produktion am Beispiel der Automobilindustrie
2005 · 190 Seiten · 99 Abb. · 20,5 x 14,5 cm · ISBN 3-8316-0467-3

189 Thomas Mosandl
Qualitätssteigerung bei automatisiertem Klebstoffauftrag durch den Einsatz optischer Konturfolgesysteme
2005 · 182 Seiten · 58 Abb. · 20,5 x 14,5 cm · ISBN 3-8316-0471-1

190 Christian Patron
Konzept für den Einsatz von Augmented Reality in der Montageplanung
2005 · 150 Seiten · 61 Abb. · 20,5 x 14,5 cm · ISBN 3-8316-0474-6

191 Robert Cisek
Planung und Bewertung von Rekonfigurationsprozessen in Produktionssystemen
2005 · 200 Seiten · 64 Abb. · 20,5 x 14,5 cm · ISBN 3-8316-0475-4

192 Florian Auer
Methode zur Simulation des Laserstrahlschweißens unter Berücksichtigung der Ergebnisse vorangegangener Umformsimulationen
2005 · 160 Seiten · 65 Abb. · 20,5 x 14,5 cm · ISBN 3-8316-0485-1

193 Carsten Selke
Entwicklung von Methoden zur automatischen Simulationsmodellgenerierung
2005 · 137 Seiten · 53 Abb. · 20,5 x 14,5 cm · ISBN 3-8316-0495-9

194 Markus Seefried
Simulation des Prozessschrittes der Wärmebehandlung beim Indirekten-Metall-Lasersintern
2005 · 216 Seiten · 82 Abb. · 20,5 x 14,5 cm · ISBN 3-8316-0503-3

195 Wolfgang Wagner
Fabrikplanung für die standortübergreifende Kostensenkung bei marktnaher Produktion
2006 · 208 Seiten · 43 Abb. · 20,5 x 14,5 cm · ISBN 3-8316-0586-6

196 Christopher Ulrich
Erhöhung des Nutzungsgrades von Laserstrahlquellen durch Mehrfach-Anwendungen
2006 · 178 Seiten · 74 Abb. · 20,5 x 14,5 cm · ISBN 3-8316-0590-4

197 Johann Härtl
Prozessgaseinfluss beim Schweißen mit Hochleistungsdiodenlasern
2006 · 140 Seiten · 55 Abb. · 20,5 x 14,5 cm · ISBN 3-8316-0611-0

198 Bernd Hartmann
Die Bestimmung des Personalbedarfs für den Materialfluss in Abhängigkeit von Produktionsfläche und -menge
2006 · 208 Seiten · 105 Abb. · 20,5 x 14,5 cm · ISBN 3-8316-0615-3

199 Michael Schilp
Auslegung und Gestaltung von Werkzeugen zum berührungslosen Greifen kleiner Bauteile in der Mikromontage
2006 · 130 Seiten · 20,5 x 14,5 cm · ISBN 3-8316-0631-5

200 Florian Manfred Grätz
Teilautomatische Generierung von Stromlauf- und Fluidplänen für mechatronische Systeme
2006 · 192 Seiten · 20,5 x 14,5 cm · ISBN 3-8316-0643-9

201 Dieter Eireiner
Prozessmodelle zur statischen Auslegung von Anlagen für das Friction Stir Welding
2006 · 214 Seiten · 20,5 x 14,5 cm · ISBN 3-8316-0650-1

202 Gerhard Volkwein
Konzept zur effizienten Bereitstellung von Steuerungsfunktionalität für die NC-Simulation
2007 · 192 Seiten · 20,5 x 14,5 cm · ISBN 978-3-8316-0668-9

203 Sven Roeren
Komplexitätsvariable Einflussgrößen für die bauteilbezogene Struktursimulation thermischer Fertigungsprozesse
2007 · 224 Seiten · 20,5 x 14,5 cm · ISBN 978-3-8316-0680-1

204 Henning Rudolf
Wissensbasierte Montageplanung in der Digitalen Fabrik am Beispiel der Automobilindustrie
2007 · 200 Seiten · 20,5 x 14,5 cm · ISBN 978-3-8316-0697-9

205 Stella Clarke-Griebsch
Overcoming the Network Problem in Telepresence Systems with Prediction and Inertia
2007 · 150 Seiten · 20,5 x 14,5 cm · ISBN 978-3-8316-0701-3

206 Michael Ehrenstraßer
Sensoreinsatz in der telepräsenten Mikromontage
2008 · 160 Seiten · 20,5 x 14,5 cm · ISBN 978-3-8316-0743-3

207 Rainer Schack
Methodik zur bewertungsorientierten Skalierung der Digitalen Fabrik
2008 · 248 Seiten · 20,5 x 14,5 cm · ISBN 978-3-8316-0748-8

208 Wolfgang Sudhoff
Methodik zur Bewertung standortübergreifender Mobilität in der Produktion
2008 · 276 Seiten · 20,5 x 14,5 cm · ISBN 978-3-8316-0749-5

209 Stefan Müller
Methodik für die entwicklungs- und planungsbegleitende Generierung und Bewertung von Produktionsalternativen
2008 · 240 Seiten · 20,5 x 14,5 cm · ISBN 978-3-8316-0750-1

210 Ulrich Kohler
Methodik zur kontinuierlichen und kostenorientierten Planung produktionstechnischer Systeme
2008 · 232 Seiten · 20,5 x 14,5 cm · ISBN 978-3-8316-0753-2

211 Klaus Schlickenrieder
Methodik zur Prozessoptimierung beim automatisierten elastischen Kleben großflächiger Bauteile
2008 · 204 Seiten · 20,5 x 14,5 cm · ISBN 978-3-8316-0776-1

212 Niklas Möller
Bestimmung der Wirtschaftlichkeit wandlungsfähiger Produktionssysteme
2008 · 260 Seiten · 20,5 x 14,5 cm · ISBN 978-3-8316-0778-5

213 Daniel Siedl
Simulation des dynamischen Verhaltens von Werkzeugmaschinen während Verfahrbewegungen
2008 · 200 Seiten · 20,5 x 14,5 cm · ISBN 978-3-8316-0779-2

214 Dirk Ansorge
Auftragsabwicklung in heterogenen Produktionsstrukturen mit spezifischen Planungsfreiräumen
2008 · 146 Seiten · 20,5 x 14,5 cm · ISBN 978-3-8316-0785-3

215 Georg Wünsch
Methoden für die virtuelle Inbetriebnahme automatisierter Produktionssysteme
2008 · 224 Seiten · 20,5 x 14,5 cm · ISBN 978-3-8316-0795-2

216 Thomas Oertli
Strukturmechanische Berechnung und Regelungssimulation von Werkzeugmaschinen mit elektromechanischen Vorschubantrieben
2008 · 194 Seiten · 20,5 x 14,5 cm · ISBN 978-3-8316-0798-3

217 Bernd Petzold
Entwicklung eines Operatorarbeitsplatzes für die telepräsente Mikromontage
2008 · 234 Seiten · 20,5 x 14,5 cm · ISBN 978-3-8316-0805-8

218 Loucas Papadakis
Simulation of the Structural Effects of Welded Frame Assemblies in Manufacturing Process Chains
2008 · 260 Seiten · 20,5 x 14,5 cm · ISBN 978-3-8316-0813-3

219 Mathias Mörtl
Ressourcenplanung in der variantenreichen Fertigung
2008 · 210 Seiten · 20,5 x 14,5 cm · ISBN 978-3-8316-0820-1

220 Sebastian Weig
Konzept eines integrierten Risikomanagements für die Ablauf- und Strukturgestaltung in Fabrikplanungsprojekten
2008 · 232 Seiten · 20,5 x 14,5 cm · ISBN 978-3-8316-0823-2

221 Tobias Hornfeck
Laserstrahlbiegen komplexer Aluminiumstrukturen für Anwendungen in der Luftfahrtindustrie
2008 · 150 Seiten · 20,5 x 14,5 cm · ISBN 978-3-8316-0826-3

222 Hans Egermeier
Entwicklung eines Virtual-Reality-Systems für die Montagesimulation mit kraftrückkoppelnden Handschuhen
2008 · 210 Seiten · 20,5 x 14,5 cm · ISBN 978-3-8316-0833-1

223 Matthäus Sigl
Ein Beitrag zur Entwicklung des Elektronenstrahlsinterns
2008 · 185 Seiten · 20,5 x 14,5 cm · ISBN 978-3-8316-0841-6

224 Mark Harfensteller
Eine Methodik zur Entwicklung und Herstellung von Radiumtargets
2009 · 196 Seiten · 20,5 x 14,5 cm · ISBN 978-3-8316-0849-8

225 Jochen Werner
Methode zur roboterbasierten förderbandsynchronen Fließmontage am Beispiel der Automobilindustrie
2009 · 210 Seiten · 20,5 x 14,5 cm · ISBN 978-3-8316-0857-7

226 Florian Hagemann
Ein formflexibles Werkzeug für das Rapid Tooling beim Spritzgießen
2009 · 226 Seiten · 20,5 x 14,5 cm · ISBN 978-3-8316-0861-4

227 Haitham Rashidy
Knowledge-based quality control in manufacturing processes with application to the automotive industry
2009 · 212 Seiten · 20,5 x 14,5 cm · ISBN 978-3-8316-0862-1

228 Wolfgang Vogl
Eine interaktive räumliche Benutzerschnittstelle für die Programmierung von Industrierobotern
2009 · 200 Seiten · 20,5 x 14,5 cm · ISBN 978-3-8316-0869-0

229 Sonja Schedl
Integration von Anforderungsmanagement in den mechatronischen Entwicklungsprozess
2009 · 160 Seiten · 20,5 x 14,5 cm · ISBN 978-3-8316-0874-4

230 Andreas Trautmann
Bifocal Hybrid Laser Welding – A Technology for Welding of Aluminium and Zinc-Coated Steels
2009 · 314 Seiten · 20,5 x 14,5 cm · ISBN 978-3-8316-0876-8

231 Patrick Neise
Managing Quality and Delivery Reliability of Suppliers by Using Incentives and Simulation Models
2009 · 200 Seiten · 20,5 x 14,5 cm · ISBN 978-3-8316-0878-2